Simulations of acoustic transmission loss of Fin whale calls reaching the LoVe Ocean Observatory

Author: Sigrid Husebø Øygard

Master of Science
Thesis in Acoustics

Department of Physics and Technology
University of Bergen

November 2018

Abstract

Equinor has plans to develop a whale monitoring station using acoustic animal destiny estimation at their cabled ocean observatory, the LoVe Observatory, in Lofoten-Vesterålen basin. The fauna of this area is of remarkable importance to the Norwegian economy due to its unique fishing banks and its newly discovered petroleum reserves. This makes it important to monitor the Fin whale population in the area, especially if human interference in the region is to be increased due to new petroleum related interventions. Moreover, the observatory will hopefully bring about new knowledge of the habitat and migratory routes of the Fin whale, which are currently poorly understood. In order to implement an animal density estimation algorithm at the LoVe Observatory it is necessary to know how the transmission loss experienced by sounds reaching the observatory varies as a function of position around the receiver. This study has developed a set of model tools fit to simulate the transmission loss at any position in the Lofoten-Vesterålen basin, by using environmental data available at various databases as input parameters to the parabolic equation model Range-dependent Acoustic Model (RAM). The study has utilized these tools to produce simulations of the transmission loss at a number of example transects, in order to present some conclusions about how the transmission loss is affected by the environmental parameters bathymetry, sound speed profiles and sedimentary geoacoustic properties. Furthermore, the simulations have been repeated for each of the four seasons, to look at how the transmission loss varies across the year. Generally, the study will show that the variation of transmission loss with position is complex and that the inclusion of environmental parameters in the simulations is necessary. It will be shown that the observatory is capable of detecting Fin whales at 190 km in low noise conditions, but that this range is limited by the angular direction of the propagation path and by increases in the noise level. Seasonal variability in the transmission loss will be shown, but it has not been possible connect this variation to the observed yearly variation in Fin whale detections.

Acknowledgements

A great thank you to my two supervisors Geir Pedersen at Christian Michelsen Research AS and Per Lunde at the University of Bergen for the support and guidance you have provided throughout this project. You have given me productive discussions and our collaboration has been enjoyable! A special thank you also to my former colleague Greg White for always taking the time to discuss topics from my research to help me reach interesting and new conclusions. Thank you also to both Greg White and Charlie House for taking the time to help me sort out technical issues. Lastly, I would like to thank my wonderful parents for their immense support throughout this project. Thank you also for valuable proofreading.

List of Symbols

A	Fractional amount of sediment composition
B	Bulk modulus
I	Sound intensity
N	Number of simulated planes
O	Area
P	The radial derivative operator
P_h	Hydrostatic pressure
Q	The square-root operator
R	Pressure reflection coefficient
S	Salinity
T	Temperature
V_R	Velocity ratio
W	Bandwidth
ΔP_{SSP}	The pressure resolution of the constructed SSP
Δr	Radial resolution
Δr_{SSP}	The radial step between each sound speed profile interpolation.
Δz	Depth resolution
Φ'	Estimated mean grain size for sediment type (mm)
Φ	Mean grain diameter in millimeters
Θ	Longitude
α_m	Attenuation coefficient in $\mathrm{dB\,m^{-1}}$

α_λ	Attenuation coefficient in dB/λ
α_{cm}	Attenuation coefficient in $\mathrm{dB\,cm^{-1}}$
α_{km}	Attenuation coefficient in $\mathrm{dB\,km^{-1}}$
η	Fractional porosity
$\frac{1}{Q^{(\alpha)}}$	Specific attenuation factor
γ	Mean vertical gradient of gravity
$\hat{D}$	Estimated population density
$\hat{P}$	Probability of detection
$\hat{m}$	Multiplication factor
λ	Wavelength
$\mathcal{R}$	Rayleigh parameter
μ, ϵ	Operators used to abbreviate q
$\overline{\Phi}$	Average grain size of sediment texture
ϕ'	Estimated mean grain size for sediment type (units of phi)
ϕ	Mean grain size in phi units
ψ	Envelope function
ρ	Density
ρ_B	Bulk density of the sediment
ρ_b	Density of the sea bottom material
ρ_g	Density of the sediment grains
ρ_w	Density of the water
DI	Directivity index
DT	Detection threshold
NL	Noise level
NSL	Noise spectrum level
SL	Source level
SNR	Signal-to-noise-ratio
TL	Transmission loss

$\mathrm{TL}_{\text{max, high noise}}$	The maximum threshold for transmission loss at high noise conditions
$\mathrm{TL}_{\text{max, low noise}}$	The maximum threshold for transmission loss at low noise conditions
θ	The angular position variable
θ_i	Incident angle
θ_t	Transmitted angle
$\tilde{\theta}$	Propagation angle, with respect to the horizontal
$\tilde{p}$	Modified pressure variable used in RAM
$\tilde{q}$	Modified depth operator used in RAM
φ	Latitude
a_0, a_1, b_0, b_1	Coefficients in rational-function approximations
$a_{j,m}$, $b_{j,m}$	Padé approximation coefficients
c	Speed of sound
c	Speed of sound
c_0	Normalization sound speed
c_b	Compressional sound velocity in the sea floor
c_w	Speed of sound in sea water
$d_f(r, \theta)$	Detection function
$d_p(r, \theta)$	Probability density function of whale calling locations
e_a	Number of detected acoustic events
f	Frequency
g	Acceleration due to gravity at sea level
g_e	Acceleration due to gravity at sea-level at the equator
h	Material specific constant
k	Wavenumber
k_0	Reference wave number
l	Frequency exponent of sediment attenuation
m	Number of terms in the Padé approximation

n	Index of refraction
n_s	Stability parameter
ndz and ndr	Decimation factors
p	Acoustic pressure
q	Depth operator used by Tappert
q^*	Depth operator used by Collins
r	Radial distance from the origin
r_b	Ranges of the specified bathymetry
r_p	Range position of a new block
r_s	Stability restriction range
t	Time
w	Maximum radial distance of detection
x	Cartesian position coordinate
y	Cartesian position coordinate
z	Depth below sea-level
z_b	Depth of the bathymetry
z_{source}	Depth of the sound source
${H_0}^{(1)}$	Hankel function of the first kind and zeroth order
CTD	Conductivity, temperature and depth
PSC	Product specification code
RAM	Range-dependent Acoustic Model
SOFAR	Sound Fixing and Ranging
SOSI	Samordnet Opplegg for Stedfestet Informasjon. Translates to Co-ordinated Scheme for Location Based Information
SSP	Sound speed profile

Contents

Chapter 1

Introduction

The Norwegian continental shelf off the coast of Lofoten and Vesterålen is a hot-spot for several important sectors of the Norwegian economy. The shelf is narrow, compared with the rest of the country, and this fosters unique oceanographic conditions because of the strong and dynamic northern drift of Atlantic water. The area hosts large oceanic fish stocks, feeding grounds for many fish predators, as well as both spawning and feeding grounds for larvae of many species (Godø and Torkelsen, 2014). The internationally renowned fishing banks in the area are therefore considered the most important areas for commercial fishing in Norway (Buhl-Mortensen et al., 2015). It is therefore controversial that investigations by the Norwegian Petroleum Directorate have indicated that the area also holds large gas and petroleum reserves (Buhl-Mortensen et al., 2015). These reserves have been subject to much political debate, and have not yet been opened for exploration. A successful potential co-existence between the fishery and the petroleum industries, as well as a sustainable continued utilization of the biological resources in the area, will require extensive knowledge of the biodynamics of the area.

Equinor (former Statoil ASA) and the Institute of Marine Research have therefore initiated a collaborative research project which has set out to monitor some of the most vulnerable habitats on and around the northern Norwegian continental shelf. The project is mainly focused on rare cold-water coral reef habitats, but also explores different biological and oceanographic phenomenon in the region. In 2013 the project launched the LoVe Ocean Observatory in a sub-sea valley about 20 km from the coast of Lofoten, Norway (Godø and Torkelsen, 2014). The observatory lies in the Norwegian Sea, in the vicinity of the Lofoten archipelago, where the continental shelf is relatively shallow (Maystrenko et al., 2017). The shelf consists of large and flat banks, separated by deeper troughs. The first of seven planned data collecting nodes have been installed in one of these troughs called the Hola valley (Buhl-Mortensen et al., 2015). This part of the observatory lies at 258 m below sea level, and has collected data on biomass distributions and densities since the launch in 2013. The observatory uses technology provided by Metas AS and includes both active and passive acoustic sensors, cameras, and several oceanographic and environmental sensors (Godø and Torkelsen, 2014). Figure 1.1, which is made by Pedersen (2018), shows an illustration of the bathymetry around the obser-

vatory. The hydrophone discussed in this thesis lies on the node marked 1 in the figure, and henceforth this is here referred to as the LoVe Observatory.

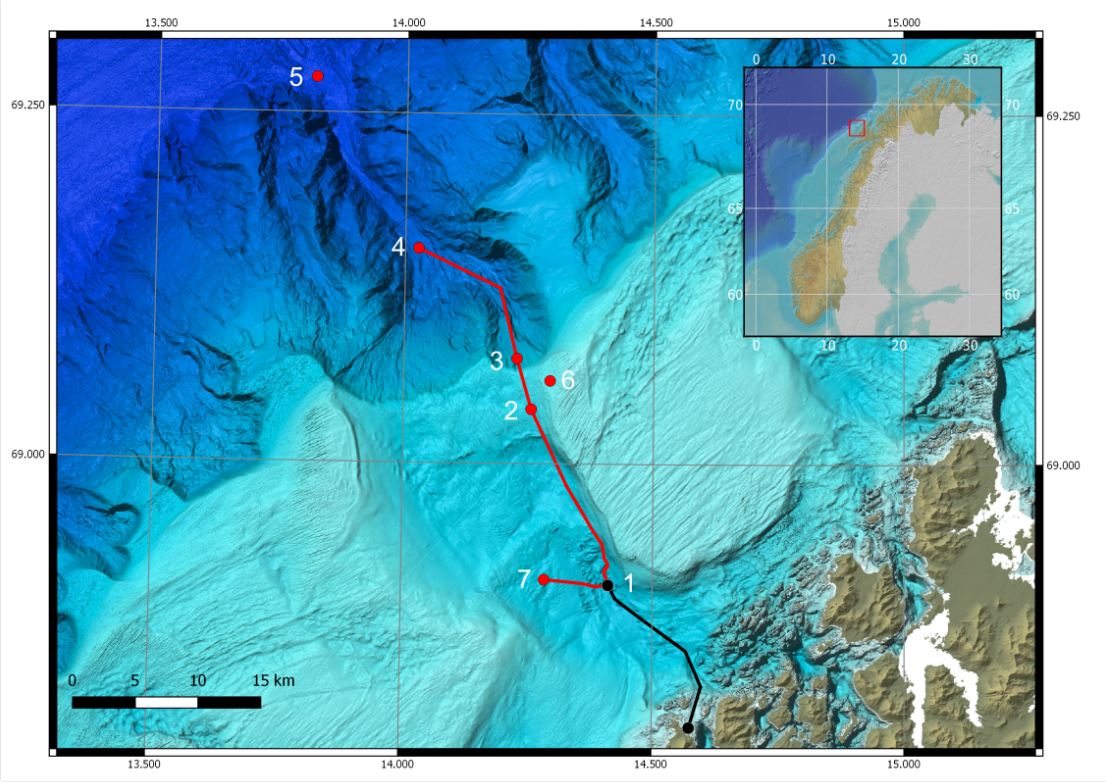

Figure 1.1: An illustration of the bathymetry in the area surrounding the LoVe Observatory. The hydrophone discussed in this thesis is located at the node marked 1 on the figure. The figure is made by Pedersen (2018), using a shadow relief of the bathymetry by Kartverket (2018c).

To the west of the flat banks and the Hola valley, there is a dramatic drop in the bathymetry, down to the deep-sea domain of the Norwegian sea, known as the Lofoten basin (Maystrenko et al., 2017). Together with Hola valley, the Egga bank, to the south of the valley, and the Vesterålen bank, to the north, these areas make up the Lofoten-Vesterålen basin. The border between the shallow banks and the deep plains is known as the Egga Ridge. The steep slope of the ridge causes up-well of nutrient rich water, making it an ideal habitat for many species. In particular, the Lofoten-Vesterålen basin houses the habitat of a many cetaceans, who prey on the rich fauna of fish, crustaceans and plankton (Institute of Marine Research, 2018).

1.1 Cetaceans in the Lofoten-Vesterålen basin

There are about 20 species of cetaceans, also known as whales, in the Norwegian seas (Institute of Marine Research, 2018). This family of marine mammals can be divided into two subfamilies; baleen whales (*Mysticetes*) and toothed whales (*Odontocetes*). Toothed whales feed by hunting prey such as fish, squid and small mammals. In lack of good light penetration in the ocean, toothed whales use acoustic echolocation to localize its prey (Bjørge et al., 2010). This sound is highly directive and its frequency content is typically in the ultrasonic range, or at least in the range of a few kilo Hertz, depending on the species (Wahlberg et al., 2011; Herzing and Johnson, 2015; Samarra et al., 2010; Møhl et al., 2003). Baleen whales feed by sieving water through a comblike structure in their mouths, called baleens, thus catching small animals and plankton. They use vocalisation to navigate and to communicate, for social reasons like mating and to mark their territories. They have a wide repertoire of sounds, like whistles, creaks, moans and grunts, and their vocalisation is often thought of as songs. (White, 2015a). The baleen whale species found in the Norwegian sea include Fin whale (*Balaenoptera physalus*), Blue whale (*Balaenoptera musculus*), Sei whale (*Balaenoptera borealis*), Common minke whale (*Balaenoptera acutorostrata*), and Humpback whale (*Megaptera novaeangliae*) (Haug, 1998).

The two latter of these are the smaller of the baleen whales. They exhibit complex vocalization repertoires. Both species' repertoires consist of multiple different call types, including low frequency whops and snorts, cries, complex songs, and high frequency shrieks and horn blasts (Oswald and Duennebier, 2011; Dunlop et al., 2008; Institute of Marine Research, 2018; Thompson et al., 1986). On the other hand, the three larger baleen whales have quite characteristic, high-intensity, low frequency calls. The lowest frequency content belongs to the Blue whale, which vocalizes between 8 to 36 Hz (Parks and Clark, 2012). The Fin whale calls in a similar range, from 15 to 30 Hz (Halkias et al., 2013), while the Sei whale repertoire is slightly higher, from 34 to 87 Hz (Calderan et al., 2014). These large baleen whales inhabit deep, open waters (Haug, 1998) and their calls have been known to travel great distances (Hiyoshi et al., 2004; Parks and Clark, 2012), because the low frequency cause little attenuation of the signal. Whereas calls from mysticetes and the smaller baleen whales are only detectable at close ranges, the high-intensity combined with the low frequency of the large baleen whale calls makes it possible to detect them at great ranges. These species are thus ideal for long-range, passive acoustic detection and monitoring.

According to Pedersen (2018), Blue whale calls have not been detected at the LoVe Observatory. It is not known whether this is because the species are not located in the proximity of the observatory, or if it is due to the propagation paths of their sounds not reaching the hydrophone. On the other hand, the calls from Fin whales, the species with the second most low frequent calls, have been readily detected at the LoVe Observatory (Pedersen, 2018). Figure 1.2 shows the long-term spectral average of recordings made by the LoVe Observatory in the period October 2014 - November 2015. The spectogram is made by Pedersen (2018), averaging over 5 minutes and using a 1 s Hann window with 50 % overlap. The recordings are not continuous, because the observatory has been out of

service in some periods. The figure clearly shows the presence of a low frequency sound, at approximately 20 Hz, shown as a horizontal yellow and red line in the plot. According to Pedersen (2018), this has been identified as Fin whale calls. Notably, the calls are not detected from March - August. It is not known if this is because the Fin whales are not present in the surrounding ocean at this time, or if the effect of the seasons on the transmission loss experienced by the calls cause the signals to be attenuated beyond detectability during these months.

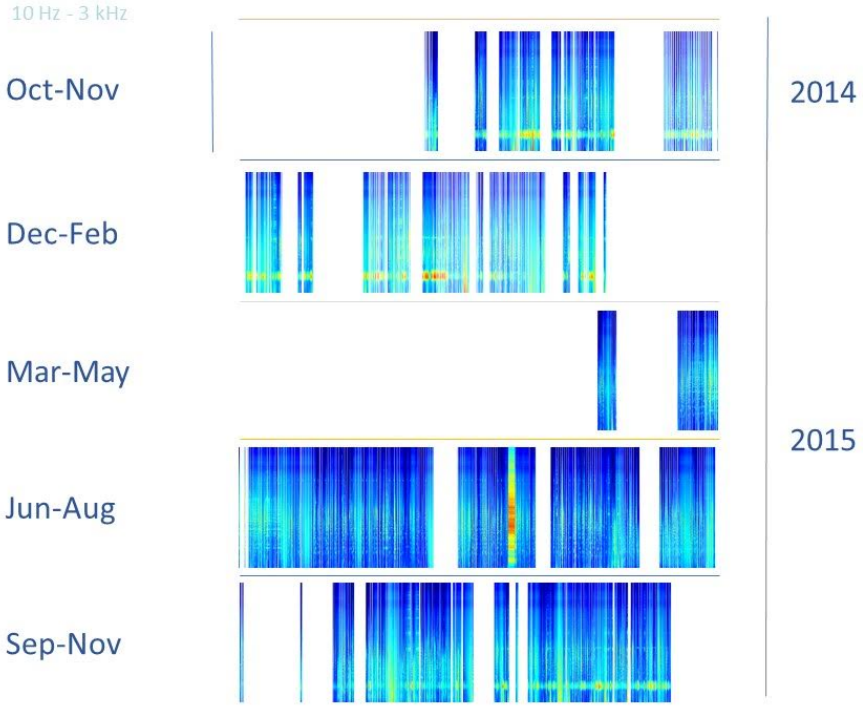

Figure 1.2: Long-term spectral average from 10 Hz to 3 kHz of recordings made by the LoVe Observatory. The plots show the spectral content of the recordings as a function of time on the horizontal axis and the logarithm of frequency on the vertical axis. The plots are made by Pedersen (2018).

The Fin whale calls recorded by the LoVe Observatory are typical in frequency content compared with published recordings. Fin whale calls are often referred to as '20 Hz-bouts', even though a downward sweeping frequency from about 23 Hz to 18 Hz is usually present (Watkins et al., 1987). Charif et al. (2002) have estimated the source level of the call by recording 34 individuals using a towed array of calibrated hydrophones. They corrected the recorded levels for effects of surface reflections, and found that the median source level was 180 dB re 1 µPa at 1 m, with a range of 159 dB - 184 dB re 1 µPa at 1 m. Watkins et al. (1987) have analysed more than 4000 hours of recordings of Fin whales at various geographical locations and found that when the Fin whale produces

the 20 Hz-bout, its behaviour is quite stereotyped. The animal moves slowly and appears to be vocalizing at 50 m depth. The 20 Hz-bouts are heard all year round and are not connected to feeding behaviour. The bouts are believed to be produced to communicate with other individuals (Watkins, 1981).

The habitat of Fin whales in the North Atlantic reaches from the ice-edge all the way south to 30° latitude. Figure 1.3 shows the habitat of the Fin whale, as it has been classified by the Institute of Marine Research (Øien, 2018). Visual surveying of the Fin whale population, on behalf of the International Whaling Commission, started in 1987. They estimated the population of Fin whales in the Norwegian Sea in the summer to some thousands (Christensen et al., 1992), and the population has since been slowly increasing (Røttingen, 2015). Most of the sightings reported by the visual surveying occurred in the Norwegian Sea and outside Lofoten (Christensen et al., 1992), curiously not coinciding with the summer feeding areas in figure 1.3. The whereabouts of the Fin whale during the winter season are even more unclear. They are more abundant in the northern latitudes during the summer season, suggesting that some north-south migration occurs (Christensen et al., 1992). Ingebrigtsen (1929) proposed that part of the population stays in the Atlantic Barents Sea during the winter season. And Haug (1998) suggest that some of the individuals are stationary outside the coast of Norway. Even so, the general consensus is that some form of migration occurs (Millais, 1906; Øien, 2018; Christensen et al., 1992; Haug, 1998). Unlike other baleen whales, the movement

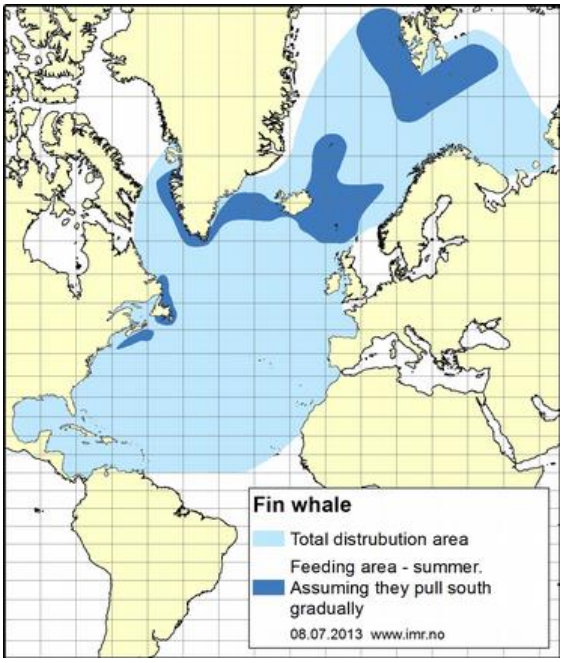

Figure 1.3: The habitat of the Fin whale in the Atlantic Ocean, as classified by the Institute of Marine Research. The figure has been copied from Øien (2018). The total distribution area is shown in light blue and the feeding area (assuming the mammals pull south gradually) is shown in dark blue.

of the Fin whale does not appear to be determined by the climate in the waters, or connected to their breeding (Kellogg, 1928). Rather, Fin whales appear to migrate according to the changes in the availability of nutrients in the water (Hjort, 1902). For example, Christensen et al. (1992) reported a connection between the migration of Fin whales and the abundance of herring and capelin in the waters. In general, little is known of these migration routes (Christensen et al., 1992; Øien, 2018).

1.2 Motivation

There remains large uncertainty about the specific locations of both the habitats and the migratory routes of Fin whales. The fact that Fin whale calls are present in the recordings made by the LoVe Observatory, and that these vary in intensity across the seasons, seem to suggest that the Lofoten basin is either a temporary habitat for Fin whales or that their migratory routes pass by the observatory. Therefore, an acoustic animal density estimation algorithm is to be implemented at the LoVe Observatory (Pedersen, 2018). This will contribute to a better understanding of the Fin whale territories. The density estimates can potentially aid understanding of both the migratory routes and any patterns in the Fin whale's whereabouts. Also, much of the current knowledge of Fin whale behaviour is based on outdated publications, such as Ingebrigtsen (1929), Millais (1906) and Kellogg (1928). And as pointed out by Christensen et al. (1992), the migratory behaviour of the Fin whale are most likely not constant with time, due to changes in the environment and in the stock of its prey. It is therefore desirable to update the current knowledge on Fin whale migration. The installation of an animal density estimation system at the LoVe Observatory allows for continued updates of this knowledge in the future.

Moreover, monitoring of the whale populations in the Lofoten-Vesterålen basin, which is utilized for commercial industries, is of paramount importance in order to assess the impacts of human interference on whale habitats. There are several reported instances of human activities adversely affecting cetaceans. Most often, these activities involve overfishing, pollution, ship-strikes, or disturbance or trauma due to acoustic events (White, 2015a). The latter is of particular concern if the Lofoten-Vesterålen area is to be opened up for petroleum exploration. Such activities will involve a heightened overall noise level in the basin, due to shipping, drilling, and other industrial activities. According to the Norwegian Petroleum Directorate, the effect of this noise is not fully known, but there is a concern that the noise will mask the acoustic signals used by the cetaceans for hunting and communication (Jarandsen, 2011). Another concerning aspect of petroleum exploration is the high-intensity noise produced by seismic surveying. Similar high-energy acoustic sources such as sonars have been attributed as the cause for several beachings of whales. For example, in 1996 a NATO sonar test caused a mass stranding of Beaked whales in Greece (Frantzis, 2003), and in 2000 a sonar exercise by the United States Navy is believed to have caused 17 cetaceans to have beached in the Bahamas (Evans and England, 2001). Other, less severe consequences, such as behavioural changes and hearing loss, are also feared as a result of human made high-intensity noises. A review of

the studies that have investigated the effect of seismic air-gun noise have been composed by Gordon et al. (2004). They remark that although the full extent to which seismic surveying affects marine mammals is fairly poorly known, regulatory restrictions and a precautionary approach is recommended.

Therefore, if the Lofoten-Vesterålen basin is to be opened up for petroleum exploration, surveying and monitoring of the local whale population should be performed. Visual monitoring of whales is common, but in rough seas, poor weather, at night, and in particular with deep-diving whales such as the baleen whales found in the Norwegian sea, this is not very effective (White, 2015a). An alternative to visual detection is acoustic monitoring using subsea hydrophones which detect the sounds made by the animals. In a comparison between visual detection of baleen whales outside the British Isles and detection using acoustic recordings of the whale calls, Charif and Clark (2009) found high acoustic detection in periods where the visual detection was low. Passive acoustic monitoring of the whales is therefore believed to be more accurate than visual monitoring.

1.3 Literature on acoustic density estimation of mammals

Acoustic monitoring of the population can be done by estimating population densities from the number of detected whale call events. This method has already been implemented at several sites across the globe, and according to Helble et al. (2013) significant progress has been made in recent years in developing reliable algorithms for such estimation. Generally, an estimate of the density of animals in the area O, is given by

$$\hat{D} = \frac{e_a}{O}\hat{m}, \tag{1.1}$$

where $\hat{D}$ is an estimate of the number of animals per unit area, e_a is the number of detected acoustic events, and $\hat{m}$ is some multiplication factor which converts the number of acoustic events to the number of animals in the area (Thomas and Marques, 2012).

In most cases, one cannot be sure that the hydrophone or hydrophones used will be able to capture all sounds produced by whales in the surveyed area. In these cases, a detection probability, $\hat{P}$, must be estimated and included in $\hat{m}$. This is a measure of the probability of detecting the whale call as a function of distance from the receiver. The multiplication factor can be comprised of a number of different variables, in order to include effects such as false positives, false negatives, group foraging behaviour of the mammals, amongst others. These factors are all multiplied together to give $\hat{m}$, so that

$$\hat{m} = \hat{P} \cdot \text{other factors}. \tag{1.2}$$

The factors can be determined using a number of different methods, depending on for instance the number of hydrophones used and the frequency range of the mammal. Many of the methods that have been applied at current ocean observatories are summarized by Thomas and Marques (2012).

One of the preferred ways of determining $\hat{P}$ is a localization method where several hydrophones are used to identify the distances to calling whales, and $\hat{P}$ is estimated based on a probability density function of the determined distances. This method has for instance been employed by Martin et al. (2013), who estimated the density of Minke whales off Hawaii, using 12 bottom-mounted hydrophones. Another approach was used by Marques et al. (2009), who estimated $\hat{P}$ by connecting tracking data from Blainville's beaked whales with the detected acoustic events at the 82 hydrophones outside the Bahamas. The advantages of these methods are that neither the source level of the whales, nor the transmission loss experienced by the sound need to be known.

However, neither of these methods are viable at the LoVe Observatory. Tracking data of Fin whales in the Lofoten basin have, to the author's knowlegde, not been collected, and doing so would most likely be very costly. Moreover, although expansion of the LoVe Observatory is planned, at the present time, only one hydrophone has been employed at the observatory. McDonald and Fox (1999a) used a single hydrophone to estimate the density of Fin whales north of Oahu, Hawaii. They suggested that $\hat{P}$ can be estimated using a multipath method, where the distance to the calling whale is determined based on the time difference between the received signal reflections from the ocean surface and the bottom. However, as McDonald and Fox (1999a) pointed out, this method is very time-consuming. In addition, the use of surface and bottom reflections is not necessarily viable in the shallow and complex bathymetric environment surrounding the LoVe Observatory. And as pointed out by Helble et al. (2013), a common mistake in analysing recordings of whales is that the effect of environmental properties, such as bathymetry, sound speed profiles, and sediment properties, on the received signal, are overlooked.

Therefore, another method, where $\hat{P}$ is estimated from a model of how sound propagates in the area must be used instead. Unfortunately, this method is both more demanding and less accurate than methods involving multiple hydrophones (Helble et al., 2013). Yet, several studies, such as McDonald and Fox (1999a), Küsel et al. (2011) and Marques et al. (2011), have estimated $\hat{P}$ using this method. According to Helble et al. (2013), when depth dependence is ignored, detection probability can be estimated as

$$\hat{P} = \int_0^w \int_0^{2\pi} d_f(r,\theta) d_p(r,\theta) r \partial r \partial\theta, \tag{1.3}$$

where r is the radial position coordinate, θ is the angular position coordinate, $d_f(r,\theta)$ is the detection function, w is the maximum radial distance of detection, and $d_p(r,\theta)$ is the probability density function of whale calling locations in the horizontal plane. The position coordinates r and θ will be formally defined in the coordinate system shown in figure 2.2 in section 2.3. The environmental variables specific to the geographical location of the receiver are here inherent in the detection function, $d_f(r,\theta)$. In the area surrounding the LoVe Observatory, these parameters can be obtained from various databases. The depth of the bathymetry has been mapped by Kartverket (2018a), and the composition of the sediment has been characterised by Geological Survey of Norway (2016). Lastly, International Council for the Exploration of the Sea (2018) provides measurements of the conductivity, temperature and depth in the water, which can be used to calculate the sound speed.

Estimating $\hat{P}$ using a model of the acoustic propagation has also been done by Küsel et al. (2011), who estimated the population density of Blainville's beaked whales. In their paper, Küsel et al. (2011) lay out a complex account of how the detection function, $d_f(r, \theta)$, and the detection probability, $d_p(r, \theta)$, are estimated using Monte Carlo simulation, in order to calculate $\hat{P}$. This involves combining the performance of the chosen detection and classification algorithm with the detection threshold (DT) of the whale call, calculating a large number of simulated whale calls, and determining if these would or would not have been detected by the hydrophone in question. According to Urick (1983), the detection threshold can in turn be calculated using the sonar equation

$$\mathrm{DT} = \mathrm{SL} - \mathrm{TL} - (\mathrm{NL} - \mathrm{DI}). \tag{1.4}$$

Here, SL is the source level of the mammal, NL is the noise level at the receiver, DI is the directivity index of the receiver, and TL is the transmission loss experienced by the sound before reaching the receiver (Urick, 1983). Both the source level of the whale, the noise level and the directivity index can be estimated based on values from literature. However, the transmission loss is unique to the specific site of the hydrophone performing the mammal density estimation, and for the LoVe Observatory it has never been calculated or otherwise characterised. It is a function of position in all three dimensions, and is dependent on both environmental parameters, and time. In order to start using the LoVe Observatory to do passive acoustic density estimation of mammals, it is necessary to first model how the site-specific transmission loss varies as a function of position and time.

Several models can be used to simulate transmission loss. These include wave number integration techniques, normal mode teqniques, finite element modelling, finite difference modelling, ray tracing, and parabolic equation modelling (Jensen et al., 2011). Generally, the two latter are most commonly used when simulating transmission loss for use in mammal density estimation. Ray tracing is based on a high-frequency approximation (Jensen et al., 2011) and is therefore often used when estimating the density of high-frequent toothed whales. For instance, Küsel et al. (2011) simulated transmission loss using the beam tracing model Bellhop (Porter and Bucker, 1987). However, when working with low frequency calls from Fin whales, the parabolic equation model is preferable. It has been used by both Helble et al. (2013) and McDonald and Fox (1999a). The parabolic equation is based on the pioneering work by Leontovich and Fock (1946), who introduced an approximation to the classical elliptic wave equation to describe propagation of radio waves in the atmosphere. The main advantage of the parabolic equation is that the acoustic field caused by an outwards propagating wave at an arbitrary range can be described by establishing an initial boundary condition and then marching the solution outwards in range. This is done instead of solving the entire acoustic field at all ranges and depths simultaneously (Coppens, 1982). The model also allows for the environmental parameters, such as the speed of sound in the water and in the seabed, as well as and the density and attenuation coefficient of the seabed to be dependent on position (Jensen et al., 2011).

The maximum detection distance, w, used in the calculation of the detection prob-

ability is often simply assumed. In Marques et al. (2009), w is set to 8 km simply based on the fact that this was the furthest away one of the tracked whales swam while it was singing. This assumption was copied in Küsel et al. (2011). Both studies also assume that the detection area, O, is circular. These are, of course, crude assumptions that limit the applicability and the accuracy of the density estimations. Given the large variability of transmission loss with position, it is unlikely that w will be constant at all directions from the receiving hydrophone. Helble et al. (2013), on the other hand, uses calculations of the position and frequency depended transmission loss to calculate w. This is done by simulating a synthetic whale call signal, and using the transmission loss together with the chosen detection and classification algorithm to determine if a signal from a given distance can be detected. Thus, to make the density estimation as accurate as possible, the transmission loss must be determined both as a function of position and as a function of frequency within the bandwidth of the whale call.

1.4 Objectives

This thesis will investigate the transmission loss experienced by Fin whale calls that reach the LoVe Ocean Observatory, so that the observatory can potentially be used for passive acoustic mammal density estimations. The study will seek to identify how the transmission loss varies with position around the observatory, and how the transmission loss varies with season, using the parabolic equation model *Range-dependent Acoustic Model* (RAM) by Collins (2001). The results of this model will then be compared with the commonly used 'simplistic semi-spherical transmission loss model', introduced in equation 2.10, in order to determine if inclusion of the complex environmental parameters is necessary. Moreover, the investigation aims to determine if any areas in the Lofoten-Vesterålen basin cannot be registered by the LoVe Observatory. Of particular interest is the transmission loss experienced by sounds originating on top of the Egga and Vesterålen banks, as well as sounds originating in the Lofoten-basin at locations without direct and straight propagation paths from the source to the receiver. To limit the scope of this thesis, the resulting transmission loss maps in this study will only be shown for 20 Hz. This frequency is chosen because it is the fundamental frequency of the Fin whale call, and as shown in figure 1.2 it is commonly detected at the LoVe Observatory. To verify the validity of the simulated transmission loss models, a convergence test of the results from RAM will be performed. The test will aim to determine the appropriate size of the resolution step-sizes used by RAM.

The study also aims to develop model tools that can be used to characterise the environmental parameters at user specified positions in the area surrounding the LoVe Observatory. The environmental parameters include the depth of the bathymetry, the sound speed in the water as a function of depth, the sound velocity of the sediment, the attenuation coefficient of the sediment, and the density of the sediment. All of these parameters are position dependent. This study will calculate the environmental parameters as a function of position in the Lofoten-Vesterålen basin. The calculations will be made based on available measurements of relevant parameters made in the region,

together with supplementary information from literature.

Moreover, the study will aim to develop a tool that will write the environmental parameters on the specific format needed to run RAM. These tools will be designed so that a user can model the transmission loss at any position in the Lofoten-Vesterålen basin, and at any frequency, within the low-frequency limit of the parabolic equation model. The intention is that these tools can be used in the further development of the LoVe Observatory's density estimation algorithms. They can be used to calculate the transmission loss at positions not shown in this thesis, and at varying frequencies. This will enable calculation of the detection probability, $\hat{P}$, and the determination of the maximum detection range, w, using the previously described method by Helble et al. (2013). It will also be possible to investigate the transmission loss experienced by the calls from other species or other types of sound sources.

1.5 Outline of thesis

Chapter 2 will introduce the theoretic principles used in the transmission loss simulations. This includes the theory of sound propagation, an introduction to models of the geoacoustic properties of ocean sediments, and a presentation of the parabolic equation model. The assumptions inherent in the parabolic equations method will be described, and the model will be derived up to the implementation that is used in RAM. Chapter 3 describes how the environmental input data used in the transmission loss simulations are sourced. This includes bathymetry data, conductivity, temperature and depth measurements used to calculate the variation of sound speed with depth, and data on the composition of the seabed. Chapter 3 then moves on to describe the alterations and processing of the sourced data that had to be performed before the environmental parameters could be used in RAM. The set of environmental parameters resulting from these processes are an important part of the model tools described in section 1.4. The second part of the model tools are the codes which have been written to allow the user to compute the environmental parameters at any position, and the development of these codes are detailed in Chapter 4. This chapter also describes the method used to find the simulation step-sizes by running convergence tests, and the value of the maximum range of the simulations is discussed. Finally, the methods used in the simulations that are run to produce the transmission loss maps shown in this thesis are described. The results of these simulations are shown in Chapter 5. This chapter also contains the calculated sound speed profiles, and the calculated geoacoustic properties of the seabed. The chapter also presents calculations of the average of the sound speed profiles, the results of the convergence tests, as well as a comparison of the transmission loss values produced by RAM with values produced by the 'semi-spherical spreading' model. The presented results are then discussed in Chapter 6. This chapter also contains a review of the chosen modelling methods and a discussion of the validity of the produced results. Finally, the work is summed up and concluded in Chapter 7, and a review of recommendations for future work will be presented.

Chapter 2

Theory

2.1 Propagation of sound in the ocean

Propagation of sound in the ocean is remarkably different from the familiar way sound travels in air. There are several properties of the water which affect how the sound is propagated, such as temperature, salinity, bathymetry, the composition of the ocean floor, hydrostatic pressure, and often these effects also vary significantly with location.

2.1.1 Speed of sound in the ocean

One of the most important of factors determining how sound propagates in the ocean is how the sound speed varies in the water column. The speed of sound, c, in a fluid is given by

$$c = \sqrt{\frac{B}{\rho}}, \tag{2.1}$$

where B is the fluid bulk modulus, and ρ is the density (Jensen et al., 2011). Both of these parameters are affected by the state and material properties of the fluid, and in sea water the most important contributors are density, temperature and salinity. Density is of course itself a function of temperature, but is primarily given by the hydrostatic pressure caused by the depth of the water column. The speed of sound in the ocean, c_w, can be calculated from the empirical function of these variables

$$c_w = 1449.2 + 4.6T - 0.055T^2 + 0.00029T^3 + (1.34 - 0.01T)(S - 35) + 0.016z, \tag{2.2}$$

where T is the temperature in degrees centigrade, S is the salinity in parts per thousand, and z is the depth in meters below sea level (Jensen et al., 2011). The dependence on z causes the speed of sound to vary through the water column. However, in typical oceanic waters c_w does not vary linearly with depth, as equation 2.2 might indicate. Rather, it has a more complex variation because both T and S are also dependent on depth. The

variation of the speed of sound with depth is known as the sound speed profile (SSP), and these profiles will vary with both position and time.

The fact that the speed of sound is not constant with depth gives rise to another important propagation effect, namely refraction. This alters the direction of sound propagation, and will cause complex propagation patterns. The direction in which the sound is travelling is altered by the variation in physical properties of the water. The direction in which the sound is travelling is at all times given by Snell's law

$$\frac{\cos\tilde{\theta}}{c_w} = const. \tag{2.3}$$

Here, $\tilde{\theta}$ is the propagation angle with respect to the horizontal (also known as the grazing angle). This causes the propagation direction to always bend in the direction of lower sound speed (Jensen et al., 2011).

The sound speed profile has been characterised by many researchers across the globe, and some commonly featured layers have been identified (Jensen et al., 2011). Generally, variation in the SSP is most complicated near the surface of the ocean. In the uppermost layer of the ocean, known as the surface layer, the water is heated by the sun and mixed by wind and waves. This typically causes the layer to have significant diurnal variation, dependent on the local weather. In some cases, the temperature in the surface layer becomes independent of depth. The processes causing this are not completely understood, but it is believed that both thermal convection and mixing by wind and waves take part (DeSanto, 1979). Isothermal surface layers are therefore often referred to as the mixed layer (DeSanto, 1979). The speed of sound in the mixed layer will increase with depth because of the dependence of c_w on hydrostatic pressure. This positive gradient in c_w causes sound rays to be continuously refracted towards the surface, giving rise to a surface duct where sound can be propagated over large distances with minimal attenuation (Caruther, 1977).

Below the surface layer, there are typically two thermoclines. A thermocline is a layer in which the temperature changes with depth. First, there is the seasonal thermocline, in which, as the name indicates, the speed of sound is dependent on the season. In this layer, the variation of c_w with depth typically has a negative gradient. The layer is most prominent in the summer and the autumn, when the shallow parts of the ocean are warm (Urick, 1983). Below this follows the main thermocline. In this layer, the temperature decreases with depth, independent of the season, and the speed of sound decreases to a minimum. Finally, below the main thermocline is the deep isothermal layer. Here, the temperature reaches a constant minimum value, determined by the thermodynamic properties of seawater at great pressure. Therefore, the sound speed will again increase with depth because of the dependence on hydrostatic pressure (Urick, 1983).

The combination of the main thermocline and the deep isothermal layer creates a duct where sound is constantly refracted towards the minimum in the SSP. The refraction can cause the sound rays to return to this axis without suffering from reflection losses at the air-water interface nor the sea bottom, thus becoming trapped as if it was travelling in a wave guide. This is known as the Sound Fixing and Ranging (SOFAR) channel (Leighton,

1994). When sound propagates in the SOFAR channel, the refraction causes sound to be concentrated at certain ranges. These areas are known as convergence zones and are typically repeated every 40 km to 60 km along the SOFAR channel (White, 2015b). For low frequency sound, which is subject to little absorption in the oceanic water, the SOFAR channel can propagate sound through remarkable distances. Loud sounds placed on the axis of the SOFAR channel have been shown to travel distances of thousands of kilometers (Jensen et al., 2011). Scientists have hypothesised that certain mammals utilize this phenomenon to communicate over great distances (Lerner, 2018).

2.1.2 Transmission loss in the ocean

Another important aspect of sound propagation in the ocean is how sound strength changes with range. This can be quantified by transmission loss, TL, which is a measure of sound intensity loss over a propagation distance, r, and is given by

$$\mathrm{TL} = 10 \log \left[\frac{I(1)}{I(r)} \right], \tag{2.4}$$

where $I(1)$ is the sound intensity at $r = 1\,\mathrm{m}$ and $I(r)$ is the sound intensity at some distance r (Kinsler et al., 2000). Generally, transmission loss can be divided into three parts; losses due to geometric spreading, losses due to volume scattering, and losses due to absorption (Jensen et al., 2011).

Geometric spreading losses occur because the area over which the sound energy is spread increases with range (Steele et al., 2009). In an open environment, such as a deep ocean, one often assumes that the sound spreads spherically from the source. According to White (2015a), if this was the only contributor to the attenuation, transmission loss would be given as

$$\mathrm{TL}_{geometric} = 20 \log r. \tag{2.5}$$

However, White (2015a) also points out that in shallow water, the sound spreading is limited by reflections off the air-water surface and the bottom of the ocean. If the reflections are perfect and lossless, the spreading will be cylindrical, making the transmission loss due to spreading

$$\mathrm{TL}_{geometric} = 10 \log_{10} r. \tag{2.6}$$

While the model for spherical spreading will often over-estimate the transmission loss in real oceans, the model for cylindrical spreading will, on the other hand, under-estimate the losses. Therefore, transmission loss is often taken to be

$$\mathrm{TL}_{geometric} = 15 \log_{10} r, \tag{2.7}$$

where the geometrical spreading is modelled in-between a spherical and cylindrical model, which can be referred to as 'semi-spherical geometric spreading' (White, 2015a).

Losses due to scattering and absorption are generally described as one quantity, because it is inherently impossible to measure the two separately in the ocean. The transmission loss due to scattering and absorption is given by

$$\mathrm{TL}_{scat+abs} = \alpha_m r, \tag{2.8}$$

where α_m is the total attenuation coefficient in $\mathrm{dB\,m^{-1}}$ (Medwin and Clay, 1998). Volume scattering causes some of the sound energy to be spread in random directions, thus causing the sound intensity in the direction of interest to be reduced. This occurs because of roughness in the air - water surface and the bottom, or because of inhomogeneities in the water, such as bubbles, particles, fish, and other biological matter (Kinsler et al., 2000). The sound intensity is also reduced as absorption turns the energy into heat. This dissipation occurs because of chemical relaxation and viscous losses, and the magnitude of the absorption is dependent on frequency (Kinsler et al., 2000). An estimate of the attenuation coefficient in sea water is given by

$$\alpha_{km} = \Big[\frac{0.08}{0.9 + f^2} + \frac{30}{3000 + f^2} + 4 \times 10^{-4}\Big] f^2, \tag{2.9}$$

where f is the frequency in kHz and the dimensions of α_{km} are $\mathrm{dB\,km^{-1}}$ (Kinsler et al., 2000). At $f = 0.02\,\mathrm{kHz}$, the attenuation becomes $\alpha_{km} = 0.002\,\mathrm{dB\,km^{-1}}$. In comparison to sound propagation in air, attenuation in the ocean is remarkably low, especially at low frequencies. Because of this, mammals are able to communicate over astonishingly large distances, without the sound being attenuated to inaudible levels. Together, the 'semi-spherical' geometric spreading losses, scattering and absorption sum to the total transmission loss

$$TL = 15 \log_{10} r + \alpha_m r. \tag{2.10}$$

This is henceforth referred to as the 'semi-spherical transmission loss model'. This is a simplistic model of transmission loss in real oceans, because it does not account for environmental parameters such as bathymetry or reflection loss at the sea bottom. Yet, the model is often used by scientist as a rough estimate of transmission loss (White, 2015a). It will therefore be used for comparison with the transmission loss modelled by RAM.

The effect of transmission loss on the signal level of the mammal can be quantified using the passive sonar equation, shown in equation 1.4. If equation 1.4 is rearranged to give an expression for the transmission loss, it can be used to determine the maximum transmission loss acceptable if the whale call is to be detected by the LoVe Observatory

$$\mathrm{TL_{max}} = \mathrm{SL} - (\mathrm{NL} - \mathrm{DI}) - \mathrm{DT}. \tag{2.11}$$

Together with a simulation of how transmission loss varies with range, this value can be used to estimate the ranges from which a whale call can be detected.

The directivity of the hydrophone at the LoVe Observatory is assumed to be omni-directional, making $\mathrm{DI} = 0\,\mathrm{dB}$. This also assumes that the directivity of the whale calls are ominidirectional, so that no array gain is added to the directivity of the receiver (Kinsler et al., 2000). According to McDonald and Fox (1999b) when whale calls are to be detected from passive recordings by a single hydrophone, like in the LoVe Observatory, an appropriate choice is to require the signal-to-noise ratio (SNR) to be ≥ 1 (on a linear scale). This will ensure that the whale call is distinguishable from the noise. This is the same as a detection threshold of $\mathrm{DT} \geq 0\,\mathrm{dB}$, since $\mathrm{DT} = 10\,\log_{10}(\mathrm{SNR})$ (Urick, 1983).

In ocean acoustic modelling, the level of noise is often estimated from the Wenz's curves, which quantifies the noise level as a function of frequency at different levels of shipping traffic and wind (Urick, 1983). However, the noise level at the LoVe Observatory has been measured by Ødegaard (2015), who found that the noise levels at low frequencies were significantly higher than those predicted by the Wenz's curves. Ødegaard (2015) plotted the noise spectrum level (NSL) of measurements made by the LoVe Observatory at various wind states and levels of shipping noise. Noise spectrum level is related to noise level as

$$NL = NSL + 10\log_{10} W, \tag{2.12}$$

where W is the frequency bandwidth (White, 2015a). At 20 Hz, the lowest measured NSL was recorded at an average wind speed of $3\,\mathrm{m\,s^{-1}}$, which gave NSL $\approx 60\,\mathrm{Pa^2\,Hz^{-1}}$. The highest levels were obtained from the measurements with wind speed of $18\,\mathrm{m\,s^{-1}}$ and the measurement with heavy shipping, which had similar values, at NSL $\approx 90\,\mathrm{Pa^2\,Hz^{-1}}$. Taking the bandwidth to be 1 Hz, the range of potential values for the noise level at the LoVe Observatory is thus

$$\mathrm{NL_{max}} \approx 90\,\mathrm{dB\,re\,1\,\mu Pa}, \tag{2.13}$$

$$\mathrm{NL_{min}} \approx 60\,\mathrm{dB\,re\,1\,\mu Pa}. \tag{2.14}$$

Of course, in an actual implementation of a density estimation algorithm at the LoVe Observatory, the bandwidth of the receiver will be wider, thus making the values for NL higher. Using the values laid out above, and equation 2.11, the maximum threshold for the transmission loss allowable when Fin whale calls of SL = 180 dB re 1 µPa at 1 m (Charif et al., 2002) are detectable at the LoVe Observatory was found to be

$$\mathrm{TL_{max,\ high\ noise}} = 180\,\mathrm{dB} - (90\,\mathrm{dB} - 0\,\mathrm{dB}) - 0\,\mathrm{dB} = 90\,\mathrm{dB}, \tag{2.15}$$

$$\mathrm{TL_{max,\ low\ noise}} = 180\,\mathrm{dB} - (60\,\mathrm{dB} - 0\,\mathrm{dB}) - 0\,\mathrm{dB} = 120\,\mathrm{dB}. \tag{2.16}$$

2.2 Bottom interaction

The extent to which the sound is interacting with the ocean floor is another deciding factor in how the sound is spread. Typically, sound can propagate over large distances in deep water without interacting with the bottom, due to upward refraction caused by the gradient of the sound speed profile in the water. However, in some cases, and especially in shallow water, reflection and attenuation by the sea floor is a crucial component of the sound spreading (Jensen et al., 2011).

The ocean floor is a lossy boundary, and the amount of sound energy that is reflected is dependent on the impedance difference between the sea water and the material of the sea floor, as well as the incident angle of the sound (Hovem, 1978). The amount of sound

energy that is reflected when the sound hits the ocean bottom can be quantified by the pressure reflection coefficient, R, which is given by

$$R = \frac{\frac{\rho_b c_b}{\rho_w c_w} - \frac{\cos\theta_t}{\cos\theta_i}}{\frac{\rho_b c_b}{\rho_w c_w} + \frac{\cos\theta_t}{\cos\theta_i}}. \tag{2.17}$$

Here, c_b is the compressional sound velocity in the bottom material, hereafter known as the sound velocity, ρ_b is the density of the bottom material, ρ_w is the density of the sea water, θ_i is the angle of the incident plane wave, and θ_t is the angle of the transmitted plane wave (Kinsler et al., 2000). Both angles are defined with respect to the normal of the sea bottom. In order to model reflection off of the bottom it is therefore necessary to know the density and the sound velocity of the sea bottom. These properties are of course dependent on the material composition of the sea floor.

2.2.1 Sediment composition classification

In most of the oceans, the top layer of the seabed is made of a loose layer of grainy sediments. This material is often classified according to grain size, and a nomenclature for the classification was first presented by Folk (1954). Based on the average grain diameter Φ, in millimeters, he defines three main textures of marine sediments; gravel ($\Phi > 2\,\text{mm}$), sand ($0.0625\,\text{mm} < \Phi < 2\,\text{mm}$), and mud ($\Phi < 0.0625\,\text{mm}$). Mud is any sediment smaller than 0.0625 mm, and includes both silt and clay. Folk then defines 15 textural groups, which are plotted in the ternary diagram in figure 2.1. As seen in the figure, each texture group contains a specified amount of the three main textures of the sediment; mud, sand, and gravel.

The Norwegian SOSI standard (Samordnet Opplegg for Stedfestet Informasjon. This translates to Co-ordinated Scheme for Location Based Information) has also made a nomenclature for the composition of common sediments (Geological Survey of Norway, 2015). This classification system is a modified version of the original definitions by Folk (1954). Folk (1954) refers to a specific sediment, which is made up of a mix of several textures, as a texture group. In the SOSI standard, on the other hand, this is named a sediment type, which is the expression that will be used in this thesis. Some of the names of sediment types bear names resembling the textures they are comprised of. Therefore, to avoid confusion, whenever the name of a sediment type is used, it will be given the special notation '*Sediment type*', while names of textures are plainly notated, without italic font and inverted commas. For example, '*Mud*' refers to the sediment type named mud, which is composed of a mix of the textures mud, sand, and gravel.

The SOSI standard provides a product specification code (PSC), which is simply a number corresponding to each sediment type, and a corresponding qualitative characterisation of the sediment type, in Norwegian. Translations of these classifications are provided by Mareano (2018). For clarity, the Norwegian nomenclature for sediment types, the corresponding English translations, and the product specification codes are provided in table A.1 in Appendix A. For each sediment type, Mareano (2018) also provides some defining properties of the sediment compositions; the ratio of clay to silt, the ratio of sand to silt and clay, percentage volume of clay and silt, percentage volume of sand, and percentage volume of gravel.

A. Gravel
B. Sandy gravel
C. Muddy sandy gravel
D. Muddy gravel
E. Gravelly sand
F. Gravelly muddy sand
G. Gravelly mud
H. Slightly gravelly sand
I. Slightly gravelly muddy sand
J. Slightly gravelly sandy mud
K. Slightly gravelly mud
L. Sand
M. Muddy sand
N. Sandy mud
O. Mud

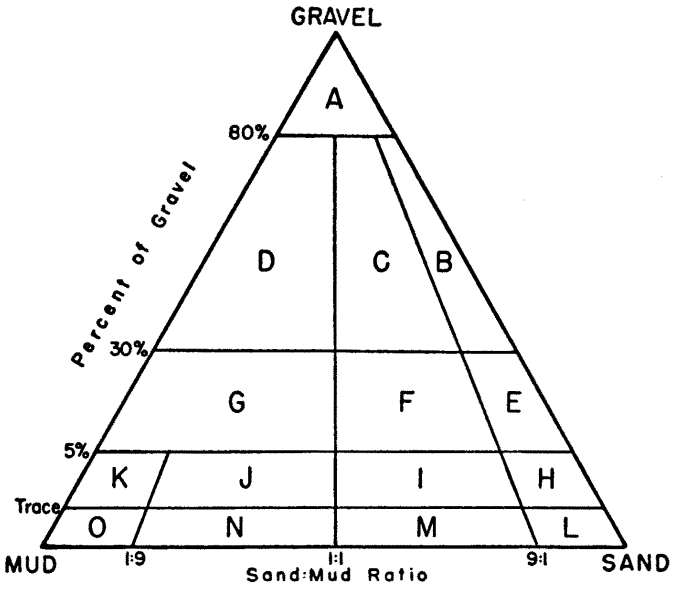

Figure 2.1: Ternary diagram defining the ratios of gravel, sand, and mud in the textural groups defined by Folk (1954). The figure is taken and re-printed from Folk (1954). The letters signify the textural group.

In addition, Mareano (2018) also specifes some limits for the grain size of the main textural components of the sediment. These limits are reproduced in table 2.1. These correspond well with the size definitions by Folk (1954), but notably include separate definitions for clay and silt instead of mud. From the limits defined by Mareano (2018), it is possible to define an average grain diameter, $\overline{\Phi}$, for each texture. The average grain diameters are shown in table 2.1 and are calculated by simply taking the mean of the two values of the limits of Φ. In the case of clay there is no lower limit, and the author chose to take the diameter to be $\overline{\Phi} = 0.0005\,\text{mm}$. And in the case of mud, the diameter was taken to be the mean of the average grain size for silt and clay.

Sediment texture	**Defined grain diameter, Φ (mm)**	**Average grain diameter, $\overline{\Phi}$ (mm)**
Clay	$\Phi <$ 0.002	0.0005
Silt	0.002 $< \Phi <$ 0.063	0.0325
Mud	–	0.0165
Sand	0.063 $< \Phi <$ 2	1.0315
Gravel	2 $< \Phi <$ 64	33.000

Table 2.1: The definitions of grain diameters for the sediment textures, given by Mareano (2018), as well as the calculated average grain diameters.

2.2.2 Models of the sediment

In coarse-grained sediments, the deformation experienced during the presence of a sound wave is dominated by stiffness and friction between the particles. This means that the sound velocity is higher than it is in water. On the other hand, in mud-sized sediments the solid particles are suspended in the water, giving the material a high porosity and a gel-like behaviour. In muds, the sound velocity is thus often lower than the speed of sound in water. Of course, most naturally occurring sediments contain a mixture of grain-sizes, making the prediction of the sound velocity from known properties of the sediment challenging (Ballard and Lee, 2017). For example, in the mixture of clay and sand, the concentration of clay merits different effects on the sound velocity. For low concentrations, the clay lays in the pores between the sand grains, making the material stiffer and the sound velocity higher. However, if the clay concentration exceeds 40 %, the sand grains become suspended in the clay matrix, giving higher porosity and lowering the sound velocity (Ballard and Lee, 2017). These intricate relations between sediment composition and its geoacoustic properties have been subject to much discussion (Jackson and Richardson, 2007; Hamilton, 1972), and prediction of the acoustic properties through models of the material remain a complicated subject (Jensen et al., 2011).

In fact, in acoustic modelling of the ocean, the most limiting factor on the accuracy of the model lies in the approximation of the geoacoustic properties of the seabed (Jensen et al., 2011). This part of the model thus requires careful consideration. The sedimentary layer is typically modelled as a fluid, even though it consist of solid grains of rock, saturated with water (Jackson and Richardson, 2007). Although this means that the modelled material will not have shear waves, this is most often a valid simplification because the rigidity of the sediment is usually much lower than that of solid rock (Jensen et al., 2011). However, due to the compound structure of the sedimentary material, which consists of both solids and a fluid, the defining acoustic parameters must be characterized for a volume large enough to contain many grains, yet smaller than the wavelength. Therefore, the density of the sediment is given in terms of its bulk density, ρ_B, which is the ratio of the total mass to the total volume of a small volume of the sediment. This density takes into account the local density of the water, as

$$\rho_B = \eta\rho_w + (1-\eta)\rho_g, \tag{2.18}$$

where η is the fractional porosity of the material and ρ_g is the density of the sediment grains, and the density of the water inside the pores of the material is assumed to be the same as the density of the water just above the sea floor (Jackson and Richardson, 2007).

Using a fluid approximation of the sediment, Wood and Weston (1964) proposed a relationship between the physical properties of the compound material and the sound velocity in the sediment. Wood's equation has, however, been shown to underpredict the velocity (Ballard and Lee, 2017). Gassmann (1951) tried to improve the model by taking into account the elasticity of the sediment material. He presented a relationship between sound velocity and measurable, physical properties of the sediment. The relationship has been shown to be reliable, particularly when permeability is low. However, the equation

requires many input parameters, many of which are very difficult to measure, rendering the equation highly impractical (Jackson and Richardson, 2007).

If the top layer of the seabed does not consist of loose sediments, the underlying rock will be exposed. In this case, the sediment must be modelled as an elastic or poroelastic medium, and the fluid approximation described above is no longer applicable (Jensen et al., 2011). The poroelastic sediment material consists of a poruous solid matrix, saturated with the fluid seawater. Biot (1956) has formulated a model of the acoustic propagation through such a porous material, which Biot describes to consist of a porous 'frame' filled with the fluid. Biot theory is acclaimed for being able to model the complexity of the composite material, with fluid motion relative to the solid frame. It can be used to predict several geoacoustic properties, including the attenuation coefficient and sound velocities. However, the drawback of the model is that it requires knowledge of 13 parameters in order to fully describe the acoustic propagation in the material. Some of these parameters, such as the pore size and bulk modulus of the frame, are difficult to measure and often not known (Jackson and Richardson, 2007). Moreover, no models have been found to fully describe the geoacoustic physics of the sediment, and the inhomogeneous nature of typical sea-beds further complicates this matter (Ballard and Lee, 2017).

Therefore, instead of using theoretical relationships to predict the sound velocity and absorption coefficient, the preferred method is, according to Jackson and Richardson (2007), to use empirically derived regressions. Hamilton and Bachman (1982) present a set of regressions which can be used to predict the sound velocity in the sediment from its fractional porosity, mean grain size, and bulk density. Porosity and grain size affect sound velocity through altering the elasticity of the medium (Hamilton and Bachman, 1982). The regressions are computed from both *in situ* and laboratory measurements made from a total of 537 samples, all corrected to 23 °C and 1 atm pressure. The samples are taken at various sites across several oceans and differing geological conditions. Bachman (1989) later reviesed these relationships. He included more samples, originally published in Bachman (1985), and gave regressional relationships between the measured physical properties of the sediment and the velocity ratio, V_R, where

$$V_R = \frac{c_b}{c_w|_{z=\text{Seafloor}}}. \tag{2.19}$$

This is the ratio of the sediment velocity, c_b, to the sound speed in the water just above the seabed, here denoted as $c_w|_{z=\text{Seafloor}}$. This representation of the sediment sound velocity is more practical than the original regressions by Hamilton and Bachman (1982), because the sediment velocity can be calculated by simply multiplying V_R by the *in situ* value of c_w just above the seafloor. This eliminates the need to correct the properties of the sediment for *in situ* temperature and pressure conditions. According to Jackson and Richardson (2007), these are the regressions which are most commonly used in acoustic modelling of the ocean. The regressions by Bachman (1989) are

$$V_R = 1.296 - 6.01 \times 10^{-2}\phi + 2.83 \times 10^{-3}\phi^2, \tag{2.20}$$

$$V_R = 1.675 - 1.639 \times 10^{-2}\eta + 9.762 \times 10^{-5}\eta^2, \tag{2.21}$$

$$V_R = 1.513 - 8.224 \times 10^{-4}\rho_B + 3.2249 \times 10^{-7}{\rho_B}^2, \tag{2.22}$$

where ϕ is the mean grain size in a unit commonly referred to as phi units. This is a non-SI unit used specifically regarding the diameter size of sediment grains. According to Hamilton and Bachman (1982), the unit phi is defined by the logarithm of the mean grain diameter in millimeters, as

$$\phi = -\log_2(\Phi). \tag{2.23}$$

Equation 2.20 to 2.22 give three separate relationships between V_R and measurable properties of the sediment. The velocity ratio is of course dependent on all three of these properties, but, unfortunately, a combined equation defining V_R as a function of both grain size, porosity, and bulk density of the sediment, has not been established. Jackson and Richardson (2007) present a regressional relation between bulk density, in units of $\mathrm{g\,cm^{-3}}$, and mean grain size

$$\rho_B = 2.17 - 0.082\phi. \tag{2.24}$$

It should, however, be noted that the coefficient of determination of equation 2.24 is only 0.80. The coefficient is a statistic measure of the wellness of fit of the regression of the data, and it is low due to a high degree of scatter in the data. This reflects the fact that mean grain size is a poor indicator of the material properties, due to the effects of sorting; how the particles are arranged with respect to one-another, known as sorting, can cause large variability in porosity and density, and thus also the sound velocity, without being reflected in the mean grain size (Jackson and Richardson, 2007).

It is also possible to predict the attenuation coefficient from empirical regressions. As in water, the attenuation coefficient in sediments is dependent on frequency as well as the material properties of the sediment. This relationship is often represented using the material specific constant h, as

$$\alpha_m = hf^l, \tag{2.25}$$

where α_m is expressed in $\mathrm{dB\,m^{-1}}$, l is a constant exponent, and f is expressed in kHz (Hamilton, 1972). This assumes that the wavelength, λ, is

$$\lambda >> \Phi. \tag{2.26}$$

Otherwise, when λ is small in comparison with the grain diameter, attenuation becomes proportional to the fourth power of frequency (Hamilton, 1972). Jackson and Richardson (2007) give a regressional relationship between h and ϕ for all sediment types. However, the coefficient of determination of this regression is low, indicating that attenuation is poorly correlated with mean grain size. Secondly, Jackson and Richardson (2007) claim that the regression might not be applicable at low frequencies, due to dispersion. This is also supported by Biot theory, which predicts that velocity dispersion gives $l =$

2 for frequencies below a material specific threshold (Jackson and Richardson, 2007). However, according to Hamilton (1972), recent reviews of large numbers of laboratory and field studies of attenuation in ocean sediments have indicated that velocity dispersion is negligible. Using the reviews, Hamilton (1972) shows that the frequency exponent, l, varies closely around 1 for a wide variety of sediment types and geological locations.

Moreover, Hamilton (1972) plots the variation in h with ϕ for the reviewed experimental results. The plot shows several distinct regions; for coarse sediments h increases gradually with ϕ, the slope of the variation then increases for medium coarse grains, reaching a maximum around $\phi = 4.5$. Then, h decreases with the square of ϕ, into the region of fine silts and clays. This non-linear behaviour explains why the regression by Jackson and Richardson (2007) found a low correlation between h and ϕ. Hamilton (1972) then gives regressional relationships between h and ϕ in each distinct region;

$$h = 0.4556 + 0.2245\phi, \qquad 0 < \phi < 2.6, \tag{2.27}$$

$$h = 0.1978 + 0.1245\phi, \qquad 2.6 < \phi < 4.5, \tag{2.28}$$

$$h = 8.0399 - 2.5228\phi + 0.20099\phi^2, \qquad 4.5 < \phi < 6.0, \tag{2.29}$$

$$h = 0.9431 - 0.2041\phi + 0.0117\phi^2, \qquad 6.0 < \phi < 9.5. \tag{2.30}$$

Notably, the regressions only describe sediments with a grain size finer than or equal to $\phi = 0$, which is equivalent to $\Phi = 1\,\text{mm}$. In the region of coarse sands, Hamilton (1972) points out that the plotted relationship might be obscured by the logarithmic nature of ϕ, and he therefore also plots the relationship between h and Φ for coarse grain sizes. From this plot, he extracts two more regressions;

$$h = 0.5374 - 0.1113\Phi, \qquad 0.6\,\text{mm} < \Phi < 0.167\,\text{mm}, \tag{2.31}$$

$$h = 0.8439 - 1.9431\Phi, \qquad 0.167\,\text{mm} < \Phi < 0.063\,\text{mm}. \tag{2.32}$$

In addition to the relationships between grain size and attenuation, Hamilton (1972) also describes how attenuation is affected by porosity, grain shape, number of inter-particle contacts, particle contact surface areas, and physiochemical forces between the particles. He points out that because many of these properties are inter-related, the experimental results of the variation of α_m with a single parameter is bound to have a significant amount of scatter. Moreover, the effects of temperature and pressure on attenuation are not well documented (Jackson and Richardson, 2007). Despite these shortcomings, the regressions shown in equations 2.27 to 2.32 might be the most applicable model of attenuation in the sediment when more detailed quantitative information on the material properties are lacking.

2.3 The parabolic equation

In order to use the parabolic equation method to simulate the transmission loss in the ocean and in the bottom around the LoVe Observatory, some simplifications must be made. Looking at the derivation on the '*Standard parabolic equation*' from the known 3D Helmholtz equation with time dependence $\exp(-2\pi ift)$, reveals some important assumptions. The following derivation is taken from Jensen et al. (2011), Chapter 6. The position coordinates used in the parabolic equation are defined by the coordinate system shown in figure 2.2. The figure is drawn by the author, and, in general, all figures in this thesis are made by the author unless another source is explicitly specified. Figure 2.2 shows that in relation to a standard Cartesian coordinate system in terms of x, y, and z, θ is the angle around the z-axis, given counter-clockwise from the y-axis. It gives the position of the r-axis, which is orthogonal to the z-axis. The r-axis gives the horizontal distance from the sound source. The origo of the coordinate system is placed on the ocean surface, so that the position of the sound source is ($r = 0$, $z = z_{source}$). The depth variable, z, is taken to be positively increasing with depth.

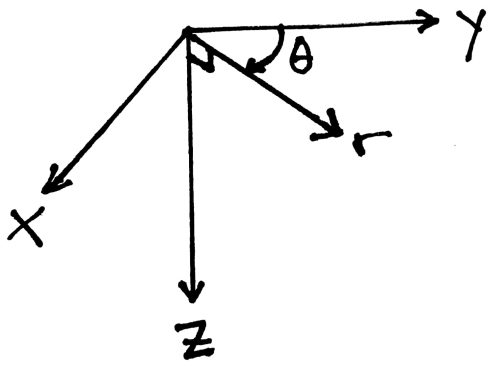

Figure 2.2: A coordinate system defining the relation between the position coordinates used in the parabolic equation.

Firstly, Jensen et al. (2011) assumes that the acoustic field has azimuthal symmetry, making it independent of θ, thus reducing the constant-density Helmholtz equation to

$$\frac{\partial^2 p}{\partial r^2} + \frac{1}{r}\frac{\partial p}{\partial r} + \frac{\partial^2 p}{\partial z^2} + k_0^2 n^2 p = 0, \tag{2.33}$$

where p is the acoustic pressure, n is the index of refraction, given by $n = \frac{c_0}{c}$, and k_0 is a reference wave number. It is given by

$$k_0 = \frac{2\pi f}{c_0}. \tag{2.34}$$

Here, c_0 is a normalization sound speed (Tappert, 1977). According to Tappert (1977), an appropriate choice of c_0, to minimize the error in the described sound field, is to let c_0 equal the speed of sound in the water at the position and depth of the sound source, and this is adhered to throughout this study. Equation 2.33 describes the 3D sound propagation in an axisymmetric environment. The density is also assumed to be independent of z. Its solution is assumed to take the form

$$p(r, z) = \psi(r, z)\, {H_0}^{(1)}(k_0 r), \tag{2.35}$$

where ${H_0}^{(1)}$ is the Hankel function of the first kind and zeroth order, and ψ is an envelope function. By assuming that

$$k_0 r >> 1 \tag{2.36}$$

which means that the solution describes a wave in the far-field, the Hankel function is replaced by its asymptotic form;

$${H_0}^{(1)}(k_0 r) \approx \sqrt{\frac{2}{\pi k_0 r}} e^{i(k_0 r - \frac{\pi}{4})}. \tag{2.37}$$

This leads to the '*Simplified elliptic wave equation*'

$$\frac{\partial^2 \psi}{\partial r^2} + 2ik_0 \frac{\partial \psi}{\partial r} + \frac{\partial^2 \psi}{\partial z^2} + k_0^2 (n^2 - 1)\psi = 0. \tag{2.38}$$

The parabloic equation was frist applied to underwater acoustics by Hardin and Tappert (1973). They introduced the '*Standard parabolic equation*'

$$2ik_0 \frac{\partial \psi}{\partial r} + \frac{\partial^2 \psi}{\partial z^2} + k_0^2 (n^2 - 1)\psi = 0, \tag{2.39}$$

which can be solved using the efficient split-step Fourier technique. This solution will be discussed further in section 2.4. In their derivation of equation 2.39, Hardin and Tappert (1973) neglected the term $\frac{\partial^2 \psi}{\partial r^2}$. This assumption caused the equation to become one-way, thus neglecting any back-scattered sound. Moreover, the assumption caused a restriction similar to applying a small-angle paraxial approximation. Because of this approximation, the solutions were only accurate for propagation angles within $\pm(10^\circ - 15^\circ)$ from the horizontal (Jensen et al., 2011).

Significant effort has been spent on making the parabolic equation more accurate at more wide angles. This was initiated at a workshop on parabolic equations by the Naval Ocean Research and Development Activity (Davis et al., 1982). The workshop developed a parabolic equation based on an operator formalism. Following the presentation of the workshop's findings by Jensen et al. (2011) reveals some further noteworthy assumptions. Firstly, Davis et al. (1982) defined the operators

$$P = \frac{\partial}{\partial r}, \quad Q = \sqrt{n^2 + \frac{1}{{k_0}^2} \frac{\partial^2}{\partial z^2}}, \tag{2.40}$$

where Q is known as *the square-root operator*. Using these operators, equation 2.38 was written on the form

$$[P^2 + 2ik_0 P + k_0^2 (Q - 1)]\psi = 0. \tag{2.41}$$

This enabled factorization of equation 2.38 into an outgoing and an incoming wave;

$$(P + ik_0 - ik_0 Q)(P + ik_0 + ik_0 Q)\psi - ik_0 [P, Q]\psi = 0, \tag{2.42}$$

where $P^2 = \frac{\partial^2}{\partial r^2}$ and $[P, Q]$ is the commutator of the operators P and Q. Notably, this is assumed to be negligible, so that

$$[P, Q] = 0. \tag{2.43}$$

This is only accurate when n is independent of r. This simplification thus means that the properties of the medium are assumed to vary slowly with range. Finally, by selecting only the outgoing part of equation 2.42, shown in the first bracket, and assuming that backscattering is negligible the '*one-way, general parabolic wave equation*' takes the form

$$\frac{\partial \psi}{\partial r} = ik_0 \left(\sqrt{n^2 + \frac{1}{{k_0}^2} \frac{\partial^2}{\partial z^2}} - 1 \right) \psi. \tag{2.44}$$

The far-field assumption and the assumption that $[P, Q] = 0$ will introduce errors if the variations in physical properties with r are too great, and equation 2.44 is therefore said to be 'weakly' range dependent (Jensen et al., 2011). This equation forms the basis for several formulations of solutions to the parabolic equation, each with its own attempt at minimizing the errors introduced by the aforementioned assumptions, and handling the challenges in numeric implementation and other limitations.

Many of the solutions to equation 2.44 are based on an approximation of the square-root operator. It is commonly written on the form

$$Q = \sqrt{1 + q} \tag{2.45}$$

where the operator q is an abbreviation for

$$q = n^2 - 1 + \frac{1}{k_0^2} \frac{\partial^2}{\partial z^2}. \tag{2.46}$$

The most basic of these approximations is a Taylor series expansion

$$\sqrt{1 + q} \simeq 1 + \frac{q}{2} - \frac{q^2}{8} + \frac{q^4}{16} + ... \tag{2.47}$$

If only the first order terms are included, this expansion results in Hardin and Tappert's '*Standard parabolic equation*', shown in equation 2.39 (Jensen et al., 2011). The local error in the sound field caused by the approximation of Q was investigated by Tappert (1977). He abbreviated q as

$$q = \epsilon + \mu, \tag{2.48}$$

where $\epsilon = n^2 - 1$ and $\mu = k_0^{-2} \frac{\partial^2}{\partial z^2}$. According to Tappert (1977), when the operator μ is applied to Ψ, its physical meaning can be interpreted as the angle of propagation with respect to the horizontal, since $\frac{\partial \Psi}{\partial z}$ is the vertical wave number. Tappert (1977) found that to make the local error small the norm of the operators ϵ and μ had to be small, or in other words, $|| \epsilon || \ll 1$ and $|| \mu || \ll 1$. In typical seawater, making $|| \epsilon ||$ small is not a

problem, since $n^2 - 1 = \frac{c_0^2}{c^2} - 1$ and $c_w(z)$ typically only varies by a few percent along the water column. On the other hand, requiring that $|| \mu || \ll 1$ can impose some restrictions on the use of the parabolic equation. Tappert (1977) found that in order to satisfy the condition, the angle of propagation with respect to the horizontal had to be limited.

The inclusion of more terms in the Taylor expansion will give better wide-angle accuracy, but the numerical implementation of this is difficult, since the operator q is higher-order. Therefore, several authors, including Green (1982) and Claerbout (1985), have investigated other linear approximations of Q that can improve the aperture limitations of Hardin and Tappert's original solution. These approximations, commonly referred to as '*wide-angle parabolic equations*' use rational functions on the form

$$\sqrt{1+q} \simeq \frac{a_0 + a_1 q}{b_0 + b_1 q}, \tag{2.49}$$

where the coefficients a_0, a_1, b_0, and b_1 are chosen to minimize the error over the desired angle interval (Jensen et al., 2011). Although these approximations have been found to be significantly more accurate than Hardin and Tappert's'*Standard parabolic equation*' (Collins and Evans, 1992), the '*wide-angle parabolic equations*' cannot handle propagation much larger than 40° from the horizontal (Collins, 1989a). According to Jensen et al. (2011), significant effort has therefore been spent in order to formulate higher-order approximations to the square-root operator which are both numerically viable and accurate at higher propagation angles.

One of these higher-order approximations is the Padé series approximation proposed by Bamberger et al. (1988). They approximated the square root operator as

$$\sqrt{1+q} = 1 + \sum_{j=1}^{m} \frac{a_{j,m} q}{1 + b_{j,m} q}, \tag{2.50}$$

where m is the number of included terms, and $a_{j,m}$ and $b_{j,m}$, are coefficients given by

$$a_{j,m} = \frac{2}{2m+1} \sin^2\Big(\frac{j\pi}{2m+1}\Big), \tag{2.51}$$

$$b_{j,m} = \cos^2\Big(\frac{j\pi}{2m+1}\Big). \tag{2.52}$$

The Padé series approximation was first implemented by Collins (1989a) and has been shown to be completely accurate for range-independent media (Collins and Westwood, 1991). This means that the wide-angle local errors associated with the approximation of Q are completely eliminated, and only the assumptions given in equations 2.36 and 2.43, as well as the assumption of azimuthal symmetry and that sound only propagates in one direction need to be considered when the equation is applied to range-dependent media. Moreover, for realistic ocean environments with range dependent properties, the approximation can be accurate at all propagation angles by including enough terms in the summation in equation 2.50 (Jensen et al., 2011). In fact, Collins (1989a) has shown that $m = 5$ is sufficient for most environments. Collins (1990) has compared the solution

of the parabolic equation using the Padé approximation with conventional normal mode solutions for a number of different test cases. He found that the Padé approximation agrees with the reference solution both for propagation at nearly ±90° and for problems involving large variations in sound speed. During the comparison of the two techniques, Collins (1990) also comments on the inefficiency of spectral decomposition methods such as normal mode solutions. The run times required to simulate the pressure field at several receiver depths were found to be more than 10 times more than the run time required for one receiver. Therefore, normal mode solutions are not favourable when simulating the transmission loss at many positions. Currently, the Padé approximation is one of the most advanced and accurate techniques that can be used to transform the parabolic equation into a solvable differential equation.

2.4 Solutions to the parabolic equation

After having established a solvable differential equation by approximating the square-root operator using equations 2.50 to 2.52, the one way, general parabolic equation, shown in equation 2.44, can be solved. Several solution methods exists, and the most commonly used techniques are the split-step Fourier technique and finite difference or finite element techniques. As shall be laid out here, the methods vary in efficiency and how well they handle bottom-interaction. As the name implies, the split-step Fourier technique is based on fast Fourier transform of the parabolic equation. It is called 'split-step' because the solution is advanced in two distinct stages. Firstly, the solution is advanced through the medium as if its density and sound speed were homogeneous, thus accounting for diffraction effects only. Then, the second step includes the range-dependent effects of refraction (Jensen et al., 2011). The method allows large steps in Δr and Δz and is popular due to its efficiency (Collins, 1993). On the other hand, in a comparison between algorithms for solving the parabolic equation, Collins et al. (1996) found that the split-step Fourier technique is limited by the local errors associated with wide-angle propagation, and is only reliable when the energy propagates close to the horizontal and when there is little variation in c. Moreover, Collins et al. (1996) found that the technique does not handle discontinuities in density well, for example at the water-bottom interface. If such discontinuities are to be described accurately, the split-step technique requires an excessively fine computational grid, which effectively eliminates its advantage in efficiency (Jensen et al., 2011). Therefore, the technique is most commonly applied to long-range, narrow angle problems (Jensen et al., 2011). Yet, the main disadvantage of the split-step Fourier technique is that out of the approximations described in section 2.3, only the linear Taylor series expansion, shown in equation 2.47, can be used together with the split-step Fourier technique (Jensen et al., 2011). As previously explained, this is not the most accurate approximation of Q, and the applicability of the split-step Fourier technique is thus rather limited, despite its efficiency.

Finite difference and finite element techniques can also be used to solve equation 2.44, and these are generally more universally applicable. After approximating Q using any technique, the parabolic equation can be solved using conventional finite difference

techniques, such as the Cranck-Nicolson scheme (Jensen et al., 2011). In the algorithm comparison by Collins et al. (1996), they found that these techniques are applicable to wide-angled propagation, to media with large property variations, as well as problems involving much interaction with elastic and poroelastic sediments. The problem with finite difference and finite element methods is that they tend to require finer computational grids than split-step Fourier algorithms and are therefore significantly less efficient (Collins, 1993).

More recently, a new solution technique has dramatically improved the capabilities of the parabolic equations for underwater sound propagation. The new split-step Padé technique by Collins (1993) is based on the aforementioned Padé series approximation by Bamberger et al. (1988). It provides both the efficiency of the split-step Fourier technique, as well as the universal applicability of the finite difference technique (Collins et al., 1996). The split-step Padé solution is applied to an alternative formulation of the '*one-way, general parabolic wave equation*', previously shown in equation 2.44. To derive the equation, Collins (1993) starts with the wave equation with depth dependent density

$$\frac{\partial^2 p}{\partial r^2} + \rho \frac{\partial}{\partial z}\Big(\frac{1}{\rho}\frac{\partial p}{\partial z}\Big) + k^2 p = 0. \tag{2.53}$$

Here, k is the wave number, given by $\dfrac{2\pi}{\lambda}$ and inherent in the equation lies the assumption that the sound field is in the far-field. Collins (1993) then applies the same methods that were used in the derivation of equation 2.44, laid out in section 2.3. This includes preforming a factorization equivalent to equation 2.42, by assuming that that backscattering is negligible and that n is independent of r. The latter effectively means that k is assumed independent of r, since $k = k_0 n$. Finally, Collins (1993) also assumes that ρ is independent of r. This results in Collins's version of the one-way, general parabolic equation;

$$\frac{\partial p}{\partial r} = ik_0\sqrt{1+q^*}\,p, \tag{2.54}$$

where q^* is a new variant of the operator q and is given by

$$q^* = \frac{1}{k_0^2}\big(\rho\frac{\partial}{\partial z}\frac{1}{\rho}\frac{\partial}{\partial z} + k^2 - k_0^2\big). \tag{2.55}$$

Collins (1993) then assumes that the solution to equation 2.54 has the form

$$p(r+\Delta r) = \exp\Big[ik_0\Delta r\sqrt{1+q^*}\Big]p(r), \tag{2.56}$$

where Δr is a discrete range step. Notably, 'marching' of the solution from one radial position to the next, determined by Δr, enables updating of the values of k and ρ with range, even though they have been assumed not to depend on radial position. Collins (1993) thereby incorporates weak range dependence in the parabolic equation. Now,

instead of approximating only the square-root operator $\sqrt{1+q^*}$, Collins applies a Padé approximation to the entire exponential part of equation 2.56, so that

$$\exp\left[ik_0\Delta r\sqrt{1+q^*}\right] \simeq 1+\sum_{j=1}^{m}\frac{a_{j,m}q^*}{1+b_{j,m}q^*}, \tag{2.57}$$

where the coefficients $a_{j,m}$ and $b_{j,m}$ are again given by equation 2.51 and 2.52. This leads to a differential equation that can be solved efficiently by repeatedly solving a tridiagonal system of equations, using for example a Gaussian elimination scheme (Collins, 1990). This solution algorithm has been shown to be valid for very wide propagation angles and for media with large variations in properties (Collins et al., 1996). In Collins et al.'s (1996) comparison between parabolic equation solution algorithms, he found the split-step Padé algorithm to be up to two orders of magnitude more efficient than a reference finite difference algorithm, and at least as efficient as the split-step Fourier algorithm. Collins et al. (1996) present some benchmark cases comparing the results of both the split-step Fourier algorithm and the split-step Padé algorithm to the reference finite difference algorithm. According to Collins et al. (1996), these cases showed that the split-Step Fourier algorithm caused some numerical errors at large ranges, while the split-step Padé algorithm was accurate. Approximating and solving the parabolic equation using the split-step Padé algorithm is thus preferable with regards to both efficiency and accuracy.

2.5 The Range-dependent Acoustic Model (RAM)

The split-step Padé algorithm has been implemented by Collins (2001) in an open source Fortran code called the 'Range-dependent Acoustic Model' (RAM). The algorithm is available for download at The Ocean Acoustics library by U.S. Office of Naval Research (1999), and according to Jensen et al. (2001), it is considered the most efficient parabolic equation algorithm for solving range-dependent ocean acoustic problems. After using the split-step Padé method to solve the parabolic equation, RAM computes the transmission loss as a function of r and z from the specified source position, and returns the transmission loss values to the user.

Since the split-step Padé technique was first proposed by Bamberger et al. (1988), several improvements to the technique have been developed. Collins (2001) has implemented three main improvements in RAM: a novel tridiagonal equation solver, energy conservation corrections, and taken steps to make the algorithm more stable. The tridiagonal solver used in RAM uses the method of alternating directions (Collins, 1989a). This means that to eliminate entries, the solver sweeps down from the main diagonal to the matrix row describing the sea bottom, and it sweeps up to the sea bottom from the other direction, before back substitution. The solver thus minimizes the required number of operations for range-dependent problems, making it more efficient than Gaussian elimination, which only sweeps in one direction (Collins, 1990). By implementing this improvement, the split-step Padé algorithm has been shown to be more than 2 orders of magnitude faster than finite difference solutions to wide-angle parabolic equations (Collins, 1993).

The second improvement made in RAM concerns energy conservation, which is a known issue in parabolic equation modelling. Most implementations of parabolic equations face the fundamental problem of energy conservation at sloping bottoms (Jensen et al., 2011). The slopes are modelled as discrete stair steps. Equation 2.54 contains two derivatives with respect to z, meaning that both continuity of pressure and continuity of the normal component of particle velocity can be applied on the horizontal parts of the stair step. On the other hand, equation 2.54 only contains one derivative with respect to r, and only one of the boundary conditions can therefore be applied to the vertical part of the stair step (Collins and Westwood, 1991). In result, the energy is not conserved at all boundaries. To investigate the effects of this, Jensen and Ferla (1989) presented a number of benchmark problems involving a penetrable sloping bottom, and compared the results of a parabolic equation model with that of a complete two-way normal mode solution. They found that the lack of energy conservation can lead to errors of a few decibels for slopes of only a few degrees. For sound travelling up-slope, energy is lost, while for sound travelling down-slope, energy is gained (Jensen et al., 2011). To combat this issue, in RAM, Collins (2001) has opted to conserve the quantity $\frac{p}{\sqrt{\frac{\rho}{k}}}$ across the vertical part of the stair step, instead of the more conventional conservation of pressure. This mitigates the issue of energy conservation, since the preserved quantity incorporates the impedance difference between the two bordering media. Collins and Westwood (1991) have validated this in a comparison between the split-step Padé algorithm with the proposed energy-conservation correction, and a very accurate complex ray model.

To implement the energy-conservation correction in RAM, Collins (1990) makes the substitution

$$\tilde{p} = p\sqrt{\frac{k}{\rho}}. \tag{2.58}$$

Following the derivation of equation 2.54, but using the alternative dependent variable $\tilde{p}$, Collins (1990) then finds that the resulting depth operator is

$$\tilde{q} = \frac{1}{k_0^2}\left[\rho\sqrt{\frac{k}{\rho}}\frac{\partial}{\partial z}\sqrt{\frac{\rho}{k}} + k^2 - k_0^2\right]. \tag{2.59}$$

RAM then solves the parabolic equation

$$\frac{\partial\tilde{p}}{\partial r} = ik_0\sqrt{1+\tilde{q}}\,\tilde{p} \tag{2.60}$$

for the moderated dependent variable $\tilde{p}$ by assuming a solution of the form shown in equation 2.56. The final solution used in RAM thus becomes

$$\tilde{p}(r+\Delta r) = \exp\left[ik_0\Delta r\sqrt{1+\tilde{q}}\right]\tilde{p}(r). \tag{2.61}$$

The drawback to the energy conservation correction is that Collins and Westwood (1991) have found that it causes Gibbs' oscillations in the solutions. Gibbs' oscillations are high-frequency ripples that are synthetically introduced to the solution to the

split-step Padé algorithm when the discontinuities in the solution are inverse Fourier-transformed into the time-domain (Radaelli-Sanchez and Baraniuk, 2007). To eliminate these oscillations, it is necessary to use complex Padé coefficients, instead of the real coefficients proposed in equation 2.51 and 2.52. This method, first described by Wetton and Brooke (1990) and further developed by Collins (1991), introduces a small artificial attenuation that filters out the Gibbs' oscillations (Collins and Westwood, 1991). The complex Padé coefficients are chosen by imposing constraints on accuracy and stability. In RAM the constraints are that $2m - n_s$ derivatives of the rational function shown in equation 2.57 are correct at $\tilde{q} = 0$, and that the rational function is annihilated at n_s points in the evanescent region. Here, n_s is a stability parameter chosen by the user. These constraints ensure accuracy in the propagation of the energy at the reference wave number, k_0, and it ensures that evanescent modes decay quickly with range (Collins, 1991, 1993). The Padé coefficents used in RAM are calculated by formulating nonlinear equations imposing the constraints and using a stabilized Newton method, detailed in Collins and Evans (1992). If the user of RAM does not want to include the artificial attenuation inherent in the complex Padé coefficients, it is possible to turn off the stability restrictions at any range, specified by the user as r_s (Collins, 2001).

The split-step Padé algorithm computes the sound field at a computational grid defined by the user of RAM. The grid is discrete, and the steps between the evaluation points are defined by Δr and Δz. As seen in equation 2.61, the solution to the parabolic equation is defined at discrete values in range by the inclusion of Δr. However, the derivative with respect to z, included in $\tilde{q}$ is continuous. It is therefore necessary to discretize the depth operator before equation 2.61 can be applied. In RAM this is done by employing Galerkin's method, which is described in detail in Collins (1989a). Finally, to apply equation 2.61, some initial conditions must be specified. In RAM, the sound field is initiated by a self-starter modelling a point source in cylindrical geometry (Collins, 2001). The source is placed at $r = 0$ and some user specified depth z_{source}. Details on the derivation of this self-starter from the normal mode solution of the wave equation, as well as validation of this method by comparison with a full normal mode solution, are described by Collins (1992).

2.6 Running RAM

Running RAM requires input of a number of parameters from the user, in a specific format. Four main categories of input parameters are needed; model parameters, bathymetry, geoacoustic properties of the seabed, and sound speed profiles. The model parameters include user decided scalar numbers, such as frequency, source depth, the discrete step-sizes Δz and Δr, the maximum range of the computed field, the number of Padé coefficients, m, the stability parameter, n_s, and the range at which the stability restrictions are turned off, r_s. The choices for these parameters are laid out in section 4.1.

The bathymetry is specified as z_b, the depth beneath sea-level, at discrete positions of range, r_b. At each of the specified z_b depths, RAM imposes the appropriate boundary conditions so that sound is both reflected off the seabed and transmitted into the sedi-

ment, depending on the impedance difference between the water and the sediment. The seabed, which is modelled as a single layer of sediment, is described by three properties: its sound velocity, attenuation coefficient, and density, all of which must be specified by the user. For the seawater, on the other hand, the user only needs to specify one property: the sound speed profile. RAM takes the density of the water to be a constant at $\rho_w = 1\,\mathrm{g\,cm^{-3}}$ and the attenuation is assumed to be negligible (Collins, 2001). How the sound speed varies with depth is described by the user as c_w at discrete intervals of z. RAM linearly interpolates the value of c_w between subsequent entries. However, RAM does not extrapolate the value of c_w beyond the deepest user specified value. This means that if the user does not specify the value of c_w all the way down to the sea floor, c_w is taken to be constant with z from its deepest specified value until $z = z_b$ (Collins, 2001). At each position in r, RAM uses the value of z_b to determine at what depth to stop treating the medium as water and start treating it as sediment. Theoretically, this can be expressed as

$$c = \begin{cases} c_w, & z < z_b, \\ c_b, & z > z_b, \end{cases} \tag{2.62}$$

$$\rho = \begin{cases} \rho_w = 1\,\mathrm{g\,cm^{-3}}, & z < z_b, \\ \rho_b, & z > z_b, \end{cases} \tag{2.63}$$

$$\alpha_\lambda = \begin{cases} \alpha_{\lambda,\,w} = 0\,\mathrm{dB}/\lambda, & z < z_b, \\ \alpha_{\lambda,\,b}, & z > z_b. \end{cases} \tag{2.64}$$

Together, the sound speed, c, the density, ρ, and the attenuation coefficient, α_λ are known as the environmental parameters of the modelled domain, and the subscripts w and b denote that the parameters describe the water and the bottom, respectively. In RAM, the attenuation coefficient α_λ is expressed in units of dB/λ. Conversion to α_λ from the previously defined attenuation coefficient in units of $\mathrm{dB\,m^{-1}}$, α_m, can be done by simply multiplying α_m by λ. This can also be expressed as

$$\alpha_\lambda = \alpha_m \frac{c}{f}. \tag{2.65}$$

The sound speed in the water and in the sediment is included in the parabolic equation through the wave number, k, seen in the modified depth operator $\tilde{q}$, in equation 2.59. Attenuation is also incorporated in the wave number, by making it complex. Collins (2001) thus expresses the wavenumber as

$$k = \frac{2\pi f}{c}\Big(1 + i\frac{\alpha_\lambda}{40\,\pi \log_{10} e}\Big). \tag{2.66}$$

As previously mentioned, ρ and k (and thereby also c and α_λ) are assumed to be independent of r in the parabolic equation 2.60 which is implemented in RAM. However, RAM still allows for these parameters to be changed with range, by updating their values at some user specified ranges. The modelled domain can thus be thought of as having

been divided into a number of discrete blocks, as illustrated in figure 2.3. Within each block, the values of c, ρ and α_λ are kept constant, while the bathymetry can vary. The solution algorithm is 'marched' forward in steps of Δr, and when it reaches the transition from one block to the next, the values of c, ρ and α_λ are updated. The length from one block to the next is specified by the user, and should be at least $\geq \Delta r$. How often new blocks are created is of course dependent on how the environmental parameters vary with range in reality at the specific modelled location. How the range blocks are designed will be discussed further in section 4.3. The environmental parameters of each block, and the ranges for beginning of new blocks are all specified by the user in a text-file called `ram.in`. The file is written in a specific format, so that RAM can locate each variable at a specific row in the text file. An example of the file format can be seen in the appendix of Collins (2001).

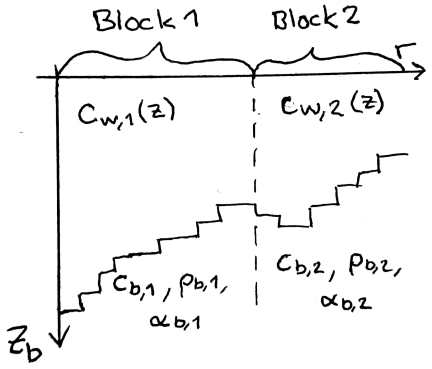

Figure 2.3: An illustration of how the environmental parameters c, ρ and α_λ are constant within each block, while z_b changes discretely with r.

It has been shown that the parabolic equation satisfies the principle of reciprocity (Nghiem-Phu and Tappert, 1985), and it is therefore commonly adopted by users of RAM (Jensen et al., 2011) because it simplifies simulation of transmission loss from several receiver positions. By placing the source at the position of the receiver when using RAM and then applying reciprocity when interpreting the simulation results, a single run of RAM will produce the transmission loss between sources at any position in a r-z-plane and the receiver. If the simulations were to be preformed without utilizing reciprocity, an individual RAM simulation would have had to be run for each investigated source position. The principle of reciprocity will therefore be applied for all simulations performed in this study. Because of this, the origo of the coordinate system defined in figure 2.2 is moved from the previously defined placement above the sound source to now lie above the receiver.

Due to the assumption of azimuthal symmetry in the Helmholtz equation, discussed in section 2.3, RAM is a 3D axisymmetric model. This entails that while range dependence and depth dependence of the environmental parameters are included in the model, these

parameters are taken to be constant with θ for each simulation. Therefore, in order to capture how the sound transmission is affected by the actual 3D variation of the environmental parameters, the volume around the LoVe Observatory has to be divided into a number of r-z planes and RAM is used to simulate the transmission loss between the LoVe Observatory and all positions in each plane. These planes are henceforth referred to as 'transects' and the direction of a transect is defined by θ. The transects are placed around the observatory in a fan-like structure, originating at $(r = 0, z = 0)$, and each transect is separated by an angle θ. This way of dividing up the volume into transects is commonly used in axisymmetric models of sound propagation, and is often referred to as a Nx2D-model, where N is the number of transects (Jensen et al., 2011). An example of a transect running from the LoVe Observatory straight out of the Hola valley is introduced in figure 4.3. RAM is used to simulate the transmission loss in N number of r-z planes, and together these simulated planes may be used to interpret how transmission loss varies in the whole 3D volume. Of course, these results are limited in that the θ-coupling term in the parabolic equation is ignored. This means that any effects caused by horizontal variation in the environmental properties are neglected. This includes horizontal refraction due to variation in c_w with θ, horizontal diffraction effects, as well as scattering and reflections in any other direction than those parallel to the modelled transect.

Chapter 3

Environmental parameters

Simulations of the transmission loss in the Lofoten-Vesterålen basin were based on known oceanographic properties of the area, including depth of the bathymetry, the speed of sound, and the physical properties of the sea floor. It is not within the scope of this study to measure these data, and they have instead been gathered from or calculated from data in known databases, or otherwise decided upon based on literature. The sources of the data, and the way in which they are processed before they are utilized in the simulations, will be laid out in sections 3.1 - 3.3.

3.1 Bathymetry

The bathymetry around the listening position was acquired from Kartverket (2018a; 2018b) and the General Bathymetric Chart of the Oceans by British Oceanographic Data Centre (2018). Kartverket has mapped the bathymetry along the coast of Norway. Within 12 nautical miles from the coast, the resolution is limited to 50 m x 50 m, due to restrictions imposed by the Norwegian military authorities (Kartverket, 2018c). Part of the area of interest lays within this classified region. The bathymetry in this region has been downloaded from the database *Depth data 50 m grid*, accessed through Kartverket (2018a). For areas outside the military restriction, the bathymetry has been downloaded from the database *Sea terrain models DTM 5*, accessed at Kartverket (2018b), which has a resolution of 5 m x 5 m. Beyond the region mapped by Kartverket, the bathymetry has been downloaded from British Oceanographic Data Centre (2018). It provides a coarse bathymetric data set covering the whole world. The data have a resolution of 30 arc seconds in degrees longitude and latitude. In the area around the listening position, this translates to a resolution of approximately 929 meters North and 325 meters East, calculated using the `m_ll2xy` function by Pawlowicz (2018). Before the TL simulations were performed, it was not known how far from the shoreline bathymetric data would be needed. Therefore, the whole Greenland sea and the whole Lofoten basin was downloaded pre-emptively, as an overestimate of the needed range. The downloaded data are shown in figure 3.1.

These two databases from Kartverket both provide the bathymetry data in ASCII XYZ format, using Universal Transverse Mercator coordinate system (UTM) sone 33 (U.S. Geological Survey, 1997). Kartverket (2018b) provided the data in cells with dimensions of 0.5° latitude and 0.5° longitude. 13 such cells were downloaded, and some of

these cells partly overlapped with the 50 m grid data set. The data from British Oceanographic Data Centre (2018) was provided in netCDF format in longitude and latitude coordinates.

In order to combine all the downloaded data sets into one, it was first necessary to choose a common coordinate system. Coordinates of longitude and latitude is preferable, because the UTM coordinate system, although it uses easily understood units of meters, is prone to errors when the map covers a large area. Therefore, the two data sets from Kartverket were converted to units of longitude and latitude. Then, the three data sets were combined into one by removing overlapping areas. The borders between the data sets were not straight lines, so care was taken to define the vertices of the overlapping areas by hand, by graphing the coordinates of both data sets and using MatLab's `impoly` -function. Once the overlapping area had been defined, the data with lower resolution was removed from each area. Figure 3.1 shows which areas ended up being taken from which data set. Due to the excessive computational capacity needed to process the format and the large number of samples in the bathymetry data from Kartverket, this has not been used to produce any visualisation of the bathymetry in this thesis. Instead, the bathymetry data presented in figure 3.1, and in all figures including bathymetry

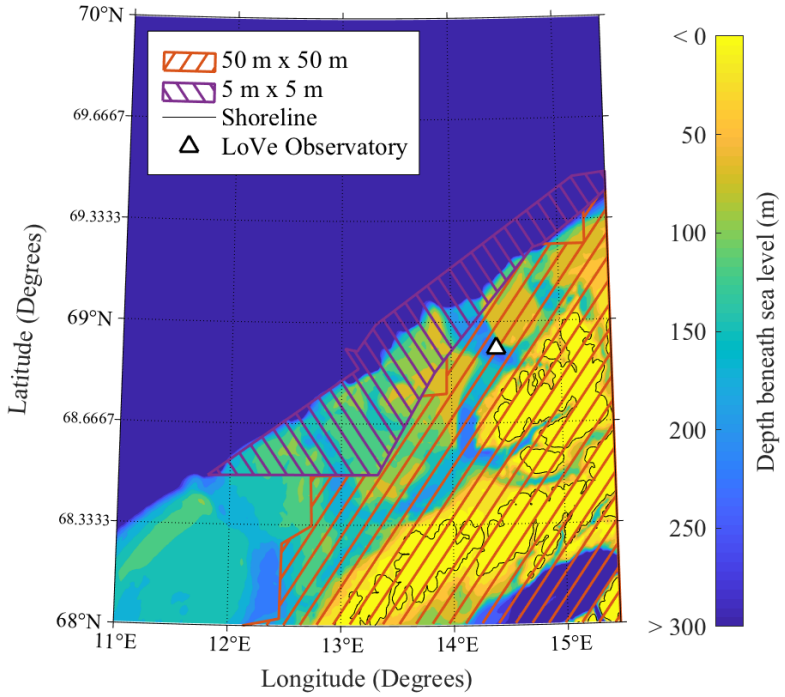

(a)

Figure 3.1: Contour maps of the downloaded bathymetry data, with hatching indicating the resolution of the area. The data downloaded from Kartverket (2018b) and Kartverket (2018a) have 5 m x 5 m and 50 m x 50 m resolution, respectively. The unhatched areas are downloaded from British Oceanographic Data Centre (2018). Figure (b) shows the entire area, and figure (a) shows the insert marked by the red box in figure (b).

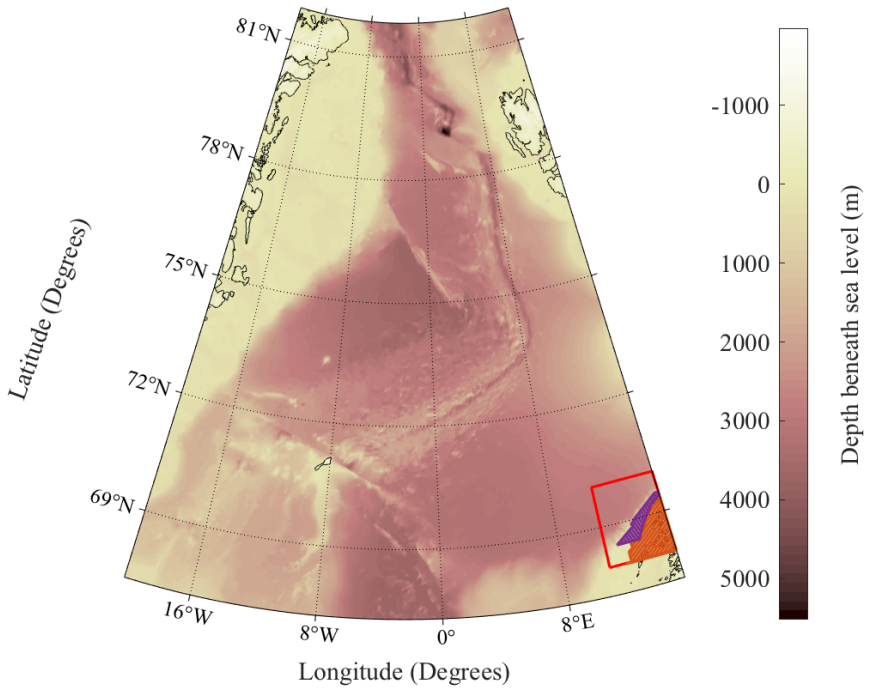

(b)

Figure 3.1: (Continued) Contour maps of the downloaded bathymetry data, with hatching indicating the resolution of the area. The data downloaded from Kartverket (2018b) and Kartverket (2018a) have 5 m x 5 m and 50 m x 50 m resolution, respectively. The unhatched areas are downloaded from British Oceanographic Data Centre (2018). Figure (b) shows the entire area, and figure (a) shows the insert marked by the red box in figure (b).

contours henceforth, has been acquired from British Oceanographic Data Centre (2018). Using this data for visualization, instead of the more detailed data from Kartverket, will not affect the reader's understanding of the data, due to how large the visualized areas are in comparison with the resolution. Unless otherwise specified, all maps are made by the author in MatLab, partly using the `m_map` package by Pawlowicz (2018).

The combined bathymetry data sets were used to compute an interpolant structure using MatLab's `scatteredInterpolant`-function. It was calculated using linear interpolation between the sample points. The interpolant, F, is used by the model tools to evaluate the interpolated bathymetry depth at any position, as

$$z_{\text{interp}} = F(\Theta, \varphi), \tag{3.1}$$

where (Θ, φ) are coordinates of longitude and latitude. A summary of the processes performed to convert the downloaded bathymetry data to a parameter usable in the model tools is shown in the process diagram in figure 3.2. In the diagram, objects are defined in rectangular boxes, processes are described in diamond shaped boxes, and use of scripts are described in rectangular boxes with round ends. This convention has also been adopted in all process diagrams to come.

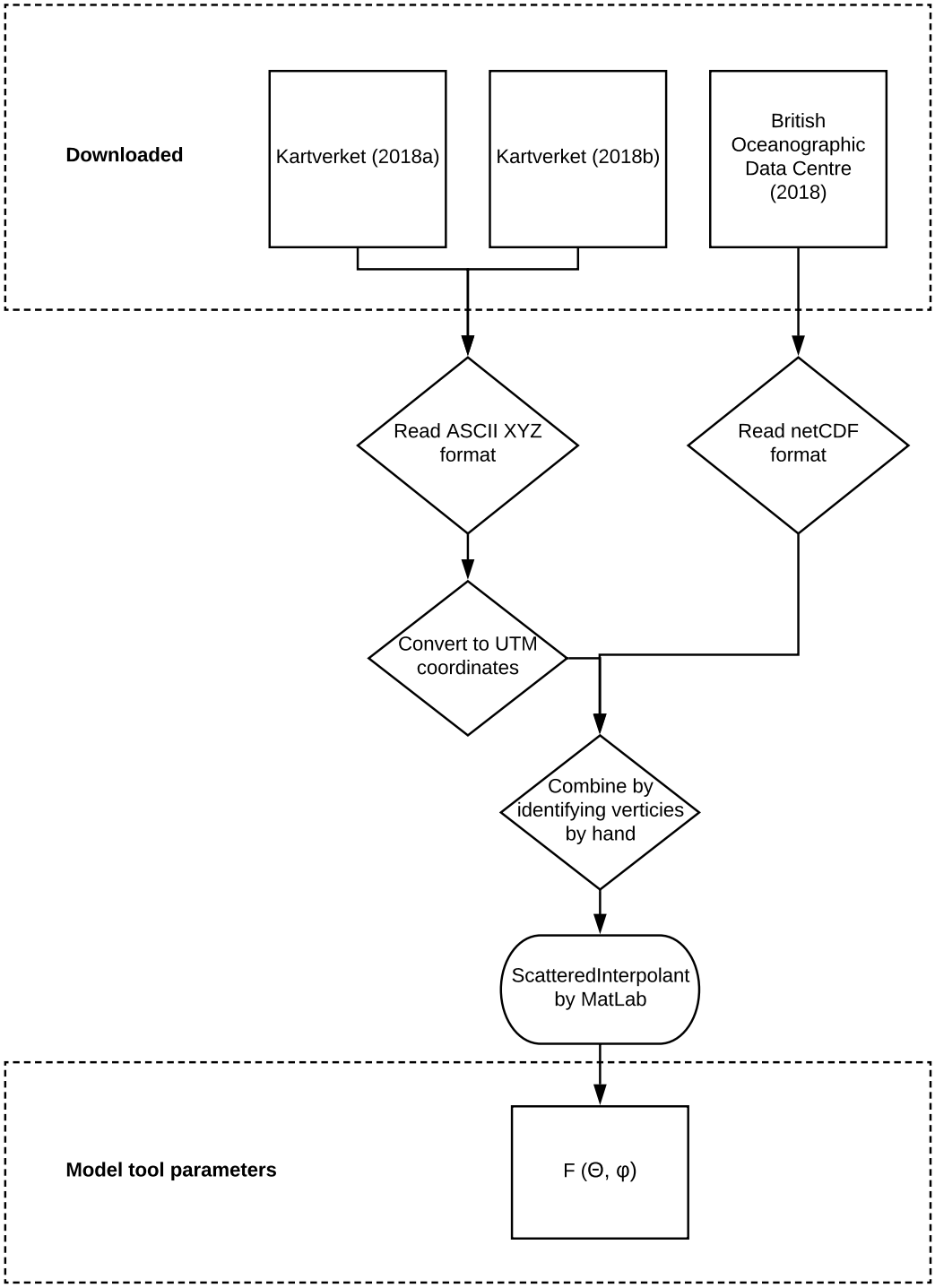

Figure 3.2: A process diagram summarizing how the downloaded bathymetric data was converted to the model tool parameter $F(\Theta, \varphi)$. The box shapes denote parameters as □, processes as ◇ and scripts as ⬭.

The bathymetry close to the LoVe Observatory is shown in figure 3.3. Here, one can clearly see that the bathymetric data, as expected, includes the semi-shallow Hola valley, the drop down from the continental shelf to the Lofoten Basin, and the Egga bank and the Vesterålen bank to the south and to the north of the valley.

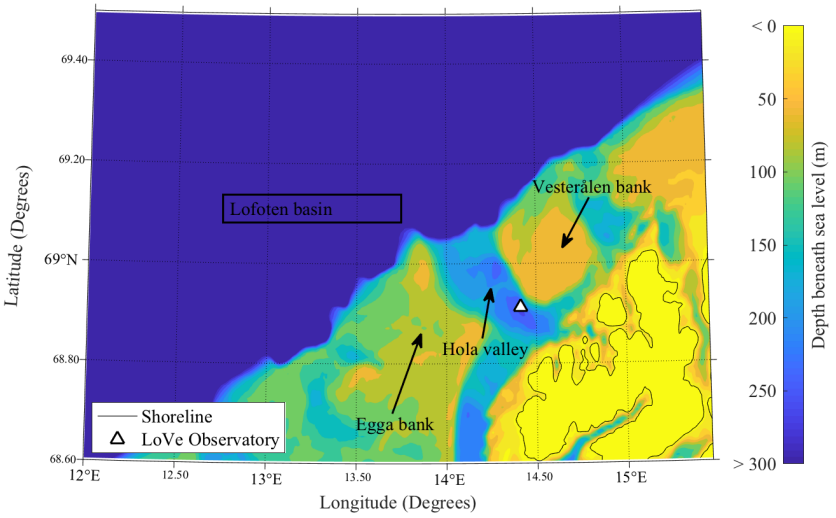

Figure 3.3: The bathymetry in the area surrounding the LoVe Observatory, with some of the prominent geographical regions annotated on the map.

3.2 Sound speed profiles

The sound speed can be calculated from measurements of the ocean temperature, salinity and depth, as seen in equation 2.2. These variables, which together are known as conductivity, temperature, and depth (CTD) measurements, are often measured by various research vessels and monitoring buoys and used for for example oceanographic and biological studies. The International Council for the Exploration of the Sea (2018) (ICES) has developed a database where such measurements are submitted from a number of different scientific communities, and made available to other researches. The database offers data sets containing the measurement position, the time of measurement, and measured temperature, salinity, hydrostatic pressure, at 1 bar intervals. Four such data sets, containing measurements from 31.05.1995 to 20.11.2016 in the area around the LoVe Observatory, were downloaded. Figure 3.4 shows the measurement position of all of the downloaded data sets. Some of the measurement positions, as indicated in figure 3.4, are deemed redundant for the simulation of transmission loss experienced by the LoVe Observatory, because the CTD measurements will not affect the calculated TL values. These CTD measurements have therefore been discarded. The choice of which measurements to keep was made graphically based purely on the measurement location in relation to the LoVe Observatory, and an exaggerated number of measurements were kept as a precaution against discarding useful information.

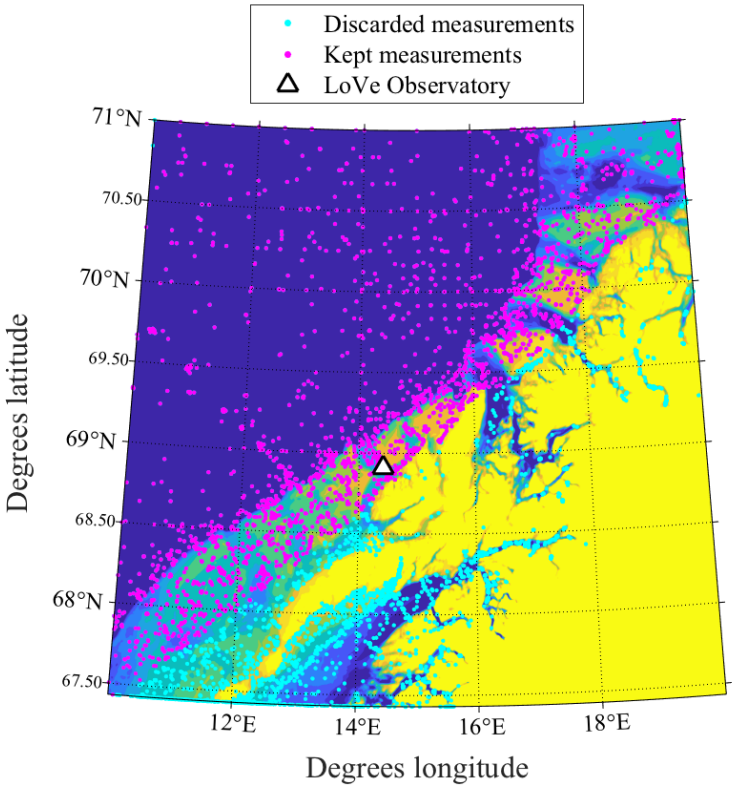

Figure 3.4: The measurement positions of all the downloaded ocean parameter measurements, showing which measurement set that will be discarded. To give a sense of where the measurements were taken, their positions are plotted on top of a map of the bathymetry (British Oceanographic Data Centre, 2018).

The database did not provide records of the depth at which the data was measured. Therefore, the depths of the measurements were calculated using Fofonoff and Millard Jr.'s [1983] relation between depth and hydrostatic pressure

$$z = \frac{9.72659P_h - 2.2512 \times 10^{-5}{P_h}^2 + 2.279 \times 10^{-10}{P_h}^3 - 1.82 \times 10^{-15}{P_h}^4}{g(\varphi) + 0.5\gamma\, P_h}. \tag{3.2}$$

Here, P_h is the hydrostatic pressure in dbar, $g(\varphi)$ is the acceleration due to gravity at sea level as a function of latitude, γ is the mean vertical gradient of gravity, which according to Fofonoff and Millard Jr. (1983) is $\gamma = 2.184 \times 10^{-6}\,\mathrm{ms^2dbar}$. Equation 3.2 is according to Fofonoff and Millard Jr. (1983) accurate to 0.1 m in z. The acceleration due to gravity is a function of latitude, φ, and Fofonoff and Millard Jr. (1983) gives a formula for this relationship that follows the Geodetic Reference System 1967. This system has, however, since been updated, and the acceleration due to gravity has thus instead been calculated from the Geodetic Reference System 1980 (Moritz, 1980). This states that

$$g(\varphi) = g_e \frac{1 + 1.931\,851\,353 \times 10^{-3} \sin^2 \varphi}{\sqrt{1 - 6.694\,380\,022\,90 \times 10^{-3} \sin^2 \varphi}}, \tag{3.3}$$

where g_e is the acceleration due to gravity at sea-level at the equator, which is $9.780\,326\,771\,5\,\mathrm{m/s^2}$ (Moritz, 1980). The depth of each measurement downloaded from ICES was thus calculated using equation 3.2 and 3.3, and recorded.

The downloaded data sets were provided in comma separated value files (.csv) with one column for each variable. In total, the files contained 2856694 rows of data, without any indicators distinguishing one measurement time or position from the next. The data were separated into sets, each containing the measured variables at one position at one time by running the contents of the files through a `for`-loop in MatLab that identified where in the column of numbers the pressure variable stopped increasing, or where in the column of numbers the position changed, indicating the start of a new measurement. The measured variation in temperature and salinity were used to calculate the sound speed at each calculated depth, using equation 2.2. For each set, the variation in c_w with z, giving the sound speed profile (SSP), was saved, together with the measurement position and time. These data are used by the model tools to construct the SSP at any position, as explained further in section 3.2.

Season	**Months**
Winter	December - February
Spring	March - May
Summer	June - August
Autumn	September - November

Table 3.1: The definitions of the seasons.

The temperature in the water will vary with season, and thus the sound speed will also vary throughout the year. It is of interest to observe how the transmission loss varies with season as a consequence of this, and the SSPs measurement times were therefore categorized into seasons. The seasons were defined as shown in table 3.1.

The resulting calculated SSPs are presented and further discussed in chapter 5. The processes that have been applied in order to convert the downloaded CTD measurements to CTD and SSP set as a function of z is shown in the process diagram in figure 3.5. Both these data sets are used in the model tools.

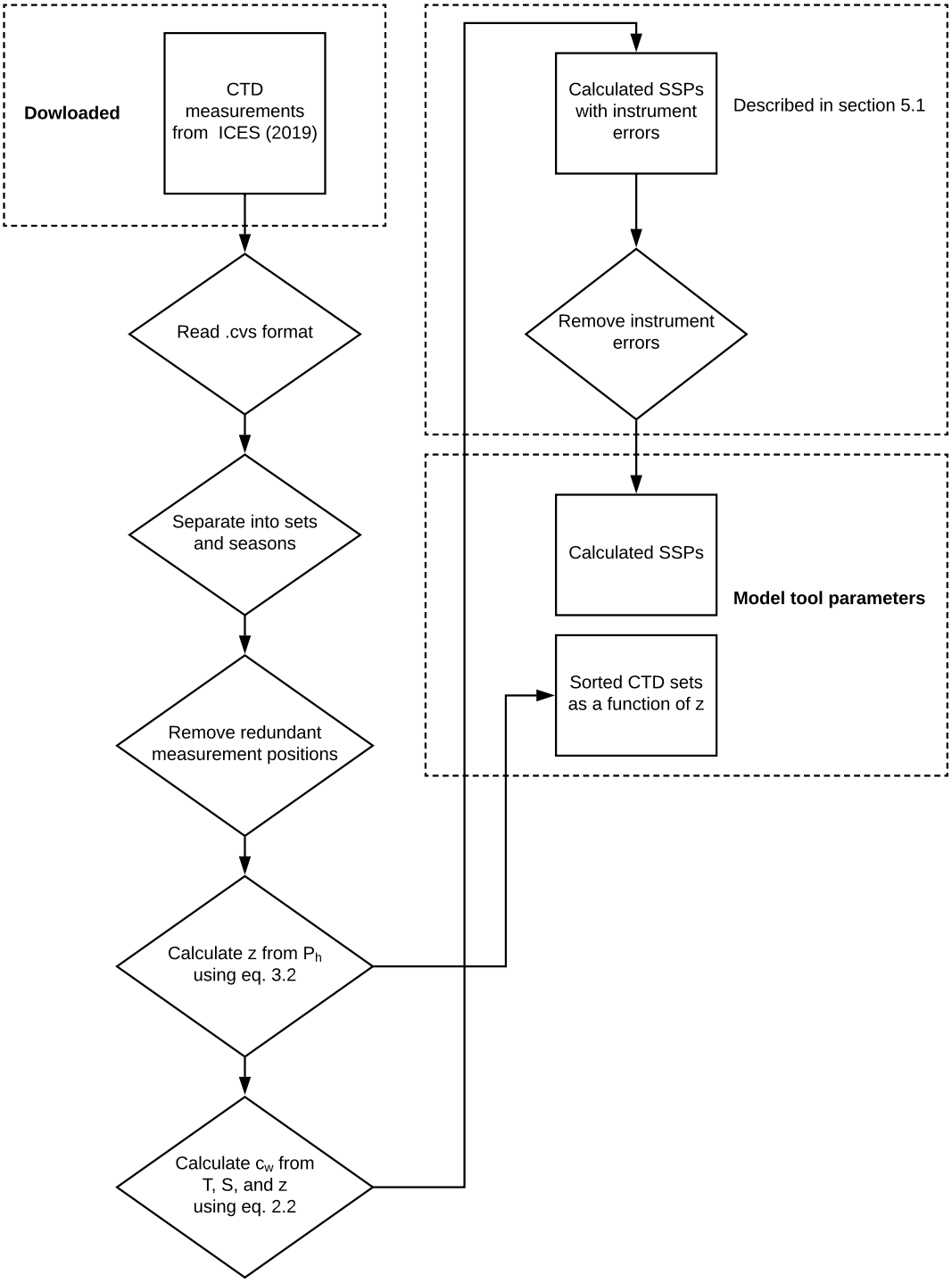

Figure 3.5: A process diagram showing how the downloaded CTD measurements were converted to two model tool parameter sets. The box shapes denote parameters as □, processes as ◇ and scripts as ⬭.

3.3 Sediment composition and properties

The sediment composition at the sea floor has been mapped by Geological Survey of Norway (Norges geologiske undersøkelse). The grain type in the 0 to 50 cm top layer of the sea floor has been determined by taking samples of the sediments, analysing acoustic reflectivity measurements, seismic surveying, analysis of the bathymetry data, as well as video recordings of the sea floor (Geological Survey of Norway, 2016). This has resulted in a characterisation of the seafloor type, where each area containing a particular type of sediment has been mapped in polygons. The polygons are defined by the Cartesian coordinates of their vertices. The coordinates of these polygons and their corresponding qualitative characterisations of the sediment type was downloaded from Geological Survey of Norway (2016) as a .shp-file (shapefile). The data were read using MatLab's `shaperead` -function which outputted a `struct`-variable containing a list of polygon vertices and their corresponding sea-floor characterisation. To the author's knowledge, the data by Geological Survey of Norway (2016) is the only available characterization of the Lofoten-Vesterålen basin which can be used to derive quantitative descriptions of the sediment.

Each polygon identifies a distinct area, which, at least in theory, only contains one type of sediment. The qualitative characterizations of the sediment types are specified according to the nomenclature by SOSI, which was described in section 2.2.1. For the sediment types found in the downloaded data, the translations of these characterisations, as defined by Mareano (2018), are reproduced in table 3.2. The table gives the amount of each sediment texture found in each sediment type. Not all of the downloaded material characterizations contained information about all of the texture components of the sediment types. Therefore, some of the missing information has been filled in by comparing the sediment type with Folk's definitions of textural groups, which were described in section 2.2.1. These additions to the table are indentified with the superscript †. In figure 3.6, a map of the downloaded data from Geological Survey of Norway (2016) has been plotted. The map is drawn from the coordinates of each sediment polygon, and the colors of the polygons indicate the sediment types.

It is thus clear that the available knowledge of the seabed composition in the Lofoten-Vesterålen basin is limited to qualitative descriptions of the sediment, some information on the percentage mix of sediment textures, and the grain size of these textures. From this, it is necessary to derive the sound velocity, density, and coefficient of attenuation in each of the sediment types. The process diagram shown in figure 3.7 summarizes how the data downloaded from Geological Survey of Norway (2016) has been utilized to produce model tool parameters. The methods chosen to calculate these parameters for unconsolidated sediment types are described in section 3.3.1. Following this, the methods used for consolidated and mixed sediment types are described in sections 3.3.2 and 3.3.3, respectively. Finally, the geoacoustic properties of the areas not mapped by Geological Survey of Norway (2016) are discussed in section 3.3.4. All of the geoacoustic properties calculated or otherwise decided in these sections are summarized in table 5.1 in Chapter 5.

State	Sediment type	Ratio of clay to silt	Ratio of sand to silt and clay	Percentage volume of mud	Percentage volume of sand	Percentage volume of gravel	Comments
Unconsolidated	**Mud**	1:2 to 2:1		>90 %	<10 %	<2 %	C.f. sect. 3.3.1
	Sandy mud	1:2 to 2:1		>50 %	<50 %	<2 %	
	Sand			<10 %	>90 %	<2 %	
	Gravelly sandy mud		From 1:9 to 1:1			2 % to 30 %	
	Gravelly muddy sand		From 1:1 to 9:1			2 % to 30 %	
	Gravelly sand		>9:1			2 % to 30 %	
	Muddy sandy gravel		From 1:1 to 9:1			30 % to 80 %	
	Sandy gravel		>9:1			30 % to 80 %	
Consolidated	**Gravel, cobbles and boulders**					>80 % †	C.f. sect. 3.3.2.1
	Compact sediments or sedimentary bedrock						C.f. sect. 3.3.2.2
	Thin or discontinuous sediment cover on bedrock						
Mixed	**Mud alternating with blocks of hard sediment**						C.f. sect. 3.3.3

Table 3.2: Definitions of the textural contents of each sediment type. The sediment type names and the presented data have been taken from Mareano (2018). The superscript † indicates that the data have been taken from the texture group definitions by Folk (1954). Comments in the last column indicate in which sections the geoacoustic properties of the different sediment types are discussed.

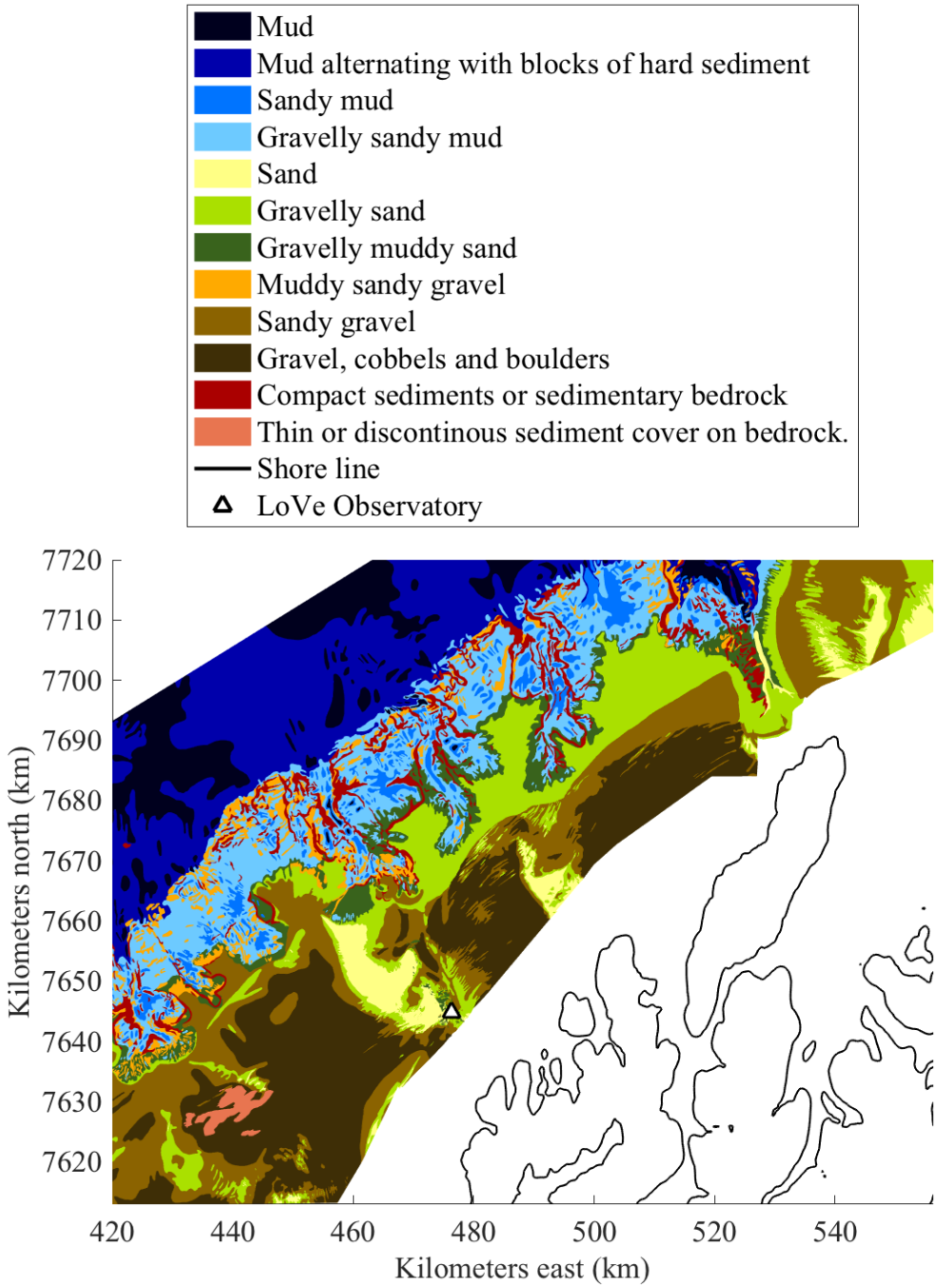

Figure 3.6: Sediment types in the Lofoten-Vesterålen basin, mapped by the Geological Survey of Norway (2016). The figure is constructed from polygon coordinates downloaded from Geological Survey of Norway (2016). The position of the shore line, provided by the British Oceanographic Data Centre (2018), has been added for clarity. The position coordinates are given in UTM zone 33, referenced to the intersection between the equator and the zone's central meridian.

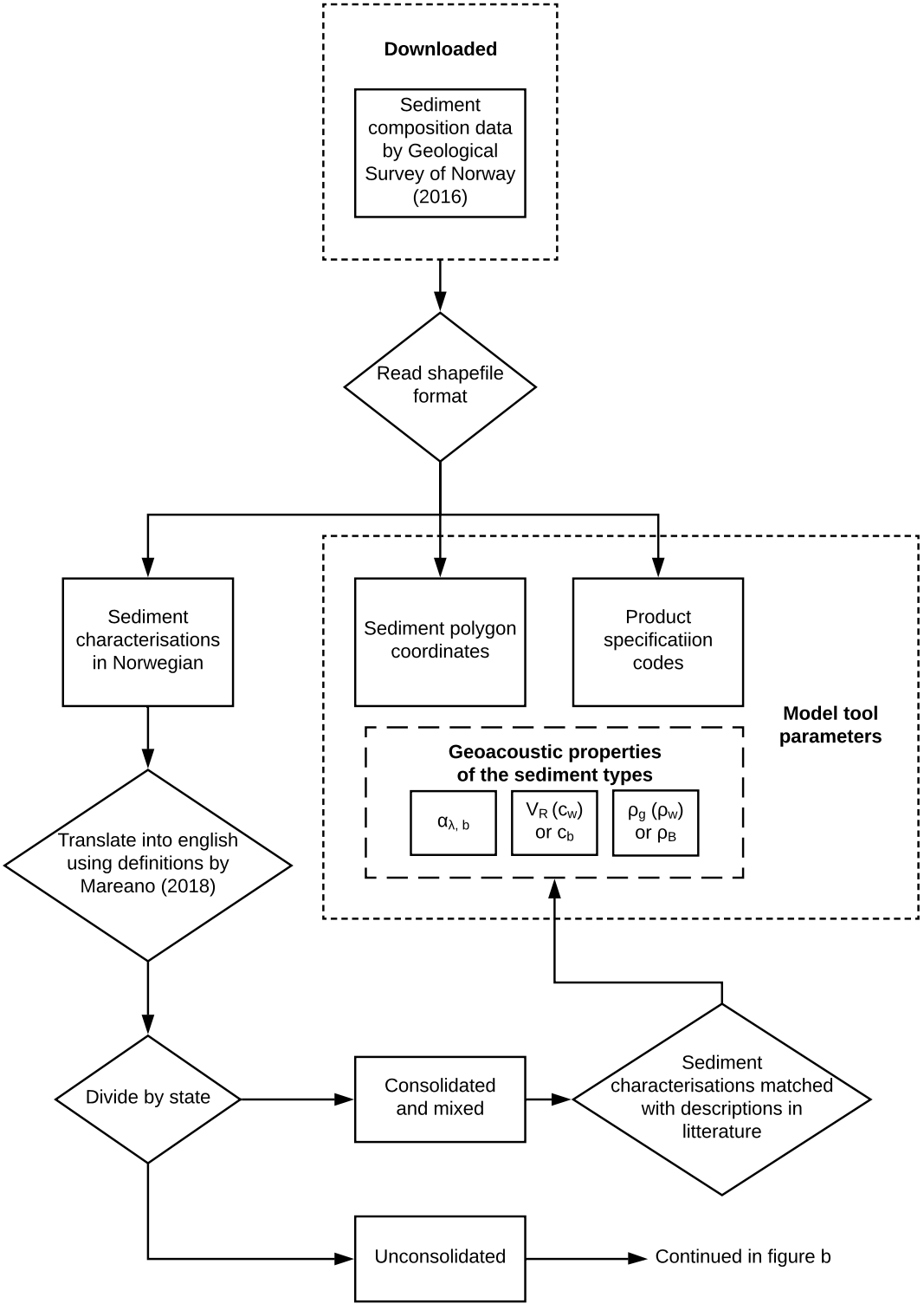

(a) Overview

Figure 3.7: A process diagram showing how the downloaded sediment composition data were converted to model tool parameter sets. Figure (a) shows and overview and figure (b) shows the details of how the geoacoustic properties of the unconsolidated sediment types were treated. The box shapes denote parameters as □, processes as ◇ and scripts as ⬭.

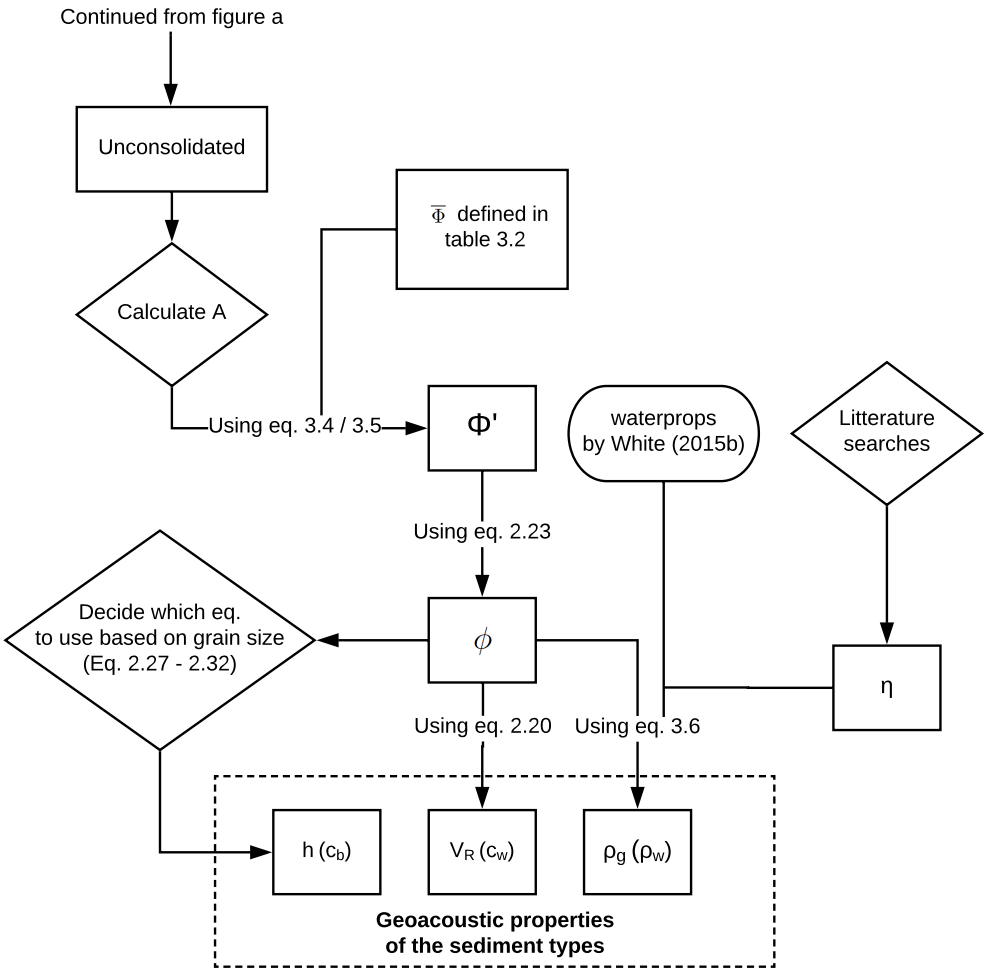

(b) Unconsolidated sediment types

Figure 3.7: (Continued) A process diagram showing how the downloaded sediment composition data were converted to model tool parameter sets. Figure (a) shows and overview and figure (b) shows the details of how the geoacoustic properties of the unconsolidated sediment types were treated. The box shapes denote parameters as □, processes as ◇ and scripts as ⬭.

3.3.1 Unconsolidated sediments

Firstly, the geoacoustic properties of the unconsolidated small grained sediments was considered. Consolidated sediments have high rigidity and should therefore be modelled as an elastic medium (Jensen et al., 2011). Out of the sediment types presented in table 3.2, most are unconsolidated, apart from '*Thin or discontinuous sediment cover on bedrock*', '*Mud alternating with blocks of hard sediment*', '*Gravel, cobbles and boulders*', and '*Compact sediments or sedimentary bedrock*', which will be dealt with separately, in section 3.3.2.

3.3.1.1 Average grain size and sound velocity

The sound velocity in the loose sediments were predicted using the regression between velocity ratio and mean grain size, presented in equation 2.20, which is based on a fluid approximation of the medium. This regression was chosen because grain size is the only available quantitative property of the sediment types. Since the grain sizes are defined in intervals, in order to apply the regression, it was first necessary to calculate an estimated mean grain size, Φ', for each of the sediment types.

A systematic method for estimating Φ' based on the available information in tables 3.2 and 2.1 was constructed by the author. Here, the superscript $'$ denotes that the parameter has been estimated by the author, and the same notation will be applied to the estimated mean grain size in units phi, ϕ'. The method of estimating these parameters was begun by estimating a fractional amount of each texture for each sediment type. This was given the symbol A. Then, for each sediment type, the fractional amount of the texture was multiplied by the average grain size of each sediment texture, so that

$$\Phi' = A_{\text{gravel}} \cdot \overline{\Phi}_{\text{gravel}} + A_{\text{sand}} \cdot \overline{\Phi}_{\text{sand}} + A_{\text{silt}} \cdot \overline{\Phi}_{\text{silt}} + A_{\text{clay}} \cdot \overline{\Phi}_{\text{clay}}, \tag{3.4}$$

where $\overline{\Phi}$ is average grain size of each texture, which was defined in table 2.1. As seen in table 3.2, for some of the sediment types, there is no information on the ratio of clay to silt. For these sediment types the clay and silt textures are combined into one mud texture, and the estimated mean grain size was calculated as

$$\Phi' = A_{\text{gravel}} \cdot \overline{\Phi}_{\text{gravel}} + A_{\text{sand}} \cdot \overline{\Phi}_{\text{sand}} + A_{\text{mud}} \cdot \overline{\Phi}_{\text{mud}}. \tag{3.5}$$

For each sediment type, the fractional amount A was determined based on the information given in table 3.2. It is a somewhat intricate calculation, so to see how A was determined, first consider the example of the calculation of the fractional amount of the sediment type '*Mud*'. This calculation is laid out schematically in the flow diagram in figure 3.8. As seen in columns 1 and 2, to begin with, the percentage volumes of sand, of mud, and of gravel were translated to decimal form. Initially, the less than and greater than symbols were disregarded, so that the decimal form of the percentage volumes gave the fractional amounts for these textures directly. Then, the portion of clay and the portion of silt was determined from the ratio of clay to silt. Because the ratio of clay to silt is specified as an interval, i.e. *1:2 to 2:1*, it had to first be converted to a single number by taking the average of the two limits, as shown in column 3 of figure 3.8, before this was also translated to decimal form. It is important to realize that mud is made up of silt and clay and that the portion of clay thus is the amount of clay within the volume of mud. Therefore, to find the fractional amount of clay and silt, their portions were multiplied by the percentage volume of mud, as seen in column 3 of figure 3.8. The fractional amounts for all of the sediment types where calculated following the method described for '*Mud*'. In summary, the method consists of reading the information given in table 3.2, translating all percentage volumes and ratios to decimal form, before multiplying the appropriate portions and percentage volumes to give the fractional amount.

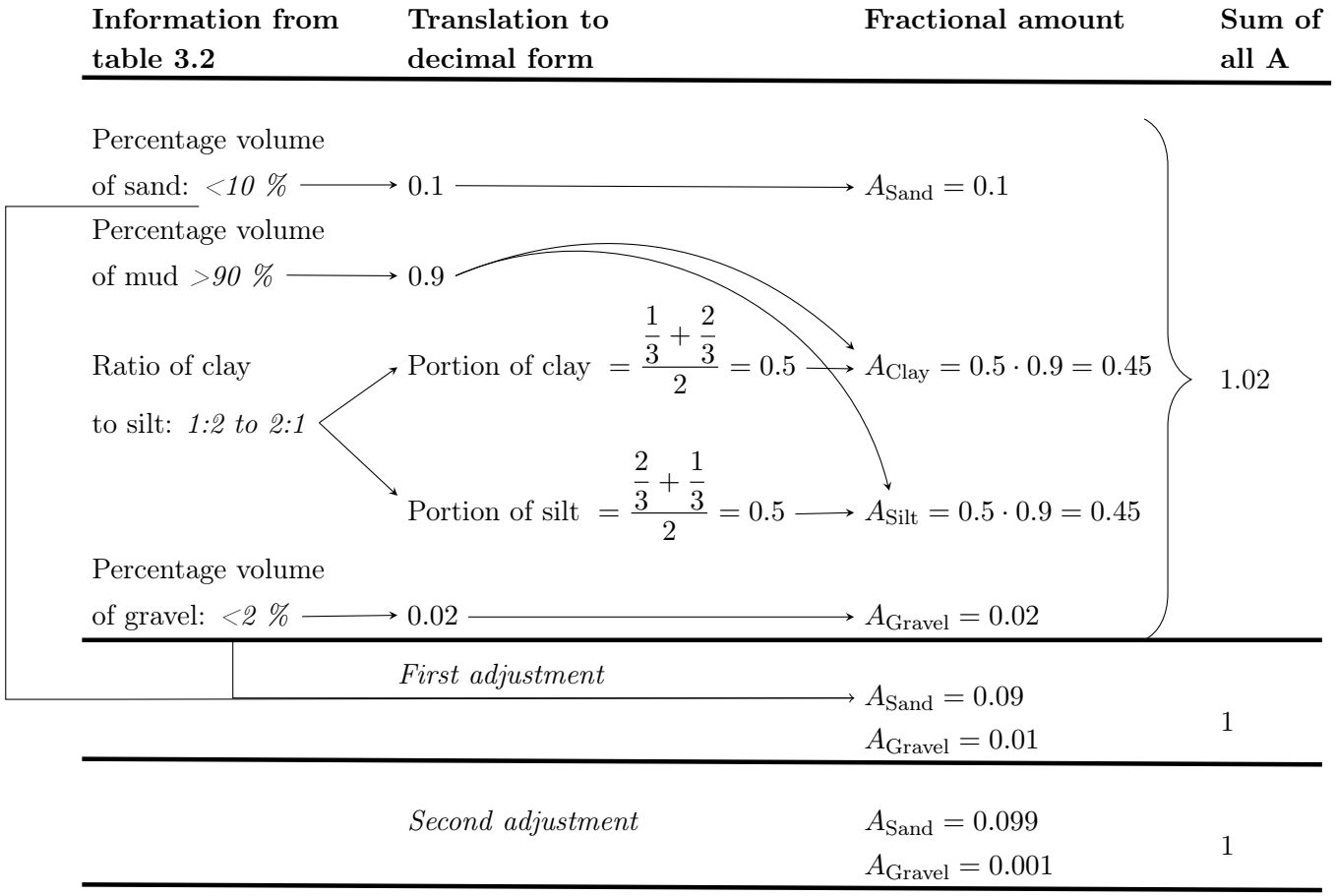

Figure 3.8: A flow diagram of how information from table 3.2 was used to calculate the fractional amounts in the sediment. The diagram shows the operations performed for the sediment type 'Mud' as an example, but the same methods were used for all sediment types.

The sum of the fractional amounts in a sediment type must equal 1, since the components in the sediment logically cannot total to more than 100 % of the sediment's volume. In the example shown in figure 3.8, the fractional amounts initially total to 1.02. It was therefore necessary to reduce some of the fractional amounts. The choices of which quantities to change was based on which textures that were denoted with a less than symbol in table 3.2. In the example shown in figure 3.8, this was true for both the percentage volume of sand, and the percentage volume of gravel. Therefore, the fractional amounts of sand and gravel were reduced by the same amount, until the total sum of all A equalled 1. This is denoted as 'First adjustment' in figure 3.8. This same logic was applied to all of the sediment types when their initial sum of A exceeded 1.

The sediment types '*Sand*' and '*Mud*' bear the same names as two textures. This does not mean that the sediment type '*Mud*' consists only of the texture mud, since, as seen in figure 3.8 there is a small amount of both gravel and sand in '*Mud*'. Yet, it is reasonable that the calculated Φ' for these sediment types are within the defined limits of the grain size diameter of the texture of the same name. Therefore, the values of A for '*Mud*' and '*Sand*' were adjusted slightly to make the resulting estimated mean grain size reasonably within the limits of the grain size diameter of the corresponding texture, which were defined by Mareano (2018) in table 2.1. This adjustment is denoted as 'Second adjustment' in figure 3.8, and the adjustment primarily consisted of reducing the amount of gravel in the sediments, down to $A = 0.001$. This is plausible, since Folk's definition of the sediment types '*Sand*' and '*Mud*' has only a trace of gravel. For consistency, this reduction was also made to the '*Sandy mud*'. The resulting fractional amounts of each texture in each of the sediment type after all adjustment have been made, can be seen in table 3.3.

	Sediment texture				
Sediment type	$\mathbf{A_{Sand}}$	$\mathbf{A_{Mud}}$	$\mathbf{A_{Clay}}$	$\mathbf{A_{Silt}}$	$\mathbf{A_{Gravel}}$
Mud	0.099	-	0.450	0.450	0.001
Sandy mud	0.499	-	0.250	0.250	0.001
Sand	0.909	0.090	-	-	0.001
Gravelly sandy mud	0.252	0.588	-	-	0.160
Gravelly muddy sand	0.588	0.252	-	-	0.160
Gravelly sand	0.756	0.084	-	-	0.160
Muddy sandy gravel	0.315	0.135	-	-	0.550
Sandy gravel	0.405	0.045	-	-	0.550

Table 3.3: The estimated fractional amounts, A, of each of the textures which make up each unconsolidated sediment type.

Finally, the estimated grain size Φ' was calculated, and equation 2.23 was used to convert the units of the grain size to units of phi. This gave ϕ'. This quantity was used to calculate the velocity ratio using equation 2.20. The resulting sediment velocity ratios are given in table 5.1. In the model tools, the sound velocity in the sediment is calculated using these values for V_R and the position dependent value of c_w at the sea floor, using equation 2.19.

3.3.1.2 Density

The mean grain size were also used to predict the density of the sediment, as seen in equation 2.24. However, as shown in equation 2.18, the bulk density of loose sediments is also dependent on the local density of the sea water. As previously mentioned, in RAM the density of seawater is taken to be constant. However, since the position and season dependent variation in temperature and salinity in the water is available in the downloaded CTD measurements, it was not necessary to make the same assumption when calculating the density of the sediments. This way, any potential effect of season on the reflectivity of the sea floor is accounted for in the estimated geoacoustic properties. Therefore, the bulk density used in the transmission loss simulations took the position dependent density of sea water into account. To enable this, the density of the sediment grains, ρ_g, was calculated by rearranging equation 2.18 and substituting in the bulk density using equation 2.20, giving

$$\rho_g = \frac{2.17 - 0.08\phi - \eta\rho_w}{1 - \eta}. \tag{3.6}$$

The density of sea water was calculated using a MatLab function called `waterprops`. This script, which can be seen in Appendix C.4, is written by White (2015b) and based on the complex set of equations by Siedler and Peters (1986), which is too lengthy to be shown here. When calculating the value of ρ_w in equation 3.6, the temperature, salinity, and pressure conditions used were $T = 23\,^{\circ}\text{C}$, $S = 35$ and $P_h = 1$ atm, since this was used by Jackson and Richardson (2007) in the calculation of equation 2.20. The porosities, η, of each sediment type were assumed based on values from literature, and are shown in table 3.4.

Sediment type	**Fractional porosity, η**	**Source**
Mud	0.45	(Zhu, 2016)
Sandy mud	0.38	(Geotechdata.info, 2013)
Sand	0.27	(Zhu, 2016)
Gravelly sandy mud	0.27	(She et al., 2006)
Gravelly muddy sand	0.25	(She et al., 2006)
Gravelly sand	0.25	(Kamann, 2007)
Muddy sandy gravel	0.18	(Geotechdata.info, 2013)
Sandy gravel	0.15	(Kamann, 2007)
Gravel, cobbles and boulders	0.40	(Zhu, 2016)

Table 3.4: Fractional porosities assumed for each sediment type, used in calculation of ρ_g.

The calculated grain density, ρ_g, of all the unconsolidated sediment types are shown in table 5.1. In the model tools, these values are used to calculate the local bulk density of the sediment, using equation 2.18. The equation is dependent on ρ_w which in the model tools are calculated by feeding the position and season dependent values of T and

S to the script `waterprops`. The values of ρ_B are therefore position dependent, and a single value for each sediment type cannot be presented.

3.3.1.3 Attenuation coefficient

Lastly, the calculated mean grain sizes were used to predict the attenuation coefficient, $\alpha_{\lambda,\,b}$, of the sediment. It was calculated using equation 2.25, by chosing $l = 1$, based on the aforementioned reviews by Hamilton (1972). Equation 2.25 gives $\alpha_{m,\,b}$ in units of $\mathrm{dB\,m^{-1}}$, so the units of the attenuation coefficient were converted to dB/λ by applying equation 2.65. The constant h was calculated by applying the appropriate regression from equations 2.27 to 2.32. The choice of regression was made based on the calculated mean grain size. For $0.063\,\mathrm{mm} < \Phi' < 0.6\,\mathrm{mm}$ the detailed regressions between h and Φ (shown in equations 2.31 and 2.32) were chosen, while for sediment types outside this range, the regressions between h and ϕ (shown in equations 2.27 to 2.30) were chosen. The resulting values of h, and the equation number for the regression chosen for each sediment type, can be seen in table 5.1. Notably, as pointed out in section 2.2.2, the regressions only extend to $\phi = 0$ units phi, so the attenuation coefficient in any coarser grain types could not be predicted using the regressions by Hamilton (1972). This issue was also encountered by Wensveen (1995), who also modelled transmission loss due to bottom interaction using an older version of the sediment mapping by Geological Survey of Norway (2016). For the sediment types with $\phi < 0$ units phi, he estimated that the attenuation coefficient was $\alpha_{\lambda,\,b} = 0.8\,\mathrm{dB}/\lambda$, at frequencies around $f = 2\,\mathrm{kHz}$. This is of course a drastically different frequency than the 20 Hz used in this study, but, unfortunately, no other source of information on the attenuation in coarse sediment types was found. Using equation 2.25, this makes the constant

$$h = \frac{0.8 \times 10^3}{c_b}. \tag{3.7}$$

For unconsolidated sediments, this was taken to be the value of h. In the model tools, this equation is applied using the position dependent value of c_b, before equation 2.25 is applied to give $\alpha_{\lambda,\,b}$.

3.3.2 Consolidated and mixed sediments

The remaining sediment types are '*Thin or discontinuous sediment cover on bedrock*', '*Mud alternating with blocks of hard sediment*', '*Gravel, cobbles and boulders*' and '*Compact sediments or sedimentary bedrock*'. These are all either consolidated or mixes between consolidated and unconsolidated sediment types, and thus require a different approach than the purely unconsolidated sediments. As already mentioned, rigid sediments should ideally be modelled as elastic materials. It is possible to predict the geoacoustic properties in the sediment types using Biot theory (Biot, 1956). However, that would require knowledge of many parameters describing the sediment types, which were not available. Only knowing qualitative descriptions of the sediment and some information on the average grain size was unfortunately not enough to predict the sound velocity in the consolidated sediments. It was therefore necessary to look to literature to try to

identify measurements of the sound velocity, attenuation and density in similar sediment types. This is done in sections 3.3.2.1 to 3.3.3 and all of the geoacoustic properties that are identified for each sediment type are summarized in table 5.1.

3.3.2.1 Gravel, cobbles and boulders

In the case of '*Gravel, cobbles and boulders*', there has to the author's knowledge not been published geoacoustic measurements of a directly comparable sediment type. The closest match was found for measurements of gravel, and these were used for the sediment type. Walker (2016) reported the density of dry gravel to be $1682\,\mathrm{kg\,m^{-3}}$. From this, the grain density of the gravel was calculated by rearranging equation 2.18, giving

$$\rho_g = (\rho_{\mathrm{dry}} - \eta\rho_{\mathrm{air}})(1-\eta)^{-1}. \tag{3.8}$$

The grain density of the gravel was calculated by assuming that the fractional porosity was 0.4 (Zhu, 2016) and that the air saturating the dry gravel had a density of $1.229\,\mathrm{kg\,m^{-3}}$ (Hall, 2015). The calculated grain density was $\rho_g = 2802\,\mathrm{kg\,m^{-3}}$. As with the unconsolidated sediment types, in the model tools, this value is used in equation 2.18 together with the local position dependent density of the sea water to calculate the final bulk density of the water saturated '*Gravel, cobbles and boulders*'.

The attenuation coeffient of water saturated gravel was reported by Jensen et al. (2011) to be $\alpha_{\lambda,b} = 0.6\,\mathrm{dB}/\lambda$. Delleur (1998) reported that the sound velocity in water saturated gravel is $2200\,\mathrm{m\,s^{-1}}$. The temperature and pressure conditions of the measurement were not specified, but room-conditions of 20 °C and 1 atm pressure were assumed here. The saturating water was accounted for by calculating a velocity ratio, using equation 2.19. The sound speed in the water was calculated using equation 2.2 with $T = 20\,^{\circ}\mathrm{C}$, $S = 35$, and $z = 0$. This gave a velocity ratio of $V_R = 1.44$. In the model tools, the position dependent *in situ* sound velocities are calculated by multiplying V_R with the local speed of sound in the water, as shown in requation 2.19, following the method proposed by Bachman (1989) for the finer grained sediments.

3.3.2.2 Solid bedrock sediment types

Next, the sediment types '*Compact sediments or sedimentary bedrock*' and '*Thin or discontinuous sediment cover on bedrock*' were considered. Both were treated as only solid bedrock materials, although the latter contains some thin sediment cover. This can be ignored because low frequency sound will penetrate the thin top layer (Jensen et al., 2011). The bedrock in the areas off the coast of Lofoten and Vesterålen mostly consists of sedimentary rocks (Buhl-Mortensen et al., 2015). However, the area marked as '*Thin or discontinuous sediment cover on bedrock*' in figure 3.6 lies on the bank Jennegghøgda, where older crystalline rock is exposed (Mareano, 2018; Maystrenko et al., 2017). According to the map *Land and Sea Areas of Northern Europe* by Sigmond (2002), the bedrock in this area is made of the metamorphic mineral amphibole, which has a sound velocity of $7.2\,\mathrm{km\,s^{-1}}$ (Palmstrom, 1995). This was taken to be the sound velocity for the sediment type '*Thin or discontinuous sediment cover on bedrock*'. Although some

variation of c_b with pressure in rocks has been shown, the effect is minor for the pressure range caused by depth variation in the ocean (Siggins and Dewhurst, 2003), and c_b will therefore be taken to be independent of depth in the two solid bedrock sediment types. The density of '*Thin or discontinuous sediment cover on bedrock*' was taken to be $\rho_B = 2700\,\mathrm{kg\,m^{-3}}$, which is the density of metamorphic rock, according to Zhu (2016). To find the attenuation in the sediment type, seismic measurements by Matheney and Nowack (1998) of the specific attenuation factor, $\frac{1}{Q^{(\alpha)}}$, were used. They reported that for crystalline rocks, $0.0016 < \frac{1}{Q^{(\alpha)}} < 0.0027$. The mean of this interval was used to calculate the attenuation coefficient in crystalline rocks, as

$$\alpha_{cm,\,b} = \frac{\pi f}{c_b Q^{(\alpha)}} \tag{3.9}$$

in $\mathrm{dB\,cm^{-1}}$, following Attewell and Ramana (1966). The units were converted to dB/λ using equation 2.65, so that

$$\alpha_{\lambda,b} = \frac{100\,\pi}{Q^{(\alpha)}} \tag{3.10}$$

This gave $\alpha_{\lambda,\,b} = 0.6754\,\mathrm{dB}/\lambda$.

In the areas marked as '*Compact sediments or sedimentary bedrock*' in figure 3.6, the map by Sigmond (2002) shows that the bedrock is made of softer sedimentary rocks such as sandstone and limestone. The sound velocity in these rock types vary from $2\,\mathrm{km\,s^{-1}}$ to $6\,\mathrm{km\,s^{-1}}$ (Zhu, 2016). The sound velocity in the sediment type was taken to be the mean of this range, giving $c_b = 4000\,\mathrm{m\,s^{-1}}$. The density in sedimentary rock is $\rho_B = 2600\,\mathrm{kg\,m^{-3}}$ (Zhu, 2016). By reviewing 122 published measurements of attenuation in sedimentary rocks, Attewell and Ramana (1966) found that the attenuation coefficient varied with frequency in kHz as

$$\alpha_{cm,\,b} = 1.012 \times 10^{-5} f^{0.911} \tag{3.11}$$

for $1 \times 10^{-3}\,\mathrm{kHz} < f < 10^5\,\mathrm{kHz}$. In the model tools, this formula is applied and the units of the attenuation coefficient are converted to dB/λ using equation 2.65. In the case of $f = 20\,\mathrm{Hz}$, this gave $\alpha_\lambda = 0.0573\,\mathrm{dB}/\lambda$.

3.3.3 Mixed sediment types

The only remaining sediment type is '*Mud alternating with blocks of hard sediment*', which is a mix between a consolidated and an unconsolidated sediment type. Because of the alternating nature of the description, the sediment type will vary with position. There is no available information about when or how often the sediment varies, and it is therefore not possible to model the different parts of the sediment as separate materials. Instead, the geoacoustic properties of the sediment type will be taken to be the average of the properties of its two parts. As the name implies, these two parts are '*Mud*' and '*hard sediment*'. The first part is of course the same as the unconsolidated sediment type '*Mud*', described in section 3.3.1. And the second part will be taken to be the same as

the consolidated sediment type '*Compact sediments or sedimentary bedrock*', described in section 3.3.2.2. Thus, the geoacoustic properties of '*Mud alternating with blocks of hard sediment*' will be calculated as the average of the position dependent geoacoustic properties of '*Mud*' and the geoacoustic properties of '*Compact sediments or sedimentary bedrock*'. Because one part of this calculation is position dependent, while the other is not, it is not possible to show representative values in table 5.1.

3.3.4 Unmapped deep sea regions

Unfortunately, Geological Survey of Norway (2016) has not mapped the seafloor sediments beyond the area shown in figure 3.6. To the author's knowledge, other than the data from Geological Survey of Norway (2016), there exists neither mapping nor relevant point measurements of the sediment in the Lofoten-Vesterålen basin. According to personal communication with Elvenes (2018), this is because there is much less variation in the sediment types beyond the continental shelf. According to Elvenes (2018), the entirety of the deep Lofoten basin can be assumed to be covered in mud. This was therefore taken to be the sediment type whenever the modelled transect extended beyond the area shown in figure 3.6. Hamilton and Bachman (1982) reports geoacoustic measurements specifically of mud from abyssal plains, that is, mud from deep flat regions of the seabed, much like the Lofoten basin. These measurements reported a velocity ratio of $V_R = 0.999$ and bulk density of $\rho_B = 1454\,\mathrm{kg\,m^{-3}}$, corrected to $T = 23\,^\circ\mathrm{C}$, and 1 atm pressure. The basin is relatively flat, as seen in figure 3.1, and the change in sediment sound velocity due to varying hydrostatic pressure with position is therefore minimal. Moreover, the temperature in the deep ocean is relatively constant with depth and season (Jensen et al., 2011). Therefore, the sound velocity and density of the sediment in the basin were taken to be constant with both position and season. The sound velocity was calculated from the velocity ratio by Hamilton and Bachman (1982), according to equation 2.19. Equation 2.2 was used to calculate the speed of sound of the water just above the sea-floor. The temperature was taken to be $2\,^\circ\mathrm{C}$, the constant temperature of deep oceans (Jensen et al., 2011), and salinity is assumed to be $S = 35$. The depth is taken to be $z = 3000\,\mathrm{m}$, as an estimated average, based on the bathymetry map in figure 3.1. The resulting sound velocity is $c_b = 1507\,\mathrm{m\,s^{-1}}$. In table 5.1, this value is denoted as '*Abyssal mud*'.

The density of '*Abyssal mud*' reported by Hamilton and Bachman (1982) had to be corrected for temperature and pressure of the water saturating the grains. This was done by first re-arranging equation 2.18 to calculate the grain density

$$\rho_g = \frac{\rho_B - \eta\rho_w}{1 - \eta}. \tag{3.12}$$

Here, ρ_w was calculated using the function `waterprops` (White, 2015b), with the aforementioned measurement pressure and temperature conditions as input arguments. Then, the calculated grain density was substituted back into equation 2.18, only this time ρ_w was calculated using the *in situ* conditions for temperature and depth. The resulting bulk density was $\rho_B = 1450\,\mathrm{kg\,m^{-3}}$, as shown in table 5.1.

Hamilton and Bachman (1982) did not describe the sound attenuation in the measured '*Abyssal mud*'. In lack of a more detailed source, in the unmapped region, the

attenuation coefficient was therefore calculated using the same method as for the aforementioned unconsolidated sediment types. This involved using equation 3.7 to calculate h before $\alpha_{\lambda,b}$ was calculated by equation 2.25. As shown in table 5.1, this gave $\alpha_{\lambda\, b} = 1.85 \times 10^{-4}\,\mathrm{dB}/\lambda$.

Chapter 4

Simulation methods

4.1 Chosen model parameters

Here, the decided user specified model parameters in RAM are described. These choices are implemented in all simulations in this thesis, unless otherwise specified. The source frequency is set to $f = 20\,\text{Hz}$, corresponding to the middle of the frequency range of the Fin whale (Halkias et al., 2013). The simulated source is placed at the position of the LoVe Observatory, following the principle of reciprocity. The source depth is thus given by the depth of the observatory, at $z_{\text{source}} = 258\,\text{m}$. The step-size in r and z will be determined through a test of convergence, which is discussed in section 4.4. The number of Padé coefficients will be set to $m = 8$, which according to Collins et al. (1996) is an appropriate choice for running the algorithm in deep water and with large Δr steps. The stability parameter is set to $n_s = 1$, since, according to the user guide for RAM (Collins, 2001), $n_s = 1$ or 2 is effective for most problems. The range at which the stability constraints are turned off is specified by r_s. But, when r_s is set to 0, RAM imposes the stability constraints at all ranges. It is desired that RAM imposes the stability restrictions in the entire domain, so r_s is set to 0 in this study. In RAM, it is possible to reduce the resolution of the returned transmission loss results, after it has been computed. The resolution of the results are reduced by the user specified factors, *ndz* and *ndr*, known as the decimation factors. To avoid loosing potentially interesting details, this will not be done in the results shown in this thesis. The decimation factors, *ndz* and *ndr*, will therefore both be set to 1.

4.2 Reading the environmental input parameters

A number of MatLab functions, here referred to as model tool scripts, have been written in order to extract the input parameters needed by RAM from the model tool parameters described in Chapter 3 and Chapter 5. The functions have been constructed so that the location specific input arguments needed to run a RAM simulation can be identified automatically by specifying the location of the transect that will be simulated, and the season. The process diagram shown in 4.1 summarizes the entire procedure that has been

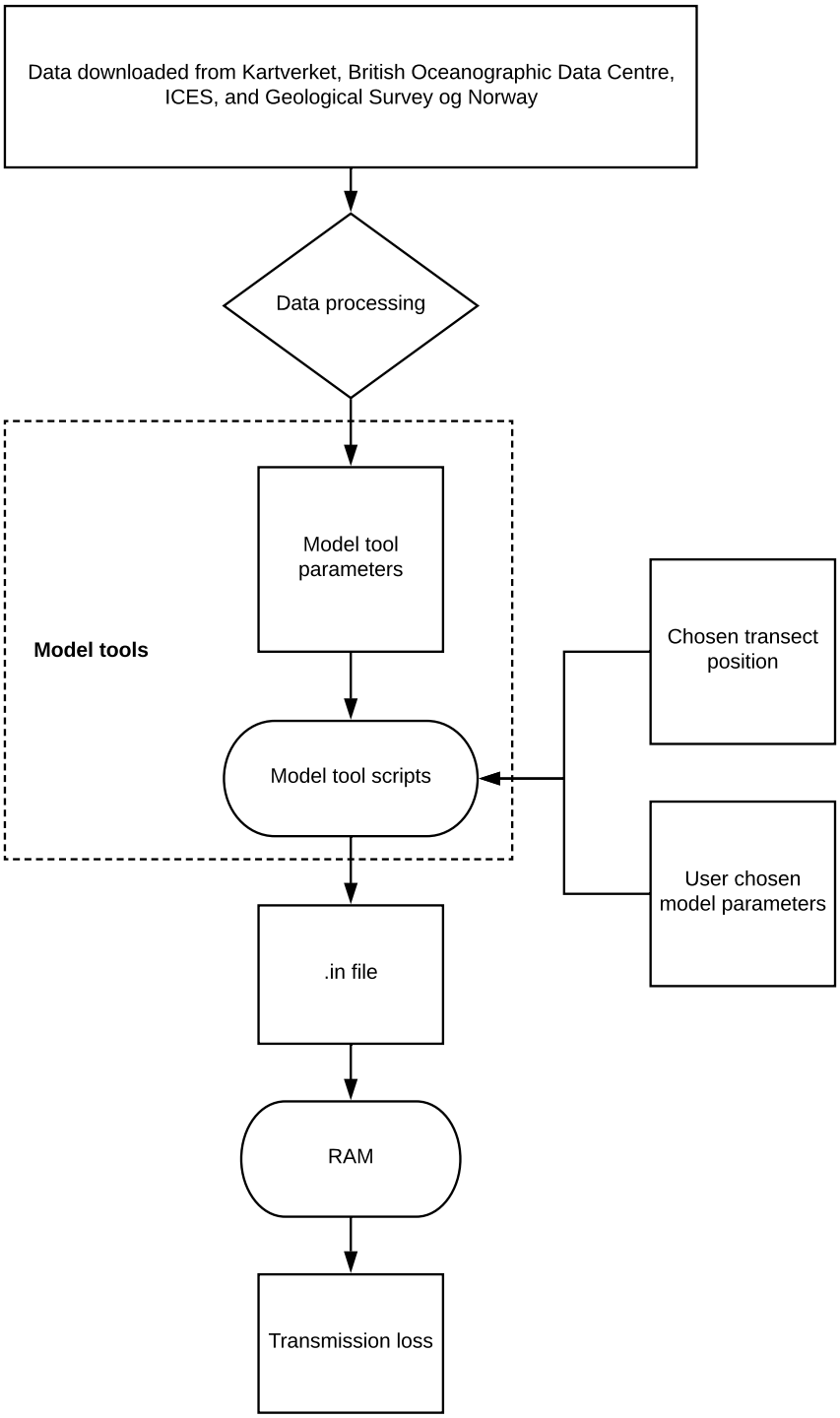

Figure 4.1: A process diagram summarizing how the procedures that had to be performed before RAM could be used to simulate the transmission loss. The box shapes denote parameters as □, processes as ◇ and scripts as ⬭.

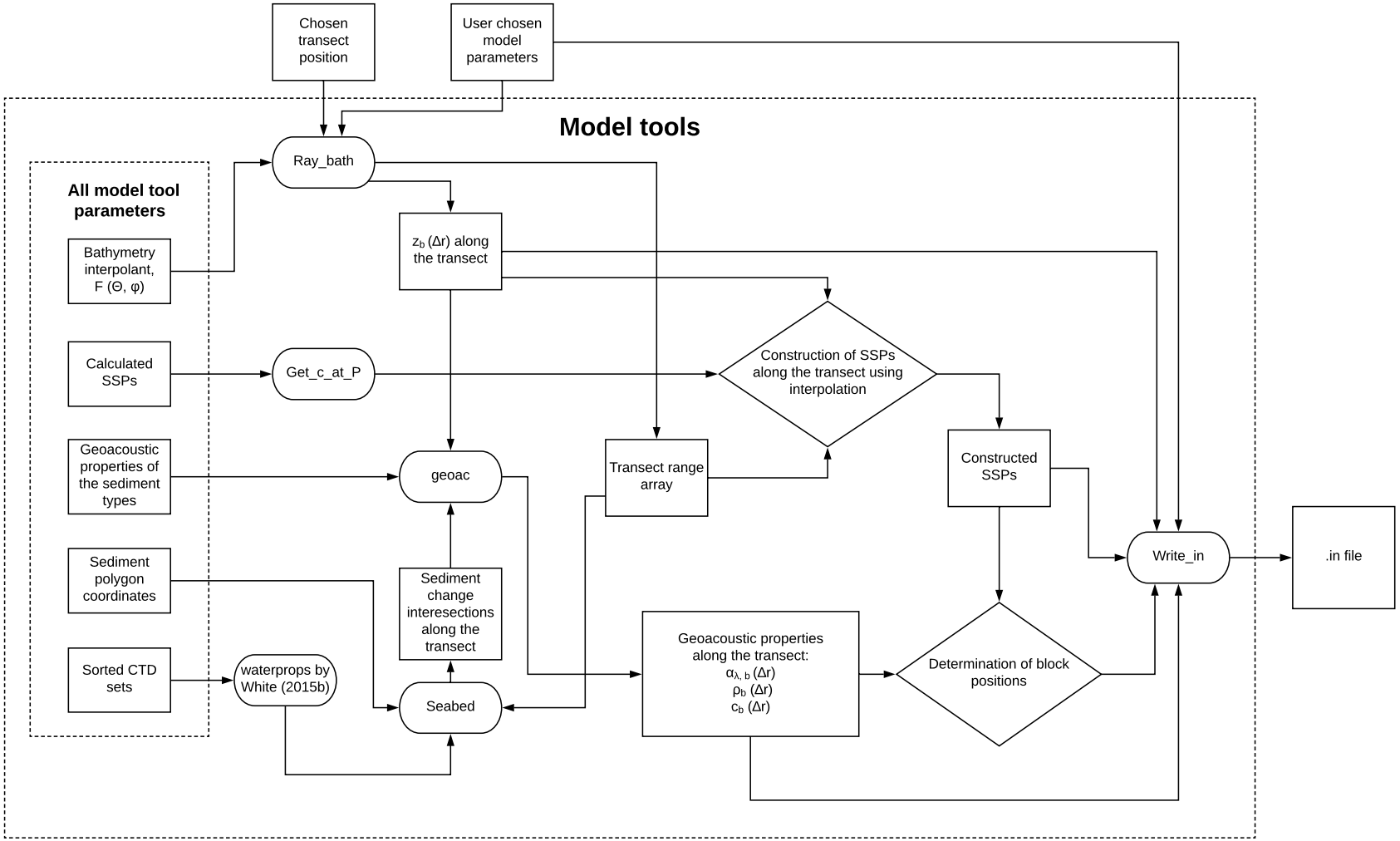

Figure 4.2: A process diagram summarizing how the model tools operate. The box shapes denote parameters as □, processes as ◇ and scripts as ⬭. The sources of the model tool parameters are laid out in figures 3.2, 3.5, and 3.7. All of the scripts, processes, and parameters in the figure are described in sections 4.2.1 to 4.3.

performed in order to turn the downloaded environmental data sets into usable `.in`-files that can be run by RAM. In the first step, the downloaded data sets have been processed to produce the model tool parameters: the bathymetry interpolant $F(\Theta, \varphi)$, the sorted CTD sets, the calculated SSPs, the geoacoustic properties of the sediment types, and the sediment polygon coordinates. How these data sets have been constructed has been detailed in figures 3.2, 3.5, and 3.7, for the bathymetry, the SSPs and CTD sets, and the geoacoustic properties and coordinates, respectively. These processes have produced the full set of model tool parameters, which are used by the model tool scripts in order to write the `.in`-file. Sections 4.2.1 to 4.2.3 describe how the model tool scripts operate for each of the main input parameters: bathymetry, sound speed profiles, and the geoacoustic properties of the seabed. These steps are summarized in the process diagram shown in figure 4.2. Since all of the model scripts have been written so that other users may utilize them to write the `.in`-file for RAM by simply specifying the transect they wish to model, they can be used to model any transect in the Lofoten-Vesterålen basin. Moreover, it should be noted that the model tools can also be used to produce environmental input parameters to other acoustic modelling software, such as Bellhop (Porter and Bucker, 1987), if some simple alterations are made to the `Write_in` script shown in the last step of the model tools in figure 4.2. The usage of the model tools is thus not limited to the results presented in this thesis.

In order to let the user of the model tools specify the location of the transect, it was necessary to relate the coordinate system used by RAM to the actual geographic position of the LoVe Observatory. A contour plot of the bathymetry in the immediate area around the LoVe Observatory can be seen in figure 4.3. The coordinate system defined in figure 2.2 has been placed on figure 4.3, so that the coordinate system is now defined in relation to real geographical orientations. The coordinate system was placed so that the y-axis points north, and the z-axis points towards the bottom of the ocean, into the paper in figure 4.3. The principle of reciprocity has been applied, and the origo is therefore placed at the ocean surface directly above the position of the LoVe Observatory, at 476 378 meters East and 7 644 811 meters North or $\Theta = 14.411\,67°$ longitude and $\varphi = 68.913\,33°$ latitude. Any position in the surrounding area can thus be described by the parameters (r, θ), where r is the radial distance from the origin.

Thus, transects run outwards from the LoVe Observatory in the direction defined by θ. To take into account the curvature of the earth, the radial positions of the transects were taken to be geodesics along an ellipsoid defined by the World Geodetic System of 1984 (Pawlowicz, 2018). The (Θ, φ)-coordinates of each point on the transect was calculated using the `m_geodesic`-function by Pawlowicz (2018). Whenever needed, these coordinates were translated to the (r, θ)-coordinate system using the function `m_ll2xy` by Pawlowicz (2018). The points on the transect are equidistant from each other, separated by the range step Δr. A transect can therefore be described by an array of radial distances from the observatory, henceforth referred to as the transect range array. Or, the transect can simply be defined by an angle θ, a range step Δr and a maximum length of the transect.

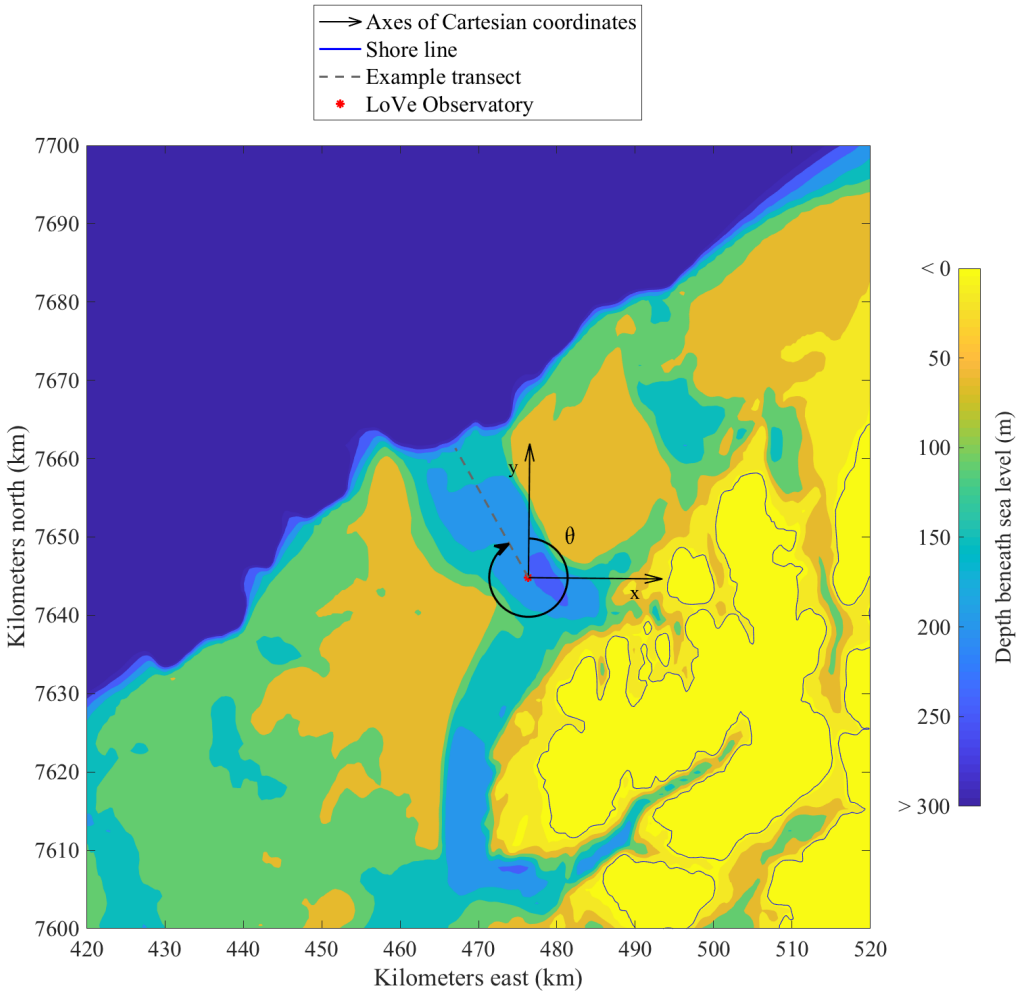

Figure 4.3: The bathymetry around the LoVe Observatory, provided by British Oceanographic Data Centre (2018), and definition of the transect coordinate system. The map's coordinates are given in UTM zone 33, referenced to the intersection between the equator and the zone's central meridian. An example transect is plotted at $\theta = 330°$, which points straight out of the Hola valley.

4.2.1 Bathymetry

The bathymetry along a given transect can be extracted using the MatLab function named `Ray_bath`, which takes the bathymetry interpolant F as an argument. The function can be seen in Appendix C.1. In addition to the interpolated bathymetry height data, the function also outputs the transect range array, as well as the Cartesian co-

ordinates of each point in the array. The geodesic distance from the listening position to each point along the transect was calculated using functions from the `m_map` package (Pawlowicz, 2018). In figure 4.3, an example transect is indicated at the angle $\theta = 330°$. The depth along this transect, as produced by the `Ray_bath`-function, can be seen in figure 4.4.

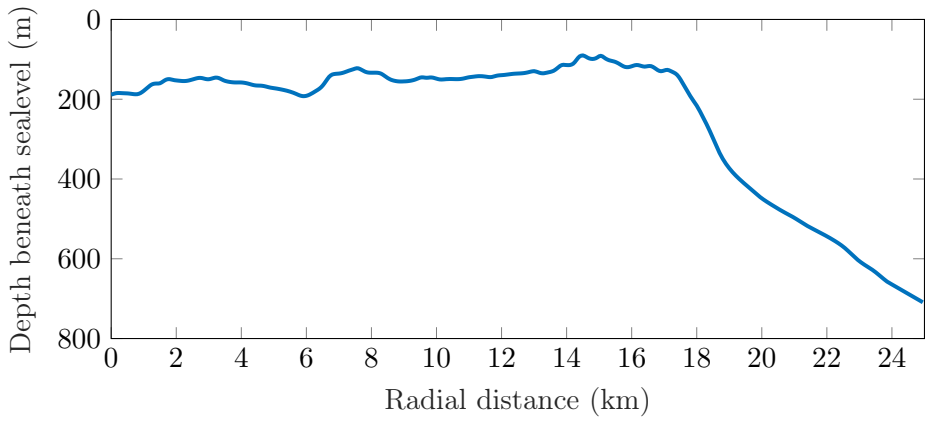

Figure 4.4: An example of the bathymetry along a transect, at $\theta = 330°$. The depth data have been taken from the bathymetry data from Kartverket [2018a; 2018c].

4.2.2 Sound Speed profiles

The sound speed in the water varies both with geographical position and with depth. The measured SSPs are made at scattered locations, and it is therefore necessary to interpolate to find a representation of how the SSPs vary along a specific transect. When setting up the simulations in RAM it is possible to change the SSP at any range. It is therefore up to the user to decide when, and how often, to include changes in the SSP. If the model includes SSPs that are measured along the same transect that is modelled, the positions of the measurements will of course decide when the SSPs will be changed in the model. However, since in this case the SSPs are measured at scattered locations, there is no indication of what positions along the transect the SSPs should be interpolated. To limit the computation time, it is desirable to change the SSP as seldom as possible. Yet, given the large number of samples in the measured SSPs, one is forced to think that the modelled SSPs should be interpolated at small intervals, in order to include all the detail inherent in the SSP measurements. If the interpolations are done at a regular interval, Δr_{SSP}, it would be possible to conduct a convergence test to try to identify how small the step needs to be to make the resulting transmission loss solutions converge. However, according to Storheim (2018), the large time span in which the SSP measurements were conducted means that the added detail one would gain from using a small Δr_{SSP} will not reflect actual detail in the *in situ* sound speed, but rather stem from the fact that sound speed changes with both year, season, and time of day. Storheim (2018) recommends interpolating the SSP at $\Delta r_{SSP} = 1000\,\text{m}$, and his advice will be

followed. Therefore, interpolated SSPs are constructed at each radial position along the transect, at $\Delta r_{SSP} = 1000\,\text{m}$ intervals.

At each radial position along the transect, a single SSP was constructed. The constructed SSP consists of variation of c_w with z, at discrete values of z. Interpolation was used to identify the value of c_w at each discrete depth position. Because the SSP measurements' variation with depth were reported in terms of hydrostatic pressure, and z varies slightly with latitude for a given pressure, c_w was interpolated at increments of P, instead of z. The resolution of the constructed SSP was named ΔP_{SSP}.

4.2.2.1 The vertical resolution of the constructed SSP

Before performing the construction of the SSP, the value of ΔP_{SSP} had to be decided. The measured SSPs were reported in increments of 1 bar, so this is the smallest reasonable value of ΔP_{SSP}. However, it is not always necessary to interpolate the SSP at such a small interval. First of all, the RAM model will only utilize depth variation in c_w at increments of the user decided depth resolution, Δz, which will be determined in section 4.4. So if Δz is large, ΔP_{SSP} can be made correspondingly large. Secondly, the plots of the measured SSPs, shown in figure 5.1, reveal that the change in c_w with depth is quite detailed in shallow water, but that all of the measured SSPs converge towards a linear relationship between c_w and z at a certain depth. As expected, this occurs below the minima in c_w, at depths where the pressure mainly determines the value of c_w.

ΔP_{SSP} does not need to be a constant value. In order to preserve detail of the measured SSPs at shallow depths, ΔP_{SSP} was made small at low values of z, but higher at larger values of z. This was done because it is constructive for the computational efficiency of the model to make the increment ΔP_{SSP} as large as possible, without sacrificing detail. Due to the linear behaviour of $c_w(z)$ at large depths, and the fact that RAM linearly interpolates with depth between the user specified values of c_w (Collins, 2001), ΔP_{SSP} can be made large when there is little variation of c_w with z. Based on the variation of c_w with z in the measured SSPs, shown in figure 5.1, it was decided that for $z > 1500\,\text{m}$, the depth increment of the interpolation of the SSPs was set to $\Delta P_{SSP} = 15\,\text{bar}$. For $z < 1500\,\text{m}$, the value of ΔP_{SSP} was set to $1\,\text{bar}$, which is the resolution of the measured SSPs.

4.2.2.2 Interpolation of the SSP

After the vertical resolution of the constructed SSP has been determined, it is now possible to construct the SSPs. At a given point along the transect, each value in the SSP was determined by interpolation based on all of the measured values c_w at each specified pressure. All the values were included since the variation with c_w at a single pressure varies with position as a smooth plane without discontinuities. The function `Get_c_at_P` was written in order to extract all measured values of c_w at a specific pressure. The function, which can be seen in Appendix C.6, takes a cell containing all of the SSPs measured in a season as its argument. The function returns the values of c_w at the specified pressure, as well as the measurement position of each value of c_w. Having

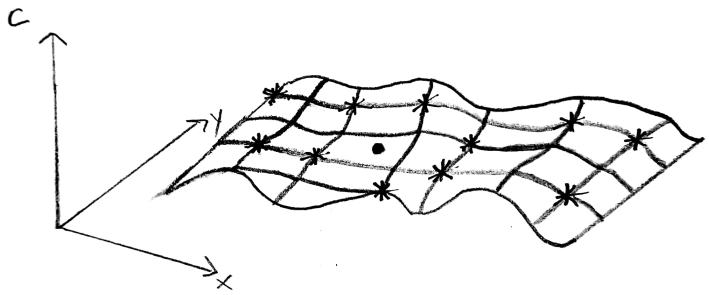

Figure 4.5: An illustration of how a surface is fitted to all measured values of c_w, here denoted by a $*$ symbol, before the value of c_w can be interpolated at the position in query, here denoted by a $\bullet$ symbol

identified all measured values of c_w at a single pressure, MatLab's `interp2`-function was used to determine the value of c_w at the specified position. The method of interpolation was chosen to be cubic. The `interp2`-function effectively fits a surface to all of the measured values of c_w, as illustrated in figure 4.5. Then, the value of c_w was read as the value of the fitted surface at the position of the constructed SSP.

The position variables of the measured values of c_w were specified as longitude and latitude, which is not a Cartesian coordinate system. Because the LoVe Observatory is relatively close to the North Pole, interpolating using longitude and latitude coordinates is likely to introduce errors. This was overcome by using the function `interp_spherical` from The Geometry and Image-Based Bioengineering Add-On Toolbox by Moerman (2018). This function takes the longitude and latitude coordinates and shifts them so that coordinates are centred around an equatorial band at the globe's equator. It then converts the coordinates from spherical to Cartesian, performs the interpolation using MatLab's standard `interp2`-function, before converting and shifting the coordinates back.

The value of c_w at a single pressure in the constructed SSP was thus found by identifying all measured values of c_w at that pressure and interpolating to find the value of c_w. This method was then repeated at increasing pressures, at ΔP_{SSP} intervals. This was done until the pressure was so high that the corresponding value of z was equal to the value of z_b at the specific location. Then the values of P_h corresponding to each interpolated value of c_w was converted to a depth. This was done using the function `gsw_P_to_z` (McDougall and Barker, 2011), which takes latitude as an argument. Thus, the constructed SSP consisted of interpolated values of c_w as a function of discrete values of z. Ultimately, this entire process was repeated at each radial position along the transect, separated by Δr_{SSP}.

4.2.3 Geoacoustic properties of the seabed

MatLab function named `Seabed` was written in order to use the sediment types mapped by Geological Survey of Norway (2016), shown in figure 3.6, to determine the properties of the seabed along a transect. The script is shown in Appendix C.2. As explained in section 2.6, the `.in`-file must include the distance from the source at which any environmental properties change, marking the start of a new block. A change in the seabed type along the transect will trigger the need for a new block. A new block will be created even if only one of the environmental properties of the seabed changes, but generally changes in the environmental properties are associated with changes in the sediment type, at which point all of the environmental properties are altered at once. The `Seabed`-function therefore identifies the ranges at which new blocks occur due to changes in the sediment type. The creation of new blocks can also be triggered by updates of the SSP, and the combination of changes in the seabed and the SSP will be further discussed in section 4.3.

The function `Seabed` identifies the changes in sediment type with range by firstly identifying which polygon each of the points in the transect range array lies in. It does this by taking the (Θ, φ)-coordinates of each point in the transect array, converting them to Cartesian UTM coordinates, and checking if each of these points lie inside each of the polygons, using MatLab's `inpolygon`-function. Marching along the points in the transect range array, the function then finds the ranges at which the identified polygon is different from that identified at the neighbouring range point. Then, the function returns an array of the radial distances from the observatory to each change in sediment type, together with the numeric product specification code corresponding to each block's sediment type. It also outputs the Cartesian coordinates of each point in the radial array, as plotted in figure 4.6. It shows an example of a transect at $\theta = 330°$, where each identified block has been marked on the figure. The map is zoomed in on a small area around the LoVe Observatory, in order to highlight that many transitions are identified along a short section of the transect.

After having established the coordinates and sediment type of each change in sediment type, the `geoac` function was written to identify the appropriate sound velocity, density and attenuation of the sediment types. The script is shown in Appendix C.3. It takes the temperature, salinity and sound speed of the water above the sediment, as well as the product specification code and a value for the bathymetry depth of the sediment patch as input arguments. The function uses the product specification code to identify the type of sediment and thus chooses which operations to perform. For the unconsolidated sediment types, the `geoac` calls the function `waterprops` by White (2015b), which calculates the density of the water just above the sediment, from the temperature, salinity, and depth. The calculated density of the water is then used to calculate the density of the sediment, using equation 2.18 and the appropriate porosity, as defined in table 3.4, and the calculated grain density, given in table 5.1. Then, to calculate the sound velocity in the sediment, the function takes the appropriate sound velocity ratio, given in table 5.1, and multiplies it with the inputted water sound speed. For the compact sediment types, the function directly outputs the appropriate sound velocity and sediment density,

as they are given in table 5.1. For the special case of '*Mud alternating with blocks of hard sediment*', the function takes and average of the properties of '*Mud*' and '*Compact sediments or sedimentary bedrock*', as explained in section 3.3. Lastly, if the `geoac`-function is fed only zeros as its input arguments, the function returns the geoacoustic properties of the abyssal mud which as explained in section 3.3 is assumed to cover any area not covered by the sediment polygonomials by Geological Survey of Norway (2016).

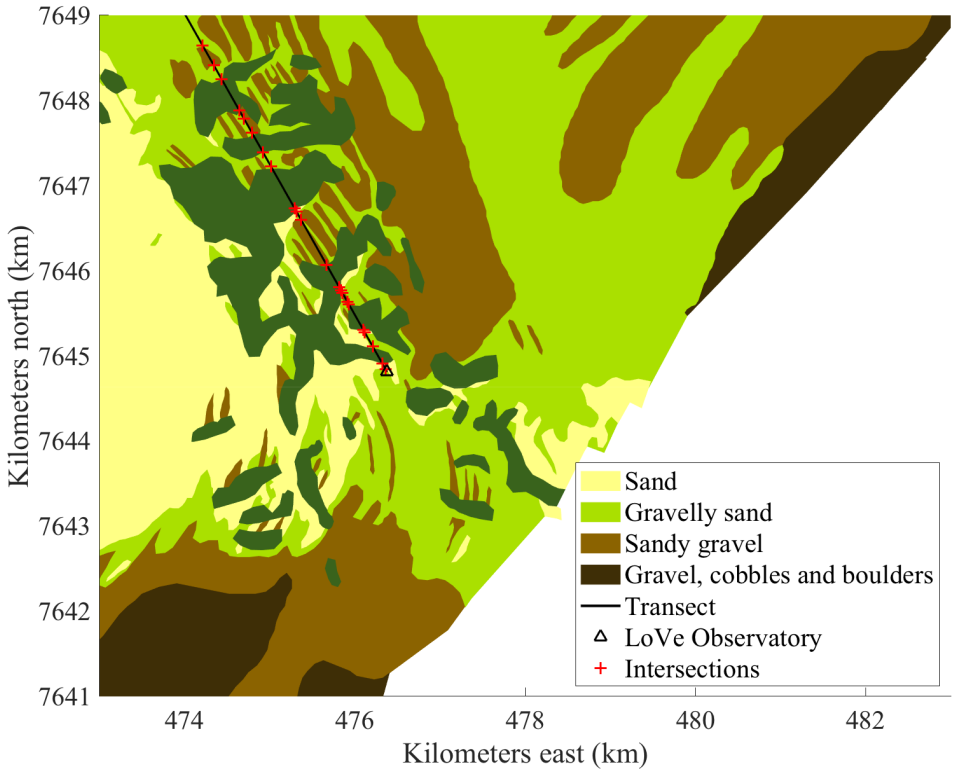

Figure 4.6: An example of a transect at $\theta = 330°$, where the intersections between each transition in seabed properties along the transect have been identified. The map's coordinates are given in UTM zone 33, referenced to the intersection between the equator and the zone's central meridian.

4.3 Writing the .in file

An individual .in file was written for each simulation that was run. To make the writing of the file less manually demanding, a function named `Write_in` was written to construct the file based on the input parameters described in Chapter 3 and the calculated input parameters shown in Chapter 5. The function also calls for the user chosen input arguments, which have been determined in section 4.1. The script can be seen in Appendix

C.5. The `.in`-files of the transects modelled in this study are quite long, and are therefore not included in the appendix. But, since the algorithm `Write_in` is available in the appendix, and all of its input arguments are specified in this text, the reader would be able to reproduce the `.in`-file of any of the discussed transects.

Sound that is transmitted into the seabed will in real ocean seabeds be transmitted into and reflected back from various layers of materials with different impedances. According to Buhl-Mortensen et al. (2015), on the continental shelf outside Lofoten and Vesterålen, there is normally a 50 - 200 m thick layer of sediments. This is of course a generalisation, because Buhl-Mortensen et al. (2015) also point out that the underlying bedrock is exposed in some local areas. Yet, based on Buhl-Mortensen et al. (2015), the sediment thickness in the model was estimated to be 125 m. In the modelled case, there was no available information about any other material than the uppermost layer. Therefore, reflections inside the seabed were not included in the model. To avoid reflections at the depth where the model domain ends, a layer of an artificial material of high absorption was included beneath the layer of sediment, as recommended by Jensen et al. (2011). This effectively imposed a Sommerfeld's radiation condition on the boundary, by absorbing close to all energy before it reaches the end of the domain. According to Jensen et al. (2011), the artificial layer had to be greater than a few wavelengths. The thickness was thus taken to be four times the wavelength, which was given by

$$\lambda = \frac{c_b}{f = 20\,\mathrm{Hz}}. \tag{4.1}$$

As previously discussed, the environmental properties in the simulated domain are updated each time a new block is created. In the `.in`-file, the ranges at which new blocks occur are described by the variable r_p (Collins, 2001). These ranges are determined in the `Write_in` algorithm, based on two factors: the detected changes in sediment type along the transect and the spatial resolution of the SSPs, Δr_{SSP}. `Write_in` calls the algorithm `Seabed` to identify all the positions where the sediment type changes along the transect. Starting from the origin of the transect, and marching outwards in range, `Write_in` then creates a new block each time either the SSP or the sediment type changes. Thus, the lengths of the blocks are variable. New blocks are created until the algorithm reaches the user specified maximum distance, R_{max}, which will be determined in section 4.5.

4.4 Convergence tests

RAM solves the parabolic equation at discrete intervals in r and z, specified by the user as Δz and Δr. The choice of these step-sizes influences the accuracy of the solution in two ways: they affect the resolution of the environmental input parameters and they influence the numeric error inherent in the split-step Padé algorithm. This error, however, has been shown to be negligible, and Collins et al. (1996) claim that the size of Δr in practice is only limited by the resolution of the environmental parameters.

The size of Δz and Δr also affect the computational time needed to produce the `.in` file. This process is lengthy, and it is therefore desirable to make the step-sizes as large as possible, without adversely affecting the solution accuracy. In an attempt to

determine the ideal step-sizes, a convergence test was performed. Using a convergence test to determine the step-size is recommended by Collins (2001) in his user guide to RAM. Yet, to the author's knowledge, no publication of convergence tests of RAM exist. Therefore, the method for the test was made by the author. Convergence tests are often performed by comparing the produced results to a reference solution (Jensen et al., 2011). However, a reference solution was not available for this study. Instead, the convergence test was set up by simulating the transmission loss using one step-size, then reducing the step-size and simulating the transmission loss again and comparing the results from the subsequent simulations. This would be repeated until satisfactory convergence was reached, which would be considered achieved once several subsequent iterations produced the same transmission loss result. This was used as the convergence criterion for all tests in this study. Once this criterion was reached, the reduction of Δr and Δz would be stopped, and their values would be taken to be the current smallest step-sizes from the tests. The consequence of choosing this as the convergence criterion, and a discussion of whether it was reached during the tests are presented in section 5.3. The tests were performed along a test transect, which was taken to run along the length of the Hola valley, at $\theta = 330°$. The test was performed for the spring season, since this has the highest number of measured SSPs, leading to the most variability in environmental parameters.

The convergence tests started with investigating the effect of iteratively halving Δz. During this test, the step-size in r was kept constant, so that only the effect of the size of Δz was considered. According to Storheim (2018), $\Delta r = 250$ is a 'conservative choice' (in the meaning that the step-size is small enough) for the range step-size. Therefore, the constant Δr was set to 10 % of Storheim's recommendation, at $\Delta r_{\text{const}} = 25$, in an attempt to make Δr_{const} so small that it does not influence the solution accuracy. The largest choice of Δz, which initialized the iterations, was taken to be

$$\Delta z_{\max} = \frac{\lambda}{2} = \frac{c_w}{2f}, \tag{4.2}$$

which according to Jensen et al. (2011) is the largest value Δz can take, while still ensuring adequate spatial spectral resolution. Here, the sound speed was estimated to be $c = 1480\,\mathrm{m\,s^{-1}}$, based on the values shown in figure 5.1. This resulted in $\Delta z_{\max} = 37\,\mathrm{m}$. The transect was simulated out to a medium range of $r = 10\,000\,\mathrm{m}$, which is deemed appropriate, since the accuracy in z will not depend on position in r once the sound-field is well outside the far-field and has filled the entire water column. The resulting simulated transmission loss values for each value of Δz are compared in section 5.3, where the appropriate value of Δz is determined.

After having established a value for Δz, a new convergence test was performed to investigate the appropriate choice of Δr. The test was started at value of Δr large enough to be deemed an inappropriate choice. As an overestimation, the initial maximum value of Δr was taken to be the same as Δr_{SSP}, so that each range step marched the solution to a new property block. Then, the value of Δr was iteratively reduced, down towards an appropriate choice. First, Δr was iteratively halved from $\Delta r = \Delta r_{\text{SSP}} = 1000\,\mathrm{m}$ to $\Delta r = 100\,\mathrm{m}$. Then, the value was further reduced from 100 m to 40 m in steps of 10 m

and from 40 m to 10 m in steps of 2 m. For these iterations, the value of Δz chosen based on the results of the first convergence test, which will be presented in section 5.3. The transmission loss values were simulated and compared for the $\theta = 330°$ transect, up to $R_{max} = 10\,\text{km}$, which was deemed an appropriate intermediate length covering enough distance for potential cumulating errors to become apparent. Unfortunately, as explained in section 5.3, the chosen convergence criterion was not reached during this test. A second test was therefore performed, where the value of Δr was further reduced from 50 m to 10 m in steps of 5 m and from 10 m to 1 m in steps of 1 m. It was not possible to run this convergence test out to $r = 10\,000\,\text{m}$, because the best available computer ran out of memory while trying to run the simulations using the required number of range points. Therefore, this test was limited to $r_{\text{max}} = 1000\,\text{m}$. The results of all of the convergence test are presented in section 5.3. Here, the results are discussed and the values of Δz and Δr are decided.

For reference and comparison, the values of Δz and Δr commonly used in literature have been studied. Step-sizes as small as $\Delta r = 5\,\text{m}$ and $\Delta z = 0.25\,\text{m}$ have been used by Collins (1989a) in his simple bench-mark test calculations using a 25 Hz source in RAM. However, Jensen et al. (2011) claim that the value produced by equation 4.2, in this case $\Delta z = 37\,\text{m}$, is an appropriate estimation for Δz. Further, Jensen et al. (2011) proposes that $\Delta r =\mid 2 - 5\Delta z \mid$ is an appropriate choice for the range-step in bottom-interacting sound fields . In this case this would give $\Delta r = 183\,\text{m}$. In a description of a different RAM-algorithm, implemented by Dushaw (2015) in Fortran 95, Dushaw claims that $\Delta z = 0.5\,\text{m}$ and $\Delta r = 250\,\text{m}$ are conservative choices, without specifying the frequency. According to Storheim (2018) the step-sizes used by active users of RAM are commonly around the order of magnitude proposed by Dushaw (2015).

4.5 Determining the maximum range

One of the aims of this study has been to create tools that determine the environmental parameters of the area around the LoVe Observatory so that, amongst other things, the maximum detection range, w, can be determined in further studies. Therefore, R_{max}, the maximum distance the RAM simulations run to, should be estimated to some distance that is plausibly longer than w. As an initial estimate, the maximum detection range was calculated using the simple model for transmission loss with 'semi-spherical' spreading and attenuation, shown in equation 2.10 and the transmission loss threshold for low noise conditions, $\text{TL}_{\text{max, low noise}} = 120\,\text{dB}$. The equation

$$120 = 15 \log_{10} R_{max} + 0.002 \times 10^{-3} R_{max} \tag{4.3}$$

was solved graphically, giving $R_{max} = 8162\,\text{km}$. This is a gross overestimation. A transect of this length at $\theta = 330°$ would reach further than the west-coast of the United States. The simple 'semi-spherical' spreading model used here is often used by scientists as initial estimates of the detection range of hydrophones (Pedersen, 2018). If this model is reliable at the LoVe Observatory, this means the detection range of the observatory would reach all positions in the entire volume of the northern Norwegian sea and the

Greenland sea. It would, of course, not reach further than this, as it would be cut off by land masses, shown to the very west in the map in figure 3.1b. Instead of using the calculated value for R_{max}, it will be estimated as the distance to the coastline of Greenland. Based on figure 3.1b, the point on the coastline furthest from the LoVe Observatory was roughly estimated to be ($\Theta = 80°$, $\varphi = -16°$). The distance between this point and the observatory was calculated using the function `m_lldist` by Pawlowicz (2018), and was found to be 1263 km.

Therefore, initially, the value of R_{max} was set to 1263 km, to enable simulation of the transmission loss all the way across the Greenland sea. However, a computational issue was encountered. Seemingly, the computer used to run RAM was not able to compute the model over such a large domain. When the model was executed, RAM returned the error message 'Need to increase parameter mp to 1169209344'. The cause of this message was suspected to be a bug. Effort was made to try to resolve this issue, both by debugging the RAM Fortran code and by changing some of the user specified model parameters, such as the decimation factors, the number of Padé constants, the stability parameter, and stability range, r_s. Unfortunately, none of these modifications resolved the issue.

This particular issue has not been described in literature, nor has it been encountered by other users of RAM that the author have communicated with. Even so, it is the author's belief that the problem is not due to user error, but rather that some previously unknown limitation of RAM has been encountered. One possible explanation is that the computer used to compute the models has experienced limitations in capacity. The used computer has 198 GB total memory and 16 processors, each with 3.60 GHz CPU. A reason why limitations in capacity might not have been encountered, or at least not published, by others may be two-fold. Firstly, other researchers might have run RAM on a computer with greater capacity than the machine used here. Secondly, the choices for Δz and Δr have been set using a strict convergence test, as explained in section 4.4. Often, scientists skip the convergence test to save time. This was for example seen in Tollefsen (2006). Therefore, the values of Δr and Δz used in this study might be smaller than those conventionally chosen, resulting in a greater need for computational capacity. As shall be seen in section 5.3, the results of the convergence test gives step-sizes considerably smaller than those proposed by Jensen et al. (2011) and Dushaw (2015). However, having a converged solution is of utmost importance if the simulated results are going to be trustworthy, and the steps sizes will therefore not be increased. Unfortunately, another computer with more computational capacity was not available at the time of this study.

Therefore, R_{max} was set to the greatest distance that the RAM model could run to without encountering computational errors. This distance was found by trial and error, by running several test models and increasing the maximum range each time. Eventually, the maximum range was set to $R_{max} = 190$ km. This will be the value of R_{max} in all the RAM simulations run in this study, unless otherwise specified.

4.6 Simulating the transmission loss

After having established all of the input parameters needed to run RAM and developed a set of model tool codes fit to extract these parameters at any location, it was then possible to run RAM to investigate how the transmission loss varied with position. The transmission loss is a function of 3D space, as well as time, and it is therefore not feasible to visualize the transmission loss at every position in the volume surrounding the LoVe Observatory. Instead, a number of carefully chosen example transects will be produced and shown in Chapter 5, in order to draw some conclusions about which areas that are detectable by the observatory.

To begin with, the transmission loss was modelled along the transect at $\theta = 330°$. This is deemed to be heading straight out of the middle of the Hola valley. Looking at this transect will hopefully give an indication of the maximum range that the observatory can detect. The resulting transmission loss, calculated at all four seasons, can be seen in figure 5.13 in section 5.4. Then, to investigate how the transmission loss is affected by the shallow plateaus to the north and south of the Hola valley, the transmission loss was modelled along 8 transects at 30° intervals running across the Vesterålen and Egga banks. These transects were chosen since they will highlight the effect on the transmission loss of the bathymetry changing from the Hola valley to the shallow banks. Since this was the objective, the value of R_{max} was limited to 50 km, which is long enough to cover the extent of the banks and within the region mapped by Geological Survey of Norway (2016), shown in figure 3.6. All the results produced by varying θ are presented and discussed in section 5.4.1. To further investigate the effect of varying θ on the simulated transects, the transmission loss was simulated along every transect between 220° to 40° at 1° intervals. For these transects R_{max} was set to the maximum possible range, 190 km. Given the large amount of simulated transect this produced, it is not feasible to present each transect here. Instead, the transmission loss value at a single depth was extracted from all of the simulated transects. This way, it was possible to construct plots of how the transmission loss varied in a horizontal plane, as a function of range and azimuthal angle. This method was attempted for all four seasons. However, due to time restrictions and the fact that producing a large number of `.in`-files is a lengthy process, only the winter, spring and autumn seasons were completed. The resulting plots are shown in figures 5.21 and 5.22.

Chapter 5

Results

The calculated input data that were used in the TL simulations are presented in sections 5.1 and 5.2. The data have been collected and processed using the methods laid out in chapter 3. For some of the data, the results of these methods had to be reviewed before the data could be used to compose TL simulations, in order to expose any artefacts in the processed data or in the underlying calculations. These artefacts will be identified in section 5.1 and the methods used to compensate for the abnormalities will be discussed. Then, the results of the convergence test are presented in section 5.3, before the simulated transmission loss results are finally presented in section 5.4.

5.1 Calculated sound speed profiles

The SSPs that have been calculated using CTD-measurements downloaded from International Council for the Exploration of the Sea (2018), as explained in section 3.2, can be seen in figure 5.1. The figure includes the calculated SSPs at all available measurement positions, apart from those excluded in figure 3.4. Henceforth, this set of calculated SSPs will be referred to as the full set of calculated SSPs. As expected, the profiles exhibit a variation of c_w with depth resembling a Munk-profile in medium to deep waters. However, the data also show some unexpected abrupt variations in the sound speed, which can be seen in figure B.1 in Appendix B. Upon inspection of the downloaded raw data, what appears to be random discontinuities in some of the temperature and salinity variations with depth were discovered. As an example, the variations of salinity with depth for each of the SSPs which portray the unexpected variation in figure B.1b is shown in figure B.2 in Appendix B. The figure shows a discontinuity jumping down to $S = 0$ in the variation of salinity with depth, which cannot be explained by physics. The same discontinuity is found in some of the data sets' temperature variations, where T goes abruptly to 0 °C. This is deemed to be an instrument error. Therefore, the data sets were passed through a script in MatLab which identified any sets containing values of 0 salinity or 0 °C temperature. Where this was found, these measurements were removed. The remaining variation of either T or S with depth was then used to interpolate the value of the respective variable at the removed data points.

It was also discovered that three of the measurement sets contained double values for some readings, meaning that the values for T and S were listed twice for the same hydrostatic pressure in the original data. This was also taken to be an instrument error, and at the hydrostatic pressures where two values occur, their average was taken to be the true value. The SSPs calculated after the instrument errors had been corrected is shown in figure 5.1.

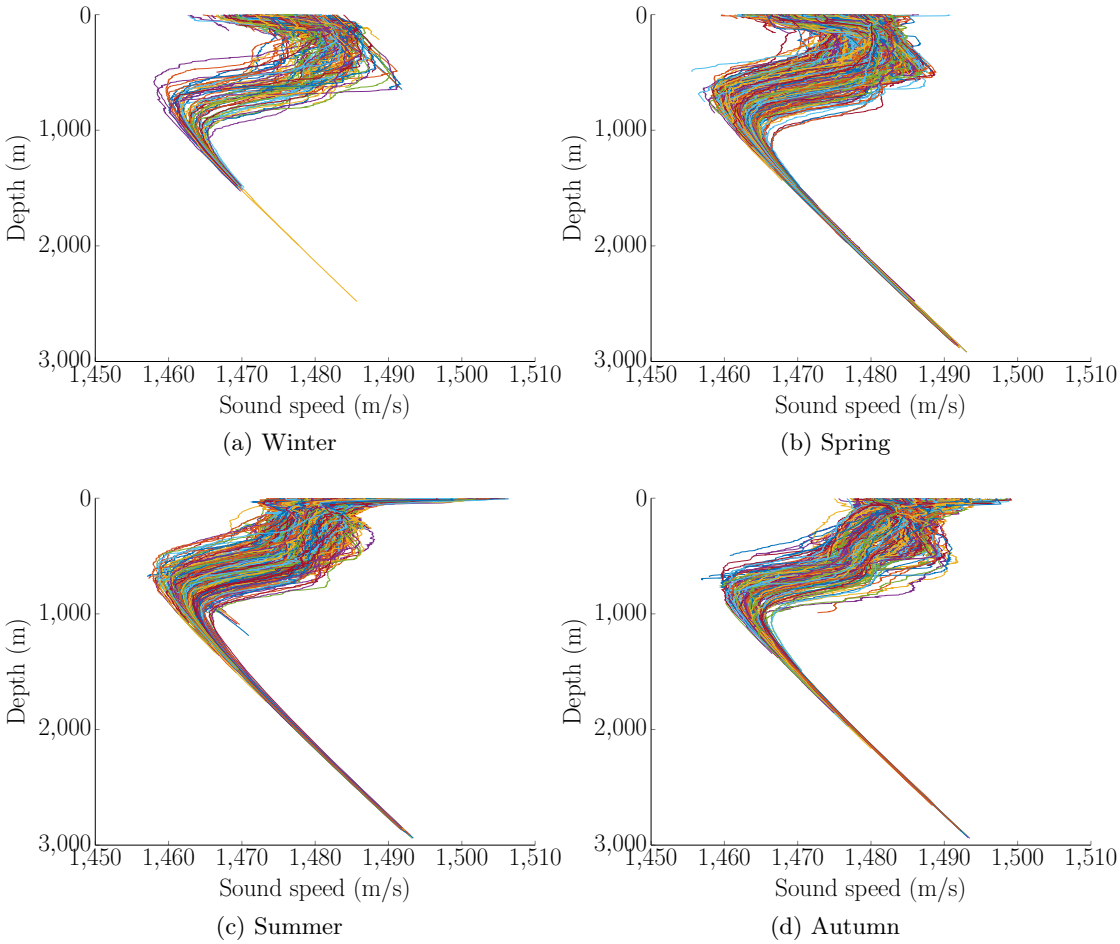

Figure 5.1: The full set of sound speed profiles, $c_w(z)$, calculated from CTD measurements, with instrument errors corrected. Each line in the plot represents an individual measurement position, and both shallow and deep waters are included.

To get a sense of the general shape of the SSP for each season, the mean value of the full set of SSPs was calculated at each measurement pressure. The measurement pressure was then converted to depth using equation 3.2, taking φ to be the latitude of the LoVe Observatory, for simplicity. The resulting average SSP for each season is shown in figure 5.2. The figure also shows the 25% and 75% percentiles of the data, to give an indication of the spread in the values of c_w.

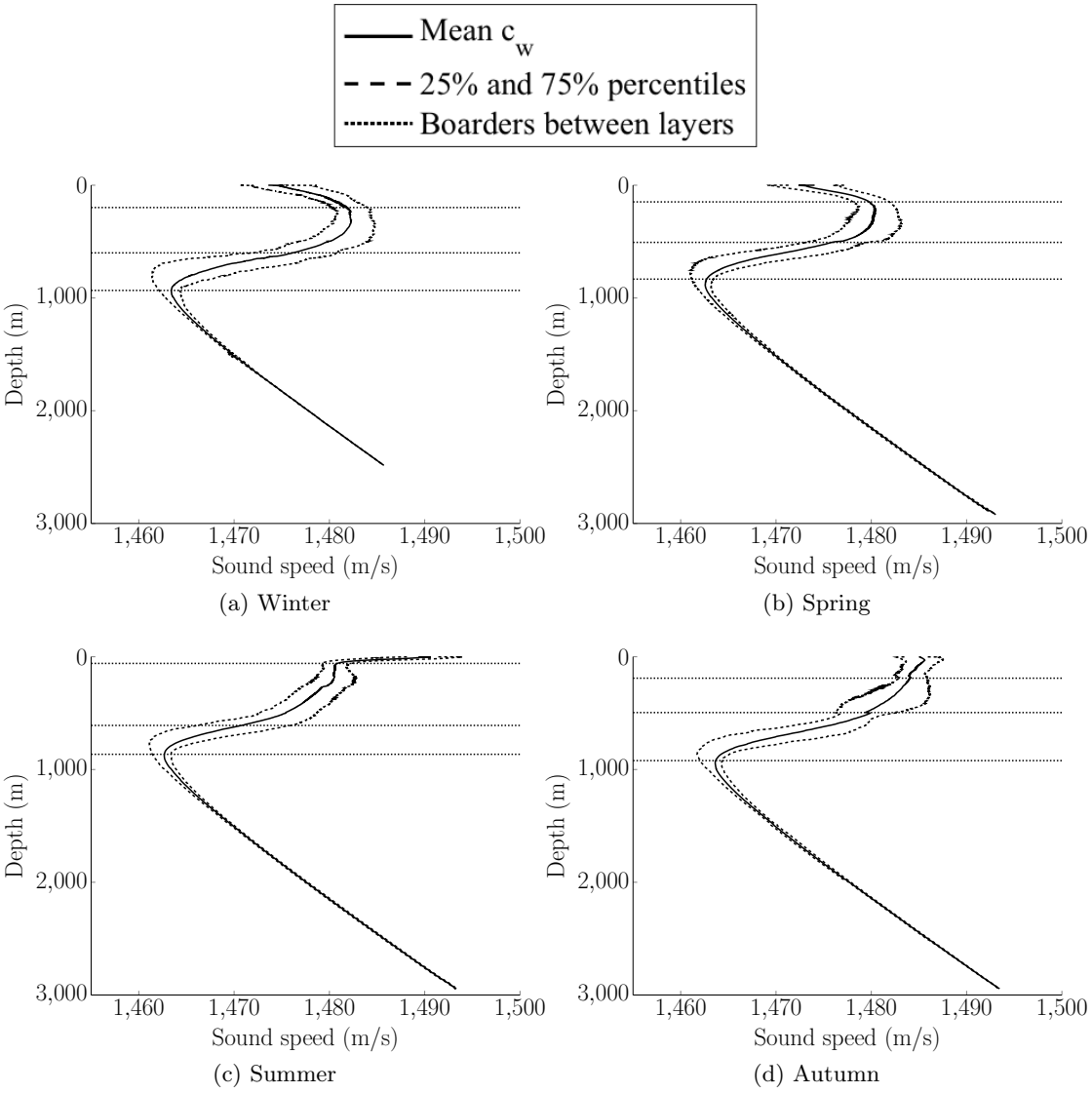

(a) Winter (b) Spring

(c) Summer (d) Autumn

Figure 5.2: The calculated mean of the variation of c_w with depth. The 25% and 75% percentiles indicate the spread in the averaged data at each depth. The approximate depth of the borders between characteristic layers of the SSPs are marked by horizontal lines.

Both the calculated SSPs shown in figure 5.1 and the mean values shown in figure 5.2 show some of the expected traits of SSPs, as described in section 2.1.1. A characteristic SSP can, as previously mentioned, be divided into 4 distinct layers: the surface layer, the seasonal thermocline, the main thermocline, and the deep isothermal layer. All of these layers can be distinguished in each season's mean SSP. The approximate depths of the borders between these layers have been indicated in figure 5.2. The winter and spring SSPs have a negative gradient in the surface layer, indicating that the layer is mixed and that the temperature is constant. The summer SSP has a sharp positive gradient in the surface layer, typical of sun-heated water. This is also the most shallow surface

layer of the four seasons, which is probably due to more calm wind conditions during the summer (DeSanto, 1979). As predicted by Urick (1983), the seasonal thermocline has a close to linear gradient during the summer and autumn seasons. Moreover, as expected, all of the seasons have a clearly noticeable minimum in c_w at the border between the main thermocline and the isothermal layer. The minima all lie above $z = 1000\,\text{m}$, which is to be expected at such a northerly latitude, where the water generally is quite cold (White, 2015b). The deepest minimum occurs in the autumn, which is also the season when oceanic water is typically the warmest, because of the way in which water retains heat (Urick, 1983). All of the averaged SSPs show little spread in the value of c_w in the isothermal layer. This is both because there are fewer measurements at depth, but also because the sound speed is typically unaffected by seasonal or diurnal changes at deep waters.

5.1.1 Control of the SSP-construction method

In order to control the method that was designed to construct the SSPs along any transect, which is described in section 4.2.2, an example use of the method was made. Figure 5.3 shows an example transect and the resulting SSPs constructed at $\Delta r_{SSP} = 1\,\text{km}$ intervals along the transect, using the calculated SSPs of the summer season. The SSPs are interpolated from sea level down to the depth of the bathymetry at their location. The interpolated SSPs, shown in figure 5.3b, reveal some unexpected rapid changes in c_w with z. The changes are so rapid that they might appear to be discontinuities, but inspection of the data show that they are not. These artefacts are most likely caused by the variable lengths of the measured SSPs. Close inspection of figure 5.1 shows that some

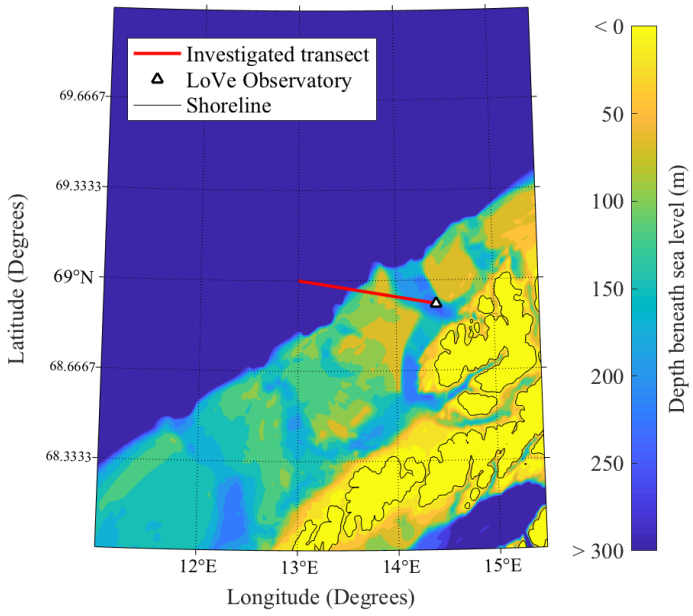

(a)

Figure 5.3: An example of constructed SSPs interpolated from the calculated summer SSPs at 1 km intervals along a transect shown in the map in (a). The SSPs, shown in (b), reveal unexpectedly rapid changes in c_w with z.

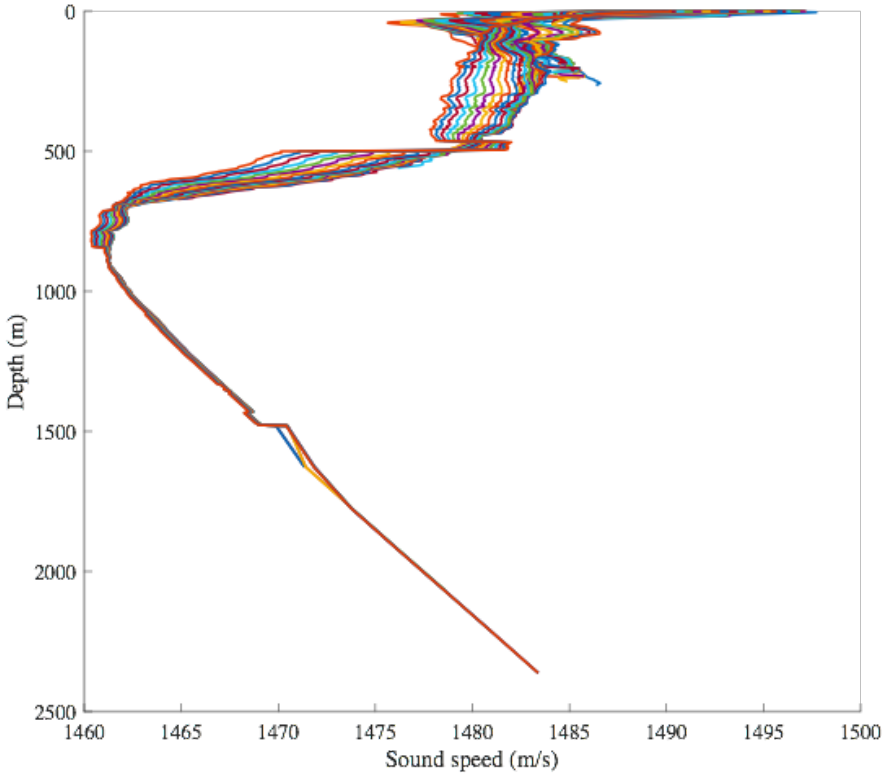

(b)

Figure 5.3: (Continued) An example of constructed SSPs interpolated from the calculated summer SSPs at 1 km intervals along a transect shown in the map in (a). The SSPs, shown in (b), reveal unexpectedly rapid changes in c_w with z.

of the calculated SSPs end at shallower depths than others. In some cases the CTD has not been measured all the way down to the depth of the sea floor, but rather it has been terminated at a much shallower depth. This was revealed when plotting each individual SSP calculated from the measured CTD data, together with its measurement position (not shown here). Because of this, some short SSPs exist at locations with deep bathymetry. These short SSPs will have been included in the interpolations of SSPs at positions with deep bathymetry, and it is plausible that their premature termination will have caused artefacts in the interpolated SSP. Figure 5.4 illustrates an interpolation based on one long and one short SSP. Above the depth marked z^* on the illustration, the two SSPs are combined to give the interpolated value of c_w. And below z^*, only the long SSP contributes to the interpolation. However, because the value of c_w below z^* is greater in the long SSP than in the short one, in the transition between $z < z^*$ and $z > z^*$, a jump-like artefact appears. The artefacts in the interpolated SSPs are concerning, because such rapid changes in c_w with z can drastically affect the modelled travel direction of the sound, and the drastic changes are not believed to represent the *in situ* SSPs. It is therefore decided that at any given position, the interpolation of the SSP will only utilize SSPs which are measured to a depth equal to or greater than the depth

of the bathymetry at that location. Figure 5.5 shows the SSPs again interpolated at the locations shown in figure 5.3a, but with the depth restriction imposed. It is clear that the changes has been effective in removing the concerning artefacts from the interpolated SSPs. However, whether or not these SSPs genuinely represent the *in situ* sound speed should be questioned. It is possible that some measured SSPs are removed from the interpolation at deep waters, even though they are in fact measured close to the position in question. Some of the relevant information in the measured SSPs are thus lost, and the resulting interpolated SSPs diverge from the actual sound speed at the specific location. It is important to keep this in mind when interpreting the final modelled transmission losses.

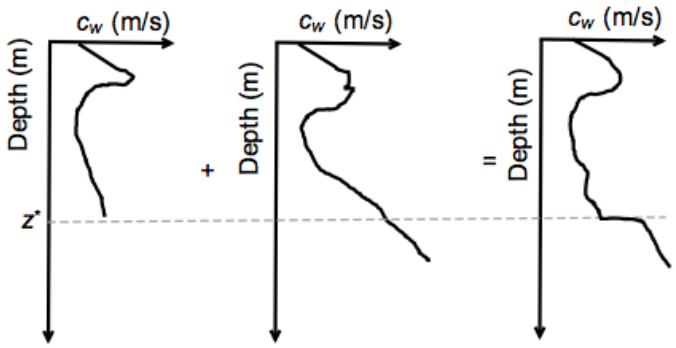

Figure 5.4: An illustration of how jump-like artefacts in the interpolated SSPs can occur when shallow SSPs are used in the interpolation.

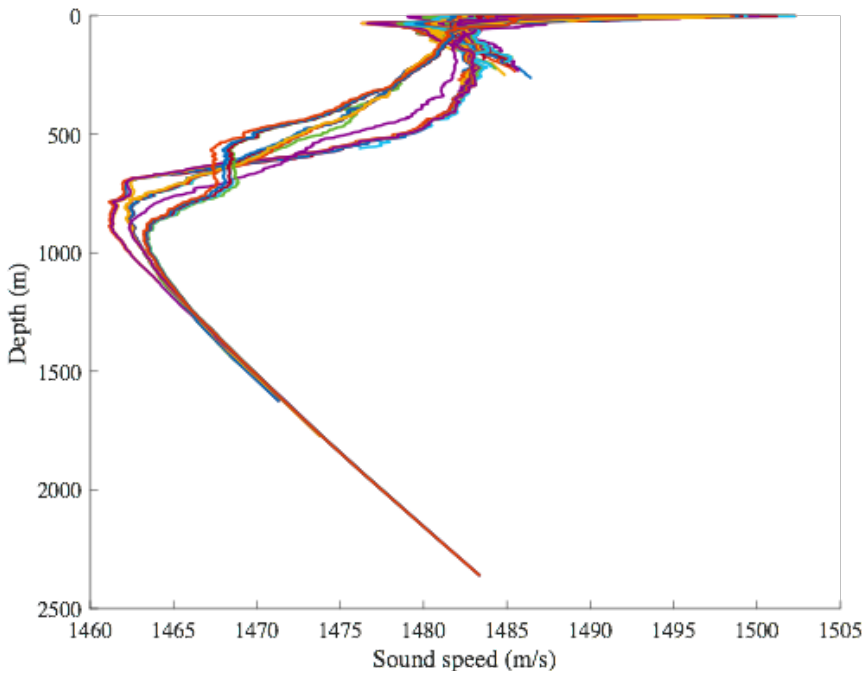

Figure 5.5: SSPs interpolated at the positions given in figure 5.3a, using SSPs which are measured to a depth equal to or greater than the depth of the bathymetry at the given location.

5.2 Geoacoustic properties

In table 5.1, shown overleaf, all of the calculated geoacoustic properties of all of the sediment types are summarized. This includes the sound velocity, the grain diameter both in units of mm and units phi, the velocity ratio, the bulk density, the grain density, the attenuation coefficient, and the constant of attenuation frequency dependence, h. Not all of these parameters are listed for every sediment type, because they have not been calculated and are not needed. For example, whenever a velocity ratio is provided, this indicates that the sound velocity in the sediment is a function of position, and the sound velocity is therefore not listed, but rather calculated for each sediment block using equation 2.19. Similarly, whenever a grain density has been listed, it has been used to calculate the position dependent bulk density, using equation 2.18. Lastly, the listed values for h are used to calculate the attenuation coefficient, $\alpha_{\lambda,\,b}$, using equations 2.25 and 2.65. These values are also position dependent, because the *in situ* sound velocity of the sediment is used to convert the units of $\alpha_{m,\,b}$ to dB/λ, as seen in equation 2.65.

State	**Sediment type**	η	$\mathbf{\Phi'}$ **(mm)**	ϕ' **(phi)**	V_R	$\mathbf{c_b}$ $(\mathrm{m\,s^{-1}})$	$\rho_\mathbf{B}$ $(\mathrm{kg\,m^{-3}})$	$\rho_\mathbf{g}$ $(\mathrm{kg\,m^{-3}})$	$\alpha_{\lambda,\mathbf{b}}$ (dB/λ)	$\mathbf{h}$ $(\mathrm{dB\,s\,m^{-1}})$	
Unconsolidated	Mud	0.45	0.0596	4.07	1.10			2501		0.70	(Eq. 2.28)
	Sandy mud	0.38	0.5560	0.85	1.25			2760		0.49	(Eq. 2.32)
	Sand	0.27	0.9721	0.04	1.29			2589		0.47	(Eq. 2.27)
	Gravelly sandy mud	0.27	5.5496	-2.47	1.46			2872		$\frac{0.8\times10^3}{c_b}$	(Eq. 3.7)
	Gravelly muddy sand	0.25	5.8907	-2.56	1.47			2832		$\frac{0.8\times10^3}{c_b}$	(Eq. 3.7)
	Gravelly sand	0.25	6.0612	-2.60	1.47			2836		$\frac{0.8\times10^3}{c_b}$	(Eq. 3.7)
	Muddy sandy gravel	0.18	18.4772	-4.21	1.60			2842		$\frac{0.8\times10^3}{c_b}$	(Eq. 3.7)
	Sandy gravel	0.15	18.5685	-4.21	1.60			2779		$\frac{0.8\times10^3}{c_b}$	(Eq. 3.7)
	Abyssal mud					1507	1450		1.85×10^{-4}		
Consolidated	Gravel, cobbles and boulders	0.40			1.44		2802		0.6		
	Compact sediments or sedimentary bedrock					4000	2600		0.0573		
	Thin or discontinuous sediment cover on bedrock					7200	2700		0.6754		
Mixed	Mud alternating with blocks of hard sediment $\star$										

Table 5.1: The calculated sediment properties: estimated mean grain size (Φ') in units of millimeters, estimated mean grain size (ϕ') in phi units, velocity ratio, sediment bulk density ρ_B, sediment grain density, ρ_g, attenuation coefficient $\alpha_{\lambda,b}$, the constant of the attenuation frequency dependence h, and the number of the equation used for the calculation of h, which is given in parentheses next to the value.
$\star$ The properties c_b, ρ_B and $\alpha_{\lambda,b}$ are calculated locally as the average of the value of these parameters for '*Compact sediments or sedimentary bedrock*' and the local values for '*Mud*'.

5.3 Findings from the convergence test

The results of the convergence test described in section 4.4 will be presented in this section. As previously explained, this involves comparing the transmission loss simulated using iteratively decreasing values of Δr and Δz, in order to identify the step-sizes when the solutions are considered covered. The criterion for convergence is taken to be that a number of consecutive iterations produce the same transmission loss values. All of the presented transmission loss models have been simulated for the test-transect at $\theta = 330°$, using all of the model parameters described in 4.1.

Figure 5.6 shows how the transmission loss varies with range using iteratively decreasing values of Δz, while the range-step is kept constant at $\Delta r = 25\,\text{m}$. For large values of Δz, the transmission loss is markedly different from the consequent iteration, and the solutions have thus not converged. However, at smaller values of Δz, it is not clear from this figure whether the solutions have converged. Looking specifically at one point, for example at $r = 10\,000\,\text{m}$, it is easier to visualize whether the iterations produce a similar result. This is shown in figure 5.7.

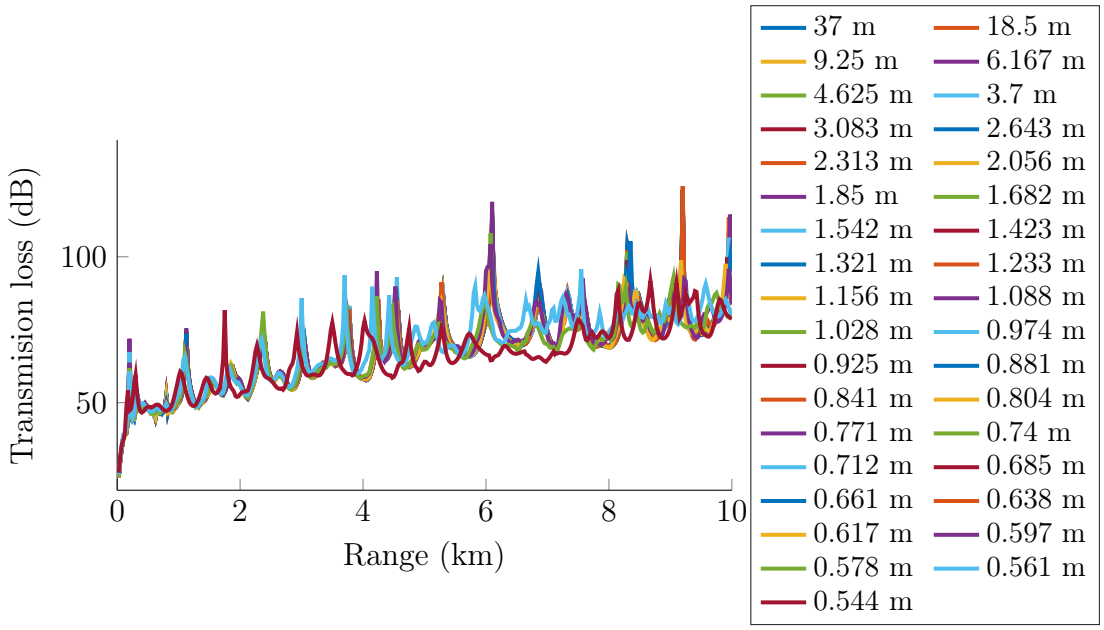

Figure 5.6: The simulated transmission loss along the $\theta = 330°$-transect, using varying values of Δz from 37 m to 0.544 m, and $\Delta r = 25\,\text{m}$. Each simulation's Δz step is shown in the legend.

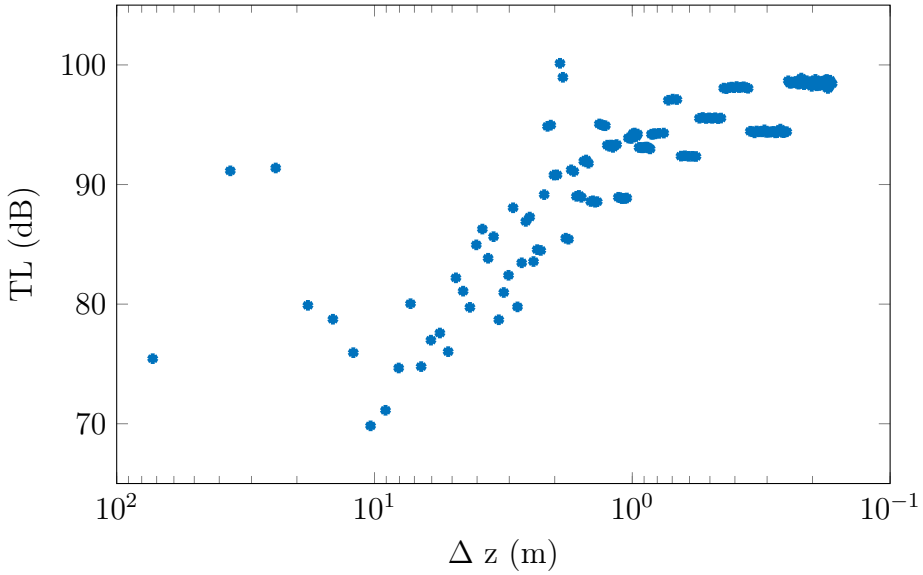

Figure 5.7: The simulated transmission loss at $r = 10\,000\,\text{m}$ and $\theta = 330°$, using varying values of Δz, and $\Delta r = 25\,\text{m}$.

For values of $\Delta z > 10\,\text{m}$, it is clear from figure 5.7 that the resulting transmission loss values are not stable, and the solution has thus not converged. On the other hand, when Δz is made smaller than 10 m, the resulting transmission loss starts to approach a similar value of TL at every iteration of Δz. Since Δz has been halved for each new simulation, the change in Δz from one simulation to the next is very small when Δz is small, resulting in seemingly continuous horizontal lines on the plot in figure 5.7. Looking at one such 'line' in isolation indicates that the solution seemingly has converged, given the large number of points giving the same value of TL. Curiously, the seemingly horizontal 'lines' in figure 5.7 appear to take two values, at TL $\approx 94\,\text{dB}$ and at TL $\approx 98\,\text{dB}$. This is not expected, and the reason for this alternating behaviour is unfortunately not known. However, it does not appear like this behaviour will vanish at decreasingly smaller values of Δz, and thus the value of Δz must, unfortunately, be chosen based on the results presented in figure 5.7. The lack of convergence in the z-dimension is a major drawback that needs to be considered when utilizing the results of the RAM simulations. Nevertheless, in order to make a model of the acoustic propagation around the LoVe station, like this thesis set out to do, it is necessary to choose a step-size in the z-dimension. The general trend in figure 5.7 appears to be that TL starts to stabilize at a constant value with an uncertainty band of $\pm$ 2 dB in the region around $\Delta z = 0.2\,\text{m}$. Therefore, this is chosen to be value of Δz used in all of the rest of the simulations in this thesis.

Having determined the value of Δz, the convergence tests were then run for the value of Δr. Looking firstly at the effect of reducing Δr from 1000 m to 100 m, as shown in figure 5.8, it is clear that the solutions have not converged. In this range of values for Δr, the resulting transmission loss is not the same for different values of Δr, both because

the solutions have not converged and because the range resolution in some cases is too coarse to capture the true variation of TL with r.

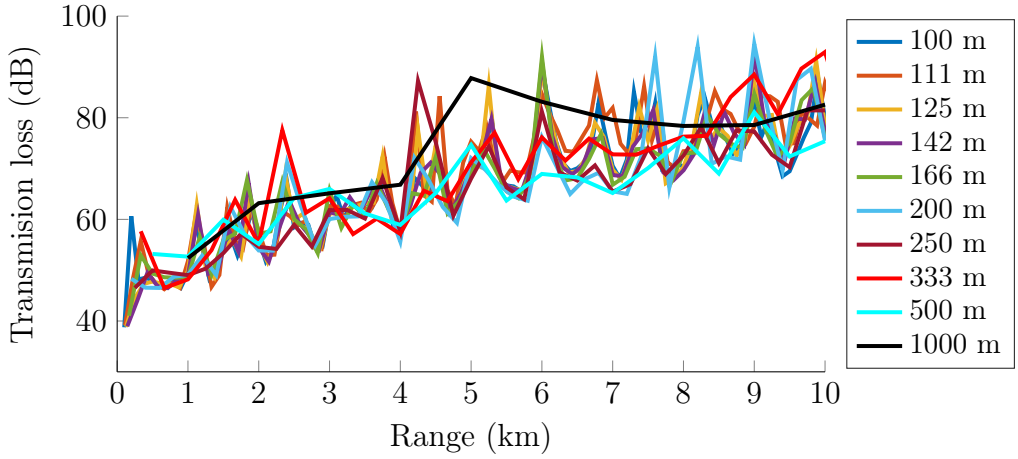

Figure 5.8: The simulated transmission loss at the $\theta = 330°$-transect, using varying values of Δr and $\Delta z = 0.2\,\text{m}$. Each simulation's Δr step is shown in the legend.

Next, the Δr was gradually reduced from 100 m to 10 m. Looking at the resulting transmission loss as a function of range, as shown in figure 5.9, it appears as if the radial position of the maxima and the overall pattern of TL as a function of r is the same for all values of Δr, and that these solutions thus have converged and that coarse resolution is no longer an issue. However, closer inspection of a smaller range interval, shown in figure 5.10, reveals large discrepancies in the values of TL. Here, it appears that $\Delta r = 100\,\text{m}$ - 50 m might be too coarse to resolve the peaks of the maxima. Moreover, even for smaller values of Δr, the maximum values at the peaks are not the same.

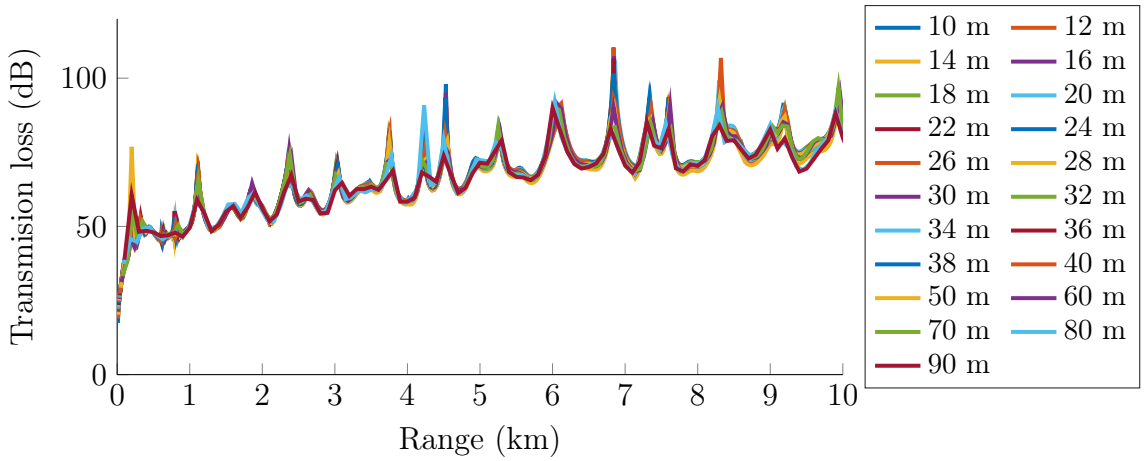

Figure 5.9: The simulated transmission loss for small, varying values of Δr and $\Delta z = 0.2\,\text{m}$, along the $\theta = 330°$-transect. Each simulation's Δr step is shown in the legend.

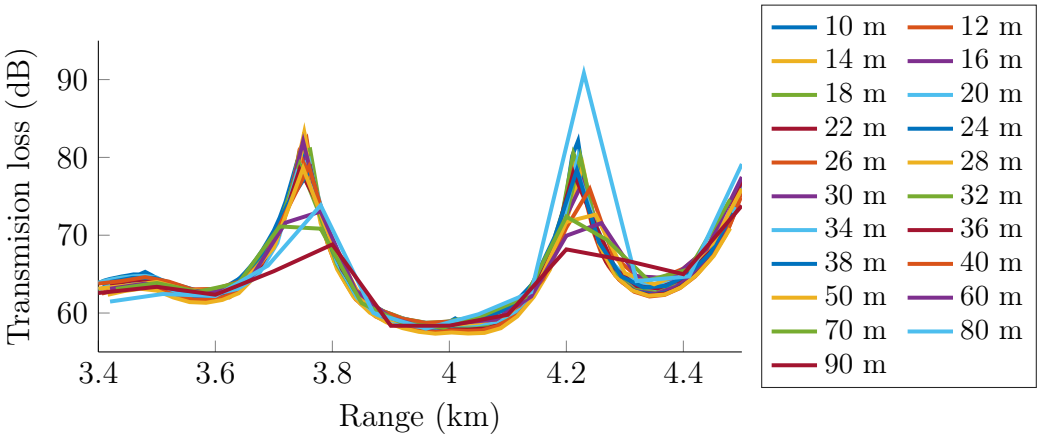

Figure 5.10: Examples of the simulated transmission loss at two maxima along the $\theta = 330°$-transect, showing discrepancies in TL for varying values of Δr and $\Delta z = 0.2\,\text{m}$. Each simulation's Δr step is shown in meters in the legend.

The lack of convergence becomes even more clear when looking at the values of TL at just a single position in r. For example, figure 5.11 shows the simulated values of TL at $r = 10\,000\,\text{m}$. If the solutions had converged, one would expect to see that the value of TL stabilised at a single value as Δr decreased. This does not occur in figure 5.11, but there does appear to be some degree of stabilisation for values smaller than $\Delta r = 50\,\text{m}$, indicated by how the scatter in the plot is contained within $\text{TL} = 79.8 - 85.8\,\text{dB}$. In this region, TL seems to take on a constant linear relationship with Δr, but with significant scatter.

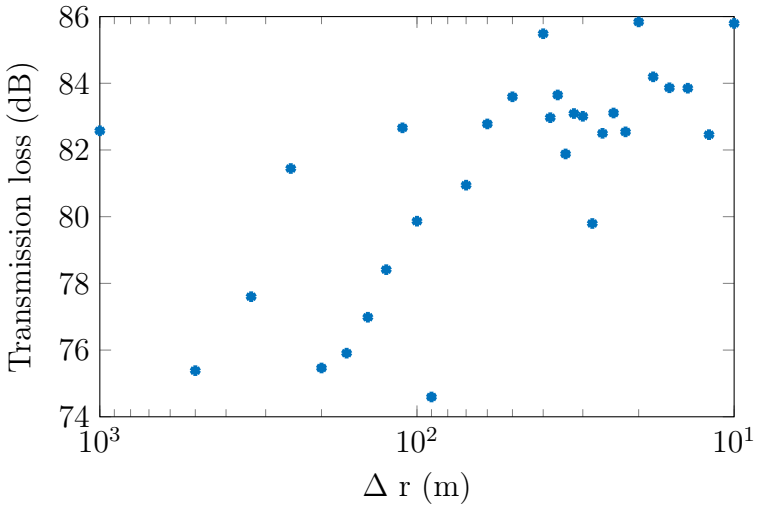

Figure 5.11: An example of the simulated transmission loss at $r = 10\,000\,\text{m}$ and $\theta = 330°$ using $\Delta z = 0.2\,\text{m}$, indicating that the solutions are not converged even for values of Δr down to 10 m.

The lack of convergence might be because Δr simply has not been tested for small enough values. Therefore, the transmission loss was simulated along the same transect using step-sizes of $\Delta r = 50 - 1\,\text{m}$. The resulting transmission loss is shown in figure 5.12. Figure 5.12 shows the same overall results as the previous convergence test; the maxima occur at the same range positions, indicating that the various values of Δr give similar results, but there are still significant variations in the values of TL, even for very small values of Δr. This is especially clear in the zoomed in view of the maximum at $r = 780\,\text{m}$, shown in figure 5.12b. At the peak of the maximum, the values of TL seem arbitrary and vary from $66.4 - 51.4\,\text{dB}$. Reducing the value of the step-size has thus not appeared to make the solutions converge. Furthermore, at very small values of Δr, figure 5.12 reveal the presence of very rapid variations of TL with r. This has been interpreted as Gibbs' oscillations, which has also been observed by Collins (1990). Gibbs' oscillations are artefacts caused by lack of stability in the RAM code. These oscillations are likely to have occurred because small values of Δr cause rapid variations in environmental properties with r, meaning that the domain can no longer be said to be weakly range dependent. The occurrence of these artefacts, together with the both the fact that $\Delta r = 1\,\text{m}$ is remarkably small compared with the values of Δr recommended by Jensen et al. (2011) and Dushaw (2015), and the excessive computation time needed to write the `.in`-file using such a small range step justifies that further convergence tests with even smaller values of Δr were not performed. In fact, the large discrepancies in transmission loss values shown in both figure 5.11 and 5.12 makes the author believe that the solutions will not converge for any values of Δr. Although the convergence criterion has not been reached, in figure 5.11, it appears like the transmission loss values start to stabilize when $\Delta r < 50\,\text{m}$, indicating that the solutions, hopefully, are as converged as they can be. Based on this, Δr is chosen to be 38 m. Thus, the step-sizes used in the rest of this thesis are $\Delta z = 0.2\,\text{m}$ and $\Delta r = 38\,\text{m}$.

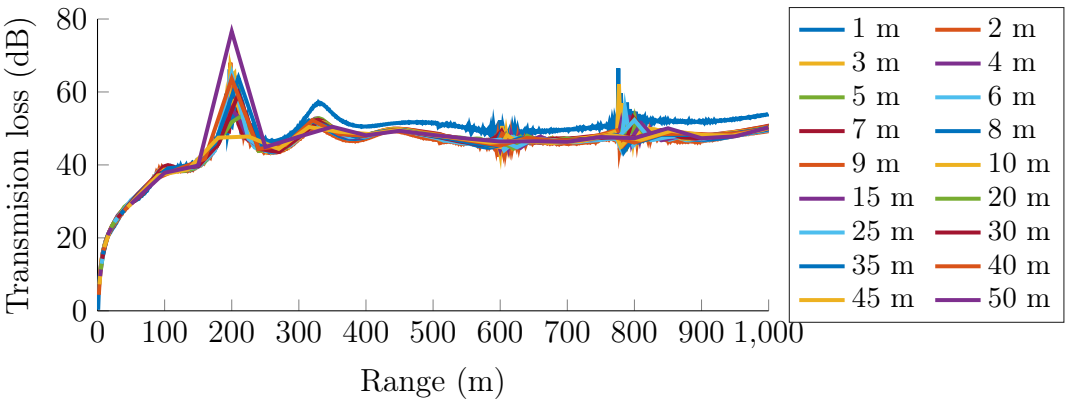

(a)

Figure 5.12: The results of the convergence test for $\Delta r = 50 - 1\,\text{m}$ using $\Delta z = 0.2\,\text{m}$. Figure (a) shows the transmission loss along the $\theta = 330°$-transect along the entire simulated range, while figure (b) shows a zoomed in view of an example maximum exhibiting Gibbs' oscillations.

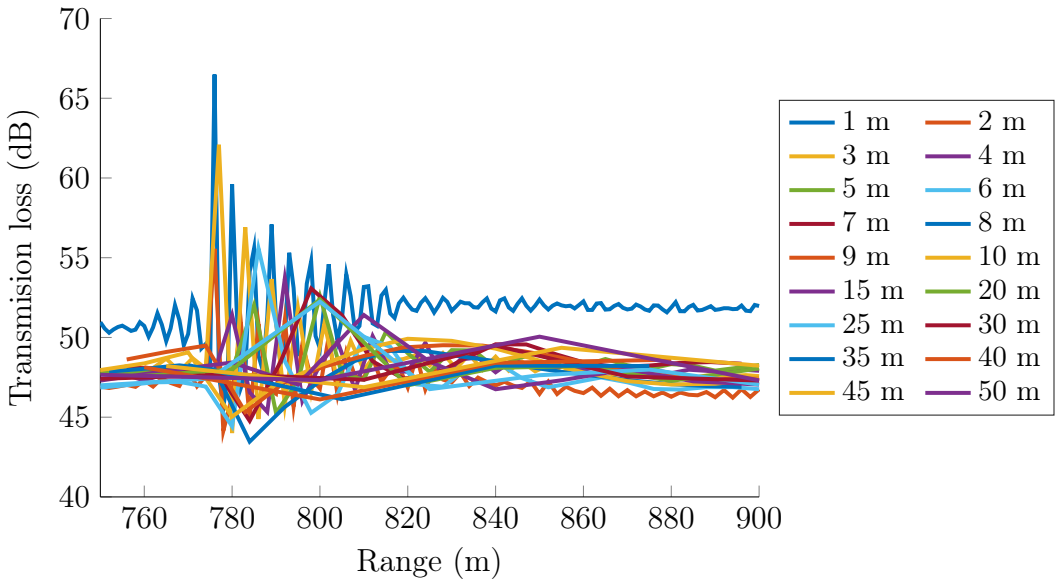

(b)

Figure 5.12: (Continued) The results of the convergence test for $\Delta r = 50 - 1\,\text{m}$ using $\Delta z = 0.2\,\text{m}$. Figure (a) shows the transmission loss along the $\theta = 330°$-transect along the entire simulated range, while figure (b) shows a zoomed in view of an example maximum exhibiting Gibbs' oscillations.

5.4 Transmission loss

In this section, the results of the transmission loss simulations that were described in section 4.6 are presented. The chosen model parameters are described in section 4.1, and following the convergence test results given in section 5.3, the step-sizes are $\Delta z = 0.2\,\text{m}$ and $\Delta r = 38\,\text{m}$. The following discussion of the results will assume that the simulated results are accurate and credible. The validity of this assumption will be examined in section 6.3.

The transmission loss calculated along the transect at $\theta = 330°$, which points straight out of the Hola valley, is shown in figure 5.13. The figure shows the calculated transmission loss at all four seasons. The colour map used in the figures has been designed so that blue through green and yellow indicates transmission loss values between 0 dB and 90 dB. The minimum value of the color scale, given by the darkest shade of blue is set to 30 dB. This does not mean that the transmission loss is always greater than 30 dB, but the lower limit is set to 30 dB simply to give the rest of the color scale a dynamic range appropriate for visualizing the results. Following the color scale from blue to yellow, the white colour indicates that the transmission loss is equal to the threshold for detection in high noise states, $\text{TL}_{\text{max, high noise}} = 90\,\text{dB}$. From there follows a transition from white to gray, further increasing the value of the transmission loss above $\text{TL}_{\text{max, high noise}}$, before the threshold for detection in low noise states is reached at $\text{TL}_{\text{max, low noise}} = 120\,\text{dB}$. This is indicated by a solid black colour which is used when $\text{TL} \geq \text{TL}_{\text{max, low noise}}$. Thus,

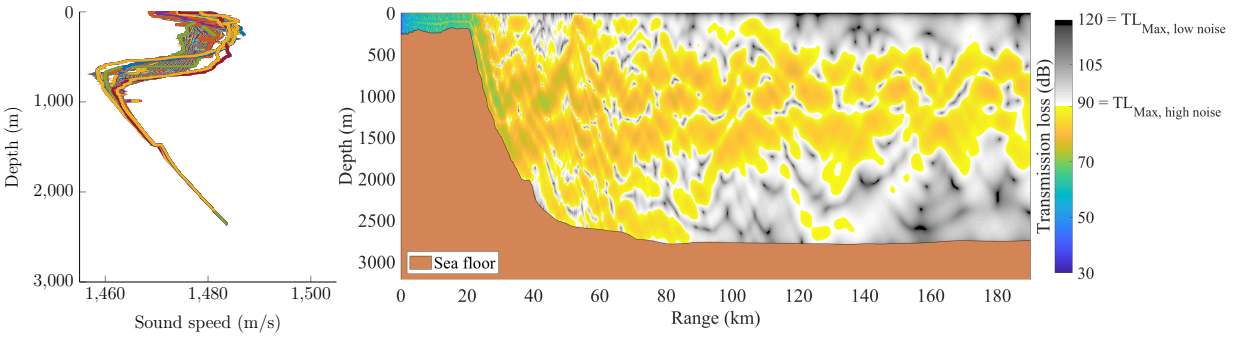

(a) Winter

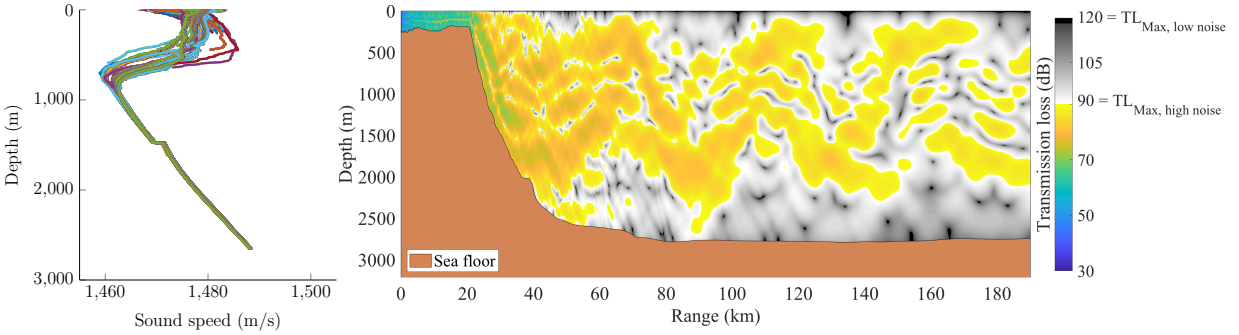

(b) Spring

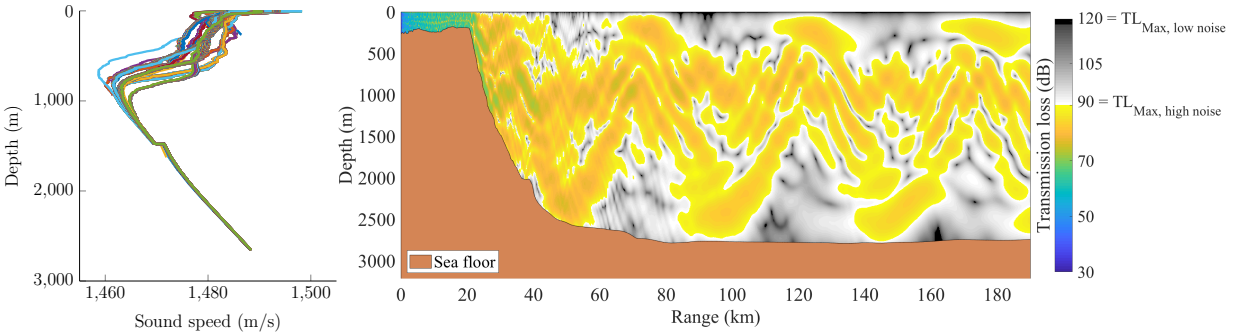

(c) Summer

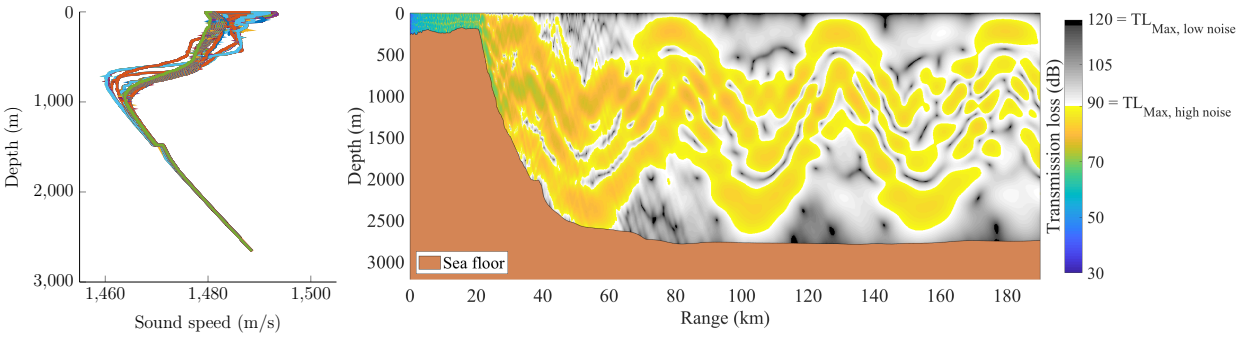

(d) Autumn

Figure 5.13: The modelled transmission loss for each season along the $\theta = 330°$-transect, running straight out of the Hola valley. The constructed SSPs used in each simulation are shown in the left column.

whether or not a whale can be heard by the LoVe Observatory will be ambiguous if the whale is located in an area in figure 5.13 that is coloured by any shade of grey. In these areas, the current state of the noise, which is of course not limited to the two states defined here, will determine if the whale call is detectable by the observatory.

Figure 5.14 shows how the sediment type varied along the $\theta = 330°$-transect. The figure has been constructed from the sediment map by Geological Survey of Norway (2016), shown in figure 3.6, and the output of the `Seabed`-function described in section 4.2.3 using $\Delta r = 38\,\text{m}$ as the step-size. Figure 5.14 thereby shows how the sediment type was varied with range in the simulations run to produce the transmission loss values shown in figure 5.13. The plot does not show the entirety of the transect, because there is no change in sediment type beyond $r = 71\,\text{km}$.

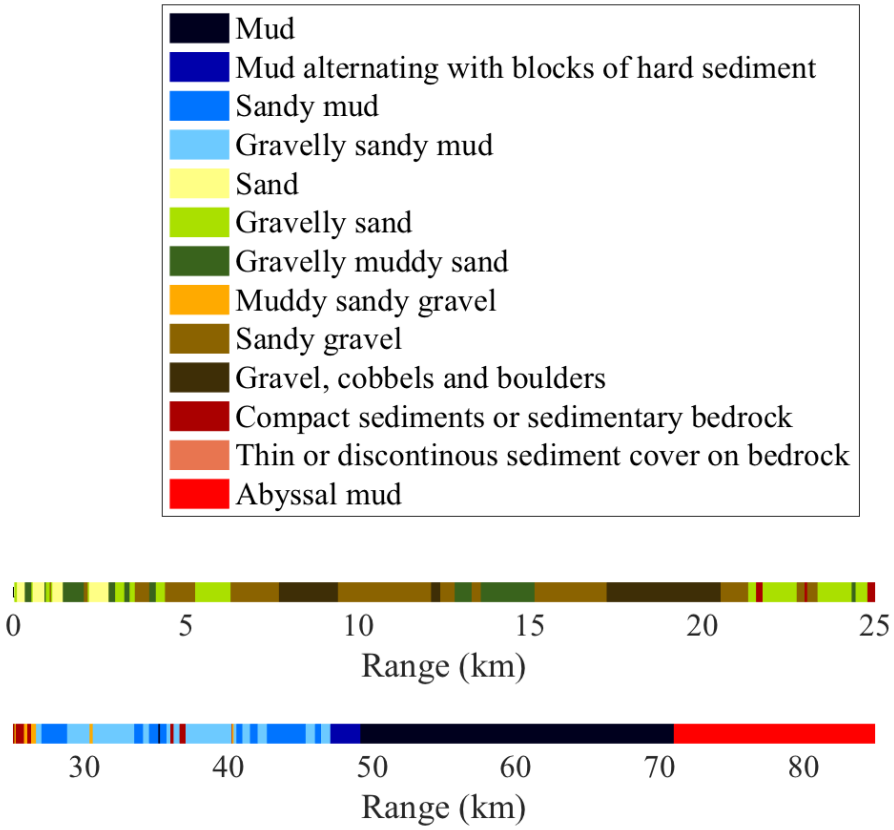

Figure 5.14: The sediment types used in the simulation of along the $\theta = 330°$-transect. Notably, the plot continues across two lines of different scale. Beyond $r = 71\,\text{km}$, the sediment type '*Abyssal mud*' continues until the end of the transect.

As expected figure 5.13 shows that the variation in transmission loss with position is complex and variable dependent on the season. In the deep Lofoten basin there appears to be a cyclical pattern of low transmission loss alternating between shallow and deep

water as a function of range. The regions of low transmission loss are taken to be convergence zones, and as expected, these regions are repeated at regular intervals in range. The presence of convergence zones suggests that sound originating at any point in the low transmission loss region will be propagated by the SOFAR channel. As explained in section 2.1.1, this means that the sound will experience little attenuation because it likely never interacts with the sea floor. The regions of transmission loss greater than $\mathrm{TL}_{\text{max, high noise}}$ are taken to be shadow zones, which are regions which are not reached by the sound rays from the SOFAR channel (White, 2015b).

Notably, the transmission loss in the shadow zones is for the most part not greater than $\mathrm{TL}_{\text{max, low noise}}$, meaning that there are viable propagation paths from the shadow zones to the observatory, albeit with more attenuation than in the convergence zones. For the shadow zones near the ocean bottom, this likely occurs because the sounds originating in the shadow zones will reflect off the sea bottom, thus being attenuated by reflection loss. Yet, the sounds are still propagated up to the observatory, which is remarkable given how deep the Lofoten basin is in comparison with the opening of the Hola valley. On the other hand, sounds originating in the shadow zones near the sea surface are not attenuated by reflection loss, since RAM treats the sea surface as a perfectly reflecting boundary. It is therefore not clear what causes the attenuation of sounds originating in the shallow convergence zones to be greater than the attenuation of sounds originating in the convergence zones.

Another surprising aspect of the simulated transmission loss near the ocean surface is the lack of coupling between transmission in the Hola valley and surface-duct propagation in the deep basin. As mentioned in section 5.1, the mean of the calculated SSPs show that in the winter and the spring, there is a mixed and isothermal surface layer with a positive gradient in the SSP, while the thermocline layers have a negative gradient. This typically gives rise to a surface duct (Brekhovskikh and Lysanow, 1991), where sound is propagated with little attenuation by being continuously refracted upwards and reflected off the surface. It is expected that this occurs in the Lofoten basin during winter and spring. However, figure 5.13 shows that the transmission loss values along the surface of the ocean are consistently higher than $\mathrm{TL}_{\text{max, high noise}}$. This indicates that even if a surface duct exists, the sound propagating in the duct does not continue to propagate into the Hola valley. The reach of the LoVe Observatory will therefore not benefit from low attenuation, surface-duct propagation.

Interestingly, figure 5.13 show that if a whale call is produced in a convergence zone and is thus propagated by the SOFAR channel, the sound appears to couple with the wave-guide produced by the shallow continental shelf and the sea surface, so that the whale call reaches the LoVe Observatory with little attenuation. This is true if the whale call is produced in convergence zones along the surface of the ocean, and, remarkably also for the convergence zones present at around $z = 2500\,\mathrm{m}$. Although it was expected that a SOFAR channel existed in the Lofoten basin, and that this would enable sound to propagate far, it is not straight forward to trust that this sound will propagate from the SOFAR channel and into the shallow Hola valley. This result shows that the LoVe Observatory has potential for monitoring a vast domain in the Lofoten basin.

The pattern of alternating convergence zones and shadow zones is present in all the

seasons, but is less pronounced in the winter. This results in fewer regions of transmission loss $< \mathrm{TL}_{\text{max, high noise}}$ near the surface in the winter for ranges greater than $r \approx 100\,\text{km}$. This could potentially affect the maximum range the LoVe Observatory is able to monitor during harsh and consequently loud weather conditions. A plausible explanation of the lack of distinguishable convergence zones is that there might be large variation in the SSPs along the modelled transect during the winter season. Variation in the SSP will cause the convergence zones to 'smear' together (Brekhovskikh and Lysanow, 1991). However, the lack of distinguishable convergence zones is possibly not an effect of the true conditions around the observatory, but rather a result of missing information in the RAM simulations. As seen in figure 5.1, the winter season does not contain CTD measurements all the way down to the sea floor. In the winter, the deepest CTD measurement was made at $z = 2484\,\text{m}$, whereas the other seasons have deeper measurements. And as previously mentioned, RAM does not extrapolate the value of c_w beyond the deepest specified value (Collins, 2001). This means that the maximum value of c_w below the minimum in c_w is lower in the winter measurements than in the other seasons. The width of the SOFAR channel is determined by the two depths at which the values of c_w are equal, on either side of the minimum in c_w (Urick, 1983). The fact that the winter season does not have measurements at great enough depths might have made the SOFAR channel in the simulations more narrow than it is in reality, and more narrow than it is in the simulations of the other seasons. This explains why the regions of $\mathrm{TL} < \mathrm{TL}_{\text{max, high noise}}$ appear at a more narrow range of depths in the winter season than in the other seasons. Moreover, in the RAM simulations, sound travelling at great depths, below $z = 2484\,\text{m}$, will not have been refracted upwards because the SSPs did not have a positive gradient below $z = 2484\,\text{m}$. It is likely that this will have caused more sound rays to interact with the sea floor, causing more attenuation, and that a repeated pattern of convergence zones and shadow zones was therefore not established in the transmission loss results for the winter season.

In the spring, summer, and autumn season it is possible to identify the rate at which the convergence zones are repeated. The peak of a convergence zone was taken to be where the transmission loss was equal to $\mathrm{TL}_{\text{max, high noise}}$ at the most shallow depth. $\mathrm{TL}_{\text{max, high noise}}$ is of course not the true limit of the convergence zone, since this threshold is defined specifically for the signal detection capability of the LoVe Observatory, but identifying this point will still give an indication of how often the pattern observable in figure 5.13 repeats itself. And identifying the depths at which the transmission loss reaches the threshold for detection at each convergence zone will aid understanding of how well the LoVe Observatory can detect mammals inhabiting shallow waters. The radial positions of the convergence zones were named r_1, r_2 and r_3, counting outwards from the position of the observatory. The corresponding depth coordinates were named z_1, z_2 and z_3. These coordinates were identified on figure 5.13b to 5.13d, and are shown in table 5.2. The winter season was not included due to the lack of a distinct convergence zone pattern.

	Spring	**Summer**	**Autumn**
Radial position (km)			
r_1	67	75	78
r_2	114	123	128
$r_2 - r_1$	47	48	50
r_3	155	173	179
$r_3 - r_2$	41	50	51
Depth (m)			
z_1	41	33	43
z_2	85	53	73
z_3	132	73	74

Table 5.2: The position coordinates of the convergence zones identified in figures 5.13b to 5.13d.

Table 5.2 also shows the difference between each consecutive convergence zone. These differences are similar across all three seasons, and within the expected range of 40 km to 60 km (White, 2015b). This validates that the simulated sound propagating in the Lofoten basin is exhibiting classical SOFAR propagation. Table 5.2 also shows the depths of each convergence zone peak. These depths increase as the range increases, and this trend is present in all three seasons. It is noteworthy that only the first convergence zone peaks lie above $z = 50$ m, which, as previously mentioned, was identified by Watkins et al. (1987) as the depth at which Fin whales typically vocalize. If the trend in the depth of the convergence zone peaks continues at ranges beyond 190 km, this means that the LoVe Observatory will not be able to detect Fin whales vocalizing at z = 50 m at any ranges greater than r_1, when the noise level is high.

In summary, in the simulated range, there are no clearly distinguishable regions which are not detectable at low noise conditions. This means that in low noise conditions, the observatory can detect mammals at nearly ever position in the Lofoten-Vesterålen basin along the $\theta = 330°$-transect. Propagation of sound in the SOFAR channel is mainly limited by attenuation from the sea water, which is minimal at 20 Hz (Brekhovskikh and Lysanow, 1991). It is therefore very likely that the observed convergence zone pattern, with transmission loss values lower than $\mathrm{TL}_{\text{max, high noise}}$, will exist at much larger ranges than the maximum simulated range of 190 km. To find the maximum detectable range of the observatory, longer ranges must be investigated.

Since modelling of the transmission loss using a complex software such as RAM is often too time consuming or costly for many researchers, the simplistic 'semi-spherical spreading' model for how transmission loss varies with range only, shown in equation 2.10, is often used instead (White, 2015b). It is therefore natural to compare the results from the RAM-simulations with the corresponding values from the simplistic model. Figure 5.15 shows the difference between the two models for the $\theta = 330°$-transect, calculated as

$$\text{Difference} = \mathrm{TL}_{\text{semi-spherical}} - \mathrm{TL}_{\text{RAM}}. \tag{5.1}$$

Here, $\mathrm{TL}_{\text{semi-spherical}}$ is the transmission loss calculated by equation 2.10 and TL_{RAM} is the transmission loss calculated by RAM.

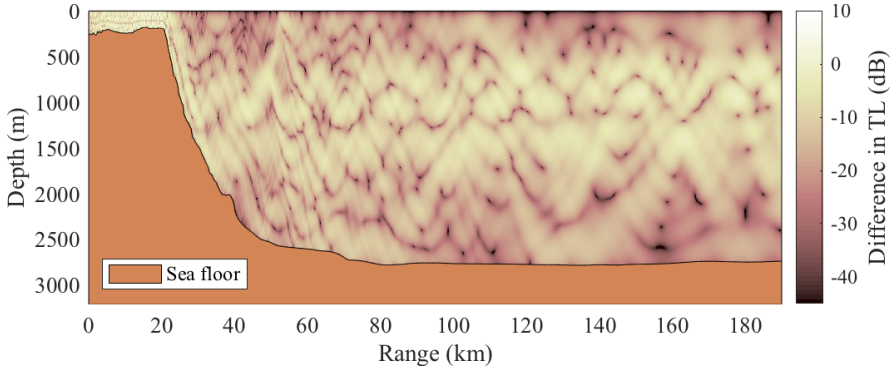

(a) Winter

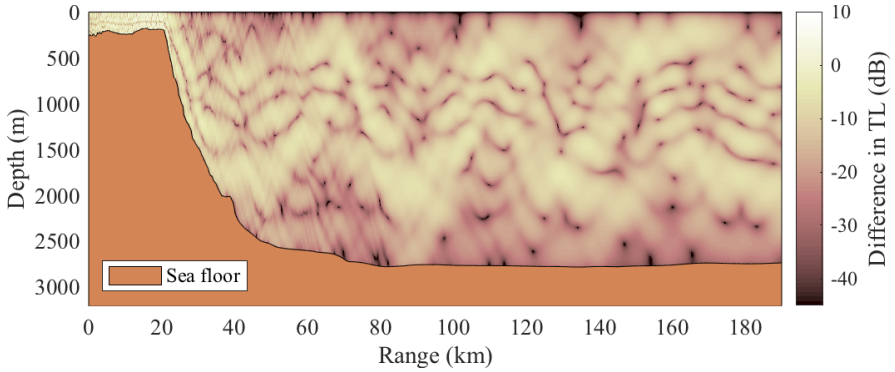

(b) Spring

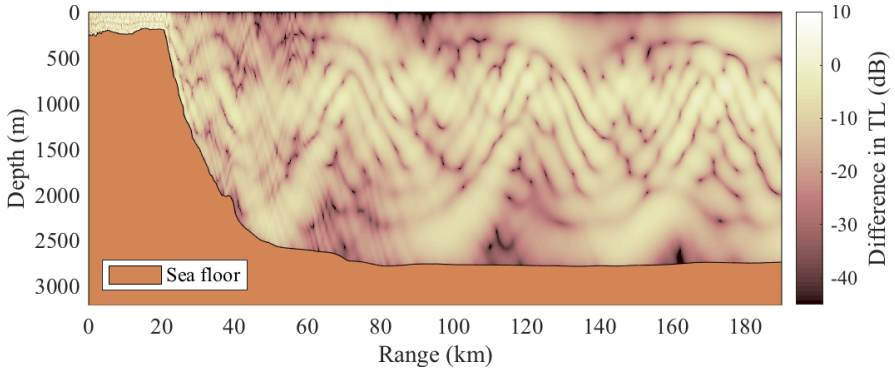

(c) Summer

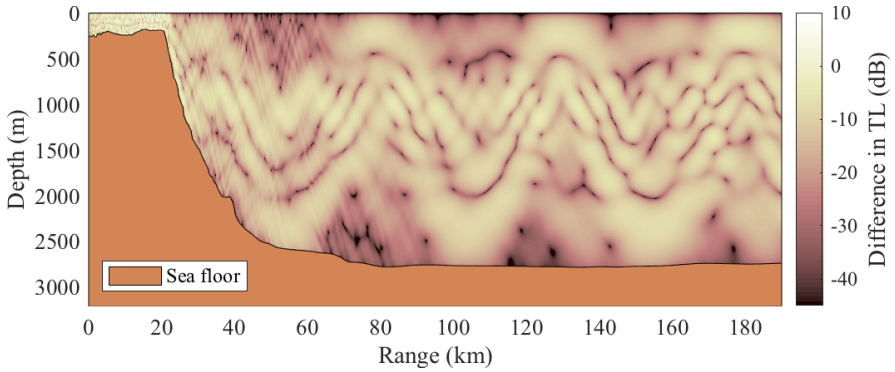

(d) Autumn

Figure 5.15: The difference between the transmission loss calculated by the simplistic 'semi-spherical spreading' model shown in equation 2.10 and the transmission loss modelled by RAM along the $\theta = 330°$-transect.

Figure 5.15 shows that $TL_{\text{semi-spherical}}$ is generally smaller than TL_{RAM} in all four seasons. In fact, close inspection of the figures reveal that the difference between the two models is only positive at a few positions in the shallow Hola valley, where $r < 20\,\text{km}$. The same cyclical pattern as was seen in figure 5.13 is observable in where the difference between the model approaches 0 in figure 5.15. This again underlines that propagation by the SOFAR channel reduces transmission loss. It is important to note that the simplistic transmission loss model consistently under-predicts the transmission loss. If this model were to be used for example to calculate the maximum range at which the LoVe Observatory could detect sounds, the range would have been severely overestimated.

After having looked at the effects of surface duct propagation and SOFAR-propagation in the deep basin, the attention is turned to the transmission loss experienced in the Hola valley itself. Figure 5.16 shows the simulated transmission loss at $\theta = 330°$, the same results as discussed above, but zoomed in at the Hola valley where the bathymetry is shallow. The transmission loss in the Hola valley looks strikingly similar across all seasons. This is somewhat surprising, given the large seasonal variations in SSP. The full set set of calculated SSPs shown in figure 5.1 of course does not show the SSPs measured in the Hola valley specifically, so the variation shown in figure 5.1 might not be representative along the simulated transect. Therefore, the SSPs interpolated along the $\theta = 330°$ transect up to $r = 21\,\text{km}$ are shown in figure 5.17. The interpolated SSPs appear to be varied across the seasons. In the winter and the spring, there is a prominent positive gradient in the SSPs, indicating that the water is mixed and isothermal. The gradient will cause the propagating sound to be refracted upwards, towards the surface of the ocean. In the summer season, there is a shallow surface layer of sun-heated water, giving a negative gradient in the top layer of the SSP. In theory, this should give rise to a wave-guide like propagation between the positive and the negative gradient in the SSPs. Finally, in the autumn season, the SSPs are of mixed shapes, with both positive and negative gradients in the surface layer. But, most of the SSPs have a positive gradient below $z \approx 150\,\text{m}$. This is true for all of the four seasons, and offers an explanation of why the simulated transmission losses are so similar. In all seasons, when sound rays approach the ocean surface, they will either be refracted back towards the bottom, or, reflected off the surface of the ocean. Similarly, when sound rays approach the bottom, they will either be refracted back towards the top by the positive gradient in the SSP, or, reflected off the bottom. The sound thus propagates along the valley as if it was a wave-guide.

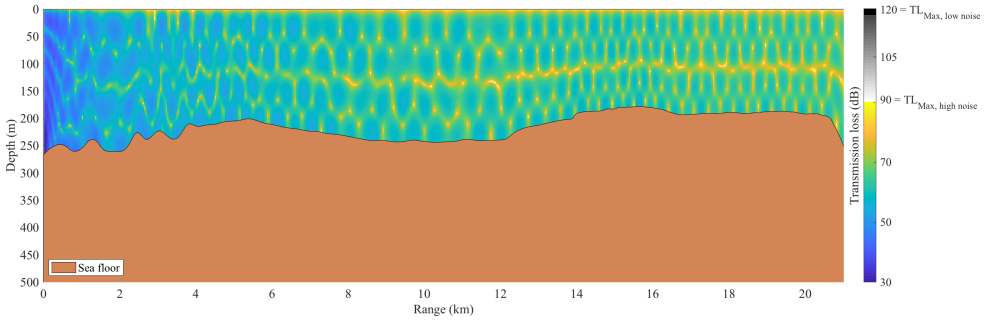

(a) Winter

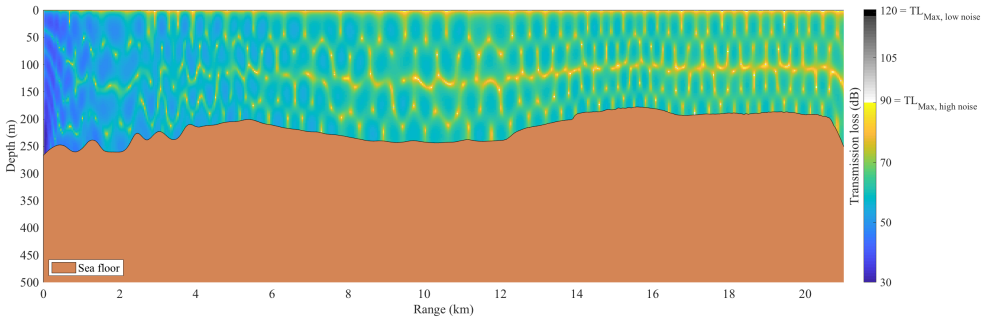

(b) Spring

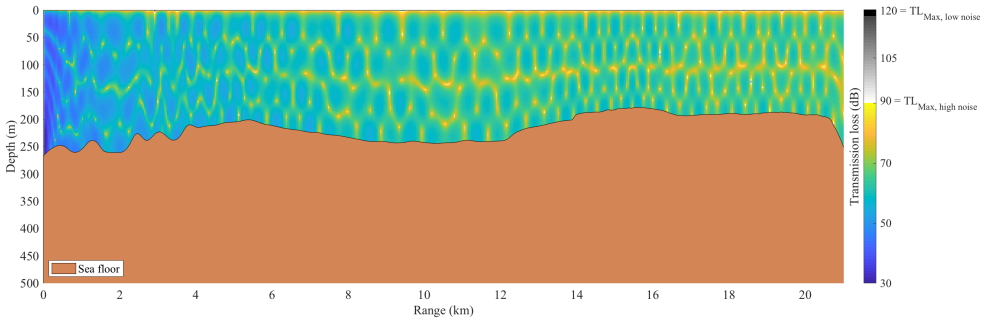

(c) Summer

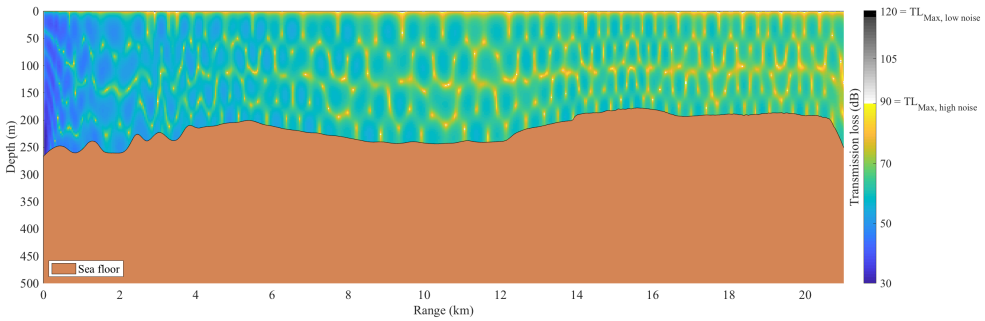

(d) Autumn

Figure 5.16: The simulated transmission loss at $\theta = 330°$ in the shallow Hola Valley, during all four seasons

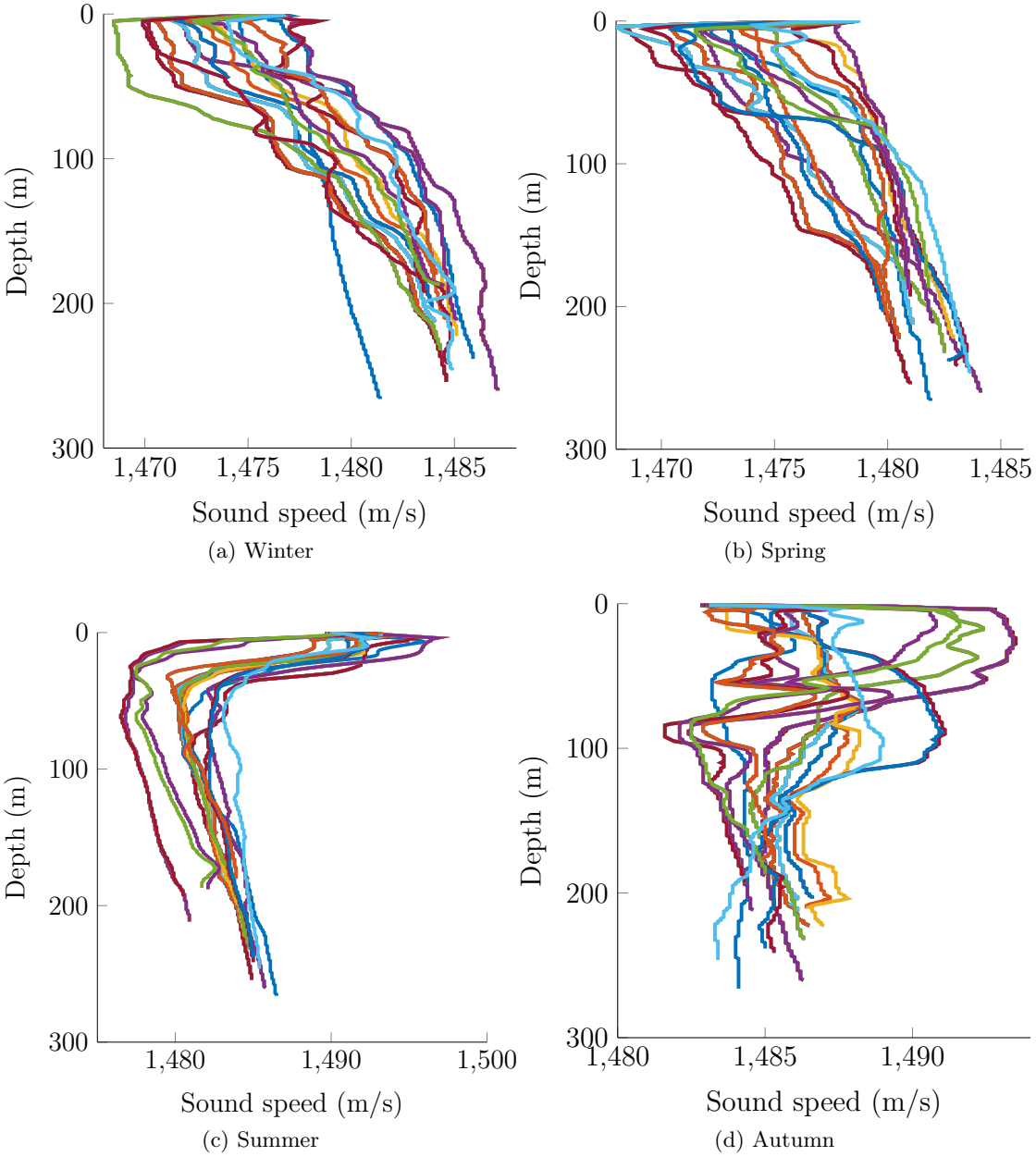

(a) Winter (b) Spring

(c) Summer (d) Autumn

Figure 5.17: The SSPs interpolated along the $\theta = 330°$-transect, up to $r = 21\,\text{km}$. Different colors indicate different interpolation positions.

The valley is shallow, but deep enough to support propagation of the 20 Hz-mode. The cut-off frequency for propagation of modes in a wave-guide is

$$f_{\text{cut}} = \frac{c_w}{4h}\sqrt{\frac{1}{1-\left(\frac{c_w}{c_b}\right)^2}}, \tag{5.2}$$

where h is the depth of the wave-guide (Urick, 1983). As shown in figure 3.6, the seabed in the Hola valley is mainly dominated by '*Sand*'. The factor $\frac{c_w}{c_b}$ in equation 5.2 equals $\frac{1}{V_R}$ and according to table 5.1, for '*Sand*', $V_R = 1.29$. Based on figure 5.17, the speed of sound in the water is estimated to be $c_w = 1480\,\mathrm{m\,s^{-1}}$. Finally, based on the bathymetry in figure 5.16 the depth of the valley is estimated to be $h = 225\,\mathrm{m}$. From this, the cut-off frequency is calculated to be $f_{\mathrm{cut}} = 2.6\,\mathrm{Hz}$. This is well below the modelled frequency, showing that wave-guide like propagation of the 20 Hz-mode is viable in the Hola valley.

5.4.1 Transmission loss as a function of θ

To investigate the effect of the shallow plateaus next to the Hola valley, the transmission loss has been modelled along 8 transects at varied angles. The locations of the transects are shown in figure 5.18, and figure 5.19 shows the simulated transmission loss along all of these transects for the winter season. The transmission loss has been simulated for all four seasons, but only the winter season is shown in figure 5.19. The results for the other seasons can be seen in figures B.3 to B.5 in appendix B. The figures reveal several important aspects regarding the transmission loss experienced by sound reaching the LoVe Observatory from locations on top of or beyond the two shallow banks next to the Hola valley. First of all, there appears to be little significant variation in the transmission loss plots across the four seasons. This is surprising, given the observed effect season had on the transmission loss along the $\theta = 330°$-transect in the Lofoten basin discussed above. This difference might indicate that seasonal variation in SSP is more significant when the sound propagates in deep water. The only plots where season does appear to significantly affect the transmission loss are in the plots of the $\theta = 270°$-transect. To ease comparison, the plots of the $\theta = 270°$-transect for each season are reproduced in figure 5.20.

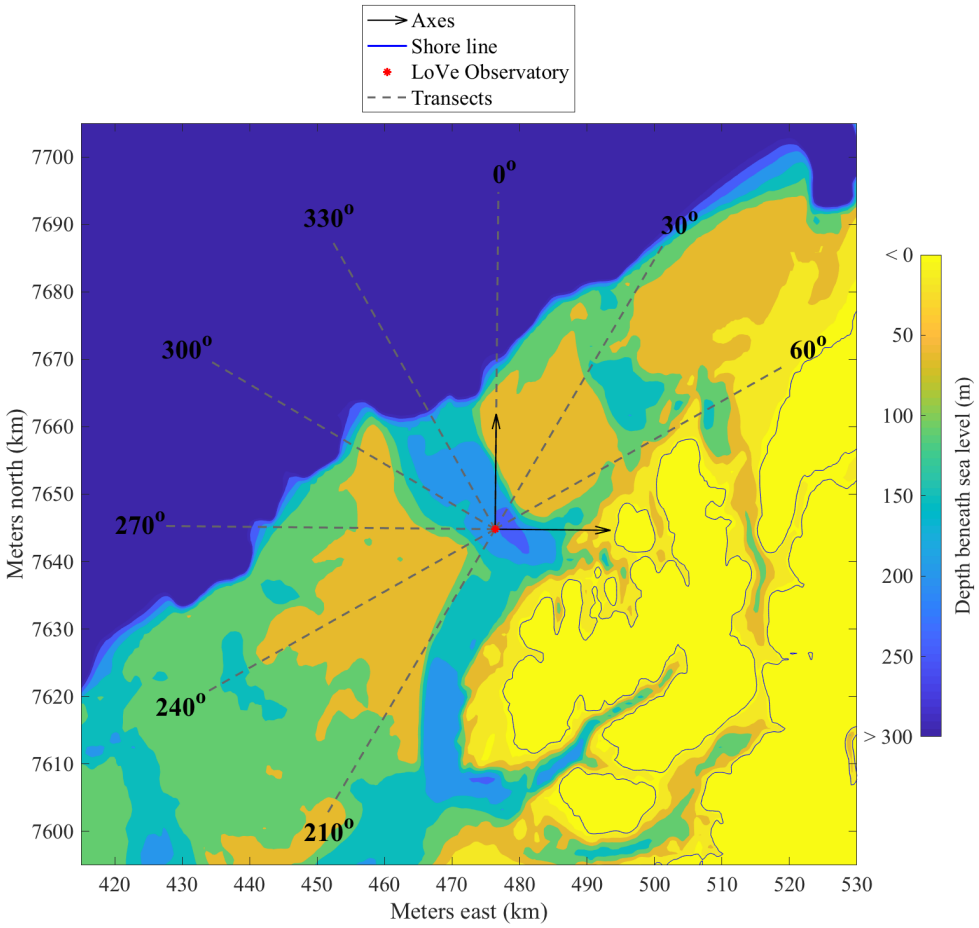

Figure 5.18: The location of the modelled transects at varying angles.

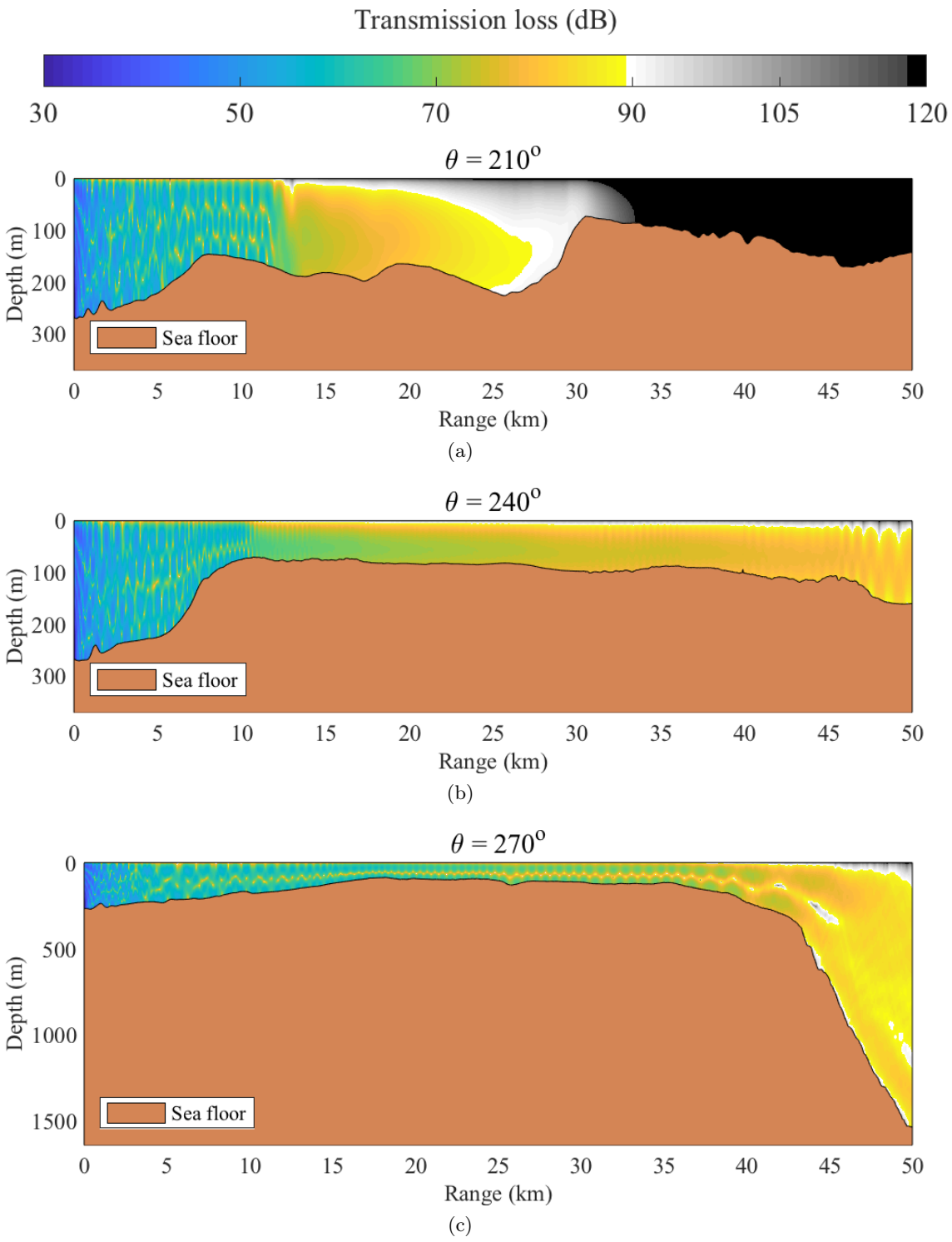

Figure 5.19: The transmission loss at varying angles, during the winter season.

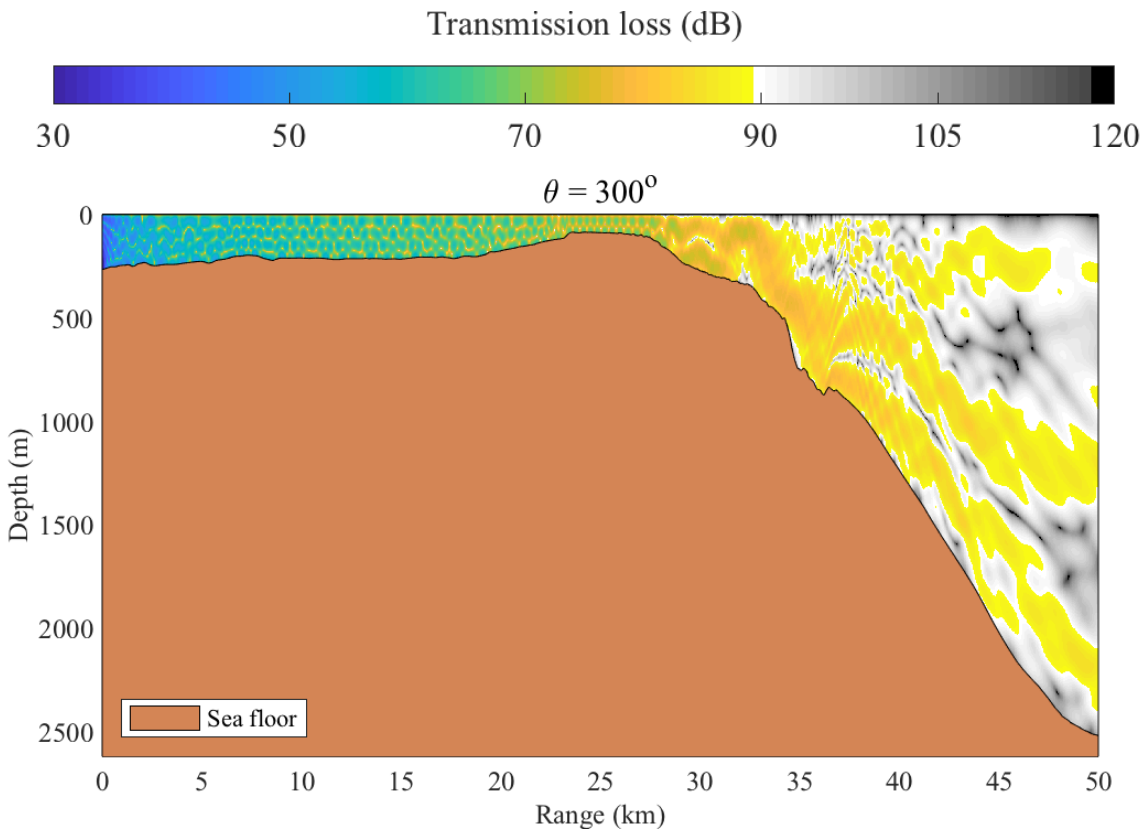

(d)

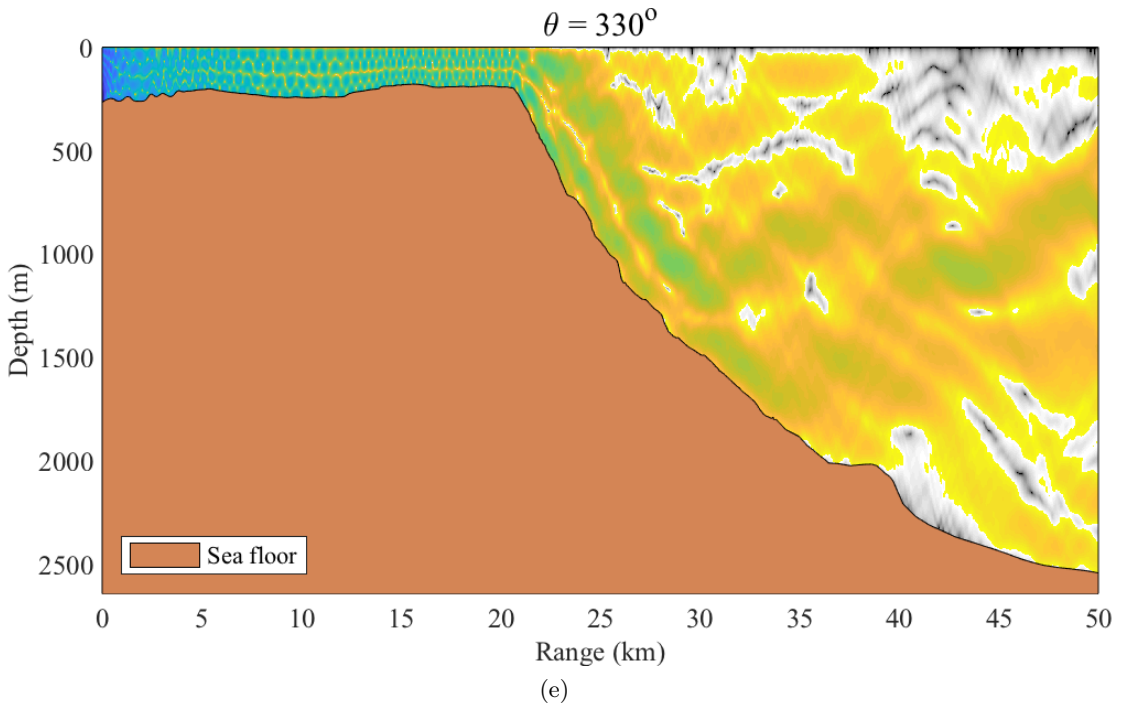

(e)

Figure 5.19: (continued) The transmission loss at varying angles, during the winter season.

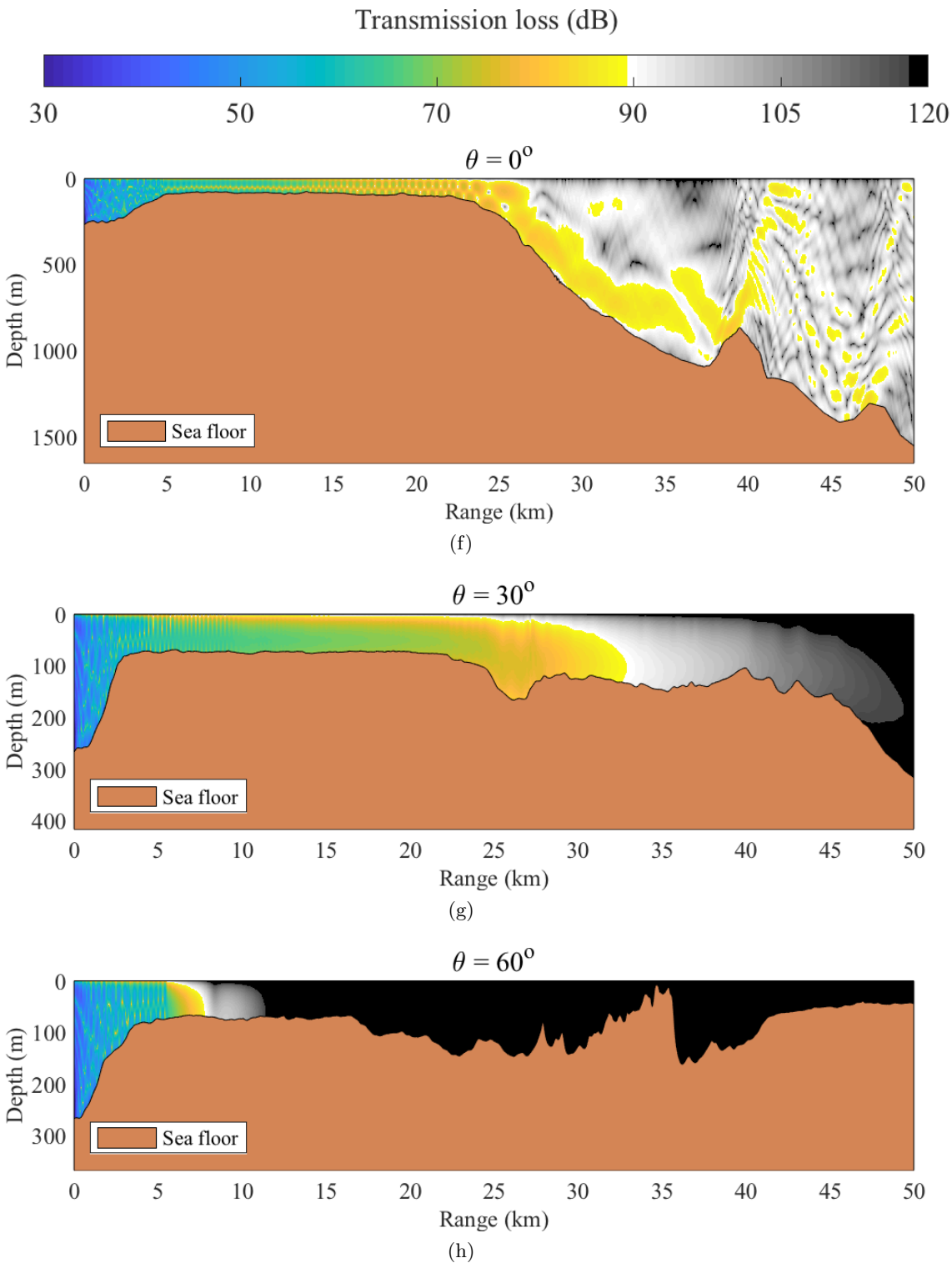

Figure 5.19: (continued) The transmission loss at varying angles, during the winter season.

The $\theta = 270°$-transect runs south-west from the LoVe Observatory, across the shallow Egga bank, before reaching the steep downhill slope into the Lofoten basin, starting at $r \approx 44\,\text{km}$. Figure 5.20 shows that sounds originating above this slope will experience transmission loss lower than $\text{TL}_{\text{max, low noise}}$. But, more importantly, the figure reveals that the level of transmission loss is different for the different seasons. In the summer and autumn, only sound sources positioned close to the seabed will experience transmission loss lower than $\text{TL}_{\text{max, high noise}}$. Contrastingly, in the winter, the entire water column above the slope has transmission loss lower than $\text{TL}_{\text{max, high noise}}$. Simulating the transmission loss along the $\theta = 270°$-transect has thus showed that the observatory might be able to detect some locations beyond the Egga bank during the winter season that it cannot detect during the summer and autumn seasons. This might contribute towards understanding why Fin whales typically are not detected by the LoVe Observatory from March to August. However, the same conclusion cannot be drawn when comparing the transmission loss in each season along the other transects plotted in figure 5.18. Some seasonal difference in the transmission loss experienced by sounds travelling to the LoVe Observatory from the Lofoten basin and across the Egga bank are observed in the plots of the $\theta = 300°$-transect (as seen in figures 5.19d, B.3d, B.4d, and B.5d). But the differences are complex and it is difficult to point to specific deviations that can support concrete conclusions about the effect of season on transmission loss.

The $\theta = 240°$ and $\theta = 270°$ transects (shown in figures 5.19b and c) show that sound originating in the water above the Egga bank will reach the observatory without experiencing transmission loss above $\text{TL}_{\text{max, high noise}}$. Similarly, the $\theta = 30°$-transect reveals that sound originating above the Vesterålen bank will also reach the observatory without being attenuated more than $\text{TL}_{\text{max, high noise}}$. Thus, the observatory can be used to monitor whale activity in the shallow water on top of the banks, even though direct sound propagation paths between the whales and the observatory are blocked by the step changes in bathymetry. The plot of the transmission loss along the $\theta = 60°$-transect, shown in figure 5.19h, does not necessarily support this conclusion. However, almost all of this transect extends beyond the area in which the sediment composition has been mapped by Geological Survey of Norway (2016), shown in figure 3.6. In such a shallow region, the simulated transmission loss becomes quite unreliable without including information about the sediment composition. The simulated transmission loss along the $\theta = 60°$-transect will therefore be disregarded.

Having said this, propagation in shallow water with high-impedance sediments is not unaffected by attenuation. The $\theta = 210°$ and the $30°$ transects (shown in figures 5.19a and g, respectively) show that sounds originating in shallow water at ranges beyond the Egga and Vesterålen banks are highly attenuated. In fact, these are the only transects where the transmission loss at some ranges reaches $\text{TL}_{\text{max, low noise}}$ in the entire water column. This is likely caused by changes in the bathymetry, causing sound to be reflected back towards the source, and thus never reaching the LoVe Observatory. In the $\theta = 210°$-transect, transmission loss is greater than $\text{TL}_{\text{max, low noise}}$ at all positions in z at $r > 34°$. Comparing this with how far sound propagates without being significantly attenuated along the $\theta = 330°$-transect really highlights how much scattering by the changing bathymetry in shallow water contributes to the transmission loss.

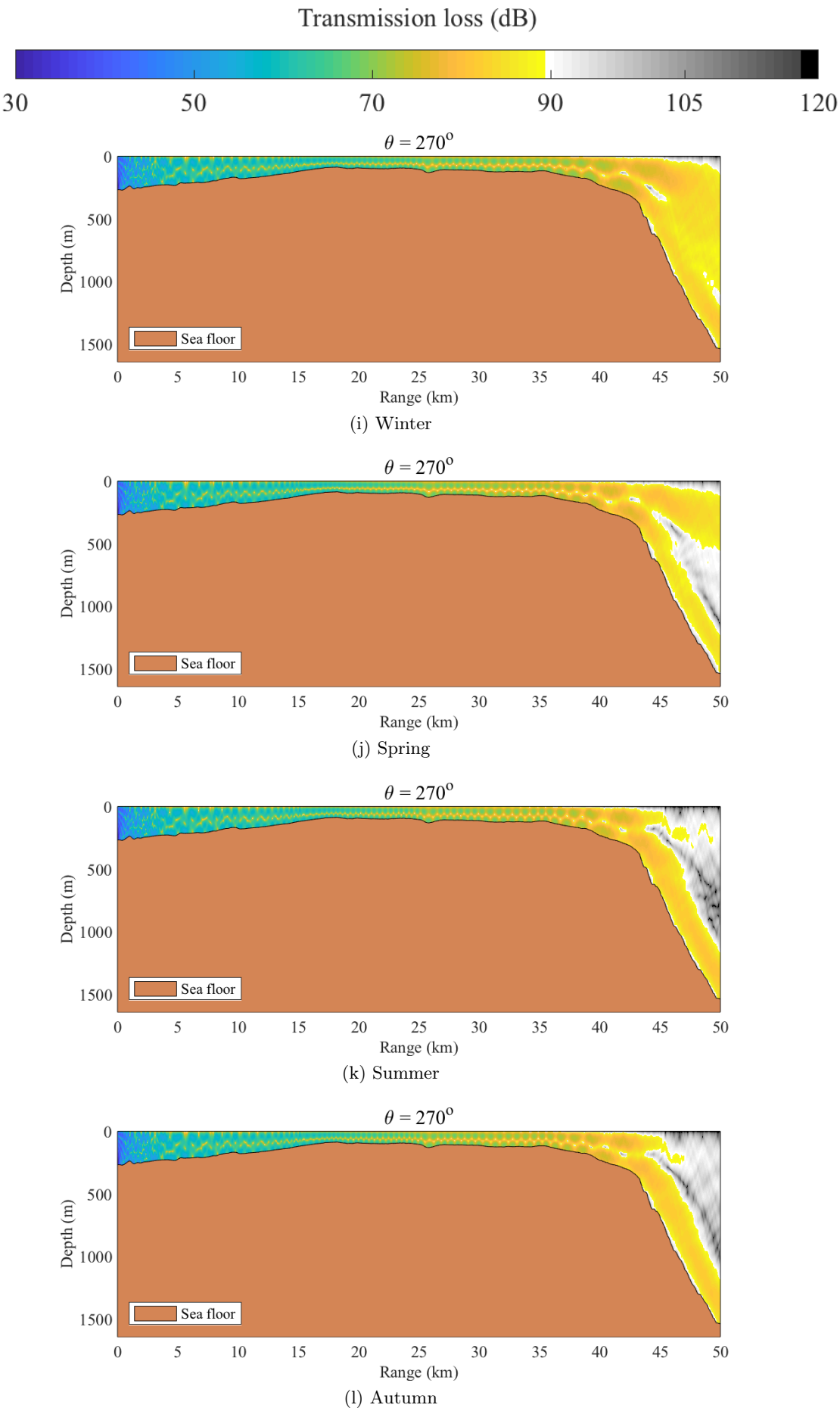

(i) Winter

(j) Spring

(k) Summer

(l) Autumn

Figure 5.20: The transmission loss along the $\theta = 270°$-transect for the four seasons.

Several of the transmission loss plots are simulated along transects with varying bathymetry that causes some positions in the water column to not have direct straight propagation paths to the LoVe Observatory. This is the case for the $\theta = 270°$, $\theta = 300°$, and the $\theta = 0°$ transects (shown in figures 5.19c , d, and f, respectively). The plots of the simulated transmission loss for these transects all show that the transmission loss is rarely above $\mathrm{TL}_{\text{max, low noise}}$, even at positions without direct propagation paths. Remarkably, this indicates that the LoVe Observatory is not hindered by 'shadows' from the Egga or Vesterålen banks.

The transmission loss has also been simulated along every transect between 220° to 40° at 1° intervals. These simulation results were processed so that horizontal planes giving the variation of TL with θ and r were produced. For example, figure 5.21 shows the transmission loss at $z = 50°$, depth at which Fin whales vocalize, according to Watkins et al. (1987). To compose the results presented in figure 5.21, the transmission loss at $z = 50\,\mathrm{m}$ at all ranges was extracted from the results of each of the modelled transects. This was done for the winter, spring and autumn season. Little distinct variation was observed between the seasons, and the plots for the spring and autumn have therefore been placed in Appendix B in figure B.6, while the winter season is shown in figure 5.21. The figures include the outline of the sediment map, which refers to the region mapped by Geological Survey of Norway (2016), shown in figure 3.6. At ranges beyond this region, there is little or no available information about the composition of the seabed, and the sediment has therefore been assumed to be '*Abyssal mud*'. As discussed in section 3.3.4, this is an appropriate assumption in the deep regions of the Lofoten basin. However, comparison of the outline shown in figure 5.21 with bathymetry contour maps, shown for example in figure 4.3, reveals that not every region outside the sediment map has deep bathymetry. The transects at $\theta = 220°$ to approximately 260° and $\theta = 40°$ to approximately 30° run across shallow banks that lie partly outside the region mapped by Geological Survey of Norway (2016). Looking for example at the transmission loss at $\theta = 240°$ in figure 5.21, the value of TL changes quite abruptly at the outline of the sediment map, indicating that sediment type significantly affects the transmission loss. The presented results for transects running across shallow banks outside the mapped region are therefore untrustworthy. Notably, this is not to say that all simulated transmission loss results outside the outlined sediment map are unreliable.

Figures B.6 and 5.21 all show that the transmission loss is generally lower than $\mathrm{TL}_{\text{max, high noise}}$ at ranges $r < 50\,\mathrm{km}$, but greater than $\mathrm{TL}_{\text{max, high noise}}$ beyond this range. This again highlights the fact that only the first convergence zone exists at $z = 50\,\mathrm{m}$. This is an important conclusion if Fin whales only vocalise at this depth (Watkins et al., 1987). Notably, this means that the observatory can only detect whales up to approximately $r = 50\,\mathrm{km}$ in severe noise conditions. Moreover, the fact that $\mathrm{TL} < \mathrm{TL}_{\text{max, high noise}}$ in most regions within $r \leq 50\,\mathrm{m}$ supports the previous conclusion that sound originating on top of the Egga and Vesterålen banks will reach the observatory with little attenuation. The fact that sound seemingly propagates well across the shallow banks is not unexpected, given the sediment types present on the banks. In the shallow water above the banks, the sound will propagate by reflecting off of the ocean surface and the bottom, and the sediment therefore plays an important role in how much the sound is attenuated. Figure

3.6 shows that the sediments on the bank mainly consist of '*Gravel, cobbles and boulders*' and some '*Sandy gravel*'. As shown by the velocity ratio and the grain density of the sediments, shown in table 5.1, these are sediment types with relatively high impedance, in comparison with water. This means that the boundary between the water and the sediment will be highly reflective, and the sound will not experience much attenuation when it is reflected. In fact, equation 2.17 has been graphed (not shown here) as a function of incidence angle, θ_i, using the material properties for '*Gravel, cobbles and boulders*'. This revealed that the pressure reflection coefficient is 1 for all incidence angles $> 44°$. At steep incidence angles, the sound will thus be reflected without experiencing any attenuation at all.

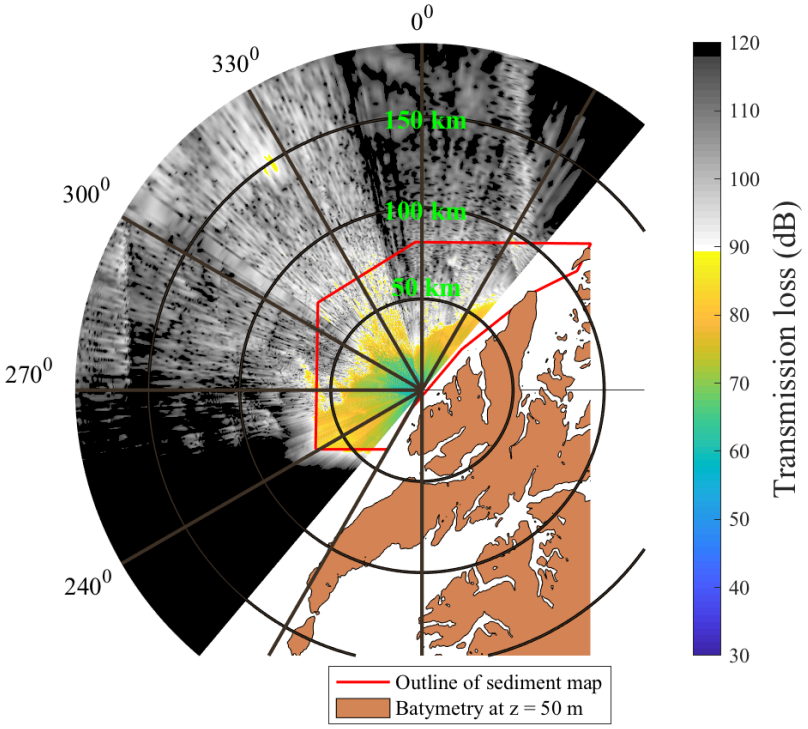

Figure 5.21: The simulated transmission loss at $z = 50\,\text{m}$ for the winter season.

Outside $r = 50\,\text{km}$ figure 5.21 shows that the transmission loss is generally distinctly lower than $\text{TL}_{\text{max, low noise}}$, for transects between $\theta \approx 290°$ to $345°$. For angles outside this 'beam', the transmission loss transitions towards more areas having $\text{TL} \geq \text{TL}_{\text{max, low noise}}$. This demonstrates that the angular reach of the observatory is limited, an effect which most likely occurs because the observatory is hindered by the shallow banks. But, notably, the banks have not completely blocked the observatory's detection capabilities, even when the banks cause there to be no direct propagation path between the sound source and the observatory. This is apparent for example along the $\theta = 0°$-transect, which runs across the Vesterålen bank. Although the bank is more shallow than the position of the

observatory, there are still some regions with TL $<$ $\text{TL}_{\text{max, low noise}}$ at ranges greater than 50 km.

Its interesting to investigate if the convergence zones seen in figure 5.13 are also present at other transects. The transmission loss variation with range was therefore extracted from all the simulated transects at $z = 235$ m. This is the approximate depth at which the middle of the convergence zones close to the surface in 5.13 are located. The resulting transmission loss values as a function of θ and r are shown in figure 5.22 for the winter, spring and autumn seasons. These figure include a map of where the bathymetry is more shallow than $z_b = 235$ m. This highlights the fact that the LoVe Observatory is surrounded by more shallow bathymetry at all sides, even in the direction running out of the valley. It is therefore slightly surprising that the observatory is able to detect whales even in severe noise conditions, despite being blocked by the bathymetry. Figure 5.22 shows the presence of regularly repeating convergence zones at transects between $\theta = 300°$ and 340°. This confirms the angular limitation of the observatory; only transects within this 'beam' have transmission loss values below $\text{TL}_{\text{max, high noise}}$ at ranges greater than approximately $r > 50$ km. As seen also in figure 5.13, the convergence zone pattern is most pronounced in the warmer seasons, and less distinguishable in the winter.

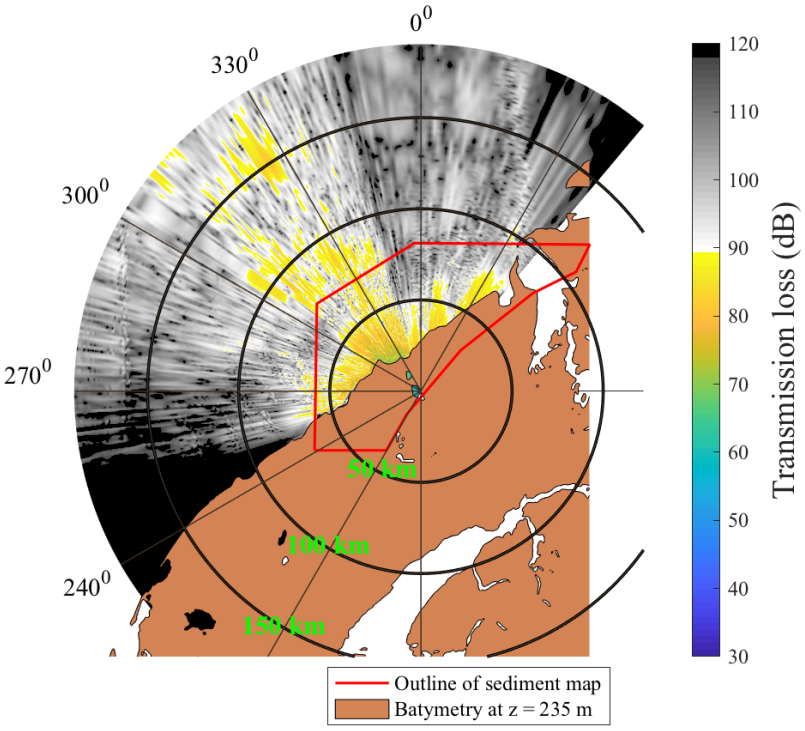

(a) Winter

Figure 5.22: The simulated transmission loss at $z = 235$ m for the winter, spring and autumn seasons.

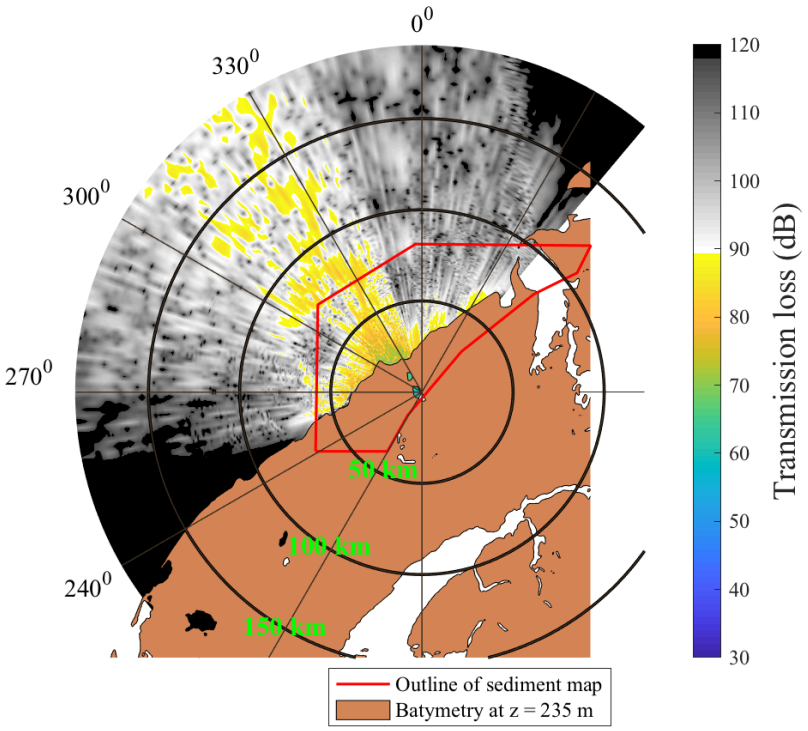

(b) Spring

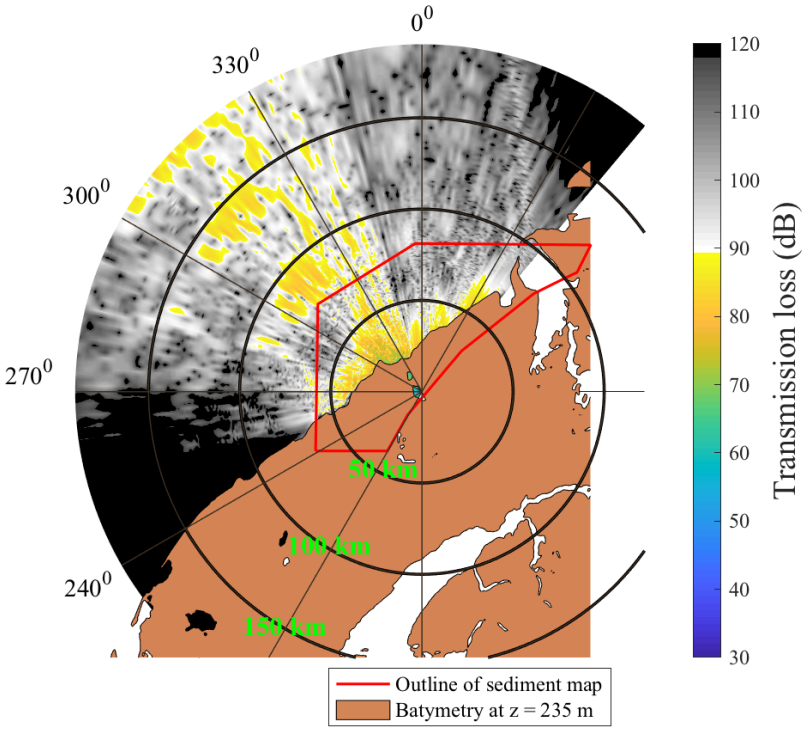

(c) Autumn

Figure 5.22: (Continued) The simulated transmission loss at $z = 235\,\mathrm{m}$ for the winter, spring and autumn seasons.

Chapter 6

Discussion

6.1 Outcomes of the RAM-simulations

The presentation of the simulated transmission loss values in sections 5.4 and 5.4.1 have indicated that the LoVe Observatory is suitable for monitoring of whales using acoustic animal density estimation. Generally, the detectable ranges are as great (or potentially greater than) the simulated ranges in low noise conditions, but more limited as the noise level increases. The transmission loss at the depth of vocalizing Fin whales is unfortunately higher than $\mathrm{TL}_{\mathrm{max,\ low\ noise}}$ at ranges greater than approximately $r = 50\,\mathrm{km}$, which might indicate that the Fin whales commonly detected by the observatory are staying within this range. It has been shown that sounds originating on top of the Egga and Vesterålen banks can be detected by the observatory, even though these sound sources might not have direct straight propagation paths to the receiver. The observatory thus does not seem to be significantly limited by 'shadows' from the shallow banks. Having said this, it has also been shown that the observatory has an angular limitation in its detectable area, which most likely stems from the banks either blocking the observatory's access to the deeper waters with their bathymetry, or from the added transmission loss stemming from more bottom interaction due to the very shallow water on top of the banks. Generally, seasonal variability has been shown to be most pronounced at deeper waters. The observed convergence zones in the Lofoten basin are affected by season, and are most distinguishable in the warmer seasons. Remarkably, this does not offer any conclusions towards why Fin whales are generally not detected by the observatory between March to August.

6.2 Discussion of the chosen methods

The transmission loss around LoVe has been simulated using RAM with environmental input parameters gathered from various online databases. Using RAM to simulate transmission loss is a well established method. The validity of the results produced by the algorithm will be discussed in section 6.3. The bathymetric data have been interpolated, which is considered a reliable method. It is only limited by the resolution of the original

bathymetry maps. Likewise, the SSPs are also calculated using a reliable method. The values are calculated from CTD measurements, which are commonly measured specifically for SSP calculations (Urick, 1983). After the SSPs were calculated, interpolation was used to identify the values of c_w at any position. This method was designed by the author. One potential flaw with the method comes from the exclusion of short SSPs, which was discussed in section 5.1.1. Although removing the short SSPs seemingly alleviated the issue of jump-like artefacts in the constructed SSPs, it also removes viable information from the interpolation, thus making the results less likely to reflect the real value of c_w. This raises the interesting question of whether to include all available information when modelling real oceans, even if the information causes artefacts in the modelled results, or to exclude some information to avoid artefacts. In this case, the latter was chosen, even though this deliberately diminishes the veracity of the input parameters to RAM. The chosen model was effective in removing artefacts along the test transect used in figures 5.3 and 5.5. However, in the SSPs constructed for the $\theta = 330°$-transect, shown in figure 5.13, there are still some traces of the jump-like artefact at $z \approx 1480\,\text{m}$. These artefacts might not stem from the issue of short SSPs after all, or it might be that the method chosen to correct the issue has failed in this instance. In either case, if the model tool algorithms presented in this study are to be used for further studies, it is recommended that the exclusion of short SSPs and the treatment of jump-like artefacts in the constructed SSPs are reviewed.

The last environmental input parameter, the geoacoustic properties of the sea floor, were partly calculated using a method constructed by the author, and this approach thus requires some analysis. Determining the geoacoustic properties involved determining methods for translating the qualitative sediment descriptions in the downloaded characterisation of the seabed by Geological Survey of Norway (2016) into quantitative properties of the different sediment types. For the unconsolidated sediments, this involved making a novel systematic method for determining an estimate of the mean grain size ϕ' based on the available information on the ratios of different sediment structures contained in each sediment type, in addition to estimated average grain sizes. The resulting values for the estimated mean grain sizes are shown in table 5.1.

Some of the sediment type descriptions used by Geological Survey of Norway (2016) are the same as descriptions used in the High Frequency Environmental Acoustics (HFEVA) model by Jackson (1994), and the model can thus be used to check the validity of the method used to estimate ϕ'. Chotiros (2018) has published some values of ϕ' constructed using the HFEVA model. Those sediment types that have the same qualitative descriptions as those used by Geological Survey of Norway (2016) have been re-printed from Chotiros (2018) in table 6.1. To ease comparison, the values estimated for ϕ' for the same descriptors, originally shown in table 5.1 are also shown in table 6.1. And, to aid comprehension, each of the sets of values for ϕ' have been converted to units of mm using equation 2.23, and the results of this conversion are also shown in table 6.1.

Sediment type	ϕ' (Phi units) by author	Φ' (mm) by author	ϕ' (Phi units) (by HFEVA)	Φ' (mm) (by HFEVA
Sandy mud	0.85	0.55	6.5	0.01
Gravelly sandy mud	-2.56	5.89	1.0	0.50
Gravelly sand	-2.60	6.06	0.5	0.70
Muddy sandy gravel	-4.21	18.50	0.0	1.00
Sandy gravel	-4.21	18.50	-1.0	2.00

Table 6.1: Comparison between the estimated mean grain sizes calculated by the author, and values for the same parameter produced by Chotiros (2018) using the HFEVA model by Jackson (1994).

HFEVA is a commercially available tool for estimating sediment properties, and it is therefore reasonable to believe that the properties estimated by the model are trustworthy. When comparing the values of ϕ' estimated by Chotiros (2018) using HFEVA with the values of ϕ' estimated by the author, it is therefore assumed that the values by Chotiros (2018) are correct. It is clear from the comparison that the values for ϕ' calculated by the author are consistently too low. Since HFEVA is commercially available it is not open source and the author did not have access to the tool. The way the grain size is determined by the model is therefore not known. This, combined with the fact that not all of the sediment types present in the Lofoten-Vesterålen basin were described by Chotiros (2018) were the reasons why the model was not used in the simulations presented in this study. Unfortunately, this also means that it is challenging to pinpoint the reason why the results of the constructed grain size estimation method used in this thesis differs so much from the results by the HFEVA model.

The comparison shows that it is likely that underestimated values of ϕ' have been used in this study. This will have caused several effects on the environmental parameters predicted from ϕ'. Firstly, the linear relationship between the bulk density, ρ_B, and ϕ', shown in equation 2.24 reveals that the calculated bulk density will be too high. Secondly, the velocity ratio is also calculated from the estimated grain size. The relationship between V_R and ϕ', shown in equation 2.20, is not as clearly interpreted, since it is a convex parabolic relationship. However, plotting of the relationship (not shown here) shows that in the considered interval of grain sizes, too low values of ϕ' will cause the velocity ratio to be too high. Therefore, the sound velocities of the sediment will be too high. Together, the high velocity ratio and the high bulk density causes the specific impedance of the sediment to be large, and looking at the pressure reflection coefficient in equation 2.17, it is clear that this will cause more energy to be reflected when the sound hits the sea floor. Analogously, if the grain sizes predicted by HFEVA had been used in the model tools and RAM simulations, more energy would have been transmitted into the sea floor and therefore absorbed.

The overestimation of V_R has not only caused the overall value of the pressure re-

flection coefficient to be too great, but it has also affected how it varies as a function of incident angle. The estimated values of V_R shown in table 5.1 are all greater than 1. This in turn means that the sound velocities calculated from the velocity ratio will always be greater than the sound of speed in the seawater, but in reality, this is not always the case. For example, according to Jackson and Richardson (2007), the sound velocity in muddy sediments are as much as 3% lower than c_w. Figure 6.1 shows how the pressure reflection coefficient varies with the incident angle for two cases: when $V_R = 1.10$, which is the value calculated for '*Mud*' in this study, and when $V_R = 0.97$, which, according to Jackson and Richardson (2007) is the correct value for muddy sediments. The values of the pressure reflection coefficient shown in figure 6.1 are calculated by applying equation 2.17 and Snell's law, shown in equation 2.3. The densities of the water and the mud are kept constant in the two cases. The density of the seawater is assumed to be $\rho_w = 1020\,\mathrm{kg\,m^{-3}}$ and the density of '*Mud*' was calculated from ρ_w and the values of ρ_g and η shown in table 5.1. This resulted in $\rho_b = 1835\,\mathrm{kg\,m^{-3}}$. Figure 6.1 reveals that having overestimated the value of V_R has drastically affected the value of R at large incidence angles. In the case of V_R calculated by the author, R increases to a maximum around $\theta_i = 65°$, giving the pressure reflection coefficient a critical angle. This means that all of the incident sound energy is reflected back into the water. On the other hand, in the case of V_R predicted by Jackson and Richardson (2007), R has a minimum, known as an angle of intromission, at $\theta_i = 80°$. At this particular incident angle, all of the incident sound energy is transmitted into the seabed. Figure 6.1 also shows that at values of θ_i leading up to the minimum, the value of R decreases, leading to significantly different values of R for the two cases. In general, it is clear that $V_R > 1$, which is the case for all the sediment types shown in table 5.1, causes more energy to be reflected into the water,

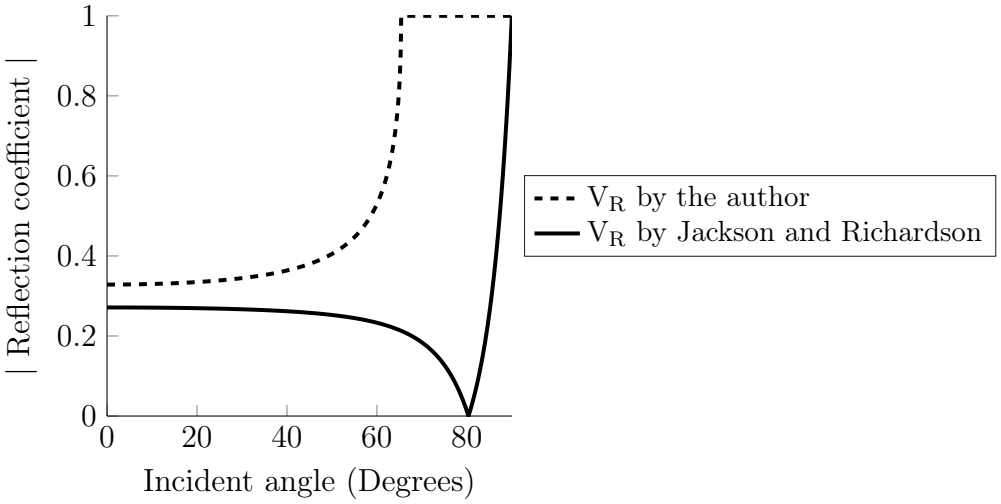

Figure 6.1: An example of how the pressure reflection coefficient of '*Mud*' varies with incident angle for two different values of V_R. In the case of V_R estimated by the author, $V_R = 1.10$ has been used. In the case of V_R estimated by Jackson and Richardson (2007), $V_R = 0.97$ has been used. In both cases ρ_w was assumed to be $1020\,\mathrm{kg\,m^{-3}}$ and ρ_b was calculated to be $1835\,\mathrm{kg\,m^{-3}}$.

while when $V_R < 1$, more energy is transmitted into the sediment and absorbed. Therefore, the underestimation of ϕ' (which in fact is an overestimation of the grain size diameter in mm) and the subsequent overestimation of V_R has caused the reported values of TL to be too low.

Moreover, the underestimation of ϕ' has affected the calculated values of the attenuation constant, h. Equations 2.27, 2.28, and 2.32 were used to calculate h from the grain size, and all of these relationships give too low values of h when ϕ' is underestimated. In turn, this has caused the attenuation coefficient to be underestimated. The attenuation coefficient was only calculated from h for the sediment types '*Mud*', '*Sandy mud*', and '*Sand*'. Yet, as shown in the map in figure 3.6, the latter sediment type covers most of the sea floor in the Hola valley, where most of the bottom interaction will occur, due to water being shallow. It is thus probable that the underestimation of ϕ' and the consequent underestimation of $\alpha_{\lambda,b}$ for some sediment types, have caused significant underestimation of the modelled transmission loss.

6.3 Validity of the results

It is important to pose questions about whether the results produced by the RAM simulations should be taken to be accurate and true. The factors affecting this can be divided up into three main categories: consequences of the convergence tests, limitations of the RAM algorithm, and limitations of the input parameters.

6.3.1 Consequences of the convergence test

The results of the convergence test presented in section 5.3 are unfortunately somewhat inconclusive. The chosen criterion for convergence was that several consecutive iterations with decreasing step sizes should produce the same transmission loss values. This was not reached in either the convergence test for Δz nor the convergence test for Δr. In the test for Δz, the results of consecutive simulations produced similar transmission loss values, and it appeared as if the solutions started to stabilize as Δz was decreased. But, a peculiar alternating behaviour was discovered. In the region of values of Δz where the convergence criterion seemingly was nearly satisfied, the transmission loss values still seemed to waver between TL ≈ 94 dB and TL ≈ 98 dB. Even though the results were interpreted as having stabilized, the alternating behaviour makes this conclusion dubious. The reason for this alternating behaviour is not know. If more time had been available, the cause of this alternating behaviour should have been pursued further. It might, for example, have been worthwhile to repeat the convergence test of Δz using a smaller constant Δr, or it might have revealed new information to look at the change in transmission loss with Δz at a different radial position than the arbitrary position chosen in figure 5.7. If the transmission loss results presented in this study are to be used in further works, the lack of a confident convergence test result should be kept in mind, and at least a an error of ± 2 dB should be assigned to the results.

Moreover, the results of the convergence test of the Δr-variable makes the resulting transmission loss simulations even less credible. The results of this test showed that

the convergence criterion was not satisfied, even for values of Δr much smaller than those conventionally used by other RAM users. Reducing the value of Δr resulted in stability issues, seen as Gibbs' oscillations in the resulting transmission loss values. It is plausible that the instability was encountered because small Δr values caused the modelled environment to no longer be weakly range dependent. Figure 5.14 shows how the sediment type varied as a function of range along the $\theta = 330°$-transect using $\Delta r = 38\,\text{m}$. The figure reveals that the variation in environmental properties with range is rapid, especially between $r = 0\,\text{km}$ to $5\,\text{km}$ and $r = 30\,\text{km}$ to $45\,\text{km}$. And because the function `Seabed` (described in section 4.2.3) identifies the changes in sediment types with range by marching along the points in the transect range array, which are given by Δr, a smaller range step could potentially result in a even more rapid variation in the geoacoustic properties used in the simulations. Most likely, convergence was not achieved in the r-dimension because as the Δr-step was reduced in the convergence tests, it did cause a change in the geoacoustic properties. And because the water is shallow in the Hola valley, these differences affect the resulting transmission loss. Had the step-size been reduced even further, the solutions would most likely eventually have converged, when the change in Δr no longer caused variation in where the function `Seabed` located changes in the sediment type. However, before this was achieved, the variation in geoacoustic properties became too rapid and the assumption of a weakly range dependent environment broke down. Running the convergence test further than $\Delta r = 1\,\text{m}$ was therefore deemed futile. Effectively, this means that the variation in sediment types in the Hola valley, shown in its entirety in figure 3.6, are too rapid for RAM to produce stable results.

Although the convergence criterion was not satisfied, the solutions seemed to approach convergence for values of $\Delta r < 50\,\text{m}$. A range step of $\Delta r = 38\,\text{m}$ was chosen based on this, as a trade-off between accuracy and computational calculation time. The fact that a more convincing conclusion could not be reached is highly concerning. The lack of convergence undermines the validity of any result produced using the algorithms presented in this study. If the model tools and RAM are to be used in the development of an animal density estimation algorithm implemented at the LoVe Observatory, the lack of convergence in the r-dimension will have to be addressed first.

The conclusions from the convergence tests are remarkable, particularly given the wide-spread use of RAM as a tool for underwater acoustic modelling in the scientific community (White, 2015b). This begs the question, have other users neglected to perform convergence tests before using RAM, and thus not discovered this flaw, or is it the particular environmental conditions along the $\theta = 330°$-transect in the Hola Valley that makes it difficult for the model to converge? Considering the latter, it is plausible that the rapid variation with range in the sediment types mapped by Geological Survey of Norway (2016) combined with the shallow water in the valley makes the modelled domain somewhat unique. This type of environment is not commonly modelled by other users of RAM, which may explain why there does not appear to be any mention of convergence issues in literature. Moreover, it is interesting to compare the chosen step sizes with the step sizes used or recommended by other users of RAM, which were reviewed in section 4.4. The chosen value of Δz is comparable with the step size used by Collins (1989a)

and with the value recommended by Dushaw (2015). However, the chosen value of Δr is considerably smaller than the recommendations and usages found in literature. This is curious, and indicates either that the results of the convergence test are untrustworthy, or that there is something extraordinary about the modelled domain that causes the needed value of Δr to be small.

The convergence tests were performed along a test-transect at $\theta = 330°$, but convergence of results along other transects were not investigated. This is a flaw in the legitimacy of the convergence test results. One cannot be sure that the results simulated along the $\theta = 330°$-transect are representative for results simulated along other transects. Only one transect was included in the convergence test in this study due to time limitations. Performing the convergence test is a very lengthy process, because an individual `.in`-file needs to be produced for every change in the step-sizes. Although the production of the `.in`-files has been automatized by the `Write_in`-algorithm, running this function is slow, especially when R_{max} is large. If the developed model tools are to be used in further studies, inclusion of more transects in the convergence test should be included in order to ensure that the results of any new convergence tests are valid for the entire modelled domain.

6.3.2 Limitations of the RAM algorithm

The RAM algorithm is first of all limited by assumptions inherent in the parabolic equations the algorithm is based on. In the derivation of the parabolic wave equation discussed in Chapter 2, several assumptions are revealed. However, not all of these assumptions affect the validity of the results of RAM. For example, the derivation assumes that $k_0 r \gg 1$, meaning that the modelled sound field is in the far-field. When $c = 1480\,\text{m}$ for instance, this condition is satisfied when $r \ll 0.08\,\text{m}$. This is clearly not an issue for the interpretation of the results produced by RAM. RAM also assumes that back-scattered energy is negligible. This is of course not strictly true, but it is deemed an appropriate assumption since only sound reaching the observatory is of interest in this study. Moreover, as already discussed in Chapter 2, since RAM uses the split-step Padé approximation to solve the parabolic equation it is not limited by any small-angle approximation, which is the case in other solutions to the parabolic equation.

Having said that, some of the assumptions exposed in Chapter 2 are not as easily discounted. The first assumption that is made in the derivation of the parabolic equation is that the sound field has azimuthal symmetry. Any dependence on the angular position variable θ is thus ignored. This leads to two limitations: any refraction in the horizontal direction is neglected and the sound is taken to only travel in a single vertical plane along the transect. Horizontal refraction occurs when there is change in c_w with horizontal position, and is accounted for by a derivative with respect to θ in a full 3D-version of the parabolic equations. If c_w changes with longitude and latitude, the sound will be refracted in some horizontal direction. The full set of calculated SSPs show that c_w is dependent on longitude and latitude, and so neglecting this effect in RAM will introduce errors. Unfortunately, it is not possible to quantify how much this has affected the accuracy of the results, without performing a full 3D-modelling of the sound field for comparison.

However, according to Collins and Chin-Bing (1990), horizontal variation in the c_w with position create greater effects than the derivatives of c_w with respect to θ that account for refraction. Collins and Chin-Bing (1990) claims that no conclusive evidence exists to support that the θ-derivative term will significantly affect the results. It is therefore possible to speculate that a small spread in the values of c_w at any one depth indicates that there is little horizontal refraction in the Lofoten-Vesterålen basin. Figure 5.2 in deed shows that the spread in the values of c_w at any one depth is insignificant. At most the value of c_w changes by 0.95 % (which occurs during the winter season at $z = 692\,\mathrm{m}$) from the 25 % percentile to the 75 % percentile. Therefore, there is reason to believe that neglecting the $\frac{\partial}{\partial\theta}$-term in the parabolic equation has not introduced significant errors.

Another effect that is neglected when assuming azimuthal symmetry is sound that changes direction while propagating and ends up no longer propagating parallel to the modelled transect. This is known as out-of-plane sound propagation. Neglecting this is a much more concerning limitation to RAM, especially given the shape of the bathymetry around the LoVe Observatory. First of all, in reality sounds travelling into the Hola valley will in many cases be reflected off of the valley walls before reaching the observatory. This possibly means that the observatory is better equipped to detect sounds travelling at angles different from $\theta = 330°$ than the results presented in this study propose. Figure 6.2 shows an example where a sound ray travelling from the north west reaches the LoVe Observatory by reflecting off of the valley wall. The figure also shows that the sound source could reach the LoVe Observatory with a direct ray, but that this crosses the Egga bank. As discussed in section 5.4, travelling across the shallow banks significantly attenuates the signal, and it is therefore likely that the ray reflecting off of the valley wall is less attenuated than the direct ray once it reaches the LoVe Observatory. Many such propagation paths with single, or multiple reflections, exist. But, these paths are not included when RAM calculates the transmission loss, because the reflection causes the signal to travel out of plane.

Assuming azimuthal-symmetry also means that horizontal diffraction caused by the bathymetry is neglected. In real sound fields, when propagating sound encounters an obstacle, such as a sea mound, the sound will be 'bent' around the barrier. This effect is not accounted for in the RAM algorithm. This is especially concerning at the opening of the Hola valley. In reality sound will hit the downwards-sloping sides of the Egga and Vesterålen banks and diffract into the opening of the valley, like sound diffracting around the corner of a house. In RAM, however, this effect is disregarded, and sound that in reality would diffract horizontally is effectively lost from the model. If sound that is diffracted into the valley had been included in the algorithm, one might have seen that sounds originating in the basin outside the Egga and Vesterålen banks had been less attenuated than the levels of attenuation proposed by the presented RAM simulations. To quantify or include the effects of assuming azimuthal-symmetry, a full 3D parabolic equation must be used.

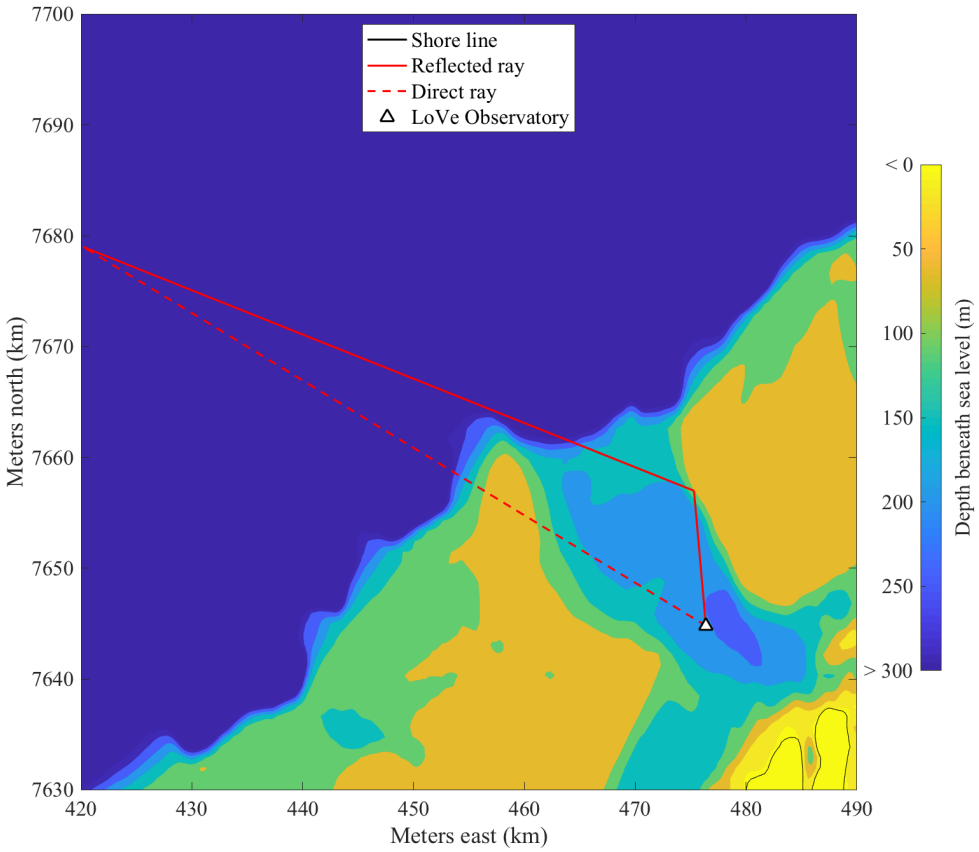

Figure 6.2: An example of how a sound ray can reach the LoVe Observatory by reflecting off of the valley wall.

The next assumption that is made in the derivation of the parabolic equation is that n and ρ are independent of r. The variation of these parameters with range are accounted for by 'marching' the solution out in range and updating the environmental parameters at Δr intervals, but, errors are introduced if the variation of n and ρ with r are too great. In the real ocean, n and ρ are of course continuously varying with range. Modelling their variation at discrete intervals therefore undermines the validity of the RAM results. To determine if the parameters are slowly varying, one must look at the values used in the RAM simulations. The refractive index n is equal to $\frac{c_0}{c}$. As discussed above, the potential change in c_w with r is small because of the small spread in values of c_w at any one depth in the calculated SSPs. The potential change in n is therefore also small,

which means that n in the water can be said to be slowly varying with range. In the case of c_b there is greater variation in the calculated values. The maximum potential change of c_w can be found by comparing the sediment types with the highest and the lowest velocity ratio, namely '*Sandy gravel*' and '*Mud*', respectively. When a transect traverses a change between these sediment types, the percentage change in c_b is 45 %. This is cause for concern. As explained in section 6.3.1, the lack of convergence in the r-dimension is likely caused by rapid changes in the environmental properties of the seabed which causes the modelled environment to no longer be weakly range dependent. This will likely also have introduced errors in the modelled transmission loss, especially in the shallow regions of the Lofoten-Vesterålen basin. Lastly, the density of sea water is taken to be a constant by RAM (Collins, 2001). This is an appropriate assumption, since the change of ρ_w with hydrostatic pressure is small (Duxbury et al., 2018). The density of sea water does vary with temperature and salinity, and will as such vary with r. But, the small spread in the values of c_w discussed above also implies little spread in the values of T and S, since the SSPs are calculated from CTD measurements. It is therefore likely that the variation of ρ_w with r in the seawater around the LoVe Observatory is negligible, and that the assumption of constant density does not introduce significant errors. In summary, of the measured and calculated environmental properties only the rapid variation in sediment types has likely introduced errors in the simulated transmission loss by due the assumption that ρ and n are independent of r.

The validity of the presented results are also limited by shortcomings of the RAM algorithm. Particularly three acoustic phenomena that occur in real sound fields have been omitted from the algorithm, even though excluding them is not dictated by the assumptions of the parabolic equation. These omissions include both scattering, layered ocean floors, and elastic materials in the ocean floor. Firstly, RAM does not include models of scattering. In real sound fields scattering occurs when sound incident on a rough surface is reflected in any direction other than the specular direction, and in real oceans, this occurs both at the air-water interface and the sea bottom (Medwin and Clay, 1998). This leads to out-of-plane reflections, that were discussed above. The intensity of the scattered sound is proportional to the ratio of the vertical scale of the scattering geometry to the wavelength of the incident sound (Urick, 1983). The wave length of a 20 Hz sound at $c_w = 1480\,\mathrm{m\,s^{-1}}$ is 74 m. The vertical scale of a rough surface can be quantified by the Rayleigh parameter, $\mathcal{R}$, which is given by

$$\mathcal{R} = kH \sin\theta_i. \tag{6.1}$$

Here, H is the root-mean-square of the height of the roughness (Urick, 1983). When $\mathcal{R} \gg 1$, there is considerable scattering at a wide interval of angles relative to the incident sound, while when $\mathcal{R} \ll 1$, the scattered sound energy is negligible (Brekhovskikh and Lysanow, 1991). The effects of scattering are therefore most prominent when the vertical scale of the roughness of the boundary are large in comparison with the wavelength of the incident sound. Small geometrical variations such as roughness in the bathymetry will therefore not cause considerable scattering of the Fin whale calls. But any roughness or variation in the bathymetry or sea surface that is larger than the wavelength will cause scattering.

To accurately represent the sound field, the reflections caused by scattering must be included in the algorithm, using a full 3D model. However, more limited Nx2D models often incorporate the effects of scattering in the pressure reflection coefficient. The models thus account for sound energy that is scattered out of the modelled plane by reducing R so that the scattered sound is effectively attenuated at the reflection (Urick, 1983). This could have been included in RAM, without having to incorporate θ dependence. However, RAM takes the pressure reflection coefficient of the sea-surface to be $R = -1$, meaning that the boundary is perfectly reflecting (Collins, 1989a). This might seem unrealistic, since roughness is bound to be present at the sea surface due to ocean waves. However, the low frequency of the modelled sound can be shown to validate the assumption. Scattering at the ocean surface consists of scattering from air-bubbles in the water and scattering due to the ocean waves. According to Rosenberg (1999), scattering from air bubbles is insignificant when $f < 1\,\mathrm{kHz}$, and this effects thus does not need to be accounted for in the present model. Moreover, the ocean waves will have to be high (scaled to the wavelength of the sound) to cause significant scattering (Brekhovskikh and Lysanow, 1991). The height of the ocean waves depend partly on the wind speed, and Schulkin and Shaffer (1964) has estimated H from the wind speed, V, as

$$H = 7.9248 \times 10^{-4}(1.94384449\,V)^{\frac{5}{2}} \tag{6.2}$$

Looking for example at the highest and the lowest wind speeds at the LoVe Observatory calculated by Ødegaard (2015), the same wind-states that were used to define the thresholds for transmission loss in section 2.1.2, the rms wave heights of the ocean surface becomes

$$H = 0.0651\,\mathrm{m} \text{ at } \mathrm{V} = 3\,\mathrm{m\,s^{-1}} \tag{6.3}$$

$$H = 5.7388\,\mathrm{m} \text{ at } \mathrm{V} = 18\,\mathrm{m\,s^{-1}} \tag{6.4}$$

Using equation 6.1, this makes the maximum value of $\mathcal{R} = 0.0055$ at $V = 3\,\mathrm{m\,s^{-1}}$ and $\mathcal{R} = 0.4808$ at $V = 18\,\mathrm{m\,s^{-1}}$. Since both Rayleigh parameters are considerably smaller than 1, these examples indicate that scattering from the sea surface can be neglected when the frequency is $f = 20\,\mathrm{Hz}$. This is supported by the findings of Addlington (1963), who found a median 0 dB reflection loss due to scattering at the ocean surface of a 530 Hz incident sound wave. RAM's assumption that $R = -1$ at the sea surface is therefore valid. Still, if the transmission loss of more high-frequent mammals are to be modelled in the future, scattering must be considered.

Scattering also occurs at the ocean floor, and this process is slightly more complex. Scattering at a water-sediment interface consists of two main processes: interface scattering from roughness and volume scattering from within the sediment (Jackson and Briggs, 1992). Interface scattering is the same effect as that which occurs at the ocean surface; the reflected sound is spread in several directions due to roughness at the border. On the other hand, volume scattering occurs when inhomogeneities in the sediment cause sound to be reflected (Jackson and Briggs, 1992). In RAM, the sediment is modelled as a single, homogeneous material. However, most naturally occurring sediments consist of a

heterogeneous mixture of differently sized particles. And, natural sediments also contain both gas and organic content such as by-products of plants or algae (Ballard and Lee, 2017). All of these inhomogeneities contribute to volume spreading of the incident sound. Having said this, most such inhomogeneities are small compared with the wavelength of a 20 Hz incident sound wave. As with reflection off of the ocean surface, scattering off of the ocean floor is not significant if the wavelength of the incident sound is large compared with the scale of the scatterer. This applies both to volume scattering and interface scattering. This is likely why Isakson et al. (2012) found that adding scattering to a model of low frequency reflection off of a sedimentary ocean bottom only added 1 dB to the reflection loss. It therefore seems likely that the effects of scattering can justly be neglected in the transmission loss simulations, if the scale of the roughness and sediment inhomogeneities are smaller than the wavelength of the incident sound wave. This is likely the case for most of the sediment types in the Lofoten-Vesterålen basin. However, a few of the consolidated sediment types, such as '*Mud alternating with blocks of hard sediment*' and '*Gravel, cobbles and boulders*' will include objects that are large enough to cause scattering even of the low frequency sound. This is especially concerning when simulating the transmission loss across the Vesterålen and Egga banks, which are to a large extent covered with '*Gravel, cobbles and boulders*'. According to Collins and Chin-Bing (1990), when the effects of scattering are significant, it contributes to several decibels of transmission loss. It is therefore likely that the transmission loss values predicted in this thesis for the propagation across the Vesterålen and Egga banks are underestimated.

Another phenomena that is neglected in the RAM model is reflections from layers within the sediment. Ocean bottoms are typically made up of a number of distinct layers containing materials of different properties (Urick, 1983). RAM does allow variation with z of the geoacoustic properties in the sea floor, but it is not possible to model separate distinguishable layers because the geoacoustic properties are interpolated between the in-putted values so that the variation in both c_b, α_b, and ρ_b with z are smooth (Collins, 2001). This means that the model does not include any reflections within the sediment. In reality, sound propagating into the seabed will potentially reflect off of boundaries between different materials. Not including a layered sea bottom is especially concerning when the modelled sound is low frequent, since attenuation in sediments are proportional to the frequency (Hamilton and Bachman, 1982). This means that the sound can propagate far into the sediment and experience a number of reflections, before being fully attenuated. Reflections in the sediment will potentially direct the sound back towards the water, and in some cases the sound can be transmitted back into the water. Thus, the fact that RAM does not allow for layered materials in the sea floor might have caused the transmission loss values simulated in this thesis to be overestimated.

Lastly, RAM also neglects elastic effects in the sea bottom materials. RAM assumes that the sea bottom is a fluid (Collins, 1989a), which means that the material only supports a compressional wave, and not a shear wave (Jensen et al., 2011). For most sediment types, this is a valid assumption, because of the materials' low rigidities (Jensen et al., 2011). However, for the consolidated sediment types included in the RAM models in this thesis, the fluid approximation falls short. In these sediment types, it is likely that some of the sound energy incident on the sea floor will be converted to a shear

wave (Jackson and Richardson, 2007). Hughes et al. (1990) modelled the transmission loss across three types of single layered sediment materials: sand, chalk, and solid-rock, using a full wave model which took the sediments to be fluids. They also measured the transmission loss across patches of corresponding sediment types in shallow water at the Scotian continental shelf. Hughes et al. (1990) found that the modelled transmission loss matched the experimental results for both sand and chalk, but that for the solid-rock sediment the values differed by as much as 60 dB. They attributed this difference to the excitation of shear waves in the real sediment, which were not included in the model. If this effect also occurs in the consolidated sediment types in the Lofoten-Vesterålen basin, the transmission loss values simulated by RAM are highly inaccurate. This is especially concerning for the simulated transmission loss across the Vesterålen and Egga banks, which are covered by the consolidated sediment types '*Gravel, cobbles and boulders*' and '*Thin or discontinuous sediment cover on bedrock*'. Exclusion of elastic properties in the sea floor has thus caused the simulated transmission loss experienced by sound propagating across consolidated sediment types to be overestimated.

6.3.3 Limitations of the environmental input parameters

The validity of the presented results are also limited by the accuracy and availability of the input parameters. The methods used to calculate these parameters have already been discussed in section 6.2, and the limitations uncovered there will undermine the validity of the results presented in this study. Further to this, here, the limitations introduced by the sources of the environmental input parameters are considered. The bathymetric data were gathered from three sources, with differing resolution. As shown in figure 3.1, the innermost part of the continental shelf has a resolution of 50 m x 50 m, the outermost part of the continental shelf has a resolution of 5 m x 5 m, and the rest of the Lofoten-Vesterålen basin has a resolution of approximately 929 meters North and 325 meters East. The latter of the three has an especially coarse resolution. This is, however, acceptable, since the area mapped with this resolution is quite flat and deep. Since the sound in the Lofoten-basin has been shown to be propagated by the SOFAR-channel, lack of fine resolution of the bathymetry in this region is likely not to introduce great errors in the simulated transmission loss. What is more concerning is the resolution on the continental shelf. In this region, the sound will interact with the sea floor a lot, due to the shallow water. Both the 50 m-resolution and the 5 m-resolution is smaller than the wavelength, and it is therefore easy to jump to the conclusion that a finer resolution would not have affected the transmission loss. However, a finer resolution would potentially have uncovered more fine scale roughness in the ocean bottom. Isakson and Chotiros (2012) found that the rms bottom roughness as small as 1 - 6 % of the wavelength of the incident sound has a significant effect on the reflection loss. This is because the bottom roughness affects the local incident angle, and as shown in equation 2.17, the pressure reflection coefficient is dependent on the incident angle. Isakson and Chotiros (2012) found that for large incident angles, the reflection loss off of a rough ocean bottom can be as much as 25 dB higher than reflection loss off of a smooth ocean bottom. The accuracy of the transmission loss presented in this thesis is therefore limited by the resolution of the

bathymetry.

The SSPs used in the model are calculated from CTD measurements downloaded from International Council for the Exploration of the Sea (2018). The data had been collected by various researchers across a 21 year period. This is quite a long time frame, and as such one can presume that the SSPs calculated for each season are representative for the sound speed in the area during each season, also for seasons to come. But, variation of the SSP within each season does of course exist, and this effect is not treated here. Moreover, one must be aware that the last CTD measurement was made in 2016, already two years ago, and that long-term climate changes can affect the sound speed in the Lofoten-Vesterålen basin in the future. This would in turn affect the credibility of the simulated transmission loss presented here. One should also note that sound speed is known to vary on a diurnal basis (DeSanto, 1979). This means that the transmission loss experienced by Fin whale calls also varies throughout the day. More detailed measurements of how SSP varies with time, both on a monthly and a diurnal scale are therefore recommended if the LoVe Observatory is to be used for animal density estimation.

The sediment types used to predict the geoacoustic properties of the ocean floor have been downloaded from Geological Survey of Norway (2016). As previously explained, these data characterize the mean sediment type in the top 50 cm of the sea floor. The sediment data is limited by two aspects: the extent of the mapped area and the fact that the downloaded data do not contain any information about the variation of the geoacoustic properties with depth. As shown in figure 5.21, the area mapped by Geological Survey of Norway (2016) is considerably smaller than the area of interest when investigating the transmission loss experienced by sound sources at positions around the LoVe Observatory. In the areas beyond the continental shelf, this limitation can be overcome by assuming that the sea floor consists mainly of '*Abyssal mud*'. However, on top of the shallow banks, this assumption is not valid. The fact that Geological Survey of Norway (2016) (nor other sources, to the author's knowledge) has mapped the sediment composition beyond the area shown in figure 3.6 therefore imposes a severe restriction on which transects it has been possible to investigate in this study. The other limitation of the downloaded data is the lack of variability with depth. Compression due to increasing pressure with depth typically cause the sound velocity in natural sediments to increase with depth (Urick, 1983). RAM allows for the geoacoustic properties of the sea bottom to be varied with depth, but, since a sediment type average over the top 50 cm of the material is the only available information it has not been possible to include variation with z in the current model. The simulations run in this thesis have therefore taken the sea floor to be a single layer of homogeneous material. Had the variation of c_b with z been included, it would have caused an upwards refraction of the sound in the sediment (Urick, 1983). This could have led to sound being returned to the water, and thus affected the simulated transmission loss. Thus, if more information about the change in sediment material with depth had been available and included in the model, the simulated transmission loss would have been lower than the values predicted in this thesis.

Chapter 7

Conclusion

Equinor is planning to establish Norway's first ever whale monitoring facility using acoustic density estimation at their cabled ocean observatory in the Hola valley. This will give the company more accurate and time-dependent density estimations of the whales in the Lofoten-Vesterålen basin. This information will be crucial in assessing the impact of human interference in the whale habitats if, for example, the Lofoten-Vesterålen basin is to be opened up for petroleum exploration. In order to implement the density estimation algorithm, the transmission loss of the whale calls reaching the observatory need to be known. This has never before been calculated or otherwise characterized. Therefore, this study has set out to develop a novel model of how the transmission loss varies with position and season around the observatory. This was achieved by developing a set of model tools that produce the environmental parameters needed to calculate transmission loss using the established parabolic equation model RAM. These tools were then used to investigate the transmission loss experienced specifically by Fin whale calls reaching the LoVe Observatory. The investigation involved using the developed model tools to produce the necessary input parameters, then using RAM to calculate the transmission loss as a function of range and depth for a number of selected example transects.

The preparation of the model tools involved generating three environmental parameter sets: the bathymetry, sound speed profiles, and geoacoustic properties of the seabed. Firstly, the bathymetric data were provided by Kartverket (2018a), Kartverket (2018b) and British Oceanographic Data Centre (2018). These data sets were combined to produce an interpolant that can be evaluated at any position in the Lofoten-Vesterålen basin, giving the depth of the sea floor. Secondly, the sound speed profiles were calculated from measurements of CTD data provided by International Council for the Exploration of the Sea (2018). From this, the model tools can construct the SSPs at any position in the Lofoten-Vesterålen basin using interpolation. Lastly, the geoacoustic properties of the seabed were calculated from the estimated grain size, or gathered from literature. A novel technique was constructed to estimate the grain size from the qualitative descriptions of the seabed composition downloaded from Geological Survey of Norway (2016). Reviewing the input variables used to construct the environmental parameters showed that each parameter carries some inaccuracy which will contribute to the uncertainty of

the simulated transmission loss. The resolution of the bathymetric data causes uncertainty in the transmission loss. Moreover, the age of the CTD measurements opens for the possibility that the current sound speed profiles might have changed or will change with time, compared with the SSPs calculated from the CTD measurements. This means that the validity of the transmission loss values simulated using the model tools is questionable. Lastly, lack of information on the variation of the geoacoustic properties in the seabed with depth in the data downloaded from Geological Survey of Norway (2016) means that this variation could not be included in the model. This will most likely have caused overestimation of the simulated transmission loss. Furthermore, the methods used to construct the model tools were reviewed, and comparison of the estimated grain sizes with corresponding values produced by the HFEVA model suggested that the grain sizes (in mm) have been overestimated. This has likely lead to errors in several of the geoacoustic properties. Ultimately, this shortcoming of the model tools will lead to an underestimation of the simulated transmission loss.

After the model tools were developed, they were employed to investigate the transmission loss experienced by Fin whale calls reaching the LoVe Observatory. Firstly, this was studied by simulating the transmission loss along the $\theta = 330°$-transect. This revealed that the variation of transmission loss with range and depth is complex. No clearly distinguishable regions of the basin had transmission loss values higher than the estimated maximum allowable transmission loss threshold in low noise conditions, $\mathrm{TL}_{\text{max, low noise}}$, meaning that the simulation results suggest that the entire investigated modelled domain is detectable in low noise conditions. It is therefore difficult to conclude on the maximum detection range of the LoVe Observatory without further studies of the transmission loss at ranges greater than 190 km. Comparison with the commonly used simplistic 'semi-spherical' transmission loss model revealed significant discrepancies. This suggests that the effects of the environmental parameters on the transmission loss are considerable, and that a complex model such as the parabolic equation used in RAM need to be employed to simulate the transmission loss in complex environments such as the Lofoten-Vesterålen basin.

The simulated transmission loss along the 330°-transect did reveal a few interesting aspects of the propagation of the sound reaching the LoVe Observatory. Firstly, a pattern of repeating convergence zones was recognized and attributed to SOFAR-propagation. Interestingly, the simulations revealed that sound propagated by the SOFAR channel couples with the wave guide made by the shallow bathymetry in the Hola valley. It seems like the detection capabilities of the LoVe Observatory are therefore able to benefit greatly from the low attenuation of SOFAR-propagation. Even so, keeping in mind that research by Watkins et al. (1987) have suggested that Fin whales vocalize around 50 m from the sea surface, the deep water detection capabilities of the LoVe Observatory are not needed for Fin whale animal density estimation. Only the first convergence zone has transmission loss lower than the transmission loss threshold in high noise conditions, $\mathrm{TL}_{\text{max, high noise}}$, at $z = 50\,\mathrm{m}$, and the depth at which the transmission loss is lower than this limit increases for the subsequent convergence zones. Moreover, somewhat surprisingly, the simulations suggest that sound propagated by the surface duct is not transmitted into the Hola valley. The observatory might not be fit to detect Fin whales

vocalizing at shallow depths and great ranges when the noise conditions are severe.

The transmission loss was also simulated for transects of varying angular direction. In general, these simulations revealed that the observatory is capable of detecting Fin whale calls originating on top of the Egga and Vesterålen banks in both low and high noise conditions. This indicates that the observatory is not hindered by lack of direct and straight propagation paths between the sound source and the receiver. However, it has also been shown that the presence of the shallow banks causes an angular limitation in the detectable volume in the Lofoten basin. The volume where propagation by the SOFAR channel causes the presence of convergence zones is likely limited to transect at approximately $\theta = 300°$ to $\theta = 340°$.

All of the presented examples of simulated transmission loss were calculated for each of the four seasons to investigate the effect of seasonality. In general, the effect of different seasons seemed to be most pronounced when the water was deep. Little observable differences were observed both for transmission loss simulated across the Egga and Vesterålen banks, as well as in the Hola valley. On the other hand, in the deep Lofoten basin, the cyclical behaviour of the convergence zones apparent in the simulations along the $\theta = 330°$-transect differed between the season. The contrast was most pronounced in the winter season, where the convergence zone pattern was not distinguishable and the depths where the transmission loss chiefly was lower than $\mathrm{TL}_{\mathrm{max,\ high\ noise}}$ was deeper than in the other seasons. This suggests that the LoVe Observatory is less capable of detecting Fin whales vocalizing at shallow depths in the winter season. Curiously, this does not explain why Fin whales are generally not detected by the observatory between March and August. Since the simulated transmission loss examples have not offered an explanation of this gap, it is reasonable to hypothesise that the lack of detections in March to August is rather caused by Fin whale migration.

To examine the validity and accuracy of the results produced by the model tools and the RAM simulations, the study has reviewed the assumptions inherent in RAM, the shortcomings of RAM, and the limitations caused by the input-data. RAM assumes that the solution lies in the far-field, that back-scattered energy can be neglected, and that the derivative with respect to θ can be neglected. All of these assumptions were deemed negligible, thus not significantly affecting the accuracy or validity of the simulation results. RAM also neglects any sound that travels out of the modelled plane, which eliminates both out-of-plane reflections and horizontal diffraction due to the bathymetry. This is a harsh simplification of how sound in reality behaves in a 3D environment, and this likely results in substantial inaccuracies in the results, particularly since the observatory lies in a valley. Excluding sound reaching the observatory by reflecting off of the valley walls from the model will have depreciated the observatory's ability to detect whale calls that do not propagate straight into the valley. Moreover, all of the identified shortcomings in RAM contribute to inaccuracy in the results. Firstly, scattering is neglected, which leads to significant errors when the roughness of the sea floor is great, which is likely the case for the consolidated sediment types which are found on top of the two shallow banks. RAM has also not included elastic effects in the sediment material. This is again concerning for the consolidated sediment types covering the two shallow banks. Neglecting scattering and shear waves here can potentially lead to an overestimation of

several dB in the simulated transmission loss. The results simulated across the Egga and Vesterålen banks are therefore less reliable than the simulations across areas dominated by unconsolidated sediment types. Lastly, RAM does not include reflections from within the sediment, which again causes an overestimation of the resulting transmission loss values. Furthermore, the accuracy of the simulated transmission loss is limited by all of the input data. The bathymetry causes errors due to its resolution. And the seabed data does not include variation of the geoacoustic parameters with depth, which causes the simulated transmission loss to be too large. Lastly, the age of the CTD-measurements used to calculate the SSPs make the resulting transmission loss unreliable if the current SSPs have changed since the measurements. This is especially problematic if the results are to be used in the future.

Yet, the main limitation to the validity of the simulated transmission loss is the fact that it was not possible to show that the solutions converged sufficiently as the step-sizes were decreased. A convergence test along the $\theta = 330°$-transect was performed for both Δr and Δz. For the latter, the solutions appeared to stabilize around $\Delta z = 0.2\,\mathrm{m}$, but an unexplained alternating behaviour in the results introduced an uncertainty of approximately $\pm 2\,\mathrm{dB}$ to the simulation results. When testing Δr, the solutions did not converge even as Δr was reduced to values much lower than those conventionally used by other users of RAM. Lack of convergence in the r-dimension has been associated with the assumption that n and ρ are weakly range dependent. This assumption has been shown to be appropriate for the environmental properties of the sea water. However, the change in environmental properties of the seabed have been shown to be rapid, thus causing the environment to no longer be weakly range dependent. Subsequently, it was not possible to identify an appropriate value for the range step Δr. Without converged solutions, the choices of Δr and Δz will have affected the simulation results. This makes the resulting transmission loss values somewhat untrustworthy. If the model tools presented in this study are going to be used for further studies, this issue will need to be resolved to make the results more reliable.

Generally, the simulations have indicated that the LoVe Observatory is suited for acoustic density estimation of Fin whales in the Lofoten-Vesterålen basin, given that the presented limitations are taken into account. Seasonal variability of the transmission loss is observed, but all seasons seem to be viable for density estimation. SOFAR-propagation enables the observatory to monitor considerable ranges as well as depth. The observatory does appear to be somewhat hindered by the walls of the valley obscuring the potential angular reach of the observable area. The examples of simulated transmission loss explored in this study have been limited to a few transects, due to the difficulty of portraying results from a 3D domain. Therefore, not every facet of the transmission loss variation with position has been inspected, and some potentially important aspects might have been missed. Fortunately, the developed model tools will facilitate future investigation of the transmission loss in the basin.

7.1 Future work

To continue the work towards developing mammal density estimation algorithms at the LoVe Observatory, it is recommended that some of the uncovered limitations in this thesis are investigated and improved. First of all, the lack of converged solutions in the tests of Δr and Δz need to be resolved. It is recommended that more thorough convergence tests are performed along varied transects, in order to, hopefully, pin point the problems in the convergence tests of the performed in this thesis. Moreover, it is necessary to reconsider how variation in geoacoustic properties of the seabed are incorporated in the model, in order to avoid violating the assumption of weak range dependence inherent in the parabolic equation. It might be worthwhile to take some averages of the properties with range, so that the variation is not as rapid. This could, hopefully, resolve the lack of convergence in the r-dimension. Having said this, neglecting to incorporate the true variation of sediment properties with range in the model will, of course, make the resulting transmission loss less accurate. Furthermore, the fact that an apparent bug in RAM prevented simulation to ranges greater than 190 km needs to be addressed. The issue can potentially be resolved by closer inspection of the Fortran code of RAM (by a competent computer scientist). The transmission loss along the $\theta = 330°$ transect showed that the maximum detection range of the observatory in low noise conditions was not reached within 190 km, and simulations to greater ranges are therefore needed.

It is also suggested that the effects of the discussed limitations in RAM are examined. This will help determine if the assumptions and shortcomings of the model will significantly affect the simulation results. It is for example recommended that a full 3D model is used to look at the effects of neglecting horizontal diffraction from the valley opening and horizontal reflections from the valley walls. Although full 3D models have long been considered too computationally heavy, recent work by authors such as Ying-Tsong et al. (2012), Collis (2011), and Strum (2001) indicate that split-step Padé solutions to the parabolic equation can be implemented without having to assume azimuthal symmetry. It is also possible to validate the results produced by RAM by simulating the transmission loss using a different acoustic model, such as for example ray tracing using Bellhop (Porter and Bucker, 1987). The effect of scattering from rough sediment types should also be treated, for example by adding a random component to the boundary as explained in Tappert and Nghien-Phu (1986) or using the more comprehensive expansion of RAM by Rosenberg (1999) to quantify the effect of forward scattering. Lastly, an elastic parabolic wave equation, described for instance by Collins (1989b) should be tried, to quantify the effects of shear waves in the consolidated sediment types.

Some improvements should also be made to the input data used in the model tools, in order to improve the accuracy of the simulation results. This could be achieved by collecting bathymetric data of finer resolution than 5 m by 5 m on the continental shelf around the Hola valley. Moreover, it is recommended that information about the sediment variation with depth is collected so that a layered sea floor can be included in the model. Importantly, sediment composition mapping should be performed in a larger area around the observatory so that all transects of interests are covered. Lastly, it is suggested that more CTD data is collected at depth, especially in the winter season. This

will hopefully mitigate the issue of jump-like artefacts in the constructed SSPs. If the issue is not resolved by adding more deep data and removing the shallow SSPs, further investigation of the source of the artefacts will need to be performed. Moreover, since the sediment grain sizes calculated in this study differed from those produced by the HFEVA model, it is recommended that method used to calculate the sediment sizes is reviewed. It is possible to redo the simulations using sediment grain sizes produced by HFEVA in order to quantify the effect of having overestimated the grain sizes.

Several steps can also be taken to improve the interpretation of the simulation results. The transmission loss thresholds defined in this thesis are calculated based on assumptions about the technical equipment at the LoVe Observatory and the planned implementation of the density estimation algorithm, such as the directivity of the hydrophone, the desired frequency bandwidth of the animal density estimation algorithm, and the signal-to-noise ratio needed for detection. For a more precise analysis of the transmission loss in the basin, these assumptions should be reviewed. The thresholds are also based on measurements of noise at the observatory by Ødegaard (2015). Using these measurements to define a high and a low noise state has given a crude estimation of the limits of the capabilities of the observatory, but when the animal density estimation is performed, the present noise state needs to be taken into account. The noise level is dependent on a number of factors, including seasonal weather. It would therefore be beneficial to include the variation in noise level with season in the interpretation of the variation of transmission loss with season. When the animal density estimation algorithm is in operation, it might also be important to consider that both noise and SSP varies on a smaller time scale than that considered in this thesis. It might therefore be beneficial to adjust the model tools to allow for investigation of the variation in transmission loss as function of months, weeks, or even on a diurnal scale.

As previously mentioned, the model tools can be used to conduct further studies of aspects of the transmission loss variation not treated here. The tools can for instance be used to simulate transmission loss at other frequencies than 20 Hz. It might, for example, be interesting to investigate the transmission loss experienced by calls from the four other baleen whales native to the Norwegian sea, to review the possibility of extending the animal density estimation to other species. It is also desirable to use the tools to simulate the transmission loss variation as a function of frequency. This will enable calculation of the probability of detection $\hat{P}$, the maximum detection range, w, and detection area O, following the method by Helble et al. (2013). This is an essential step in developing the animal density estimation algorithm. If this is achieved, the LoVe Observatory has the potential of becoming Norway's first acoustic animal density estimation station. The data collected by the observatory over time will hopefully contribute to aid further understanding of whale habitats and migration routes, as well as the impact of human activities on the species.

Appendix A

Tables

PSC	Norwegian characterization	English translation
1	Tynt eller usammenhengende sediment dekke over berg	Thin or discontuous sediment cover on bedrock. Sediment with varying grain size.
20	Slam	Mud
21	Slam med blokker av sedimenter	Mud alternating with blocks of hard sediment
40	Sandholding slam	Sandy mud
100	Sand	Sand
115	Grusholding slam	Gravelly sandy mud
120	Grusholdig slamholding sand	Gravelly muddy sand
130	Grusholdig slam	Gravelly sand
150	Slamholding sandholdig grus	Muddy sandy gravel
160	Sandholdig grus	Sandy gravel
175	Grus, stein og blokk	Gravel, cobbles and boulders
300	Harde sedimenter eller sedimentære bergarter	Compact sediments or sedimentary bedrock

Table A.1: The english translation of the norwegian nomenclature used by Geological Survey of Norway (2016), with the corresponding product specification code (PSC) in accordance with Mareano (2018).

Appendix B

Graphs

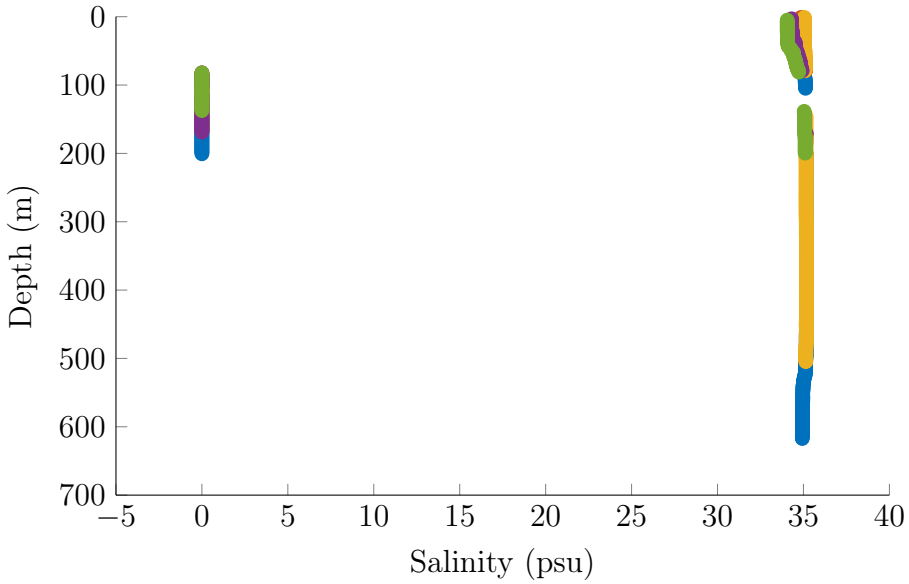

Figure B.2: The salinity variation with depth of the measurement sets which appear to have an unexpected variation of c with z in figure B.1b. Each discrete measurement is plotted as a marker, not joint to the next marker. Each color indicates a separate measurement set.

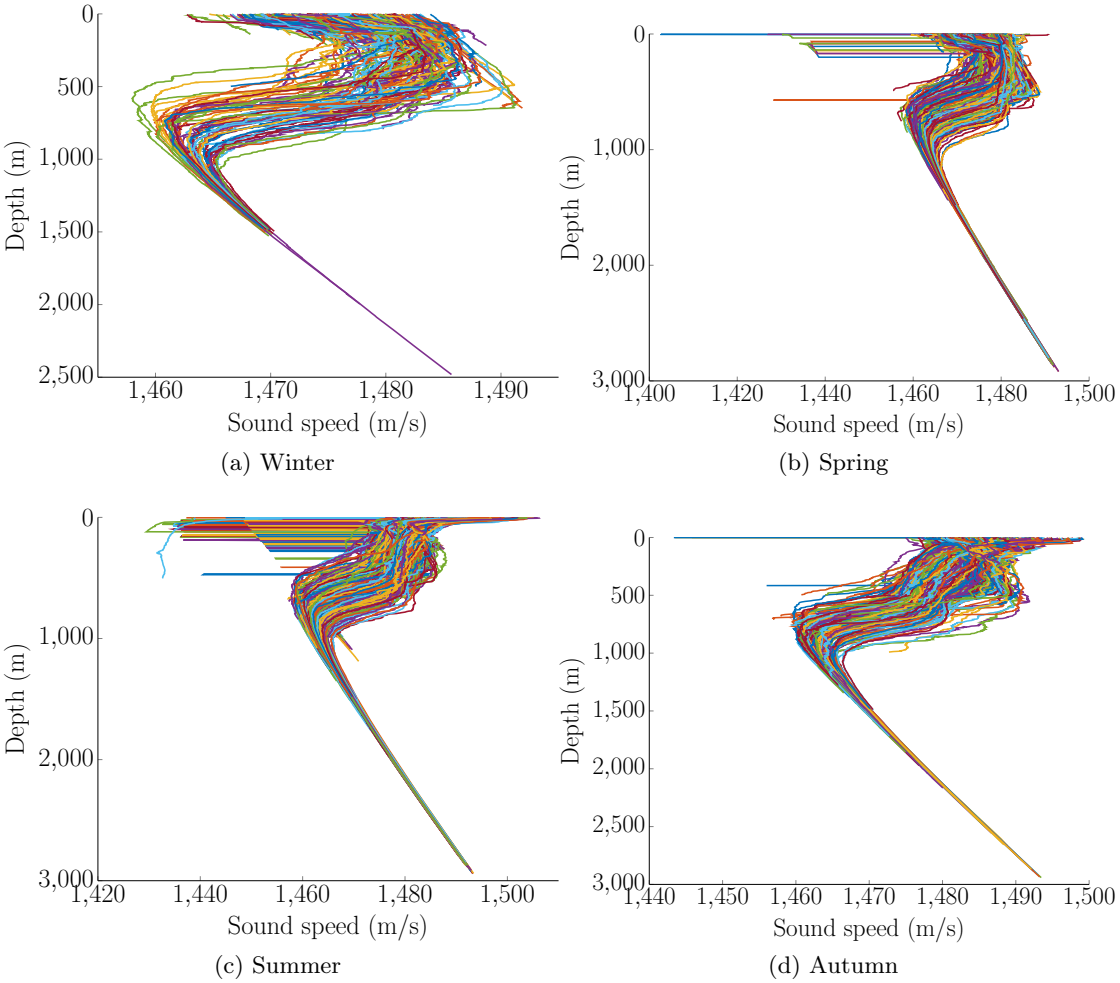

(a) Winter

(b) Spring

(c) Summer

(d) Autumn

Figure B.1: The sound speed profiles calculated from CTD measurements downloaded from ICES, divided into seasons based on their date of measurement. The plots show artefacts caused by intstrument errors reading $T = 0°$ or $S = 0$.

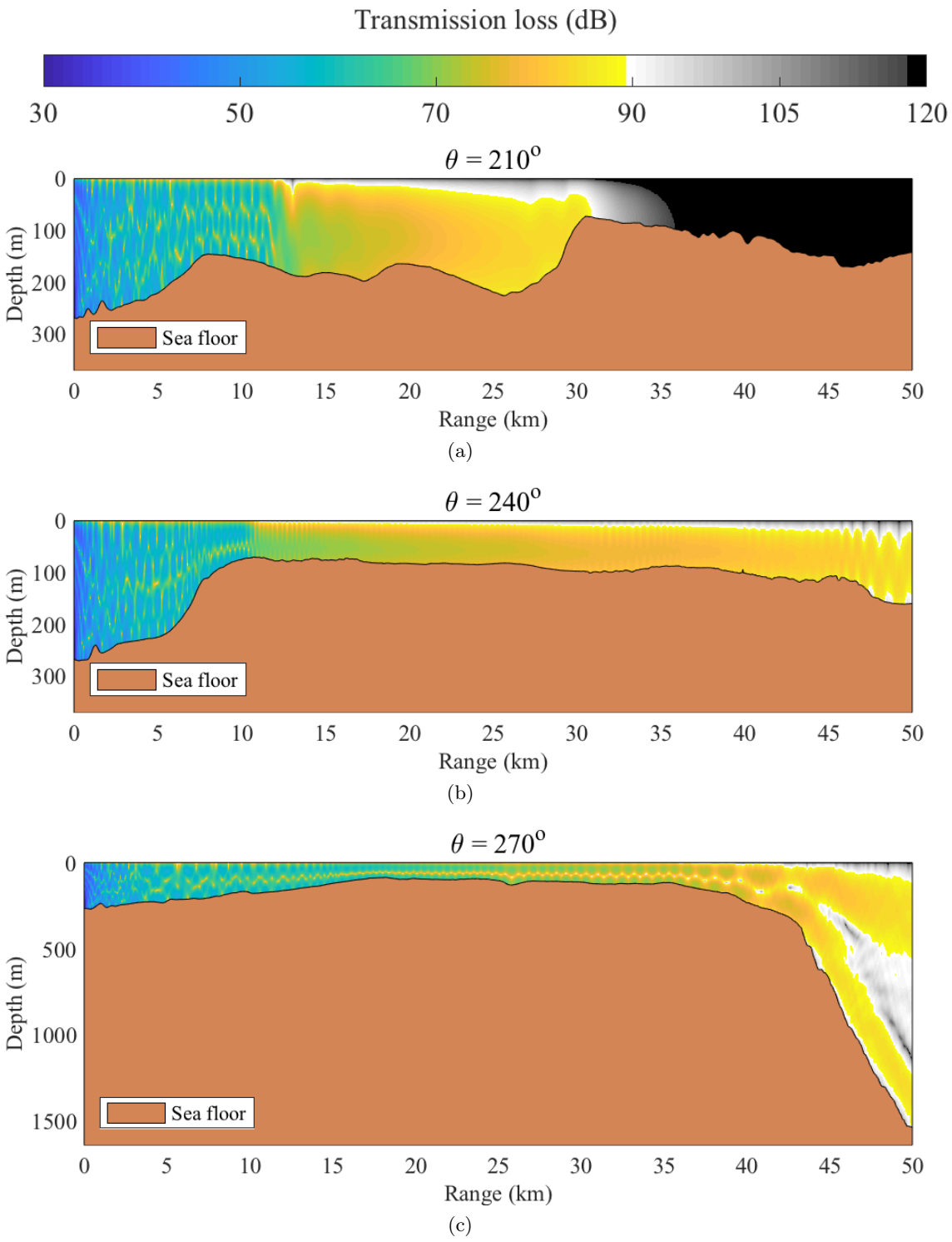

Figure B.3: The transmission loss at varying angles, during the spring season.

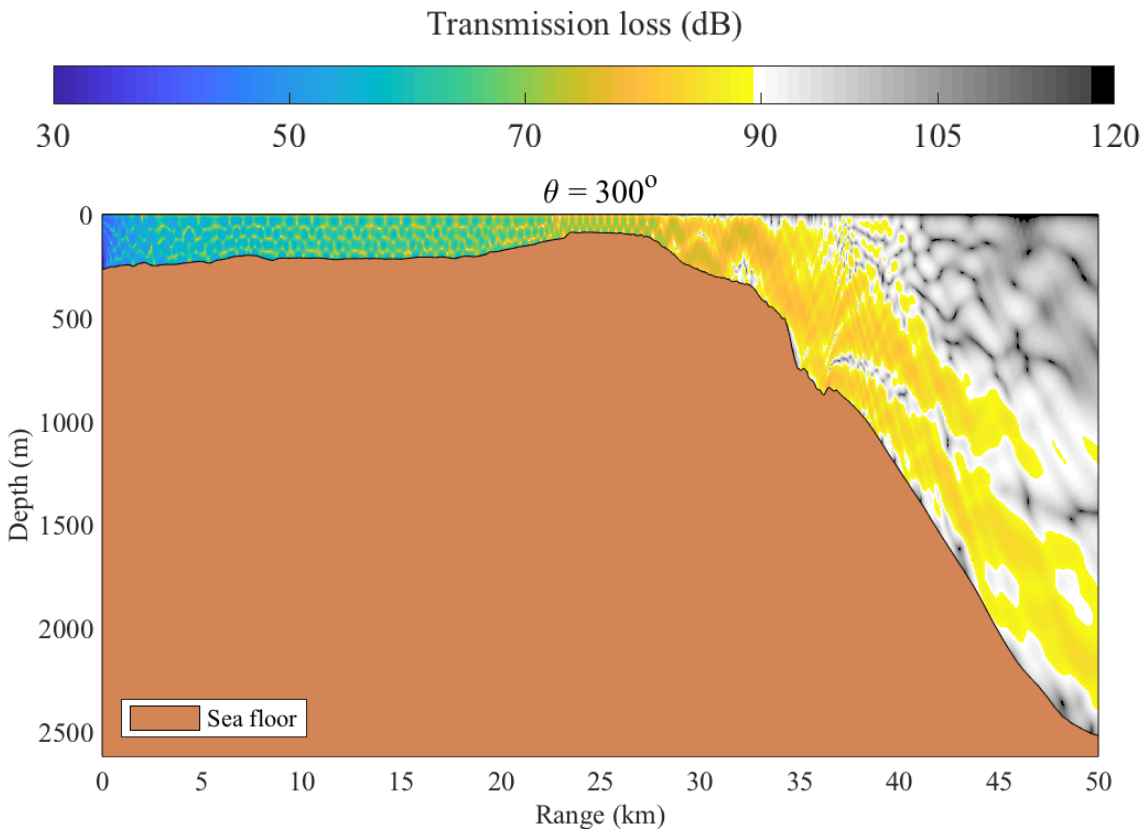

(d)

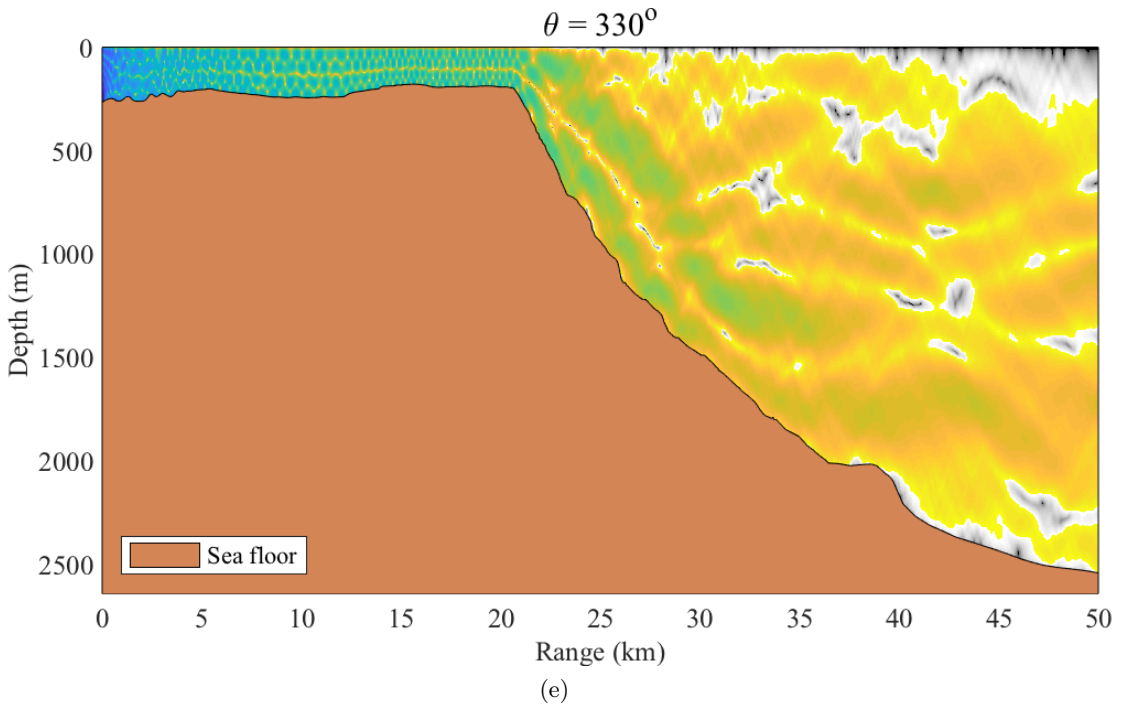

(e)

Figure B.3: (continued) The transmission loss at varying angles, during the spring season.

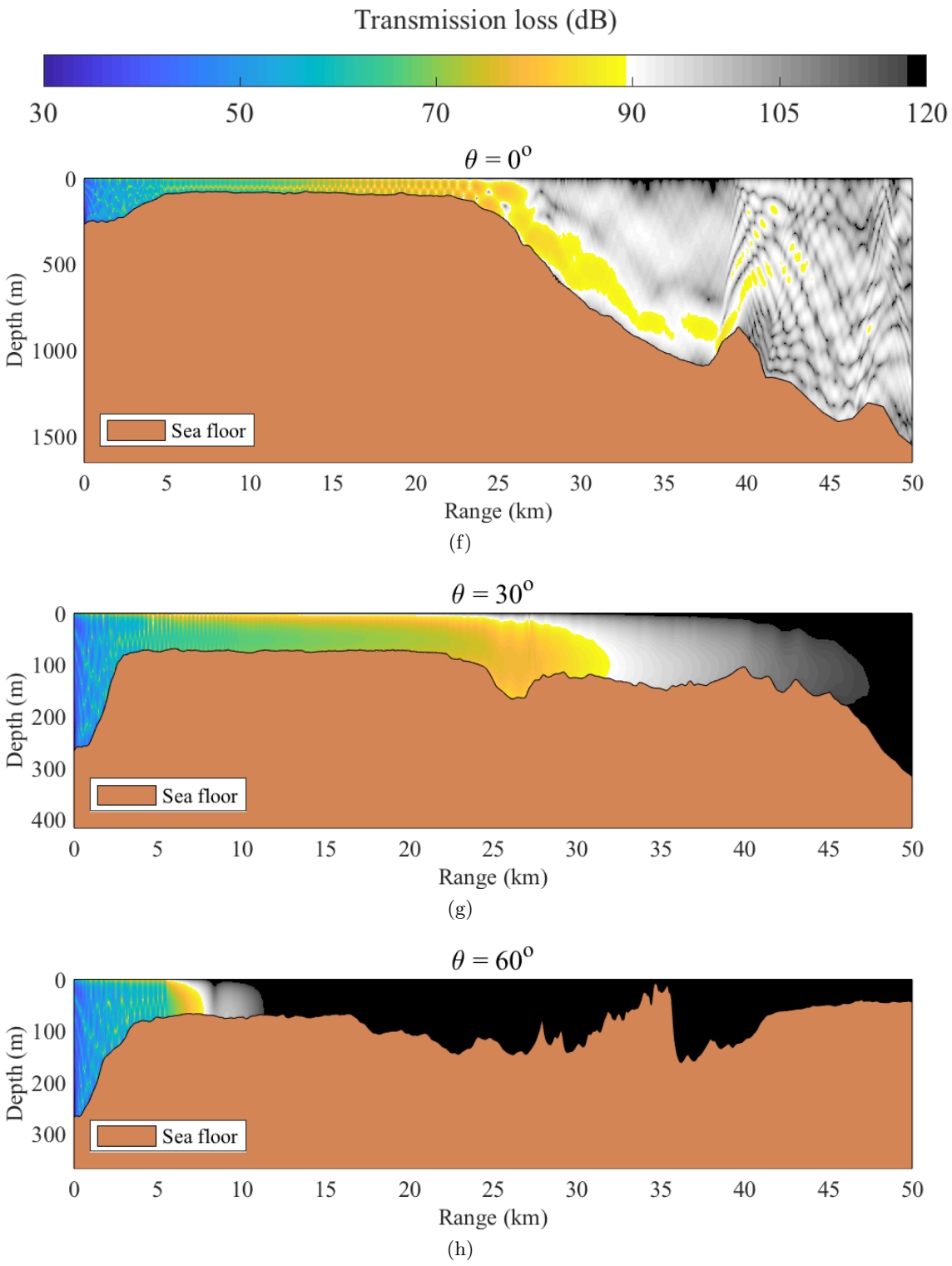

Figure B.3: (continued) The transmission loss at varying angles, during the spring season.

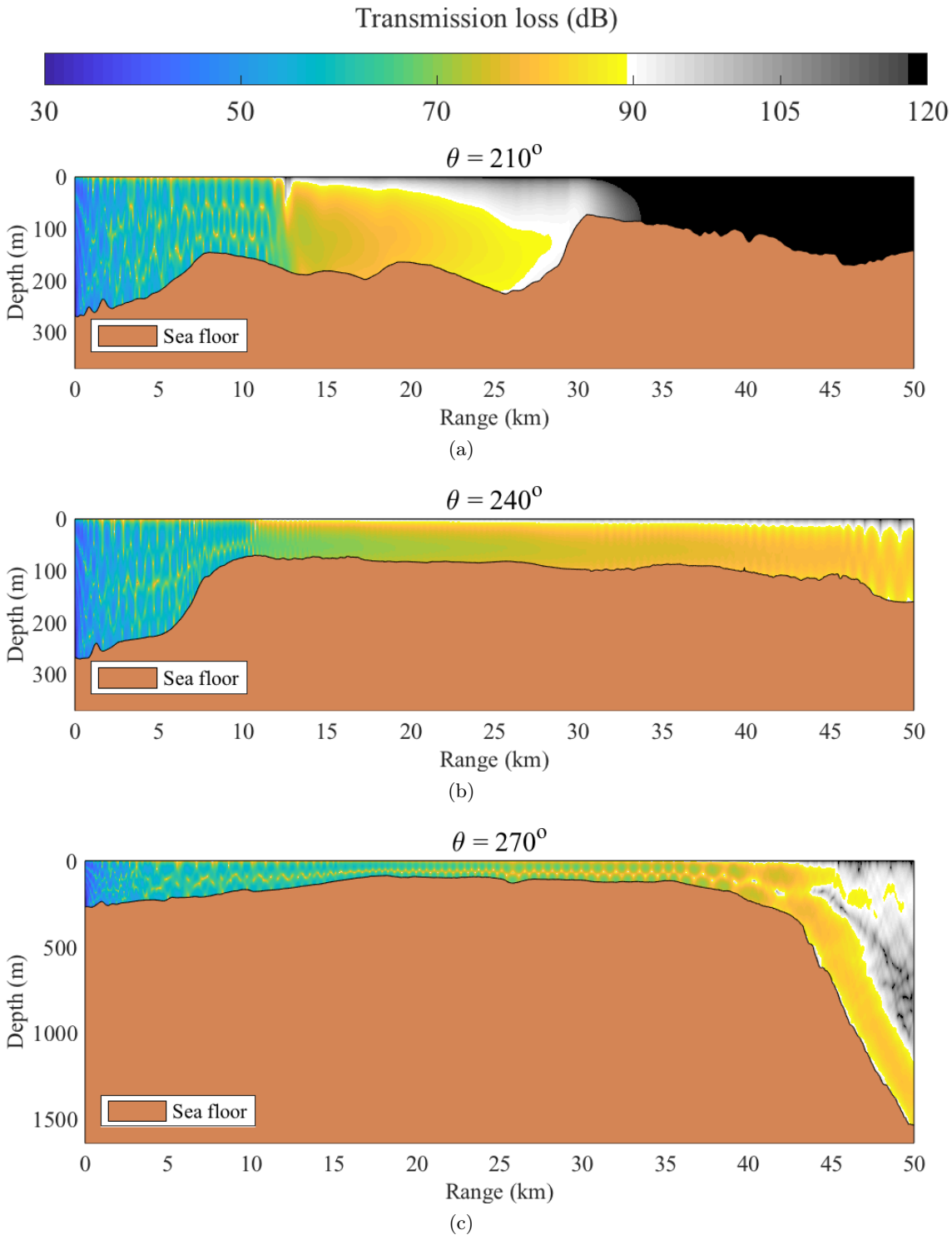

Figure B.4: The transmission loss at varying angles, during the summer season.

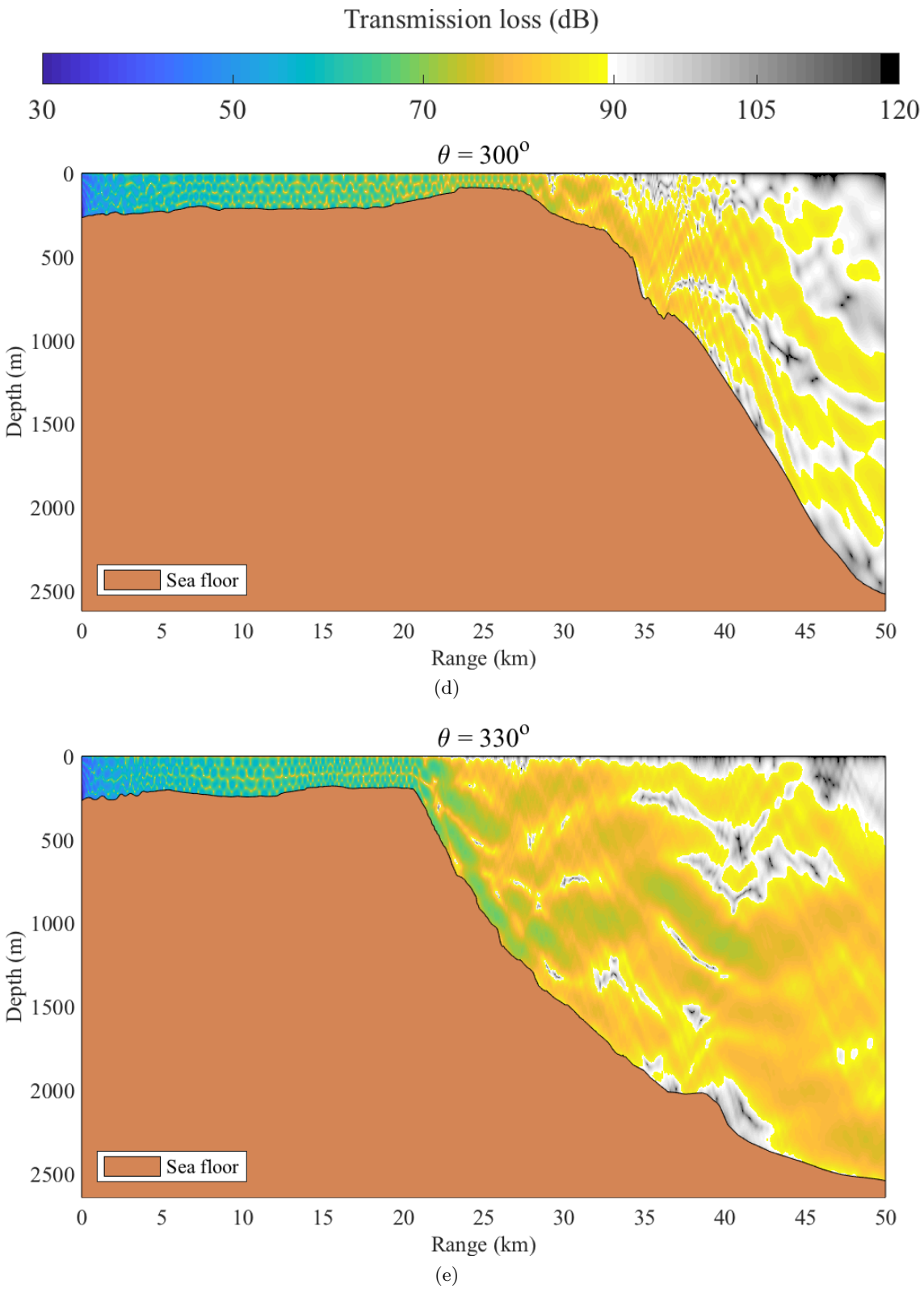

Figure B.4: (continued) The transmission loss at varying angles, during the summer season.

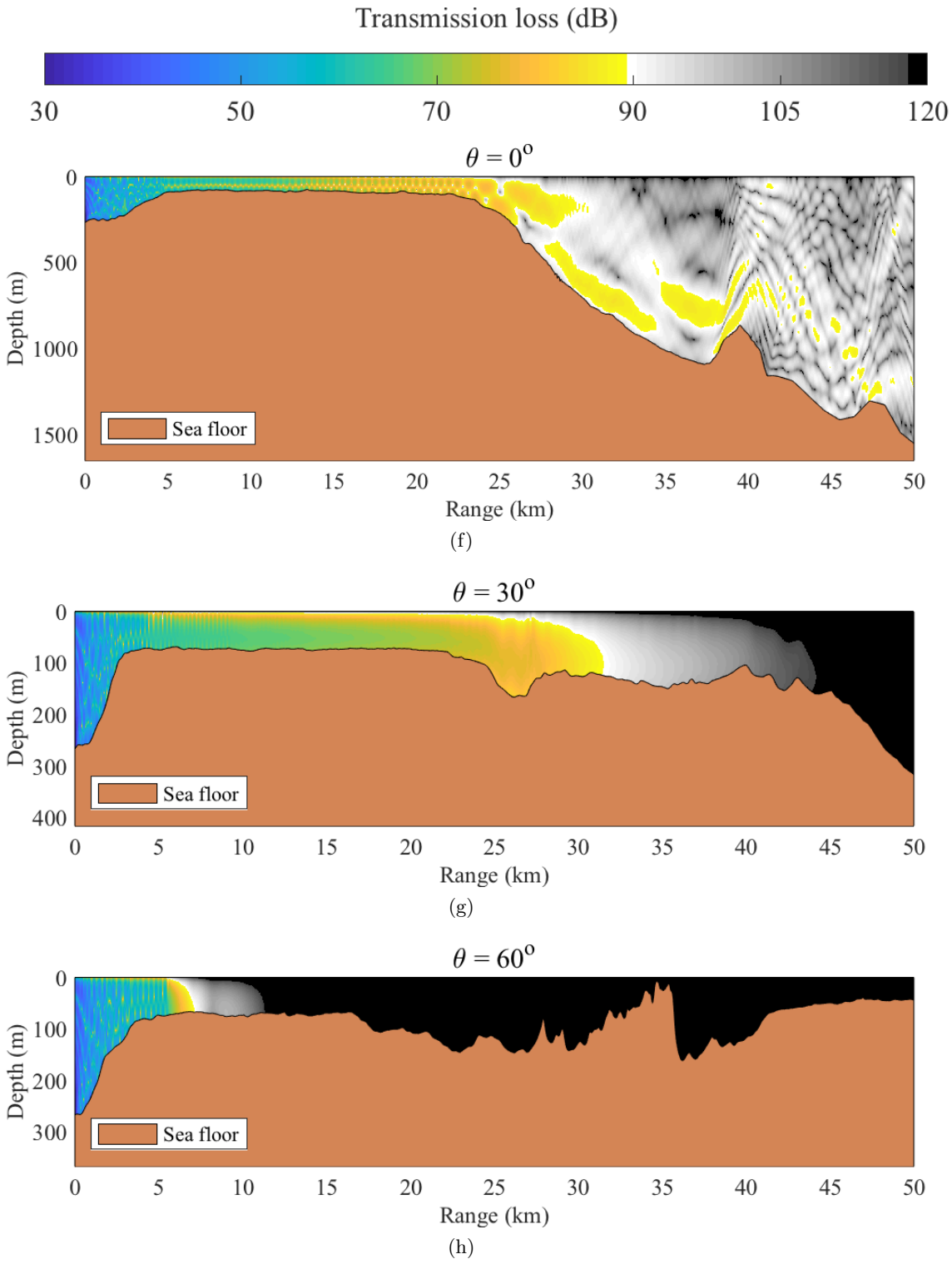

Figure B.4: (continued) The transmission loss at varying angles, during the summer season.

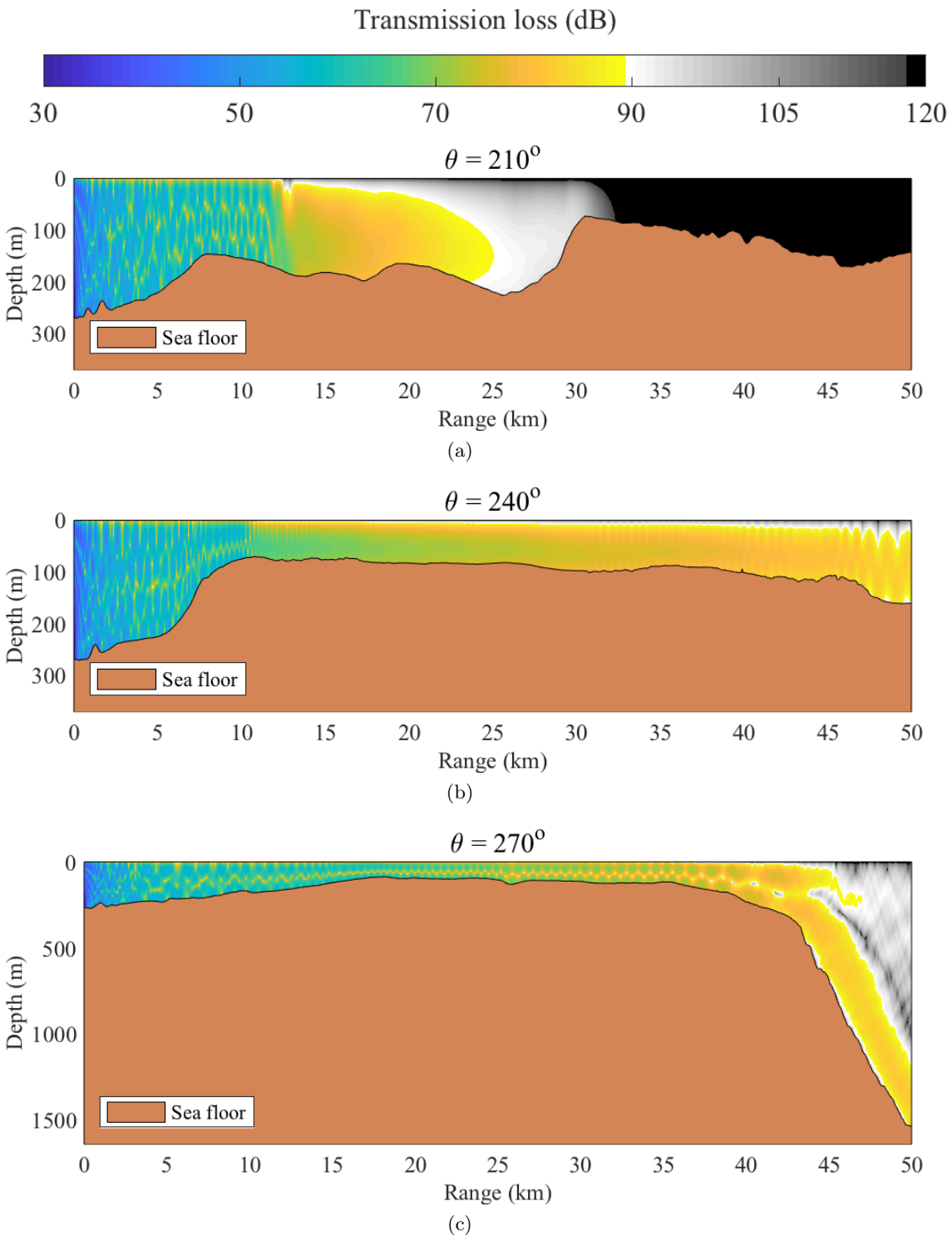

Figure B.5: The transmission loss at varying angles, during the autumn season.

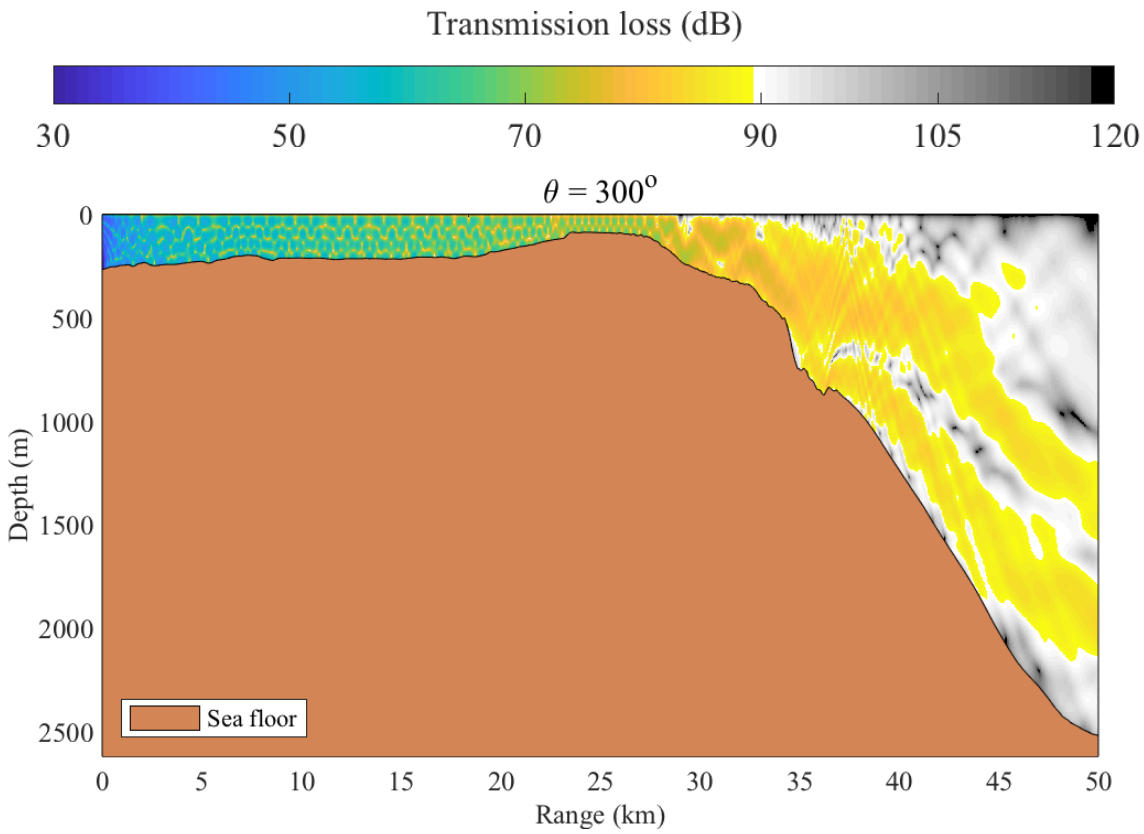

(d)

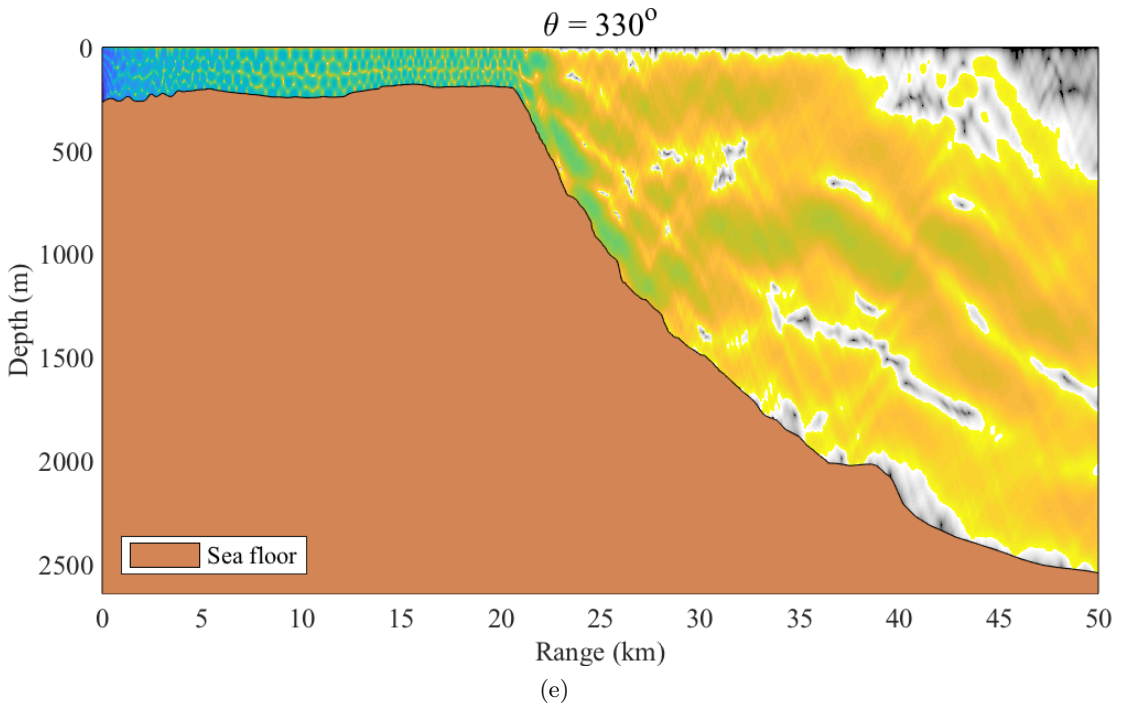

(e)

Figure B.5: (continued) The transmission loss at varying angles, during the autumn season.

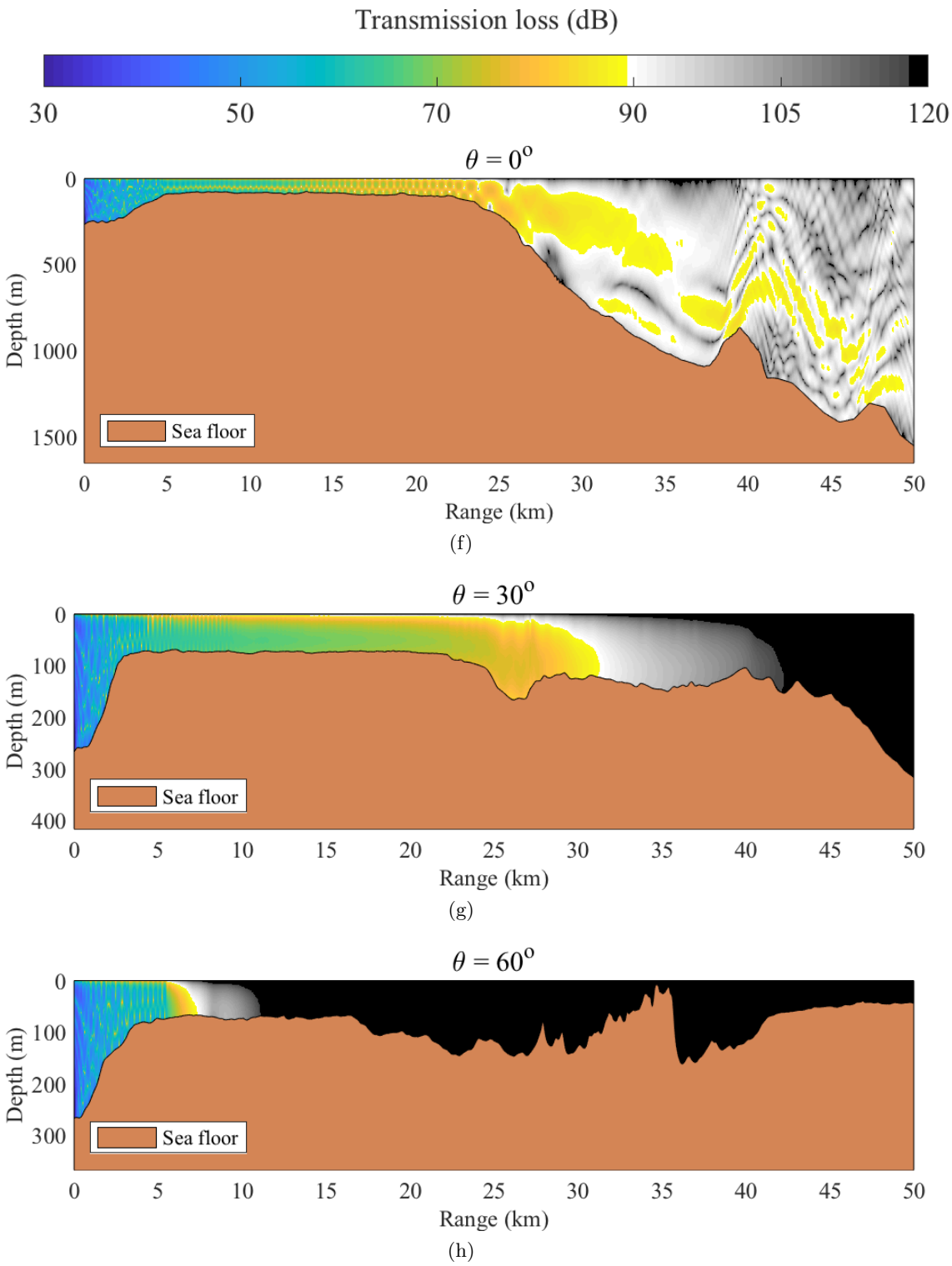

Figure B.5: (continued) The transmission loss at varying angles, during the autumn season.

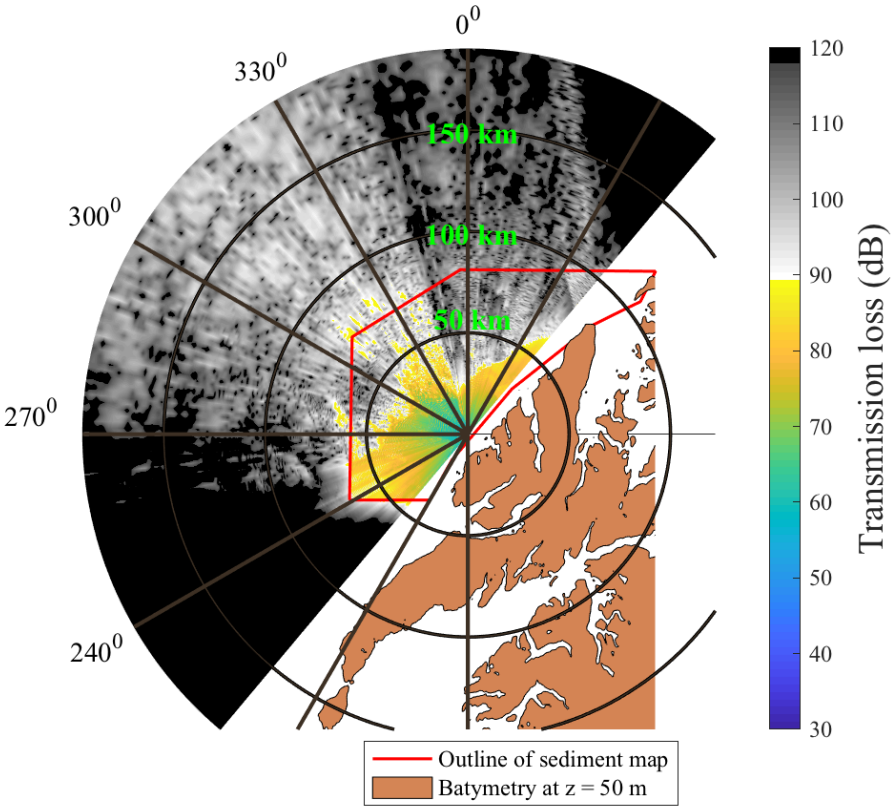

(i) Spring

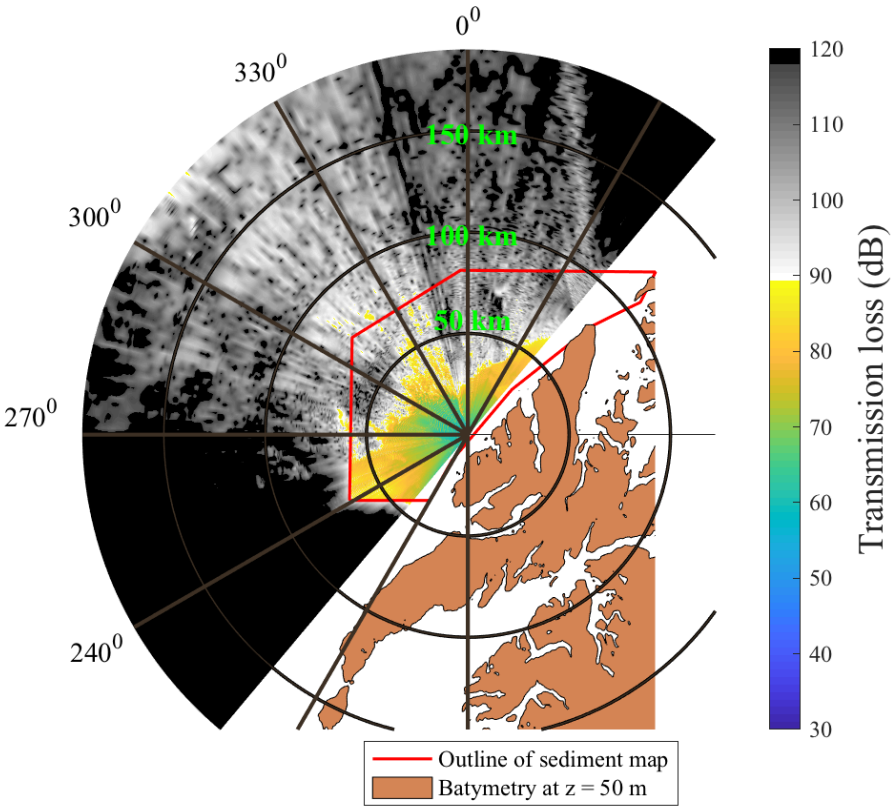

(j) Autumn

Figure B.6: The simulated transmission loss at $z = 50\,\mathrm{m}$ for the spring and autumn seasons.

Appendix C

MatLab Codes

C.1 Ray_bath

```
function [r, z, r_long, r_lat] = Ray_bath(angle_check, pos,
    r_max, delta_r, F)
% r is the radial distance vector
% a is the value of the bathymetry at each position r

% x_r and y_r are the cartesian coordinates of the array r
%
% anlge is in degrees. Can be defined both positive (counter
    clockwise) or
% negative (clockwise)

% pos is a vector and is an optional way of specifying
    direction as a
% position. If pos is 0, it is unused. If pos has a value,
    this is used instead of angle

% r_max is the spesified max length of the outputed r array.
    If pos is specified,
% r_max is unused. If specified as a single number, r_max is
% read as the radial distance from lp.

% x and y are the input positions for z (in long lat)

% delta_r is the radial resolution

% F is the interpolant of the bathymetry

% Listening position in eastern - norhern UTM coordinates
```

```
lp_ = [14.41167, 68.91333]; % Long, lat


% Check if pos is specified
if pos ~= 0
    % Check if pos is outside map
    % From map:
    x_max = 16.0000996511561;
    x_min = -20.2708333333333;
    y_max = 81.8208333333333;
    y_min = 67.3041666666667;

    if pos(1) > x_max || pos(1) < x_min || pos(2) > y_max ||
       pos(2) < y_min
        fprintf('pos is outside map!')
    end

    % Find distances from pos to the listening position

    [dist,~,~] = m_idist(lp_(1),lp_(2),pos(1),pos(2),'wgs84')
       ;

    delta_long = pos(1) - lp_(1);
    angle = sin(deg2rad(delta_long))/(cos(deg2rad(lp_(2)))*
       tan(deg2rad(pos(2))) - sin(deg2rad(pos(2)))*cos(
       deg2rad(delta_long)));

    % Get number of points
    Npoints = floor(dist/delta_r) + 1;

    % Get end position that is a multiple of delta r
    r_mult = delta_r * (Npoints -1);
    [r_mult_long,r_mult_lat,~] = m_fdist(lp_(1),lp_(2),angle,
       r_mult,'wgs84');

    [r,r_long,r_lat] = m_geodesic(lp_(1),lp_(2),r_mult_long,
       r_mult_lat,Npoints);

    if max(r) < dist
        % Add last point
        r = [r; dist];
        r_long = [r_long; pos(1)];
        r_lat = [r_lat; pos(2)];
    end
```

```
62
63      % Check the direction of the angle
64      if angle < 0
65          angle = angle + 360;
66      end
67
68  else
69      angle = angle_check;
70      % Find the quadrant
71      % Defined: 1: pos x pos y. 2: neg x pos y. 3: neg x neg y
            . 4: pos x neg y.
72
73
74      % From map:
75      x_max = 16.0000996511561;
76      x_min = -20.2708333333333;
77      y_max = 81.8208333333333;
78      y_min = 67.3041666666667;
79
80      % Check if r_max is outside map
81
82      [r_max_long,r_max_lat,~] = m_fdist(lp_(1),lp_(2),angle,
            r_max,'wgs84');
83
84      if r_max_long > x_max || r_max_long < x_min
85          fprintf('r_max is outside map!')
86      elseif r_max_lat > y_max || r_max_lat < y_min
87          fprintf('r_max is outside map!')
88      end
89
90
91      % Set up the r-array
92
93      % Get number of points
94      Npoints = floor(r_max/delta_r) + 1;
95
96      % Get end position that is a multiple of delta r
97      r_mult = delta_r * (Npoints -1);
98      [r_mult_long,r_mult_lat,~] = m_fdist(lp_(1),lp_(2),angle,
            r_mult,'wgs84');
99
100     [r,r_long,r_lat] = m_geodesic(lp_(1),lp_(2),r_mult_long,
            r_mult_lat,Npoints);
101
```

```
102
103
104     if max(r) < r_max
105         % Add last point
106         r = [r; r_max];
107         r_long = [r_long; r_max_long];
108         r_lat = [r_lat; r_max_lat];
109     end
110
111 end
112
113
114
115 if F == 0
116     z = 0;
117 else
118 z = F(r_long, r_lat);
119 end
120
121
122 end
```

C.2 Seabed

```
1  function [r, z, x_r_c, y_r_c, A_c] = Seabed(KS, r, r_long,
       r_lat, poly, z_bath)
2
3  % Extract the atribute number from KS at points along a ray
4
5  % KS is the structure containging the grain size infromation.
6
7  % r is the radial distance vector of each intersection
8
9  % x_sect and y_sect are the cartesian coordinates of the
       array r
10
11 % anlge is in degrees. Can be defined both positive (counter
       clockwise) or
12 % negative (clockwise)
13
14 % pos is a vector and is specifying direction and length of r
15
```

```
% r_delta is the radial resolution. It needs to be small if all changes in
% KS are to be detected

% poly is the bounding polygon of KS

% A is the value of the grain size atribute at each intersected polygon




%% Get coordinates of vertices
xv = extractfield(KS, 'X');
yv = extractfield(KS, 'Y');

%%
% Make the attribute nummeric
korn_ = extractfield(KS, 'SEDKORNSTR');
korn = str2double(korn_);
atr = num2cell(korn);




%% Get ray coordinates in UTM. Pos is specified in ll

m_proj('UTM', 'ellipsoid', 'wgs84', 'zone', 33)
[x_r,y_r]=m_ll2xy(r_long,r_lat, 'point');

in = inpolygon(x_r, y_r, poly(:, 1), poly(:, 2));

count = 1;
    for i = 1:length(r)
        if in(i)
            r_cut(count) = r(i);
            x_r_cut(count) = x_r(i);
            y_r_cut(count) = y_r(i);
            count = count + 1;



        end
    end
```

```
58
59
60  cn = length(KS);
61
62  xp_cell = cell(cn, 1);
63  yp_cell = cell(cn, 1);
64
65  for i = 1:cn
66      xp_cell{i} = KS(i).X;
67      yp_cell{i} = KS(i).Y;
68  end
69
70  %% Get polygons along ray
71
72  index = zeros(length(r_cut), 1);
73
74  for i = 1:length(r_cut)
75      x_r_ = x_r_cut(i);
76      y_r_ = y_r_cut(i);
77
78
79      for ii = 1:cn
80          clear in
81          xp = xp_cell{ii};
82          yp = yp_cell{ii};
83          [in, ~] = inpolygon(x_r_, y_r_, xp, yp);
84          if in
85              index(i) = ii;
86          end
87      end
88
89  end
90
91
92
93  %% Cut repeating attributes
94
95  count = 1;
96  index = [index(1); index];
97  for i = 2:length(index)
98      if  index(i-1) ~= index(i)
99          indice(count) = i-1;
100         count = count +1;
101     end
```

```
102 end
103
104 r = r_cut(indice);
105 z = z_bath(indice);
106
107 x_r_c = x_r_cut(indice);
108 y_r_c = y_r_cut(indice);
109 index_c = index(indice);
110
111
112 %% Get the attributes
113 n = length(index_c);
114
115 A_c = zeros(1, n);
116
117 for i = 1:n
118     ind = index_c(i);
119      A_c(i) = cell2mat(atr(ind));
120
121 end
122
123
124
125
126
127 end
```

C.3 geoac

```
1  function [cb, rho, atten] = geoac(A_c, T, S, c_w, z_max, f)
2  % Get the geoacoustic properties of the sediment
3
4  % cb is the sound velocity in the sediment
5  % rho is the bulk density of the sediment
6
7  % A_c is the value of the grain size atribute
8  % T is the temperature of the sea water at the max depth at
       the enquiery position
9  % S is the salinity of the sea water at the max depth at the
       enquiery position
10 % c_w is the speed of sound of the sea water at the max depth
       at the enquiery position
```

```
% z _max is the maximum depth at the enquiery position
% f is the frequency

if A_c == 1
% Thin or discontinous sediment cover on bedrock
    rho = 2700/1000;
    cb = 7200;
    atten = 0.6754;

elseif A_c == 20
% Mud
    rho_grain = 2501;
    eta = 0.45;
    rho_w = waterprops_den(T, S, z_max);
    rho = bulk_den(rho_grain, eta, rho_w)/1000;

    V_R = 1.09835570;
    cb = V_R * c_w;

    h = 0.70423278;
    atten = h*10^-3*cb;

elseif A_c == 21
% Mud alternating with blocks of hard sediment
    rho_grain = 2501;
    eta = 0.45;
    rho_w = waterprops_den(T, S, z_max);
    rho1 = bulk_den(rho_grain, eta, rho_w);
    rho2 = 2600;
    rho = mean([rho1, rho2])/1000;

    V_R = 1.10;
    cb1 = V_R * c_w;
    cb2 = 4000;
    cb = mean([cb1, cb2]);

    h1 = 0.70423278;
    atten1 = h1*f*f*10^-3/cb;
    h2 = 0.0573;
    l = 0.911;
    atten2 = (h2*cb*(f*10^(-3))^l)/f;
    atten = mean([atten1, atten2]);

elseif A_c == 40
```

```
% Sandy mud
    rho_grain = 2760;
    eta = 0.38;
    rho_w = waterprops_den(T, S, z_max);
    rho = bulk_den(rho_grain, eta, rho_w)/1000;

    V_R = 1.24712972;
    cb = V_R * c_w;

    h = 0.485520706;
    atten = h*10^-3*cb;
elseif A_c == 100
% Sand
    rho_grain = 2589;
    eta = 0.27;
    rho_w = waterprops_den(T, S, z_max);
    rho = bulk_den(rho_grain, eta, rho_w)/1000;

    V_R = 1.29355288;
    cb = V_R * c_w;

    h = 0.473958158;
    atten = h*10^-3*cb;

elseif A_c == 115
% Gravelly sandy mud
    rho_grain = 2872;
    eta = 0.27;
    rho_w = waterprops_den(T, S, z_max);
    rho = bulk_den(rho_grain, eta, rho_w)/1000;

    V_R = 1.46188993;
    cb = V_R * c_w;

    h = 0.8*10^3/cb;
    atten = h*10^-3*cb;

elseif A_c == 120
% Gravelly muddy sand
    rho_grain = 2836;
    eta = 0.25;
    rho_w = waterprops_den(T, S, z_max);
    rho = bulk_den(rho_grain, eta, rho_w)/1000;

```

```
99      V_R = 1.46828590;
100     cb = V_R * c_w;
101
102     h = 0.8*10^3/cb;
103     atten = h*f*f*10^-3/cb;
104
105 elseif A_c == 130
106 % Gravelly sand
107     rho_grain = 2836;
108     eta = 0.25;
109     rho_w = waterprops_den(T, S, z_max);
110     rho = bulk_den(rho_grain, eta, rho_w)/1000;
111
112     V_R = 1.47136113;
113     cb = V_R * c_w;
114
115     h = 0.8*10^3/cb;
116     atten = h*10^-3*cb;
117
118 elseif A_c == 150
119 % Muddy sandy gravel
120     rho_grain = 2842;
121     eta = 0.18;
122     rho_w = waterprops_den(T, S, z_max);
123     rho = bulk_den(rho_grain, eta, rho_w)/1000;
124
125     V_R = 1.59898469;
126     cb = V_R * c_w;
127
128     h = 0.8*10^3/cb;
129     atten = h*10^-3*cb;
130
131
132 elseif A_c == 160
133 % Sandy gravel
134     rho_grain = 2779;
135     eta = 0.15;
136     rho_w = waterprops_den(T, S, z_max);
137     rho = bulk_den(rho_grain, eta, rho_w)/1000;
138
139     V_R = 1.59958190;
140     cb = V_R * c_w;
141
142     h = 0.8*10^3/cb;
```

```
    atten = h*10^-3*cb;

elseif A_c == 175
% Gravel, cobbles and boulders    rho_grain = 2779;
    rho_grain = 2802;
    eta = 0.4;
    rho_w = waterprops_den(T, S, z_max);
    rho = bulk_den(rho_grain, eta, rho_w)/1000;

    V_R = 1.44;
    cb = V_R * c_w;

    atten = 0.6;

elseif A_c == 300
% Compact sediments of sedimentary bedrock
    cb = 4000;
    rho = 2600/1000;

    h = 1.012*10^-3;
    l = 0.911;
    atten = h*(f*10^-3)^l*cb/f;

elseif A_c == 0
% Outside of range
    cb = 1506.99499328387;
    rho = 1449.93128278282/1000;
    atten = 1.85*10^-4;
end
end
```

```
function rho = bulk_den(rho_grain, eta, rho_w)
rho = eta*rho_w + (1 - eta)*rho_grain;
end
```

C.4 waterprops - Written by White (2015b)

```
function [den]=waterprops(T,S,d)

% Returns  physical properties of water

```

```
% calculation of bulk modulus of water (Pa) (Siedler, 1986 section 3.1.3)
% valid range: 0=<S=<42 (ppt); -2=<T=<40 (oC); 0=<pK=<1e4 (dbar)
pK=1e-4*(1.01325e5+9.80665*d*1000);   % pressure in dbar required to get K
K_pure=1.965221e5+1484.206*T-23.27105*T^2+1.360477e-1*T^3-5.155288e-4*T^4;
K_surface=K_pure+(546.746-6.03459*T+1.09987e-1*T^2-6.167e-4*T^3)*S+(7.944e-1+1.6483e-1*T-5.3009e-3*T^2)*S^1.5;
Aw=3.239908+1.43713e-3*T+1.16092e-4*T^2-5.77905e-7*T^3;
A=Aw+(2.2838e-3-1.0981e-5*T-1.6078e-6*T^2)*S+1.91075e-4*S^1.5;
Bw=8.50935e-6-6.12293e-7*T+5.2787e-9*T^2;
B=Bw+(-9.9348e-8+2.0816e-9*T+9.1697e-11*T^2)*S;
K_dbar=K_surface+A*pK+B*pK^2;
K=K_dbar*1e4;
clear pK k_pure K_surface Aw A Bw B

% calculation of density of water (kg/m3) (Siedler, 1986 section 3.1.3)
% valid range: 0=<S=<42 (ppt); -2=<T=<40 (oC); 0=<pK=<1e4 (dbar)
pd=1e-4*(1.01325e5+9.80665*d*1000);    % pressure in dbar required to get den
den_pure=999.842594+6.793952e-2*T-9.095290e-3*T^2+1.001685e-4*T^3-1.120083e-6*T^4+6.536332e-9*T^5;
den_surface=den_pure+(8.24493e-1-4.0899e-3*T+7.6438e-5*T^2-8.2467e-7*T^3+5.3875e-9*T^4)*S+(-5.72446e-3+1.0227e-4*T-1.6546e-6*T^2)*S^1.5+4.8314e-4*S^2;
den=den_surface/(1+(pd/K_dbar));
clear pd den_pure den_surface

end
```

C.5 Write_in

```
function Write_in(angle, pos, r_max, delta_r, delta_z, z_max, freq, zs, zr, ndz, ndr, n_pade, s, rs, filename, F, KS, KS_pol, SSP)
% anlge is in degrees. Can be defined both positive (counter clockwise) or
```

```
3  % negative (clockwise)
4
5  % pos is a vector and is an optional way of specifying
       direction as a
6  % position. If pos is 0, it is unused. If pos has a value,
       this is used instead of angle
7  % pos is specified as [long, lat]
8
9  % r_max is the spesified max length of the outputed r array.
       If r_max = 0,
10 % the size of A determines r_max. If specified as a single
       number, r_max is
11 % read as the radial distance from lp.
12
13 % delta_r and delta_z are the radial resolution and depth
       resolution
14
15 % z_max is max z of output. If z_max == 0, z_max is taken as
       the max depth
16 % given by the batymethry
17
18 % zs is the source depth
19
20 % zr is the reciever depth
21
22 % freq is source frequency
23
24 % ndz and ndr are the decimation factors for the output TL
       grid.
25 % 1 = no decimation
26
27 % n_pade is the number of Pade coefficients
28 % s is the number of stability constraints (1 or 2)
29
30 % rs is the maximum range of stability constraints (= 0 turns
       stability
31 % constraints off
32
33 % filename is the title of the file, a string
34
35 % F is the interpolant for bathymetry
36
37 % KS is the grain map structure and KS_pol is the polygon
       bounding KS
```

```
38
39 % SSP is the cell containing SSPs and other ocean properties
       in the format
40 % z, P, c, [long, lat], T, S, rho
41
42 % Listening position is at:
43 lp_ = [14.41167, 68.91333]; % Long, lat
44
45
46 [r, z_bath, r_long, r_lat]= Ray_bath(angle, pos, r_max,
       delta_r, F);
47
48
49 % Set rmax
50 if r_max == 0
51     rmax = max(r);
52 else
53     rmax = r_max;
54     [pos_1, pos_2, ~] = m_fdist(lp_(1),lp_(2),angle,rmax,'
           wgs84');
55     pos = [pos_1, pos_2];
56 end
57
58 %%%%%%%%%%%%%%%%%%%%%%%%%%%%%
59 % Get SSPs
60 %%%%%%%%%%%%%%%%%%%%%%%%%%%%%
61 SSP_save = cell(1, 3);
62
63 % Make z_array up to the z where the delta P_SSP changes
64 if delta_z > 1
65     z_array = 0;
66     i = 2;
67     while z_array(end) <= 1500
68         z_array(i) = delta_z*(i-1);
69         i = i + 1;
70     end
71
72     % Convert z_array to P
73     P_array = floor(gsw_p_from_z(-z_array, lp_(1)));
74 else
75     P_array = 0:1:1500;
76 end
77
78
```

```
79 % Make P_array longer with delta P_SSP = 150 until P = 2996
       dBar
80 P_array = [P_array, P_array(end)+150:150:2996];
81
82
83 P_max_measured = 0;
84 count = 0;
85 for i = 1:length(P_array)
86     [c_at_p, ~, ~, lat_ssp, long_ssp, P_max] = Get_c_at_P(SSP
           , P_array(i));
87     if isempty(c_at_p)
88         continue
89     else
90         count = count + 1;
91         SSP_save{count, 1} = c_at_p;
92         SSP_save{count, 2} = [long_ssp; lat_ssp];
93         SSP_save{count, 3} = P_max;
94         % Get max P of the measured SSPs
95         if P_max_measured < max(P_max)
96             P_max_measured = max(P_max);
97         end
98     end
99 end
100
101 % Cut the P_array to the max P measured
102 i_P = find(P_array <= P_max_measured, 1, 'last');
103 P_array = P_array(1:i_P);
104
105 %% Getting positions of ssp ray. Chosing r_delta = 1000;
106 [r_ssp, z_ssp, long_ssp_r, lat_ssp_r] = Ray_bath(angle, 0,
       r_max, 1000, F);
107
108 % Remove last point (Not needed)
109 r_ssp = r_ssp(1:end-1);
110 z_ssp = z_ssp(1:end-1);
111 long_ssp_r = long_ssp_r(1:end-1);
112 lat_ssp_r = lat_ssp_r(1:end-1);
113
114 % Get max Ps for SSPs from bath
115 p_max_bath = gsw_p_from_z(-z_ssp,lat_ssp_r);
116
117
118 % Make cells to save SSP and z at each position
119 SSP_ray = cell(length(P_array), length(long_ssp_r));
```

```
120 SSP_ray_z = cell(length(P_array), length(long_ssp_r));
121
122 % Turn off warnings produced by interp_spherical
123 warning('off', 'MATLAB:griddata:DuplicateDataPoints')
124
125 % Interpolate
126 for i = 1:length(long_ssp_r)
127     % Get co-ordinates of one query point
128      query_long = long_ssp_r(i);
129      query_lat = lat_ssp_r(i);
130      count_ii = 1;
131    for ii = 1:length(P_array)
132        % Get all c_w at pressure P_array(ii)
133
134        % Find current pressure
135        P = P_array(ii);
136
137        % Check if P is deeper than bathymetry
138        if P <= p_max_bath(i)
139
140            % Get all c at this pressure
141            try
142            c_at_P_ = SSP_save{ii, 1};
143            catch
144                d = 1;
145            end
146
147            % Get corresponding P_max of CTDs
148            P_max = SSP_save{ii, 3};
149
150            % Get grid co-ordinates
151            ll_SSP_grid = SSP_save{ii, 2};
152            long_SSP_grid_ = ll_SSP_grid(1, :);
153            lat_SSP_grid_ = ll_SSP_grid(2, :);
154
155            % Remove NaNs from c_w and those entries that come
                   from CTDs
156            % that are shorther than current pressure
157            count = 1;
158
159            long_SSP_grid = [];
160            lat_SSP_grid = [];
161            c_at_P = [];
162
```

```
163             for a = 1:length(c_at_P_)
164                 if  or(~isnan(c_at_P_(a)) && P_max(a) >
                        p_max_bath(i), ~isnan(c_at_P_(a)) &&
                        p_max_bath(i) > P_max_measured)
165                  long_SSP_grid(count) = long_SSP_grid_(a);
166                  lat_SSP_grid(count) = lat_SSP_grid_(a);
167                  c_at_P(count) = c_at_P_(a);
168                  count = count + 1;
169                 end
170             end
171
172             % Interpolate and save if any c was found at
                    current pressure
173             % and position
174
175
176              if ~isempty(c_at_P)
177
178                 % Interpolate
179                 [c_w_at_ray_,~]= interp_spherical(
                        long_SSP_grid',lat_SSP_grid',c_at_P',
                        query_long,query_lat,'cubic',2);
180
181
182                  % Save SSP
183                  SSP_ray{count_ii, i} = c_w_at_ray_;
184                  SSP_ray_z{count_ii, i} = -gsw_z_from_p(P,
                         query_lat);
185                  count_ii = count_ii + 1;
186              end
187         end
188     end
189 end
190
191
192 % Turn warning back on
193 warning('on', 'MATLAB:griddata:DuplicateDataPoints')
194
195 % Smoot the SSPs
196 for i = 1:size(SSP_ray, 2)
197     c_ = smooth(cell2mat(SSP_ray(:, i)));
198
199     SSP_ray(1:length(c_), i) = num2cell(c_);
200 end
```

```
201
202
203
204
205 %%%%%%%%%%%%%%%%%%%%%%%%%%%%%%%%
206 % Get geoacoustic properties
207 %%%%%%%%%%%%%%%%%%%%%%%%%%%%%%%%
208
209
210
211 % Chose the r_delta used to look for changes in the seabed
212
213
214 [r_A, z_A, x_r_A, y_r_A, A_c] = Seabed(KS, r, r_long, r_lat,
       KS_pol, z_bath);
215
216
217 % Convert intersection co-ordinates to ll
218 [sec_long, sec_lat] = m_xy2ll(x_r_A,y_r_A);
219
220
221
222 % Convert z_A to pressure
223
224 P_chosen = floor(gsw_p_from_z(-z_A', sec_lat));
225
226
227 % Get all properties at these pressures
228 for i = 1:length(P_chosen)
229     [c_at_P, T_, S_, lat_ssp, long_ssp, ~] = Get_c_at_P(SSP,
          P_chosen(i));
230
231     if isempty(c_at_P)
232         P_chosen_ = P_chosen(i);
233         while isempty(c_at_P)
234             P_chosen_ = P_chosen_ - 1;
235             [c_at_P, T_, S_, lat_ssp, long_ssp, ~] =
                  Get_c_at_P(SSP, P_chosen_);
236         end
237
238     end
239
240
241     % Interpolate c_w, T_ and S_
```

```
242     try
243     [cb_at_deltar, ~]=interp_spherical(long_ssp',lat_ssp',
           c_at_P',sec_long(i),sec_lat(i),'cubic', 8);
244     catch
245         d = 1;
246     end
247
248     [T, ~]=interp_spherical(long_ssp',lat_ssp',T_',sec_long(i
           ),sec_lat(i),'cubic', 8);
249     [S, ~]=interp_spherical(long_ssp',lat_ssp',S_',sec_long(i
           ),sec_lat(i),'cubic', 8);
250
251     [cb_, rho_, atten_] = geoac(A_c(i), T, S, cb_at_deltar,
           z_A(i), freq);
252     cb(i) = cb_;
253     rho(i) = rho_;
254     atten(i) = atten_;
255     z_sediment(i) = z_A(i) + 125;
256     z_artificial(i) = z_sediment(i) + 4*cb_/freq;
257 end
258
259
260
261
262 % Get c0
263 P_lp = floor(gsw_p_from_z(-258, lp_(2)));
264 [c_at_P_lp, ~, ~, lat_ssp_c0, long_ssp_c0, ~] = Get_c_at_P(
       SSP, P_lp);
265 [c0, ~]=interp_spherical(long_ssp_c0',lat_ssp_c0',c_at_P_lp',
       lp_(1),lp_(2),'cubic', 8);
266
267 % Find deepes z_artificial and deepest z_bath
268 zmax_arti = max(z_artificial);
269 zmax_b = max(z_bath);
270
271 % Make the sediment layer of the end block
272 z_sediment_end = zmax_b + 125;
273 z_artificial_end = z_sediment_end + 300;
274
275 % Find zmax of domain
276 zmax = max([zmax_arti, z_artificial_end]);
277
278 % Check if z_max of output is specified
279 if z_max == 0
```

```
    zmplt = zmax;
else
    zmplt = z_max;
end

% Set geoproperties outside KS
if max(r_A) < rmax
    [cb_end, rho_end, atten_end] = geoac(0, 0, 0, 0, 0, 0);
end

% Sett up block ranges
r_block(1) = r_A(1);
cb_block(1) = cb(1);
rho_block(1) = rho(1);
atten_block(1) = atten(1);

% Get SSPs to go with each block

count_rssp = 2;
count_blocks = 2;
SSP_block(:, 1) =  SSP_ray(:, 1);
SSP_block_z(:, 1) =  SSP_ray_z(:, 1);
i = 2;

r_c = r_ssp(count_rssp);

% Padd to avoid problems at the end of the array
%r_ssp = [r_ssp; r_ssp(end) + 2000];
while i <= length(r_A)
    r_b = r_A(i);


    if r_b < r_c || r_c == r_ssp(end)



        SSP_block(:, count_blocks) = SSP_ray(:, count_rssp);

        SSP_block_z(:, count_blocks) = SSP_ray_z(:,
           count_rssp);
        r_block(count_blocks) = r_A(i);
        cb_block(count_blocks) = cb(i);
        rho_block(count_blocks) = rho(i);
        atten_block(count_blocks) = atten(i);
```

```
323         z_sediment_block(count_blocks) = z_sediment(i);
324         z_artificial_block(count_blocks) = z_artificial(i);
325         i = i + 1;
326     elseif r_b >= r_c && r_b < r_ssp(count_rssp + 1)
327         count_rssp = count_rssp + 1;
328 
329         SSP_block(:, count_blocks) = SSP_ray(:, count_rssp);
330 
331 
332         SSP_block_z(:, count_blocks) = SSP_ray_z(:,
               count_rssp);
333 
334         r_block(count_blocks) = r_A(i);
335         cb_block(count_blocks) = cb(i);
336         rho_block(count_blocks) = rho(i);
337         atten_block(count_blocks) = atten(i);
338         z_sediment_block(count_blocks) = z_sediment(i);
339         z_artificial_block(count_blocks) = z_artificial(i);
340         r_c = r_ssp(count_rssp);
341         i = i + 1;
342     else
343 
344         SSP_block(:, count_blocks) = SSP_ray(:, count_rssp);
345         SSP_block_z(:, count_blocks) = SSP_ray_z(:,
               count_rssp);
346         r_block(count_blocks) = r_ssp(count_rssp);
347         cb_block(count_blocks) = cb(i);
348         rho_block(count_blocks) = rho(i);
349         atten_block(count_blocks) = atten(i);
350         z_sediment_block(count_blocks) = z_sediment(i);
351         z_artificial_block(count_blocks) = z_artificial(i);
352         count_rssp = count_rssp + 1;
353         r_c = r_ssp(count_rssp);
354     end
355     count_blocks = count_blocks + 1;
356 end
357 
358 
359 % Add remaining SSPs
360 if count_rssp+1 < size(SSP_ray, 2)
361     n = size(SSP_block, 2) + 1;
362     for i = count_rssp+1:size(SSP_ray, 2)
363         r_block(n) = r_ssp(i);
364         SSP_block(:, n) = SSP_ray(:, i);
```

```
365         SSP_block_z(:, n) = SSP_ray_z(:, i);
366         n = n + 1;
367     end
368 end
369
370
371
372
373
374 %%%%%%%%%%%%%%%%%%%
375 % Write .in file
376 %%%%%%%%%%%%%%%%%%%
377
378 % Make file
379 fullfilename = strcat('/scratch/Sigrid/RAM_folders/',
       filename);
380 fileID = fopen(fullfilename,'w');
381 fprintf(fileID, filename);
382 fprintf(fileID,'\n%.1f %.1f %.1f', [freq, zs, zr]);
383 fprintf(fileID,'\n%.1f %.1f %d', [rmax, delta_r, ndr]);
384 fprintf(fileID, '\n%.1f %.1f %d %.1f', [zmax, delta_z, ndz,
       zmplt]);
385 fprintf(fileID, '\n%.1f %d %d %.1f', [c0, n_pade, s, rs]);
386 for i = 1:length(r)
387 fprintf(fileID, '\n%.1f %.1f', [r(i), z_bath(i)]);
388 end
389 fprintf(fileID, '\n%d %d', [-1, -1]);
390
391 % Print first block
392 z_print = cell2mat(SSP_block_z(:, 1));
393 cw_print = cell2mat(SSP_block(:, 1));
394
395
396 cb_b = [0, cb(1)];
397 rho_b = [0, rho(1)];
398
399
400 % Print block
401 for i = 1:length(z_print)
402 fprintf(fileID, '\n%.1f %.1f', [z_print(i), cw_print(i)]);
403 end
404 fprintf(fileID, '\n%d %d', [-1, -1]);
405 fprintf(fileID, '\n%.1f %.1f', cb_b);
406 fprintf(fileID, '\n%d %d', [-1, -1]);
```

```
fprintf(fileID, '\n%.1f %.1f', rho_b);
fprintf(fileID, '\n%d %d', [-1, -1]);
fprintf(fileID, '\n%.1f %.2g', [0, atten(1)]);
fprintf(fileID, '\n%.1f %.2g', [z_sediment(1), atten(1)]);
fprintf(fileID, '\n%.1f %.1f', [z_artificial(1), 10]);
fprintf(fileID, '\n%d %d', [-1, -1]);

% Next blocks
for i = 2:length(cb_block)
    z_print = cell2mat(SSP_block_z(:, i));
    cw_print = cell2mat(SSP_block(:, i));


    cb_b = [0, cb_block(i)];
    rho_b = [0, rho_block(i)];


    % Print block
    fprintf(fileID,'\n%.1f', r_block(i));
    for ii = 1:length(z_print)
    fprintf(fileID, '\n%.1f %.1f', [z_print(ii), cw_print(ii)
       ]);
    end
    fprintf(fileID, '\n%d %d', [-1, -1]);
    fprintf(fileID, '\n%.1f %.1f', cb_b);
    fprintf(fileID, '\n%d %d', [-1, -1]);
    fprintf(fileID, '\n%.1f %.1f', rho_b);
    fprintf(fileID, '\n%d %d', [-1, -1]);
    fprintf(fileID, '\n%.1f %.2g', [0, atten_block(i)]);
    fprintf(fileID, '\n%.1f %.2g', [z_sediment_block(i),
       atten_block(i)]);
    fprintf(fileID, '\n%.1f %.1f', [z_artificial_block(i),
       10]);
    fprintf(fileID, '\n%d %d', [-1, -1]);
end

% Blocks after KS
if length(cb_block)+1 < size(SSP_block, 2)
    for i = length(cb)+1:size(SSP_block, 2)
        z_print = cell2mat(SSP_block_z(:, i));
        cw_print = cell2mat(SSP_block(:, i));


        cb_b = [0, cb_end];
```

```
448         rho_b = [0, rho_end];
449
450
451         % Print block
452         fprintf(fileID,'\n%.1f', r_block(i));
453         for ii = 1:length(z_print)
454         fprintf(fileID, '\n%.1f %.1f', [z_print(ii), cw_print
               (ii)]);
455         end
456         fprintf(fileID, '\n%d %d', [-1, -1]);
457         fprintf(fileID, '\n%.1f %.1f', cb_b);
458         fprintf(fileID, '\n%d %d', [-1, -1]);
459         fprintf(fileID, '\n%.1f %.1f', rho_b);
460         fprintf(fileID, '\n%d %d', [-1, -1]);
461         fprintf(fileID, '\n%.1f %.1f', [0, atten_end]);
462         fprintf(fileID, '\n%.1f %.1f', [z_sediment_end,
               atten_end]);
463         fprintf(fileID, '\n%.1f %.1f', [z_artificial_end,
               10]);
464         fprintf(fileID, '\n%d %d', [-1, -1]);
465     end
466 end
467
468 fclose(fileID);
469
470 end
```

C.6 Get_at_P

```
1  function [c, T, S, lat, long, P_max] = Get_c_at_P(SSP,
       P_chosen)
2  % SSP is inputed in the format as in 'All_SSP.mat' in ICES-
       folder
3  % P is the hydrostatic pressure you want to get c's at. It
       has to be an
4  % integer
5
6
7  % Set up empties
8  c= [];
9  T = [];
10 S = [];
```

```
lat = [];
long = [];
P_max = [];

% Get array number
n = size(SSP, 1);



% Set up counter
count = 1;
i_P = 1;



for i = 1:n
    % Get P values

    P_array = SSP{i, 2};
    P_max_ = max(P_array);

    % Get indecie of P_chosen
    clear i_P
    i_P = find(P_array == P_chosen, 1);


    % Check if this c(P) has a value at P_chosen
    if isempty(i_P)
        continue
    end

    % Ge the rest of the values
    LongLat = SSP{i, 4};
    c_array = SSP{i, 3};
    T_array = SSP{i, 6};
    S_array = SSP{i, 7};


    % Save values if found
    if i_P > length(c_array)
        continue
    end
    c_ = c_array(i_P);
    T_ = T_array(i_P);
```

```
55      S_ = S_array(i_P);
56      if isnan(c_) || isnan(T_) || isnan(S_)
57          continue
58      end
59      c(count) = c_;
60      T(count) = T_;
61      S(count) = S_;
62      P_max(count) = P_max_;
63
64
65
66      long(count) = LongLat(1);
67      lat(count) = LongLat(2);
68      count = count +1;
69  end
```

Bibliography

Addlington, R. H. (1963). Acoustic reflection losses at the sea surface measured with explosive sources. *The Journal of the Acoustical Society of America*, 35:1834 – 1835.

Attewell, P. and Ramana, V. (1966). Wave attenuation and internal friction as functions of frequency in rocks. *Geophysics*, 31:1019 – 1056.

Bachman, R. T. (1985). Acoustic and physical property relationships in marine sediment. *The Journal of the Acoustical Society of America*, 78:616 – 621.

Bachman, R. T. (1989). Estimating velocity ratio in marine sediment. *The Journal of the Acoustical Society of America*, 86:2029 – 2032.

Ballard, M. S. and Lee, K. M. (2017). The acoustics of marine sediments. *Acoustics Today*, 13:11 – 18.

Bamberger, A., Engquist, B., Halpern, L., and Joly, P. (1988). Higher order paraxial wave equation approximations in heterogeneous media. *Society for industical and applied mathematics Journal on Applied Mathematics*, 48:129 – 154.

Biot, M. A. (1956). Theory of propagation of elastic waves in a fluid-saturated porous solid. I. Low-frequency range. *The Journal of the Acoustical Society of America*, 28:168 – 178.

Bjørge, A., Lydersen, C., Skern-Mauritzen, M., and Wiig, Ø. (2010). Sjøens pattedyr 2010. Technical Report 2-2010, Institute of Marine Research, Bergen, Norway.

Brekhovskikh, L. M. and Lysanow, Y. P. (1991). *Fundamentals of Ocean Acoustics*. Springer-Verlag, Berlin, Germany, 2 edition.

British Oceanographic Data Centre (2018). General bathymetric chart of the oceans. `https://www.gebco.net/data_and_products/gridded_bathymetry_data/`. [Accessed Jan. 15, 2018].

Buhl-Mortensen, L., Hodnesdal, H., and Thorsnes, T. (2015). *The Norwegian sea floor: new knowledge from MAREANO for ecosystem-based management*. MAREANO, Trondheim, Norway.

Calderan, S., Miller, B., Collins, K., Ensor, P., Double, M., Leaper, R., and Barlow, J. (2014). Low-frequency vocalizations of Sei whales (Balaenoptera borealis) in the Southern Ocean. *The Journal of the Acoustical Society of America*, 136:EL418 – EL423.

Caruther, J. W. (1977). *Fundamental of marine acoustics*. Eleiver Scientific Publishing Company, Amsterdam, The Netherlands.

Charif, R. A. and Clark, C. W. (2009). Acoustic monitoring of large whales in deep waters north and west of the British Isles: 1996 - 2005. Technical Report 08-07, Bioacoustics Research Program, Cornell Laboratory of Ornithology, Ithaca, United States of America.

Charif, R. A., Mellinger, D. K., Dunsmore, K. J., Fristrup, K. M., and Clark, C. W. (2002). Estimated source levels of Fin whale (Balaenoptera physalus) vocalizations: Adjustments for surface interference. *Journal of Marine Mammal Science*, 18:81–98.

Chotiros, N. P. (2018). Integrated model for the acoustics of sediments. `https://www.onr.navy.mil/reports/FY13/oachotir.pdf`. [Accessed Sept. 13, 2018].

Christensen, I., Haugh, T., and Øien, N. (1992). Seasonal distribution, exploitation and present abundance of stocks of large baleen whales (Mysticeti) and Sperm whales (Physeter macrocephalus) in Norwegian and adjacent waters. *ICES Journal of Marine Science*, 49:341 – 355.

Claerbout, J. F. (1985). *Fundamentals of geophysical data processing*. Blackwell Scientific Publications, Oxford, United Kingdom.

Collins, M. D. (1989a). Applications and time-domain solution of higher-order parabolic equations in underwater acoustics. *The Journal of the Acoustical Society of America*, 86:1097 – 1102.

Collins, M. D. (1989b). A higher order parabolic equation for wave propagation in an ocean overlying an elastic bottom. *The Journal of the Acoustical Society of America*, 86:1459 – 1464.

Collins, M. D. (1990). Benchmark calculations for higher-order equations. *The Journal of the Acoustical Society of America*, 87:1535 – 1538.

Collins, M. D. (1991). Higher-order Padé approximations for accurate and stable elastic parabolic equations with application to interface wave propagation. *The Journal of the Acoustical Society of America*, 89:1050 – 1057.

Collins, M. D. (1992). A self-starter for the parabolic equation method. *The Journal of the Acoustical Society of America*, 92:2069 – 2074.

Collins, M. D. (1993). A split-step Padé solution for the parabolic equation method. *The Journal of the Acoustical Society of America*, 93:1736 – 1742.

Collins, M. D. (2001). User's guide for RAM versions 1.0 and 1.0p. `http://staff.washington.edu/dushaw/AcousticsCode/ram.pdf`. [Accessed Jan. 5, 2018].

Collins, M. D., Cederberg, R. J., King, D. B., and Chin-Bing, S. A. (1996). Comparison of algorithms for solving parabolic wave equations. *The Journal of the Acoustical Sciety of America*, 100:178 – 182.

Collins, M. D. and Chin-Bing, S. A. (1990). A three-dimensional parabolic equation model that includes the effects of rough boundaries. *The Journal of the Acoustical Society of America*, 87:1104 – 1109.

Collins, M. D. and Evans, R. B. (1992). A two-way parabolic equation for acoustic backscattering in the ocean. *The Journal of the Acoustical Society of America*, 91:1357 – 1368.

Collins, M. D. and Westwood, E. K. (1991). A higher-order energy-conserving parabolic equqation for range dependent ocean depth, sound speed, and density. *The Journal of the Acoustical Society of America*, 89:1068 – 1075.

Collis, J. M. (2011). Three-dimensional underwater sound propagation using a split-step Padé parabolic equation solution. *The Journal of the Acoustical Society of America*, 130:2528 – 2528.

Coppens, A. B. (1982). An introduction to the parabolic equation for acoustic propagation. Technical Report NPS61-83-002, Naval Ocean Research and Development Activity, Arlington, United States of America.

Davis, J. A., White, D., and Cavanagh, R. C. (1982). NORDA parabolic equation workshop. Technical Report 143, Naval Ocean Research and Development Activity, Arlington, United States of America.

Delleur, J. W. (1998). *Handbook of groundwater engineering*. CRC Press, Boca Raton, United States of America.

DeSanto, J. A. (1979). *Topics in current physics: ocean acoustics*. Springer-Verlag, Berlin, Germany.

Dunlop, R. A., Douglas, C. H., and Noad, M. J. (2008). Non-song acoustic communication in migrating Humpback whales (Megaptera novaeangliae). *Marine Mammal Science*, 24:613 – 629.

Dushaw, B. (2015). MPIRAM: The RAM parabolic equation code in Fortran 95. `http://staff.washington.edu/dushaw/AcousticsCode/RamFortranCode.html#Downloads`. [Accessed October 20th, 2018].

Duxbury, A., Byrne, R. H., and Mackenzie, F. T. (2018). Density of seawater and pressure. `https://www.britannica.com/science/seawater/Density-of-seawater-and-pressure`. [Accessed Oct. 23, 2018].

Elvenes, S. (2018). Marin geologist at Geological Survey of Norway. Personal communication. Trondheim, Norway.

Evans, D. L. and England, G. R. (2001). Joint interim report: Bahamas marine mammal stranding event of 15-16 March 2000. Technical report, National Oceanic and Atmospheric Administration, Washington, United States of America.

Fofonoff, N. and Millard Jr., R. C. (1983). Algorithms for computation of fundamental properties of seawater. Technical report, UNESCO, Paris, France.

Folk, R, L. (1954). The distinction between grain size and mineral composition in sedimentary-rock nomenclature. *The Journal of Geology*, 62:344 – 495.

Frantzis, A. (2003). The first mass stranding that was associated with the use of active sonar (Kyparissiakos Gulf, Greece, 1996). In Evans, P. G. H. and Miller, L. A., editors, *Proceedings of the workshop on active sonar and cetaceans at European Cetasean Society's 17th anual conference*, Gran Canaria, Spain.

Gassmann, F. (1951). Uber die elastizitat poroser medien. *Veirteljahrsschrift der Naturforschenden Gesellschaft in Zuirich*, 96:1 – 23.

Geological Survey of Norway (2015). Produktspesifikasjon versjon 4.0: Produktspesifikasjon: Bunnsedimenter kornstørrelse. Technical report, Trondheim, Norway.

Geological Survey of Norway (2016). Seabed sediments (grain size), n100 regional. `https://kartkatalog.geonorge.no/metadata/norges-geologiske-undersokelse/bunnsedimenter-kornstorrelse-regionalt/c6738716-1954-4f88-aa5f-1be7eef36b25`. [Accessed Jan. 15, 2018].

Geotechdata.info (2013). Soil void ratio. `http://www.geotechdata.info/parameter/soil-porosity.html`. [Accessed March. 10, 2018].

Godø, O. R. and Torkelsen, T. (2014). The LoVe Ocean Observatory is in operation. *Marine Technology Society Journal*, 48:24 – 30.

Gordon, J. C. D., Gillespie, D., Potter, J., Frantzis, A., Simmonds, M. P., Swift, R., and Thompson, D. (2004). A review of the effects of seismic survey on marine mammals. *Marine Technology Society Journal*, 37:14 – 32.

Green, R. R. (1982). The rational approximation to the acoustic wave equation with bottom interaction. *The Journal of the Acoustical Society of America*, 76:1764 – 1773.

Halkias, X. C., Paris, S., and Glotin, H. (2013). Classification of Mysticete sounds using machine learning techniques. *The Journal of the Acoustical Society of America*, 134:3496 – 3505.

Hall, N. (2015). Air properties definitions. `https://www.grc.nasa.gov/www/K-12/airplane/airprop.html`. [Accessed June. 11, 2018].

Hamilton, E. L. (1972). Compressional-wave attenuation in marine sediments. *Geophysics*, 37:620 – 646.

Hamilton, E. L. and Bachman, R. T. (1982). Sound velocity and related properties of marine sediments. *The Journal of the Acoustical Society of America*, 72:1891 – 1904.

Hardin, R. H. and Tappert, F. D. (1973). Applications of the split-step Fourier method to the numerical solution of nonlinear and variable coeffcient wave equation. *SIAM Review Chronicles*, 15:423 – 423.

Haug, T. (1998). *Sjøpattedyr: om hval og sel i norske farvann*. Universitetsforlaget, Oslo, Norway.

Helble, T. A., D'Spain, G. L., Hildebrand, J. A., Campbell, G. S., Campbell, R. L., and Heaney, K. D. (2013). Site specific probability of passive acoustic detection of Humpback whale calls from single fixed hydrophones. *The Journal of the Acoustical Society of America*, 134:2556 – 2569.

Herzing, D. L. and Johnson, C. M. (2015). *Doplhin Communication and Cognition: Past, Present and Future*. MIT Press, Cambridge, United States of America.

Hiyoshi, Y., Tsuchiya, T., Naoi, J., Futa, K., and Kikuchi, T. (2004). The difference in the low frequency sound propagation across the North Pacific: sound communication in various species of Baleen Whales. In *Proceedings of OCEANS'04*, Kobe, Japan.

Hjort, J. (1902). *Fiskeri og hvalfangst i det nordlige Norge*. John Griegs Forlag, Bergen, Norway.

Hovem, J. M. (1978). *Undervannsakusikk*. Tapir Akademisk Forlag, Trondheim, Norway.

Hughes, S. J., Ellis, D. D., Chapman, D. M. F., and Staal, P. R. (1990). Low frequency acoustic propagation loss in shallow water over hard rock seabeds covered by a thin layer of elastic–solid sediment. *The Journal of the Acoustical Society of America*, 88:283 – 297.

Ingebrigtsen, A. (1929). Whales caught in the North Atlantic and other seas. Technical report, International Council for the Exploration of the Sea, Copenhagen, Denmark.

Institute of Marine Research (2018). Temasider: Sjøpattedyr. `https://www.hi.no/temasider/sjopattedyr/`. [Accessed April 9, 2018].

International Council for the Exploration of the Sea (2018). CTD and bottle data. `http://ocean.ices.dk/HydChem`. [Accessed Jan. 13, 2018].

Isakson, M. J. and Chotiros, N. P. (2012). The effect of roughness on bottom loss from elastic ocean bottoms. In *Advances in ocean acoustics: Proceedings of the 3rd International Conference on Ocean Acoustics (OA2012)*, Beijing, China.

Isakson, M. J., Chotiros, N. P., Abraham Yarbrough, R., and Piper, J. N. (2012). Quantifying the effects of roughness scattering on reflection loss measurements. *The Journal of the Acoustical Society of America*, 132:3687–3697.

Jackson, D. R. (1994). High-frequency ocean environmental acoustic model handbook. Technical Report APL-UW TR 9407, Applied Physics Labratory, University of Washington, Seattle, United States of America.

Jackson, D. R. and Briggs, K. B. (1992). High frequency bottom backscattering: Roughness versus sediment volume scattering. *The Journal of the Acoustical Society of America*, 92:962 – 977.

Jackson, D. R. and Richardson, M. D. (2007). *High-frequency seafloor acoustics*. Springer, New York, United States of America.

Jarandsen, B. (2011). Human impact and environmental consequences in the North Sea and Skagerrak. Technical Report TA-2828/2011, Norwegian Petroleum Directorate, Stavanger, Norway.

Jensen, F., Nielsen, P., and Ferla, C. M. (2001). Efficient broadband signal simulation in shallow water: A modal approach. In Shang, E., Li, Q., and Gao, T. F., editors, *Proceedings of the International Conference on Theoretical and Computational Acoustics 2001*, Beijing, China.

Jensen, F. B. and Ferla, C. M. (1989). Numerical solutions of range dependent benchmark problems in ocean acoustics. *The Journal of the Acoustical Society of America*, 87:1499 – 1510.

Jensen, F. B., Kuperman, W. A., Porter, M. B., and Schmidt, H. (2011). *Computational Ocean Acoustics*. Springer, New York, United States of America.

Kamann, P. J. (2007). Porosity and permeability in sediment mixtures. *Ground Water Journal*, 45:429 – 438.

Kartverket (2018a). Geo Norge: Dybdedata 50 m grid. `https://kartkatalog.geonorge.no/metadata/kartverket/dybdedata-50m-grid/bbd687d0-d34f-4d95-9e60-27e330e0f76e`. [Accessed Jan. 15, 2018].

Kartverket (2018b). Geo Norge: Sjø terrengmodeller DTM 5. `https://kartkatalog.geonorge.no/metadata/kartverket/sjo-terrengmodeller-dtm-5/13b707ad-a379-4bf0-a707-da237d646f44`. [Accessed Jan. 15, 2018].

Kartverket (2018c). Sjø terrengmodeller. `https://www.kartverket.no/data/kartdataer/Dybdedata/Terrengmodeller-havbunn/`. [Accessed Jan. 15, 2018].

Kellogg, R. (1928). What is known of the migration of some of the whalebone whales. *Annual report of the Board of Regents of the Smithsonian Institution*, pages 467 – 494.

Kinsler, L. E., Frey, A. R., Coppens, A. B., and Sanders, J. V. (2000). *Fundamentals of acoustics*. John Wiley and Sons, Hoboken, United States of America, 4 edition.

Küsel, E., Mellinger, D., Thomas, L., Marques, T., Moretti, D., and Ward, J. (2011). Cetacean population density estimation from single fixed sensors using passive acoustics. *The Journal of the Acoustical Society of America*, 129:3610 – 3622.

Leighton, T. G. (1994). *The acoustic bubble*. Academic Press, Cambridge, United States of America.

Leontovich, M. A. and Fock, V. A. (1946). Solution of the problem of propagation of electromagnetic waves along the earth's surface by method of parabolic equations. *Journal of Physics — USSR*, 10:13–23.

Lerner, K. (2018). Sound transmission in the ocean. `http://www.waterencyclopedia.com/Re-St/Sound-Transmission-in-the-Ocean.html`. [Accessed Sept. 13, 2018].

Mareano (2018). Classification of sediments based on grain size composition. `http://www.ngu.no/Mareano/Grainsize.html`. [Accessed Jan. 15, 2018].

Marques, T., Munger, L., Thomas, K., Wiggins, S., and Hildebrand, J. (2011). Estimating North Pacific right whale (Eubalaena japonica) density using passive acoustic cue counting. *Endangered Species Research*, 13:163 – 172.

Marques, T. A., Thomas, L., Ward, J., DiMarzio, N., and Tyack, P. L. (2009). Estimating cetacean population density using fixed passive acoustic sensors: An example with Blainville's beaked whales. *The Journal of the Acoustical Society of America*, 125:1982 – 1994.

Martin, S. W., Marques, T. A., and Thomas, L. (2013). Estimating Minke whale (Balaenoptera acutorostrata) boingsound density using passive acoustic sensors. *Marine Mammal Science*, 29:142 – 157.

Matheney, M. P. and Nowack, R. L. (1998). Seismic attenuation computed from GLIMPCE reflection data and comparison with refraction results. *Pure Applied Geophys*, 153:539 – 561.

Maystrenko, Y. P., Olesen, O., and Grandmann, S. (2017). Deep structure of the Lofoten Vesteraalen segment of the Mid Norwegian continental margin and adjacent areas derived from 3D density modelling. *Journal of Geophysical Research: Solid Earth*, 122:1402 – 1433.

McDonald, M. and Fox, C. (1999a). Passive acoustic methods applied to Fin whale population acoustic cue counting. *The Journal of the Acoustical Society of America*, 105:2643 – 2651.

McDonald, M. A. and Fox, C. G. (1999b). Passive acoustic methods applied to Fin whale population density estimation. *The Journal of the Acoustical Society of America*, 105:2643 – 2651.

McDougall, T. and Barker, P. (2011). Getting started with TEOS-10 and the Gibbs Seawater (gsw) Oceanographic Toolbox. `http://www.teos-10.org/software.htm#1`. [Accessed Apr. 10, 2018].

Medwin, H. and Clay, C. S. (1998). *Fundamentals of acoustical oceanography*. Academic Press, London, United Kingdom.

Millais, J. G. (1906). *The mammals of Great Britain and Ireland*, volume 3. Longmans, Green, and Co., London, United Kingdom.

Moerman, K. (2018). The geometry and image-based bioengineering add-on. `https://www.gibboncode.org/html/HELP_interp_spherical.html`. [Accessed March. 10, 2018].

Moritz, H. (1980). Geodetic reference system 1980. *Journal of Geodesy*, 74:18 – 162.

Møhl, B., Wahlberg, M., Madsen, P. T., Heerfordt, A., and Lund, A. (2003). The monopulsed nature of Sperm whale clicks. *The Journal of the Acoustical Society of America*, 114:1143 – 1154.

Nghiem-Phu, L. and Tappert, F. (1985). One-way wave equation for seismoacoustic propagation in elastic waveguides. *The Journal of the Acoustical Society of America*, 78:164 – 171.

Oswald, J. N. and Duennebier, F. (2011). Minke whale (Balaenoptera acutorostrata) boings detected at the Station ALOHA Cabled Observatory. *The Journal of the Acoustical Society of America*, 129:3353 – 3360.

Palmstrom, A. (1995). *RMi - a rock mass characterization system for rock engineering purposes*. PhD thesis, Univeristy of Oslo, Oslo, Norway.

Parks, S. E. and Clark, C. W. (2012). Acoustic communication in Mysticetes. *The international Journal of Animal Sound and its Recording*, 17:45 – 47.

Pawlowicz, R. (2018). M_map - a mapping package for matlab. `https://www.eoas.ubc.ca/~rich/map.html`. [Accessed June. 12, 2018].

Pedersen, G. (2018). Christian Michelsen Research. Personal communication. Bergen, Norway.

Porter, M. B. and Bucker, H. P. (1987). Gaussian beam tracing for computing ocean acoustic fields. *The Journal of the Acoustical Society of America*, 82:1349 – 1359.

Radaelli-Sanchez, R. and Baraniuk, R. (2007). Gibbs' phenomena. Tel Aviv University. Tel Aviv, Israel.

Rosenberg, A. P. (1999). A new rough surface parabolic equation program for computing low-frequency acoustic forward scattering from the ocean surface. *The Journal of the Acoustical Society of America*, 105:144 – 153.

Røttingen, I. (2015). Tilstanden i økosystem Norskehavet. Technical Report 1–2015, Institute of Marine Research, Bergen, Norway.

Samarra, F. I. P., Deecke, V. B., Vinding, K., Rasmussen, M. H., Swift, R. J., and Miller, P. J. O. (2010). Killer whales (Orcinus orca) produce ultrasonic whistles. *The Journal of the Acoustical Society of America*, 128:EL205 – EL210.

Schulkin, M. and Shaffer, R. (1964). Backscattering of sound from the sea surface. *The Journal of the Acoustical Society of America*, 36:1699–1703.

She, K., Horn, D. P., and Canning, P. (2006). Porosity and hydraulic conductivity of mixed sand-gravel sediment. In *Flood and Coastal Risk Management*, York, United Kingdom.

Siedler, G. and Peters, H. (1986). 3.1.1 Thermodynamic variables. In *Sündermann J. (eds) Subvolume A. Landolt Börnstein - Group V Geophysics (Numerical data and functional relationships in science and Technology)*, volume 3a. Springer, Berlin, Germany.

Siggins, F. A. and Dewhurst, D. N. (2003). Saturation, pore pressure and effective stress from sandstone acoustic properties. *Geophysical Research Letters*, 30:61 – 62.

Sigmond, E. M. O. (2002). Geological map; Land and sea areas of northern Europe. Scale 1:4 million. Geological Survey of Norway. Trondheim, Norway.

Steele, J. H., Thorpe, S. A., and Turekian, K. K. (2009). *Elements of physical oceanography: A derivative of the encyclopedia of ocean sciences.* Academic Press, London, United Kingdom.

Storheim, E. (2018). Scientist at the Nansen Environmental and Remote Sensing Center. Personal communication. Bergen, Norway.

Strum, F. (2001). Numerical simulations with 3d wape considering shallow water range dependent environments. *The Journal of the Acoustical Society of America*, 109:2334 – 2335.

Tappert, F. D. (1977). *Wave propagation and underwater acoustics*, chapter 5. The parabolic approximation method, pages 224 – 287. Springer-Verlag, Berlin, Germany.

Tappert, F. D. and Nghien-Phu, L. (1986). *Ocean seismo-acoustics: low-frequency underwater acoustics*, chapter Modeling og pulse response functions of bottom interacting sound using the parabolic equation method, pages 129 – 137. Plenum Press, New York, United States of America.

Thomas, L. and Marques, T. A. (2012). Passive acoustic monitoring for estimating animal density. *Acoustics Today*, 8:35 – 44.

Thompson, P. O., Cummings, W. C., and Ha, S. J. (1986). Sounds, source levels, and associated behavior of Humpback whales, Southeast Alaska. *The Journal of the Acoustical Society of America*, 80:735 – 740.

Tollefsen, D. (2006). Range dependent geoacoustic inversion using the parabolic equation and genetic algorithms range - application to gait test cases. Technical Report 02911, Forsvarets Forskningsinstitutt, Kjeller, Norway.

Urick, R. J. (1983). *Principles of underwater sound*. McGraw-Hill Book Company, New York, United States of America.

U.S. Geological Survey (1997). The Universal Transverse Mercator (UTM) grid. `https://pubs.usgs.gov/fs/0142-97/report.pdf`. [Accessed Oct. 20, 2018].

U.S. Office of Naval Research (1999). The ocean acoustics library. `http://oalib.hlsresearch.com/PE/index.html`. [Accessed Jan. 15, 2018].

Wahlberg, M., Beedholm, K., Heerfordt, A., and Møhl, B. (2011). Characteristics of biosonar signals from the Northern bottlenose whale, Hyperoodon ampullatus. *The Journal of the Acoustical Society of America*, 130:3077 – 3084.

Walker, R. (2016). Density of materials. `https://www.simetric.co.uk/si_materials.htm`. [Accessed June. 11, 2018].

Watkins, W. A. (1981). Aktivities and underwater sounds of Fin whales. Technical Report 33, Whales Research Institute, Tokyo, Japan.

Watkins, W. A., Tyack, P., Moore, K. E., and Bird, J. E. (1987). The 20-Hz signals of Finback whales (Balaenoptera physalus). *The Journal of the Acoustical Society of America*, 82:1901 – 1912.

Wensveen, P. J. (1995). *The effects of sound propagation and avoidance behaviour on naval sonar levels recieved by cetaceans*. PhD thesis, University of St. Andrews, St. Andrews, United Kingdom.

Wetton, B. T. R. and Brooke, G. H. (1990). Modeling of reciprocity in the time domain using the parabolic equation method. *The Journal of the Acoustical Society of America*, 87:624 – 631.

White, P. (2015a). Lecture notes in Underwater Acoustics. Institute of Sound and Vibration Research, University of Southampton. Southampton, United Kingdom.

White, P. (2015b). Professor of Underwater Acoustics at Institute of Sound and Vibration Research, University of Southampton. Personal communication. Southampton, United Kingdom.

Wood, A. B. and Weston, D. E. (1964). The propagation of sound in mud. *Acta Acustica*, 14:156 – 162.

Ying-Tsong, L., Collis, J. M., and Duda, T. F. (2012). A three-dimensional parabolic equation model of sound propagation using higher-order operator splitting and Padé approximants. *The Journal of the Acoustical Society of America*, 132:EL364 – EL370.

Zhu, T. (2016). GEOL 615: Some useful numbers. `http://www.jsg.utexas.edu/tyzhu/files/Some-Useful-Numbers.pdf`. [Accessed March 10, 2018].

Ødegaard, L. (2015). Ocean soundscape measurements at the LoVe Ocean Obervatory. In Papadakis, J. S. and Bjørnø, L., editors, *Proceedings of the 3rd Underwater Acoustics Conference and Exhibition*, Crete, Greece.

Øien, N. (2018). Fin whale. `http://www.imr.no/temasider/sjopattedyr/hval/finnhval/en`. [Accessed April 14th, 2018].